Experimental Study of Turbulent Flow over Inclined Ribs in Adverse Pressure Gradient

by

Jonathan Mawuli Tsikata

A Thesis Submitted to the Faculty of Graduate Studies of

The University of Manitoba

In Partial Fulfillment of the Requirements for the Degree of

Doctor of Philosophy

Department of Mechanical and Manufacturing Engineering
University of Manitoba
Winnipeg, Manitoba
Canada

ABSTRACT

This thesis is an experimental study of turbulent flows over smooth and rough walls in a channel that consists of an upstream parallel section to produce a fully developed channel flow and a diverging section to produce an adverse pressure gradient (APG) flow. The roughness elements used were two-dimensional square ribs of nominal height $k = 3$ mm. The ribs were secured to the lower wall of the channel and spaced to produce the following three pitches: $2k$, $4k$ and $8k$, corresponding to d-type, intermediate and k-type rough walls, respectively. For each rough wall type, the ribs were inclined at 90°, 45° and 30° to the approach flow. The velocity measurements were performed using a particle image velocimetry technique.

The results showed that rib roughness enhanced the drag characteristics, and the degree of enhancement increased with increasing pitch. The level of turbulence production and Reynolds stresses were significantly increased by roughness beyond the roughness sublayer. It was observed that the population, sizes and the level of organization of hairpin vortices varied with roughness and more intense quadrant events were found over the smooth wall than the rough walls.

APG reinforced wall roughness in augmenting the equivalent sand grain roughness height, turbulence production and Reynolds stresses. APG also reduced the sizes of the hairpin packets but strengthened the quadrant events in comparison to the results obtained in the parallel section.

The secondary flow induced by inclined ribs significantly altered the distributions of the flow characteristics across the span of the channel. Generally, the mean flow was less uniform close to the trailing edge of the ribs compared to the flows at the mid-span and close to the leading edge of the ribs. The Reynolds stresses and hairpin packets were distinctly larger close to the trailing edge of the ribs. Rib inclination also decreased the drag characteristics and significantly modified the distributions of the Reynolds stresses and quadrant events. In the parallel section, the physical sizes of the hairpin packets were larger over 45° ribs whereas in the diverging section, the sizes were larger over perpendicular ribs.

ACKNOWLEDGEMENTS

I am very grateful to the Almighty God for guiding me through this program. I would also like to thank my supervisor, Dr. Mark Francis Tachie for giving me the chance to work in this valuable and challenging area of research. Your invaluable patience and guidance during this research period are duly appreciated.

I am very thankful to my wife, father, and all relatives and friends for their encouragement and supports during this program. To my mother (of blessed memory), I am exceptionally pleased and appreciative of your keen interest in my education. The technical assistance provided by Paul Krueger is sincerely appreciated. I extend my profound gratitude to my Committee Members (Dr. Luciano Castillo, Dr. Bing-Chen Wang and Dr. Ying Chen) for their useful suggestions during the preparation of this thesis.

The financial supports provided by University of Manitoba via University of Manitoba Graduate Fellowship (UMGF), and Minister of Advanced Education and Literacy via Manitoba Graduate Scholarship (MGS) are gratefully acknowledged.

DEDICATION

This thesis is dedicated to my wife, Magdalene Emefa Tsikata, and my daughter, Jonalene Kekeli Tsikata for their continuous love and patience during this program. Also, to the memory of my late mother Atoeshie Akpe-Doe.

TABLE OF CONTENTS

LIST OF FIGURES

LIST OF TABLES

NOMENCLATURE

ENGLISH SYMBOLS

a	Additive constant in power law
a_1	Townsend structure parameter
C	Smooth wall constant (C = 5.0 for κ = 0.41)
C_f	Friction coefficient
C_i, C_o	Power law multiplicative coefficients
d_o	Virtual origin [mm]
H	Momentum or Karman-type shape factor
H	Hyperbolic hole size, as in Eq. 1.22 and Eq. 1.23
$I_{i,\,H}$	Indicator function
l	Mixing length [mm]
Lx_{uu}, Ly_{uu}	Length scales of R_{uu} contours in the x-y plane [mm]
Lx_{uu}, Lz_{uu}	Length scales of R_{uu} contours in the x-z plane [mm]
Lx_{vv}, Ly_{vv}	Length scales of R_{vv} contours in the x-y plane [mm]
Lx_{ww}, Lz_{ww}	Length scales of R_{ww} contours in the x-z plane [mm]
k	Roughness element height [mm]
K	Non-dimensional pressure gradient parameter
k_s	Equivalent sand grain roughness height or height of sand grains [mm]
k_s^+	Equivalent sand grain roughness height or roughness Reynolds number ($k_s^+ = k_s U_\tau / \nu$)
$M_{i,j}$	Skewness factors ($M_{ij} = \overline{u^i v^j} / {u_{rms}}^i {v_{rms}}^j$, where $i + j = 3$, $i, j \geq 0$)
N	Total number of samples
N_i	Number of quadrant event detection (i =, 1, 2, 3, 4)
p	Pitch [mm]

P	Thermodynamic pressure [Pa]
p/k	Pitch-to-height
P_q	Production term for turbulence kinetic energy [m^2/s^3]
P_{-uv}	Production term shear stress [m^2/s^3]
$Q1$	Outward motion
$Q2$	Ejection event
$Q3$	Inward motion
$Q4$	Sweep event
q	Turbulence kinetic energy per unit mass [m^2/s^2]
Re	Reynolds number
Re_h	Reynolds number based on channel half-height (= $U_m h/\nu$)
Re_θ	Reynolds number based on momentum thickness (= $U_m\theta/\nu$)
Re_τ	Reynolds number based on friction velocity (= $U_\tau\delta/\nu$)
R_{uu}	Streamwise auto-correlation function
R_{uv}, R_{uw}	Cross-correlation function
R_{vv}	Wall-normal auto-correlation function
R_{ww}	Spanwise auto-correlation function
S_D	Diverging section
S_P	Parallel section
u, v, w	Streamwise, wall-normal, spanwise turbulence intensities (also u_{rms}, v_{rms}, w_{rms}) [m/s]
u', v', w'	Streamwise, wall-normal and spanwise fluctuating velocities [m/s]
u_c	Deviation from the convection velocity [m/s]
U_c	Convection velocity [m/s]
U_i	Total instantaneous velocity [m/s]

U_m	Maximum mean velocity [m/s]
U_τ	Friction velocity [cm/s]
$\overline{u^2}$	Streamwise Reynolds normal stress [m^2/s^2]
$-\overline{uv}$	Reynolds shear stress [m^2/s^2]
$\overline{v^2}$	Wall-normal Reynolds normal stress [m^2/s^2]
x, y, z	Streamwise, wall-normal and spanwise coordinate directions
y_U	y-location where maximum U occurred [mm]
y_{uv}	y-location where the Reynolds shear stress changes sign [mm]

GREEK SYMBOLS

α	Rib inclination angle to the approach flow [°]
β	Clauser pressure gradient parameter
β	Inclination angle of R_{uu} contours in the x-y plane [°]
δ	Boundary layer thickness [mm]
δ^*	Displacement thickness [mm]
Δ	Defect thickness [mm]
ΔB	Roughness function
ΔQ_0	Sweep event – Ejection event at $H = 0$
γ	Power law exponent
κ	Karman constant for logarithm law equation ($\kappa = 0.41$ in Eq.1.12-Eq. 1.19 and $\kappa = 0.42$ in Eq. 1.20)
λ_{ci}	Swirling strength
Π	Coles wake parameter
θ	Momentum thickness [mm]
θx_{uu}, θz_{ww}	Inclination angles of R_{uu} and R_{ww} contours in the x-z plane [°]

ρ	Fluid density [kg/m^3]
ρ_{uv}	Reynolds shear stress correlation coefficient
ν	Kinematic viscosity [m^2/s]
ν_τ	Eddy viscosity [m^2/s]
τ_w	Wall shear stress [N/m^2]
ϕ_0	Ratio of ejection event to sweep event at $H = 0$

SUBSCRIPT

m, max Maximum

SUPERSCRIPT

+	Normalization with U_τ^{i} and ν/U_τ, i = 1, 2 …

ACRONYMS

APG	Adverse pressure gradient
FDC	Fully developed channel
FPG	Favourable pressure gradient
IA	Interrogation Area
LDA	Laser Doppler anemometry
LES	Large eddy simulation
LSE	Linear stochastic estimate
PIV	Particle image velocimetry
POD	Proper orthogonal decomposition
ZPG	Zero pressure gradient

CHAPTER 1

INTRODUCTION

Wall-bounded turbulent shear flows are encountered in numerous fluid engineering applications, and have been studied extensively using both experimental and numerical methodologies. All the solid surfaces encountered in nature and engineering applications have a certain degree of roughness. For example, flows over riverbeds, turbine blades, aircraft wings and flow in pipes are most likely turbulent and these surfaces are presumably rough. The roughness directly affects the flow characteristics, at least in the immediate vicinity of the wall. These effects may include enhanced mixing as well as mass, momentum and convective heat transport. In view of their prevalence in diverse technological applications, numerous experimental and numerical studies have been conducted to understand the effects of wall roughness on the characteristics of both the velocity and temperature fields in wall-bounded flows.

A number of roughness elements have been used to model surface roughness and to study their effects on the flow field. These roughness elements are generally classified into the following two main categories: two-dimensional and three-dimensional roughness elements. The two-dimensional roughness elements include transverse ribs of square, circular, semi-circular and triangular cross-sections while the three-dimensional roughness elements include sand grains, gravels, wire mesh, perforated plates, spheres and hemispheres. Two-dimensional transverse square ribs are also used in many industrial applications to augment convective heat transfer, for example, in heat exchangers, gas turbine blades and cooling system of nuclear reactors. In these applications, the ribs are often inclined at an angle to the approach flow. Prior experimental studies of the thermal field demonstrate that inclined transverse square ribs augment convective heat transfer better than ribs positioned perpendicular to the approach flow. Additionally, inclined ribs produce lower drag in comparison to perpendicularly positioned ribs. It is important to note that coherent structures are essential part of the mechanisms responsible for momentum transport and convective heat transfer. Therefore, an in-depth understanding of the velocity fields and coherent structure over ribs will lead to efficient design of devices such as heat exchangers, nuclear reactors and gas turbines.

The mean velocity and turbulence statistics over smooth and rough walls are also affected by the mean streamwise pressure gradient ($\partial P/\partial x$, where P is the thermodynamic pressure and x is the streamwise distance). The streamwise pressure gradient is defined as the rate of change of the mean pressure with respect to streamwise distance. The mean pressure gradient that is imposed on the flowing fluid may be a zero pressure gradient (ZPG), a favourable pressure gradient (FPG) or an adverse pressure gradient (APG). FPG flows are encountered in nozzles, over turbine blades and re-entry vehicles, while APG flows are also encountered in diffusers and draft tubes of hydro power plants.

The zero pressure gradient flows and internal (fully developed channel or pipe) flows are often collectively termed canonical wall-bounded flows. These flows are the most investigated near-wall turbulent flows over both smooth and rough walls because their flow fields are relatively less complex compared with those with pressure gradients. Although FPG and APG flows over smooth wall have also been studied in detail, FPG and APG turbulent flows over rough walls have not received significant research attention. As a result, our understanding of the combined effects of roughness and pressure gradients on the turbulence statistics and coherent structures is deficient compared to the velocity field over smooth walls. It is therefore critically important to conduct detailed velocity measurements in APG turbulent flows over rough walls to improve the understanding of the combined effects of roughness and APG on turbulent flows. The results from such research will lead to the design of more efficient fluid engineering devices such as gas turbines where the performance is affected by both APG and wall roughness.

This thesis pertains to a comprehensive experimental study of APG turbulent flows over rough walls in a channel that consists of a parallel section to produce a fully developed flow and a diverging section to produce an APG flow. The rough walls are modeled using two-dimensional transverse square ribs. The flow fields over reference smooth walls are also studied to facilitate the discussion of the APG flows over the ribs.

In this chapter, the governing equations of turbulent flows are presented. Also, the boundary layer parameters that are relevant for analyzing and interpreting the experimental results are presented. Distinction is made among the three main types of pressure gradients in the subsequent section. This is followed by the description of the various regions of the mean velocity profiles in a wall-bounded turbulent flow and the applicable scaling laws. The next section provides an overview of rough walls with emphasis on two-dimensional rough walls and the roughness regimes. The wall similarity hypothesis is discussed in the subsequent section. An overview of coherent structure is then presented along with some of the techniques employed for educing these coherent structures. The last two sections of this chapter address motivation and objective for this research and finally the thesis outline.

1.1 THE GOVERNING EQUATIONS

For a steady state turbulent flow of an incompressible fluid, the Reynolds-Average Navier-Stoke (RANS) equation is:

$$U_j \frac{\partial U_i}{\partial x_j} = -\frac{1}{\rho}\frac{\partial P}{\partial x_i} + \nu \nabla^2 U_i - \frac{\partial \overline{u_i u_j}}{\partial x_j} \tag{1.1}$$

where ρ is the fluid density and ν is the kinematic viscosity, the indexes i and j take values of 1, 2, 3; and x_1, x_2 and x_3 are, respectively, in the streamwise (x), wall-normal (y) and spanwise (z) coordinate directions. Similarly, U_1, U_2 and U_3, respectively, represent the velocity components (U, V and W) in the x, y and z directions. The continuity equation is as follows:

$$\frac{\partial U_i}{\partial x_i} = 0 \tag{1.2}$$

The transport equation for the turbulence kinetic energy q (=$\overline{u_i u_i}/2$) is:

$$\underbrace{U_j \frac{\partial q}{\partial x_j}}_{\text{advection}} = \underbrace{-\overline{u_i u_j}\frac{\partial U_i}{\partial x_j}}_{\text{production}} \underbrace{-\frac{\partial \overline{u_j (u_i u_i / 2)}}{\partial x_j}}_{\text{turbulence diffusion}} - \underbrace{\frac{1}{\rho}\frac{\partial \overline{p u_i}}{\partial x_i}}_{\text{pressure diffusion}}$$

$$+ \underbrace{\nu \nabla^2 q}_{\text{viscous diffusion}} - \underbrace{\nu \overline{\frac{\partial u_i}{\partial x_j}\frac{\partial u_i}{\partial x_j}}}_{\text{dissipation}} \tag{1.3}$$

1.2 BOUNDARY LAYER PARAMETERS

Some useful parameters of wall-bounded flows are defined below. In this work, the boundary layer thickness, δ is defined as the distance from the wall to the location where the local mean velocity is $0.99U_m$, where U_m is the maximum mean velocity. The boundary layer thickness is a measure of the extent by which the flow is retarded by the wall. The displacement thickness (δ^*) is defined as the distance the fixed boundary would have to be displaced normal to itself (into the fluid) in order for a flow at constant velocity (say, U_m) to have the same local mass flux over the surface as the actual flow. It is a measure of how far the streamlines of the outer flow are displaced by the boundary layer. For an incompressible flow, the displacement thickness is expressed as:

$$\delta^* = \int_0^\delta (1 - \frac{U}{U_m}) dy \tag{1.4}$$

The momentum thickness, θ is the thickness that a layer of fluid (traveling at U_m) would have had for it to have a momentum flux equal to that lost by the retarding effect of the boundary. For an incompressible flow, θ is given by:

$$\theta = \int_0^\delta \frac{U}{U_m} (1 - \frac{U}{U_m}) dy \tag{1.5}$$

The ratio of the displacement thickness to the momentum thickness is called momentum shape factor or the Karman-type shape factor, H (= δ^*/θ). The shape factor, therefore, expresses the ratio of mass flux deficit to momentum flux deficit.

1.3 MEAN PRESSURE GRADIENT

Different parameters are used to characterize the non-dimensional pressure gradient. The pressure gradient parameter, K (often referred to as deceleration parameter if the flow is APG and acceleration parameter if the flow is FPG) is one of the most common non-dimensional parameter used to characterize the pressure gradient. Outside the boundary layer, the flow is essentially inviscid, and Bernoulli's theorem implies that $P + (\rho U_m^2)/2$

is constant to a good approximation. Taking derivative with respect to x yields $dP/dx = -\rho U_m dU_m/dx$. The expression for K is then given as:

$$K = \frac{\nu}{U_m^2}\frac{dU_m}{dx} \tag{1.6}$$

If the mean pressure is invariant with the streamwise direction, then $\partial P/\partial x = 0$ and the mean pressure gradient is termed zero pressure gradient (ZPG). From Eq. 1.6, to attain ZPG, U_m should be constant with respect to x, thereby making $K = 0$. A favourable pressure gradient (FPG) occurs when the mean pressure decreases in the mean flow direction ($\partial P/\partial x < 0$) resulting in the acceleration of the fluid. In this case, U_m increases with x, so that $K > 0$ as in a converging channel. For an adverse pressure gradient (APG), the mean pressure increases in the direction of the flow ($\partial P/\partial x > 0$), and this occurs when U_m is decreasing with x, for example, in a diverging channel. In this case, K is less than zero.

The Clauser pressure gradient parameter (β) is another non-dimensional parameter and is given by:

$$\beta = \frac{\delta^*}{\tau_w}\frac{dP}{dx} \tag{1.7}$$

where τ_w is the wall shear stress and dP/dx is the pressure gradient. Clauser (1954) showed that a boundary layer with variable pressure gradient but constant β is in equilibrium. In this case, all the gross properties of the boundary layer can be scaled with a single characteristic length scale for which he proposed the defect thickness, Δ (given as $\Delta = \delta^*\lambda$, where $\lambda = (2/C_f)^{1/2}$, and C_f is the skin friction coefficient). The present study pertains to APG flows, therefore, attention will be focused on APG, henceforth.

1.3.1 ADVERSE PRESSURE GRADIENT (APG)

Compared to ZPG, APG makes the mean streamwise velocity profile 'less uniform' and the shape factor, H increases accordingly. In an APG turbulent boundary layer, the mean flow is directed outwards from the surface, which tends to cause the boundary layer to be thicken with streamwise distance. This effect is reinforced by transverse turbulent momentum transfer, and as a result, the boundary layer thickness increases rapidly. It is important to note that the fluid in the inner part of the boundary layer moves slower than in the outer region. For a large enough pressure increase, the fluid may slow to zero velocity in the wall region and may even become reversed thereby separating from the surface. This may have practical consequences in aerodynamics since flow separation significantly modifies the pressure distribution along the surface and hence the lift and drag. An adverse pressure gradient exists in draft tubes of hydroelectric power plants, near the trailing edges of airfoils or at the termination of the streamlined bodies such as submarines or ships, and often plays a critical role in their performance.

1.4 SCALING CONSIDERATION OF THE BOUNDARY LAYER

In accordance with classical theories, a turbulent boundary layer can be divided into two distinct regions, namely the inner region and the outer region. At a sufficiently high Reynolds number, there exists an intermediate layer between the inner and outer regions called overlap region. Figure 1.1 shows a sketch of the different regions of a turbulent boundary layer and their extent. The various regions are discussed below.

1.4.1 THE INNER LAYER

The inner region ($0 \leq y^+ \leq 0.2\delta^+$, where superscript denotes normalization with wall variables that are defined later) is the region adjacent to the solid boundary where the flow dynamics are strongly influenced by viscosity. The inner region is further divided into a thin viscous sublayer ($y^+ \leq 5$) adjacent to the solid surface and a buffer layer that bridges the viscous sublayer with the overlap region. The dynamics of the flow in the viscous sublayer is largely influenced by viscosity. Also, the turbulence shear stress is nearly zero in the viscous sublayer. The buffer layer ($5 < y^+ < 30$) is the home to many of the most interesting dynamical processes of turbulent flows including turbulence production. It is the transition region between the viscosity-dominated and the turbulence-dominated parts of the flow (Pope, 2000). In this region, both viscous stress and turbulence shear stress are important.

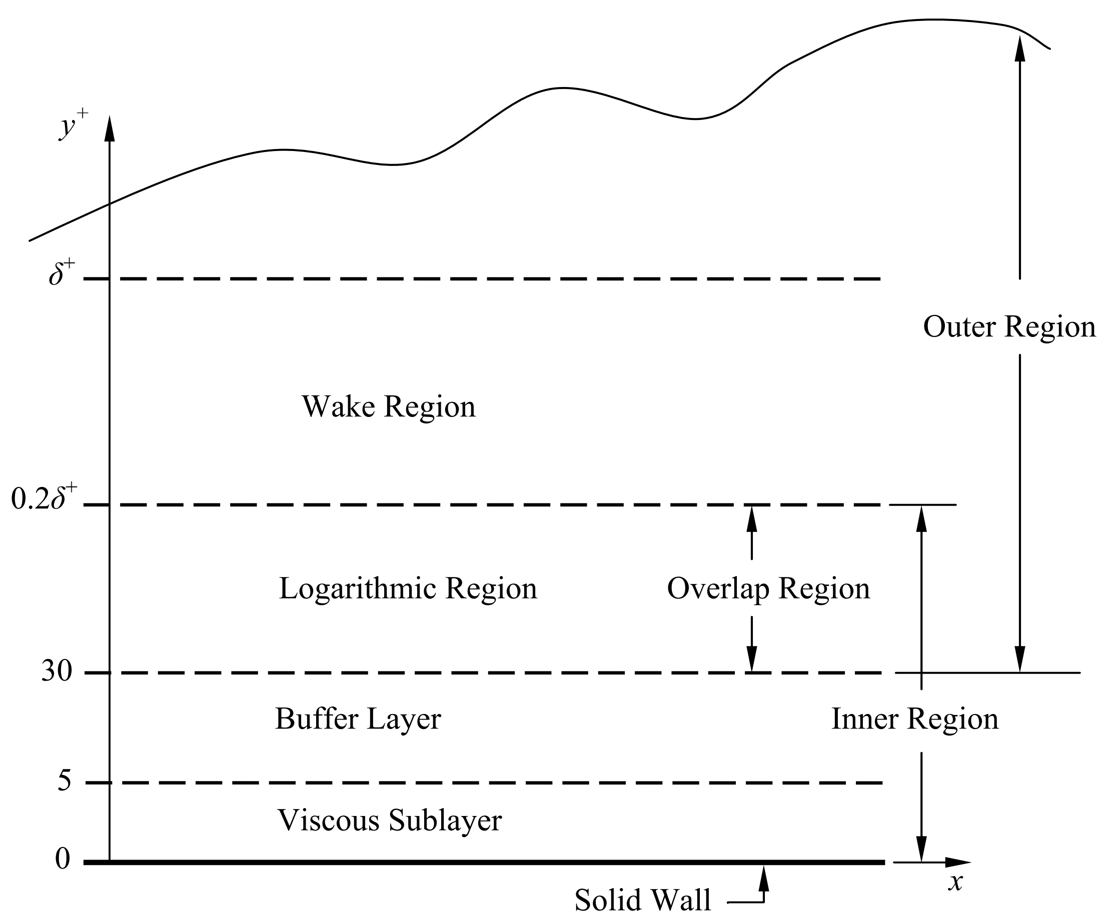

Figure 1.1: Conceptualization of turbulent boundary layer regions. Not drawn to scale.

The relevant parameters that influence the flow dynamics in the inner region are the fluid density (ρ), kinematic viscosity (ν) and the wall shear stress (τ_w). The relevant velocity scale close to the wall is the friction velocity, U_τ (= $(\tau_w/\rho)^{1/2}$) and the relevant length scale is viscous length scale, (ν/U_τ). The use of these scales (U_τ and ν/U_τ) is often referred to wall variables (or inner scaling), and are denoted by the superscript '+' in this thesis. For example, y^+, U^+, and $\overline{v^{+2}}$ denote $y/(\nu/U_\tau)$, U/U_τ, and $\overline{v^2}/U_\tau^2$, respectively. Prandtl (1925) first formulated the following inner law to describe the mean velocity profile:

$$U^+(y^+) = f(y^+) \tag{1.8a}$$

where $f(y^+)$ is a universal function presumably independent of Reynolds number and streamwise location. In the viscous sublayer (i.e., $y^+ \leq 5$), the mean velocity profile is linear, and Eq. 1.8a reduces to:

$$U^+ = y^+ \tag{1.8b}$$

1.4.2 THE OUTER LAYER

The outer region ($30 \leq y^+ \leq \delta^+$) is independent of the direct influence of the wall boundary. It is characterized by a diminishing turbulence shear stress, but dominated by inertial effects. The outer region is usually scaled using the boundary layer thickness (δ) and the fiction velocity (U_τ) or the freestream/maximum velocity (U_m).

The outer region of the mean velocity profiles is often studied using the mean velocity defect law. This is partly based on the observation made by Clauser (1954) and Hama (1954) that the mean velocity in the outer region expressed in velocity defect form is independent of wall boundary condition. Thus, the similarity of the mean velocity in the outer region is evaluated using the velocity-defect law given as:

$$U_m^+ - U^+ = g(y/\delta, \beta) \tag{1.9}$$

George and Castillo (1997) showed that, for a ZPG turbulent boundary layer, the appropriate scale for the outer region is the freestream velocity (U_m). Hence, the velocity-defect distribution is represented by,

$$(U_m - U)/U_m = g(y/\delta, \beta) \tag{1.10}$$

Later, Zagarola and Smits (1998) proposed the following so-called mixed scaling for the defect velocity profile:

$$(U_m - U)/U_m(\delta^* / \delta) = g(y/\delta) \tag{1.11}$$

1.4.3 THE OVERLAP REGION

The overlap region ($30 \le y^+ \le 0.2\delta^+$), is a region that bridges the inner region with the outer region. For near-wall turbulent flows, the scaling law for the overlap region is very important since it is often used to determine the friction velocity and wall shear stress. In the overlap region, the dynamics of the flow are dependent on the distance from the wall (y). This is because the inner length scale (ν/U_τ) is apparently too small to control the dynamics of the flow and the outer length scale (δ) is too large to be effective (Tennekes and Lumley, 1972). Millikan (1938) proposed a logarithmic law for the overlap region. Barenblatt (1993) and George and Castillo (1997) argued that the overlap region is better described by a power law.

1.4.3.1 Logarithmic Law

For sufficiently high Reynolds number, the mean velocity profile in the overlap region is well described by the logarithmic law proposed by Millikan (1938). Millikan (1938) assumes complete similarity, and matched the law of the wall (Eq. 1.8a) and the defect law (Eq. 1.9) to obtain the logarithmic law for the mean velocity profile in the overlap region. The logarithmic law for turbulent flow over a smooth wall is:

$$U^+ = \frac{1}{\kappa}\ln y^+ + C \tag{1.12}$$

where κ is the von Karman constant and C is the smooth wall constant. Typical values of these logarithmic law constants are $\kappa = 0.41$ and $C = 5.0$. Beyond the overlap region, the mean flow shows a signature of a wake flow. Coles (1956) proposed a term, $(2\Pi/\kappa).f(y/\delta)$ to describe the behaviour of the flow in the outer region thereby accounting for the wake nature of the mean flow. A complete equation that describes the overlap and outer regions of the mean velocity is:

$$U^+ = \frac{1}{\kappa}\ln y^+ + C + \frac{2\Pi}{\kappa} f(y/\delta) \tag{1.13}$$

where Π is the Coles wake parameter, f is the universal function of y/δ that represents the effect of the outer-layer dynamics. The term $2\Pi/\kappa$ measures the contribution of the outer-layer structures to the mean velocity profile. Previous studies of APG turbulent flows (Samuel and Jourbert, 1974; Cutler and Johnston, 1989; Aubertine and Eaton, 2006) have indicated that Eq.1.12 describes the overlap region of the mean velocity reasonably well. It should, however, be noted that in the presence of adverse pressure gradient, the logarithm region shrinks as the wake region begins to dominate the flow.

1.4.3.2 Power Law

Barenblatt (1993), and George and Castillo (1997) challenged the validity of the logarithm law in the overlap region. They argued that the overlap region is best described by the power, for which they individually proposed a form of a power law. In this thesis, only the power law proposed by George and Castillo (1997) is used to analyze the experimental results.

George and Castillo (1997) used the asymptotic invariance principle (AIP) to derive a power law relation for the mean velocity in the overlap region of a zero pressure gradient turbulent boundary layer. They argued that, except in the limit of infinite Reynolds number, the overlap region is Reynolds number dependent since the ratio of the inner and outer velocity scales (U_τ/U_m) is Reynolds number dependent. They assumed complete similarity in the inner and outer layers in the limit of infinite Reynolds numbers to derive power laws for these layers. The power laws for the mean velocity in the inner and outer coordinates are respectively given as:

$$U^+ = C_i(y^+ + a^+)^\gamma \tag{1.14}$$

$$U/U_m = C_o[(y + a)/\delta]^\gamma \tag{1.15}$$

where the multiplicative coefficients, C_i and C_o, as well as the exponent γ, are dependent on the local Reynolds number ($\delta^+ = \delta U_\tau/\nu$). In the above equations, a represents a shift in the origin for measuring y associated with the growth of the mesolayer region ($30 \leq y^+ \leq 300$) and the value of $a^+ = -16$ is adopted. It should be noted that the origin shift, a, was not derived from asymptotic invariance principle, but rather introduced on the basis of additional arguments. They expect a^+ to be nearly constant based on the argument that any shift of the overlap layer in y must be accomplished by the inner layer. George and Castillo (1997) showed that the friction law is also a power law:

$$U_\tau/U_m = (C_o/C_i)^{2/(1+\gamma)}(U_m\delta/\nu)^{-2\gamma/(1+\gamma)} \qquad (1.16)$$

In general, the power laws are valid for both finite and high Reynolds number flows. The above power law formulations have been used in the past to model mean velocity profiles over rough wall in open channel turbulent flows (Tachie et al., 2007; Bergstrom et al., 2001), ZPG turbulent boundary layer (Kotey et al., 2003) and APG channel flow over rough walls (Tachie, 2007).

1.5 WALL ROUGHNESS

As noted earlier, three-dimensional roughness elements and two-dimensional elements are the two main categories of roughness elements. Following the works of Perry *et al*. (1969), two-dimensional transverse ribs are classified into *d*-type and *k*-type, based on their pitch-to-height (*p/k*) ratio. Tani (1987) recommended that, for regularly spaced ribs, the demarcation between *d*-type and *k*-type should be made at $p/k = 4$ (hence, the name intermediate type). This classification follows the observation by Perry *et al*. (1969) that for $p/k < 4$, the roughness length scale is proportional to the pipe diameter or boundary layer thickness (hence the *d*) and for $p/k > 4$, the roughness length scale is proportional to roughness height (hence the *k*).

For a *d*-type rough wall, *p/k* is less than 4, suggesting that the roughness elements are more closely spaced. A *d*-type rough wall can sustain stable recirculation vortices that are set up in its grooves. Further, the vortices are isolated from the outer flow, and the eddy shedding from the elements into the flow beyond cavity height is negligible. Thus, the fluid in the outer region flows relatively undisturbed over the crest of the elements. For k-type roughness, p/k is greater than 4. In this case, eddies with a length-scale proportional to k are shed into the flow above the crests of the elements. A k-type rough wall has recirculation bubbles that may reattach ahead of the next rib, exposing it to the outer flow. Unlike a d-type rough wall, there is an interaction between the cavity flow and the overlying flow of a k-type rough wall. The intermediate type rough wall ($p/k = 4$) exhibits flow characteristics that are in-between those of d-type and k-type rough walls.

Following Nikuradse (1933), an equivalent sand grain roughness height, k_s was proposed as a more appropriate roughness length scale, since it provides a universal measure of the influence of the roughness on the mean flow. In a dimensionless form, the equivalent sand grain roughness height is expressed as $k_s^+ = k_s U_\tau/\nu$ (usually referred to as roughness Reynolds number). The value of k_s^+ is often used to classify rough walls into three roughness regimes.

Schlichting (1979) identified the following three different roughness regimes: hydraulically smooth, transitionally rough and fully rough. The roughness regime is said to be hydraulically smooth if the roughness elements are completely contained within the viscous sublayer, i.e., $k_s^+ < 5$. For a fully rough regime ($k_s^+ > 70$), the roughness elements protrude well into the overlap layer, thereby causing the viscous effect to vanish. This may break up the streamwise vortices thereby changing the near-wall turbulence and the mechanisms for turbulence generation. Between these two extremes of roughness regimes is the transitionally rough regime ($5 \leq k_s^+ \leq 70$); in this case, the roughness elements protrude into the viscous sublayer, but the protrusion does not extend deep into the logarithmic layer.

In rough wall turbulence, the origin of the wall-normal axis needs to be redefined to include a reference height called the virtual origin (d_o). Figure 1.2 shows a schematic of a two-dimensional transverse square ribs with k as the roughness element height, p as the pitch and d_o. The axis y' is in the wall-normal direction, measured from the top plane of the roughness element. From the foregoing, the effective wall-normal distance for a rough wall is $y = y' + d_o$. The value of d_o is not known *a priori*, and is often determined through a trial-error-procedure when fitting the mean velocity profile to the logarithmic law. The value of d_o is within the range $0 < d_o < k$.

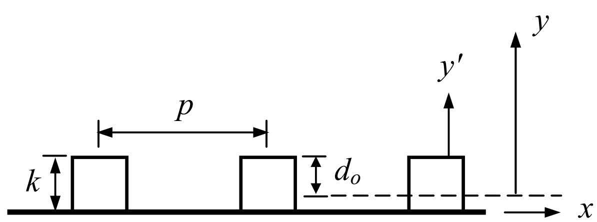

Figure 1.2: Schematic of two-dimensional rough wall

1.5.1 LOGARITHMIC LAW FOR ROUGH WALL

Clauser (1954) and Hama (1954) argued that the effect of roughness on the mean flow is confined to the inner region of the flow. As a result, the mean velocity profile over a rough surface is shifted downward relative to that over smooth wall. This downward shift of the mean velocity profiles caused by roughness is referred to as the roughness function (ΔB). Thus, the logarithmic law for a rough wall is:

$$U^+ = \frac{1}{\kappa}\ln y^+ + C - \Delta B \tag{1.17}$$

When Coles' term is introduced to account for the wake component, the complete equation that describes the overlap and outer regions of the mean velocity profile over rough wall is:

$$U^+ = \frac{1}{\kappa}\ln y^+ + C - \Delta B + \frac{2\Pi}{\kappa} f(y/\delta) \tag{1.18}$$

The roughness function, ΔB is related to roughness Reynolds number k_s^+ as follows:

$$\Delta B = \frac{1}{\kappa}\ln k_s^+ - 3.5 \tag{1.19}$$

In the study of flows over rough walls consisting of transverse square ribs in asymmetric channels, Hanjalic and Launder (1972), and Ikeda and Durbin (2007) adopted a form of the logarithm law to analyze the mean velocity profiles over the rough walls. The logarithm law format adopted by Hanjalic and Launder (1972) and Ikeda and Durbin (2007) is expressed as:

$$U^+ = \frac{1}{\kappa}\ln\frac{y}{k} + E \tag{1.20}$$

where E is an additive parameter which may vary with p/k and pressure gradient. For a k-type rough wall (p/k = 10), Hanjalic and Launder (1972), and Ikeda and Durbin (2007) found that E = 3.2.

1.6 WALL SIMILARITY HYPOTHESIS

The wall similarity hypothesis was postulated by Townsend (1976). According to Townsend (1976), at sufficiently higher Reynolds number, the turbulent flow in the region outside the roughness sublayer is independent of wall roughness. Raupach *et al*. (1991) conjectured that the roughness sublayer where the flow is remarkable dependent on the physical geometry of the roughness elements covers up to about 5k. This hypothesis implies that any effects introduced by the presence of the roughness elements to the flow are confined to the roughness sublayer so that the flow outside the roughness sublayer exhibits characteristics that are structurally similar to turbulent flow over smooth walls.

1.7 COHERENT STRUCTURE

Wall-bounded turbulent flows contain organized motions or flow structures that are collectively called vortical or coherent structures. Although the notion of coherent structures existed for the past decades, there is no consensus on the definition for coherent structures. According to Robinson (1991), coherent structure is a three-dimensional region of the flow over which at least one fundamental flow variable (e.g. velocity component, density, temperature, etc.) exhibits significant correlation with itself or with another variable over a range of space and/or time that is significantly larger than the smallest local scales of the flow. Hussain (1983) defines a coherent structure as a connected, large-scale turbulent fluid mass with a phase-correlated vorticity over its spatial extent, while Kaftori *et al*. (1995) define coherent structures as persistent flow patterns with a larger lifetime and/or spatial extent than the turbulence integral scale. From the above three definitions, it is clear that underlying the three-dimensional random fluctuations characterizing turbulence, there is an organized component of the vorticity which is phase correlated over the extent of the structure. Over the past decades, various forms of coherent or turbulence structures have been identified including vortex tubes (Farge *et al*., 2001), vortex rings, streaks and hairpin vortices (Theodorsen, 1952; Robinson, 1991). The inner and outer regions of wall-bounded flows, for example, are populated with an array of hairpin vortices spatially aligned in the streamwise direction, forming correlated packets or trains of vortices (Adrian *et al*., 2000a; Christensen and Adrian, 2001). According to Zhou *et al*. (1997) and Adrian *et al*. (2000a), this correlation leads to enhancement of Reynolds stresses by collective transfer of momentum between the hairpin vortices. Coherent structures are characteristics of turbulent flows, therefore, the benefits of understanding the physics of coherent structures cannot be overemphasized in fluid engineering applications. It has been suggested that the vital flow physics is hidden within these coherent structures. The practical implications of understanding coherent structure lie in the significant improvement of design and safety of natural and man-made systems involving turbulent flows. It also provides avenue for understanding turbulence management and control (Kostas *et al*., 2005). Coherent structures have been associated with heat, mass and momentum transport, as well as mixing and drag generation.

The identification and description of coherent structures have been done through flow visualization, instantaneous decomposition of velocity fields and statistical analysis. An example of instantaneous decomposition techniques used to visualize vortices in a given instantaneous velocity field is Galilean decomposition. The statistical analysis entails isolation and analysis of characteristics of large datasets to obtain average structure using ensemble-averaging techniques. Among these techniques are quadrant decomposition, linear stochastic estimation (LSE), conditional sampling and averaging, probability density function analysis, two-point correlation functions and proper orthogonal decomposition (POD). An overview of some of the specific techniques used in this thesis is provided below.

1.7.1 GALILEAN DECOMPOSITION

The Galilean decomposition is the simplest method of decomposition that can be used to visualize small-scale vortices (Adrian *et al*., 2000b). The technique requires that the total instantaneous velocity, U_i is represented as the sum of a constant convection velocity, U_c and the deviation, u_c:

$$U_i = U_c + u_c \tag{1.21}$$

where U_c is usually a fraction of the maximum velocity, U_m, for example, $U_c = 0.5U_m$. It should be noted that each value of the convection velocity corresponds to a different translational velocity of groups of vortices embedded within the flow (Adrian *et al*., 2000b). When the convection velocity matches the translational velocity of a vortex or an eddy, the vortex becomes identifiable as a roughly circular pattern of velocity vectors (Robinson *et al*., 1989). According to Robinson *et al*. (1989), a vortex exists when instantaneous streamlines mapped onto a plane normal to the vortex core exhibit a roughly circular or spiral pattern, when viewed from a reference frame moving with the centre of the vortex core.

1.7.2 QUADRANT DECOMPOSITION

The quadrant decomposition is an unambiguous technique for defining turbulent events occurring in the boundary layer. It is a convenient tool for extracting information about changes in coherent structures when comparing turbulent flows. It was introduced by Wallace *et al*. (1972) and Willmarth and Lu (1972). In the quadrant decomposition technique, the local flow is divided into four quadrants based on the signs of the streamwise and wall-normal velocity fluctuations (u' and v', respectively). Thus, in the quadrant decomposition technique, one considers the frequency of occurrence and contribution to the Reynolds shear stress, $-\overline{uv}$ of the velocity fluctuations lying in the four quadrants defined by: (*i*) $Q1$: $u' > 0$, $v' > 0$, (*ii*) $Q2$: $u' < 0$, $v' > 0$, (*iii*) $Q3$: $u' < 0$, $v' < 0$, and (*iv*) $Q4$: $u' > 0$, $v' < 0$. These events are illustrated on the u'-v' plane in Figure 1.3.

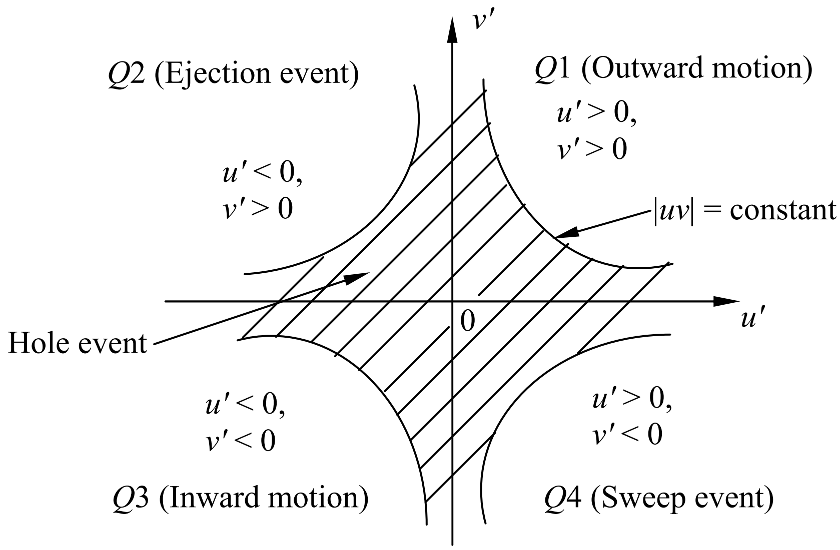

Figure 1.3: Schematic of the division of the u'-v' coordinates and the hole event

The most significant events are $Q2$ (ejections) which transport low-momentum fluid upwards, and $Q4$ events (sweeps) which transport high-momentum fluid downwards. According to Coceal *et al*. (2007), the relative frequency of occurrence of ejections and sweeps and their contribution to $-\overline{uv}$ is an indicator of coherent structure in a turbulent boundary layer. Studies have demonstrated that wall-bounded turbulence are characterized by a greater number of sweeps relative to ejections, but the fewer ejections contribute more to $-\overline{uv}$ because they tend to be stronger (Finnigan, 2000). The $Q1$ and $Q3$ events are generally rare and contribute little to the Reynolds shear stress.

Using the Lu and Willmarth (1973) concept of a hyperbolic hole of size H, defined by $|u'v'| = H\overline{uv}$, the contribution to $-\overline{uv}$ from a particular quadrant can be written as:

$$(u'v')_{i,H} = \frac{1}{N}\sum_{i=1}^{N} u'v' I_{i,H} \tag{1.22}$$

where N is the total number of samples and $I_{i,H}$ is an indicator function defined so that

$$I_{i,H}(u',v') = \begin{cases} 1 & \text{if } (u',v') \text{ is in quadrant } i \text{ and if } |u'v'| \geq H\overline{uv} \\ 0 & \text{otherwise} \end{cases} \tag{1.23}$$

The value H represents a threshold on the strength of the Reynolds-stress-producing events considered in the analysis. When H = 0, all Reynolds shear stress events are included in the decomposition and increasing value of H allows inclusion of only increasingly strong Reynolds stress-producing events. The percentage contribution from each quadrant Q_i can be obtained from

$$Q_i(\%) = \frac{(u'v')_i}{\overline{uv}} \times 100\% \tag{1.24}$$

1.7.3 TWO-POINT CORRELATION FUNCTIONS

The two-point correlation can be used to determine the distances over which the turbulence field is correlated across the flow. It can also be used to quantify the average extent and inclination of the hairpin vortex packets. For example, the angle of inclination of the spatial autocorrelation in the streamwise direction is related to the average inclination of the hairpin packets (Volino *et al*., 2007). The two-point correlation can also be used to estimate the integral length scale. In this case, the area under the two-point velocity correlation curve is often interpreted as the integral length scale.

The two-point correlation functions for any two arbitrary quantities A and B in a plane at a reference point $X_{ref}(x_{ref}, y_{ref})$ separated by ΔX is:

$$R_{ab}(X_{ref}, X) = \frac{\overline{a'(x_{ref}, y_{ref})b'(x_{ref} + \Delta x, y_{ref} + \Delta y)}}{a_{rms}(x_{ref} + \Delta x, y_{ref} + \Delta y)b_{rms}(x_{ref} + \Delta x, y_{ref} + \Delta y)} \tag{1.25}$$

where a_{rms} and b_{rms} are the standard deviations of A and B , respectively, at $X_{ref}(x_{ref}, y_{ref})$ and $X = X_{ref} + \Delta X$. The a_{rms} and b_{rms} represent the turbulence intensities, while a' and b'

are the fluctuating quantities. In the x-y plane, for example, a_{rms} and b_{rms} are, respectively, the streamwise (u_{rms}) and wall-normal (v_{rms}) turbulence intensities while a' and b' are the streamwise (u') and wall-normal (v') fluctuating velocities, respectively.

1.7.4 LINEAR STOCHASTIC ESTIMATION (LSE)

The linear stochastic estimation is a technique commonly used to estimate the average velocity field associated with a particular conditioning event. Such an estimate has been applied to various kinds of flows: homogeneous shear flow (Adrian, 1988; Adrian and Moin, 1988), turbulent channel flow (Adrian *et al*., 1987; Christensen and Adrian, 2001), ZPG turbulent boundary layer flow (Hambleton *et al*., 2006; Volino *et al*., 2009) and APG turbulent boundary layer flow (Lee and Sung, 2009). These groups of researchers used conditioning events such as swirl, prograde swirl, retrograde swirl and $\overline{uv} < 0$. The $\overline{uv}$ condition employs the combinations of $Q2$ and $Q4$ to determine the average field associated with events contributing towards the Reynolds shear stress. The general finding of the LSE is that a strong swirl motion is induced at the location of the conditioning event. The induced vortical motion formed a crease that propagates away from the event location at an angle that is generally observed to be consistent with the inclination angle of the hairpin packets observed in instantaneous realizations.

In this study, the LSE technique used is similar to that used by Christensen and Adrian (2001), Hambleton *et al*. (2006) and Volino *et al*. (2009). Such a relation is given below (Volino *et al*., 2009):

$$< u_j'(x+\Delta x, y+\Delta y) | \varphi(x, y_{ref}) >$$

$$\approx \frac{< \varphi(x, y_{ref}) u_j'(x+\Delta x, y+\Delta y) >}{< \varphi(x, y_{ref}) \varphi(x, y_{ref}) >} \varphi(x, y_{ref}) \qquad (1.26)$$

where u'_j is the velocity fluctuation vector at distance Δx and Δy from the conditioning event φ.

1.8 RESEARCH MOTIVATION AND OBJECTIVES

From the foregoing, there are both practical and fundamental motivations to understand the dynamics of rough wall turbulence with and without adverse pressure gradient. Extensive experimental and numerical studies have been conducted to investigate the characteristics of zero pressure gradient turbulent flows over both smooth and rough walls. The effects of adverse pressure gradient on smooth wall turbulent flows have also been studied quite extensively. However, only few studies have investigated flows over rough wall in the presence of adverse pressure gradient. Additionally, only few velocity field measurements have been reported on flow over inclined ribs. The combined effects of wall roughness and pressure gradient become far more complex than either ZPG (with or without roughness) or smooth wall turbulent flows subject to adverse pressure gradient. It is therefore important to perform detailed experiments to investigate the effects of pressure gradient on inclined ribs roughness. A better understanding of the turbulence statistics and coherent structures over these ribs are necessary to improve the design of more efficient fluid devices such as heat exchangers, gas turbines and nuclear reactor cooling systems. The study will also provide a comprehensive dataset for validating numerical results.

The objectives of the present study are as follows:

1. To investigate the effects of rib inclination on the turbulence statistics and coherent structures.

2. To document the combined effects of rib roughness and adverse pressure gradient on the turbulence statistics and coherent structures.

To achieve the above objectives, a particle image velocimetry (PIV) system is used to conduct detailed velocity measurements in turbulent flows over repeated inclined transverse ribs. One-point turbulence statistics such as mean velocities, Reynolds stresses, mixing length, eddy viscosity, skewness factors as well as production terms in turbulence kinetic energy and Reynolds shear stress are obtained from the velocity field data to study the effects of roughness and pressure gradients on the flow. Coherent structure analysis is done through Galilean decomposition of instantaneous velocity field, contours of swirling strength, and statistical analysis such as quadrant decomposition, two-point correlation functions of fluctuating velocities and linear stochastic estimation.

1.9 OUTLINE OF THE THESIS

This thesis is an experimental study of turbulent channel flow over smooth and rough walls with adverse pressure gradient using PIV. Chapter 2 provides a review of literatures related to the present research. The experimental setup and measurement procedure are described in Chapter 3. The results of this study are presented and discussed in Chapter 4-Chapter 6. Chapter 7 presents conclusions and recommendations for future work.

CHAPTER 2

LITERATURE REVIEW

This chapter provides a comprehensive review of previous studies on wall-bounded turbulent flows over smooth and rough walls. Section 2.1 presents a general review on canonical near-wall turbulent flows. In this section, emphasis is laid on the organization of turbulence structures over smooth wall. The section concludes with an overview of the effects of Reynolds number on flow characteristics and the differences between fully developed channel flows and turbulent boundary layers. Section 2.2 provides a review on adverse pressure gradient (APG) turbulent flows over smooth walls. Review on ZPG and fully developed channel turbulent flows over rough walls are presented in Section 2.3. In Section 2.4, the combined effects of roughness and APG on near-wall turbulence are reviewed. Summary of the findings on near-wall turbulence studies and the specific objectives of the present study are presented in Section 2.5.

2.1 SMOOTH WALL TURBULENCE

The near-wall region of wall-bounded turbulent flows consists of elongated streaky structures. This was evident in the study by Kline *et al*. (1967) which formed the cornerstone of understanding turbulence production in wall-bounded flows. Kline *et al*. (1967) used hydrogen-bubble technique to perform flow visualization study. Low-speed streaks were observed near the wall ($y^+ < 30$), and they interact with outer portions of the flow through a process of gradual lift-up, then sudden oscillation and breakup. The sequence of these events was referred to as a bursting process. The major part of turbulence production and transport of turbulence between the inner and outer regions of the boundary layer occur during this bursting process. The burst event leads to high $-\overline{uv}$ and, hence increased the level of turbulence production. Johansson *et al*. (1991) opined that the lift-up of fluid from low-speed streaks in the viscous sublayer into the buffer region results in the formation of inclined hairpin vortices. In the buffer region, hairpin vortices are three-dimensional and are inclined at a relatively shallow angle with respect to the wall. The strength and inclination are affected by the shearing action of the mean velocity gradient (Johansson *et al*., 1991).

Theodorsen (1952) first proposed the structural model of a hairpin-like vortical structure which plays vital roles in turbulence transport. This hairpin vortex model is shown in Figure 2.1, and it consists of head, neck and legs. According to Theodorsen (1952) model, vortices were formed near the wall in low-speed streaks and grew outwards with individual heads inclined downstream at 45°, and were contained within a linear envelope inclined upwards at about 20° relative to the wall. The spanwise

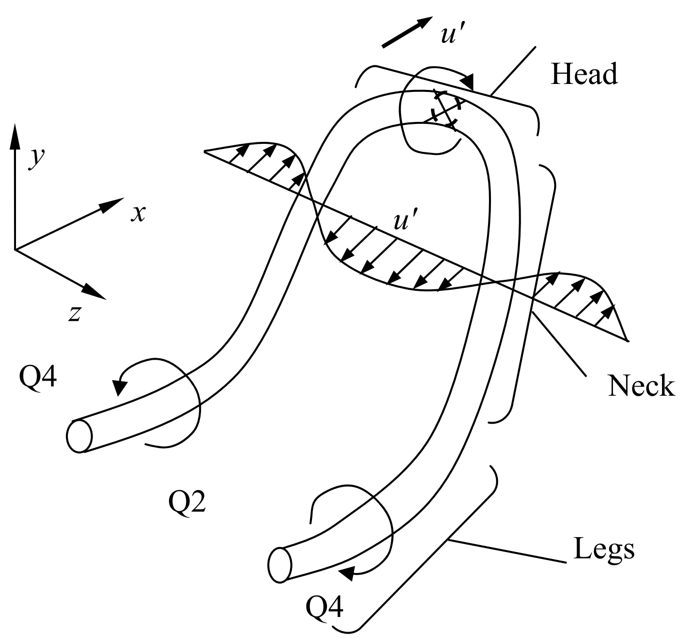

Figure 2.1: Hairpin vortex as proposed by Theodorsen (1952).

dimensions of the vortex were found to be proportional to the distance of the head measured from the wall. The vortex model was proposed as an instantaneous description of near-wall turbulence dynamics. It is therefore the fundamental structure responsible for turbulence production and dissipation in turbulent boundary layers. It is presumed that the hairpin is attached to the wall.

Adrian *et al*. (2000a) demonstrated that the velocity pattern in the x-y cross-section of a hairpin consists of (*i*) a transverse vortex core of the head rotating in the same direction as the mean circulation; (*ii*) a region of low-momentum fluid located below and upstream of the vortex head, which is the induced flow associated with the vorticity in the head and neck, (*iii*) an inclination angle of this region at approximately 35°-50° to the x-direction below the transverse vortex and more nearly tangent to the wall as the wall is approached. The legs of the hairpin were found to reside in the buffer layer and become quasi-streamwise vortices that induce low momentum fluid upwards. It is these quasi-streamwise vortices that cause fluid from the viscous layer to lift away from the wall and form near-wall low-speed streaks that are commonly observed in the buffer layer (Robinson, 1993). The sweep event was observed to oppose the ejection event, forming a stagnation point and an inclined shear layer upstream. Further, when the laser sheet of PIV cut through the mid-plane of a hairpin vortex, a pattern containing circular streamlines, a strong ejection ($Q2$) event in a region having approximately 45° inclination, and a sweep ($Q4$) event with a stagnation point is revealed (Figure 2.2). Such two-dimensional patterns have been associated with three-dimensional hairpin vortices in conditionally averaged three-dimensional fields of wall turbulence when conditioned on the occurrence of a $Q2$ event (Adrian *et al*., 1987; Zhou *et al*., 1997).

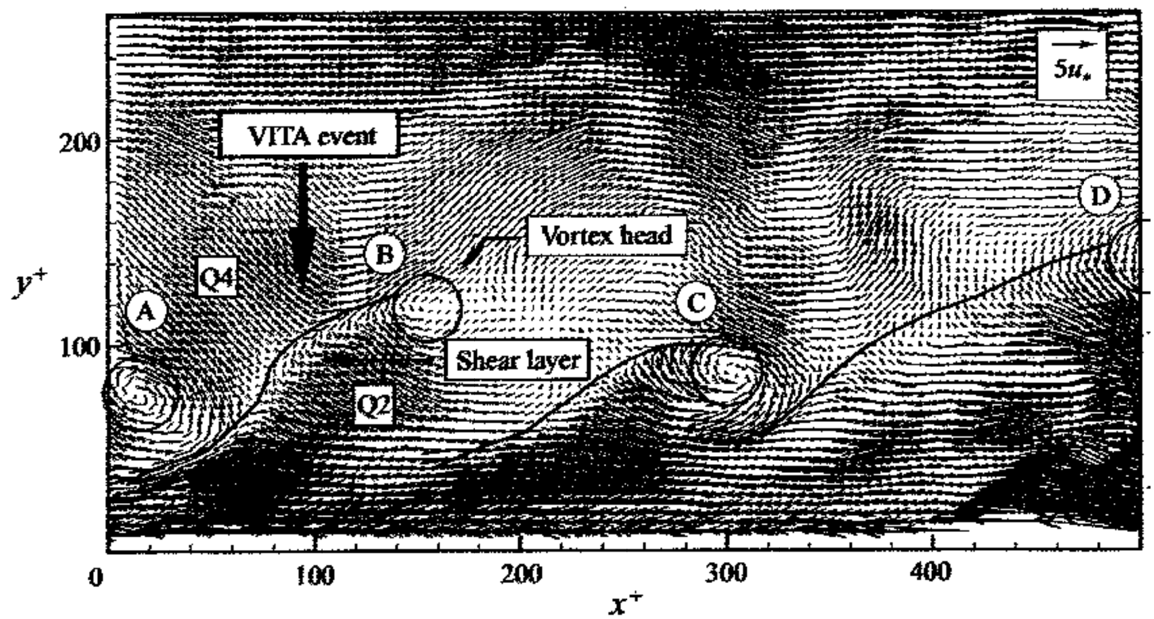

Figure 2.2: Near-wall realization at Re_θ = 930 showing four hairpin vortex signatures aligned in the streamwise direction by Adrian *et al*. (2000a). Instantaneous velocity vectors were viewed in a frame-of-reference moving at $U_c = 0.8U_m$.

Zhou *et al*. (1999) studied the evolution of an initial hairpin vortex in a direct numerical simulation (DNS) of turbulent channel flow at Re_τ (= $U_\tau h/\nu$ = 180, where h is the channel half-height). The vortices were visualized by plotting isosurfaces of the imaginary part of the complex eigenvalue of the velocity gradient tensor called swirling strength, λ_{ci}. The λ_{ci} was used to quantify the strength of the local swirling motion. Note that the eigenvalues is complex only in regions of local circular or spiraling streamline, thus, automatically eliminating regions having vorticity but no local spiraling motion, such as a shear layer. Zhou *et al*. (1999) demonstrated that for a given sufficient strength, initial single hairpin vortex inserted into a mean flow field, smaller multiple hairpin vortices spawned both upstream and downstream of the initial hairpin vortex. These collection of vortices travel together in a group with a common convection velocity, and they are termed as hairpin vortex packet. A packet may consist of primary vortex,

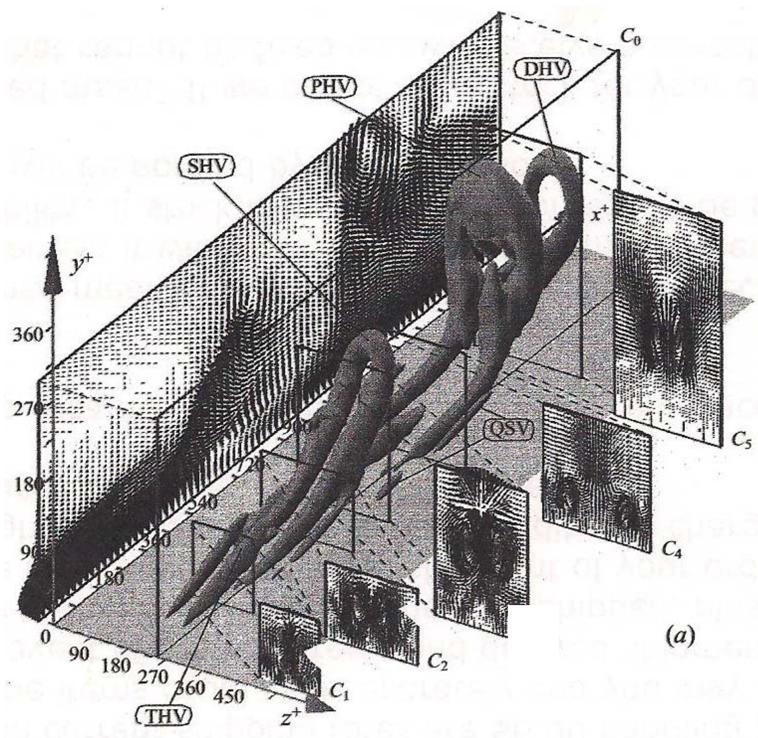

Figure 2.3: Hairpin vortices computed by Zhou *et al*. (1999). Symbols: PHV, primary hairpin vortex; SHV, secondary hairpin vortex; THV, tertiary hairpin vortex; DHV, downstream hairpin vortex; QSV, quasi-streamwise vortex; and C_i cross sections.

hairpins formed upstream of primary vortex (secondary and tertiary hairpins), downstream hairpin and quasi-streamwise vortices as shown in Figure 2.3. The quasi-streamwise vortices are generated to the side of the primary hairpin legs.

As noted earlier, in wall turbulence, ejections and sweeps are the major constitutive motions of coherent structures that contribute significantly to the Reynolds shear stress, whereas the contribution by outward and inward motions is very marginal. Bogard and Tierderman (1987) concentrated their study in the near-wall region of a fully developed turbulent channel flow and observed that $Q2$ motions contribute approximately 79% to the total Reynolds shear stress during ejections. Brodkey *et al*. (1974) and Alfredsson and Johansson (1984) also reported that at $y^+ = 50$, 78% of the Reynolds shear stress originates from the second quadrant. These observations were made for fully developed turbulent channel flows at Reynolds number (based on channel height and centerline velocity) of 7700 and 15000, respectively, for Brodkey *et al*. (1974) and Alfredsson and Johansson (1984). These findings confirm that ejection ($Q2$) events are a major component in the production of $-\overline{uv}$.

Although Kline *et al*. (1967), and later Corino and Brodkey (1969) described ejection as a near-wall region event, Alfredsson and Johansson (1984) pointed out that both ejection-type and sweep-type motions which mark large peaks in $-\overline{uv}$ can also be found in the outer flow region (logarithm region and beyond). To support their argument, they pointed out that the distribution of ejections is fairly uniform in the region where Reynolds shear stress correlation coefficient is approximately constant. The distribution of sweeps event was found to possess its peak at about $y^+ = 75$ ($y/h \approx 0.2$). Other studies (including Bandyopadhyay, 1980; Head and Bandyopadhyay, 1981; Adrian *et al*., 2000a; Christensen and Adrian, 2001; Christensen and Wu, 2005) also support the notion that the outer region of wall turbulence is populated with inclined structures that are associated with ejections and sweeps. Using smoke visualizations in a ZPG turbulent boundary layer, Bandyopadhyay (1980) reported the presence of hairpin vortices in the outer region. It was also observed that the hairpin vortices were inclined at about 20°. A model was proposed by Bandyopadhyay (1980) that predicted an inclination angle of 18.4° for the hairpin structures. Head and Bandyopadhyay (1981) also reported from their visualization study that the hairpin vortices occur in groups whose heads describe an envelope inclined at 15°–20° with respect to the wall.

Adrian *et al*. (2000a) studied a ZPG boundary layer using a PIV system for Re_θ = 930, 2370 and 6845. The focus of their study was to examine coherent structures in the outer layer at different Re_θ. They examined instantaneous velocity vector fields with different Galilean frames of reference by removing constant convection velocity from each field to reveal vortex structures whose cores are advecting at this convection speed. They found that for each Reynolds number, the outer layer was populated with hairpin vortices. The vortices were aligned coherently in the streamwise direction, creating a large-scale coherent motion of a hairpin vortex packet. The number of hairpin vortices in a packet increases as the Reynolds number increases and they conjectured that a vortex packet may contain ten or more individual vortices which propagate as a coherent entity. It was also pointed out that the streamwise extent of this packet can be as large as twice the outer length scale. It should be noted that the creation of packets of multiple hairpin vortices occurs at the wall and they grow to occupy the entire boundary layer. According to Adrian *et al*. (2000a), hairpin packet is characterized by two distinct features: (*i*) a series of hairpin vortices aligned in the longitudinal direction, with their heads forming an interface inclined away from the wall at angles ranging from 12° to 17°, and (*ii*) a region of comparatively uniform, low-momentum fluid lying below the inclined interface created by the heads of the vortices as a result of combined induction by the vortices.

Ganapathisubramani *et al*. (2003) used stereoscopic PIV system to conduct velocity field measurements in ZPG turbulent boundary layer at Re_θ = 2500. The measurements were made in the *x*-*z* planes at various *y*-locations (in the logarithm region and outer region). Feature-detection algorithm was used to identify and examine vortical structures and packets that occurred in the instantaneous velocity fields. The algorithm isolated a region of low momentum covered by cores of vortices that produce strong Reynolds shear stress. The main features of the cores identified were length, width and swirl strength, as well as contribution to Reynolds shear stress. The region identified by the algorithm was referred to hairpin packet. They reported that the algorithm identified numerous elongated packets within the logarithm region, but only few were identified in the outer region.

Statistical evidence that the outer region of wall turbulence consists of organized turbulent motion that is consistent with the pattern associated with a hairpin vortex packet in instantaneous realizations also exists. Christensen and Adrian (2001) pointed out that the organization of the hairpin vortex in the outer region of instantaneous realizations should be evident within the statistics of the flow if the structures have a consistent character (spacing of the vortex heads and angle of inclination). This implies that the imprint of the structure can be destroyed in the averaging process if the variations between instantaneous realizations of the packets are large enough. Christensen and Adrian (2001) statistically investigated the structure in the outer region of turbulent channel flow using a PIV to determine the average flow field associated with spanwise vortical motions at Re_τ = 547 and 1734. They first superimposed contours of swirling strength on the instantaneous velocity fields that have constant convection velocity ($U_c = 0.85U_m$) removed from each field to reveal vortex structures whose cores were advecting at this speed. This revealed packets that were inclined at 17° and 16°, respectively for Re_τ = 547 and 1734. They later used two-point correlation functions between swirling strength and velocity, and linear stochastic estimate technique to provide statistical evidence which supports the notion that the outer layer of the wall turbulence is populated with spatially coherent group of vortices. The linear stochastic estimate of conditionally averaged velocity field showed swirling motions which were inclined at 13°

and 14°, respectively for Re_τ = 547 and 1734. These observations provide statistical evidence that the outer region of wall turbulence is populated with hairpin vortices. The study by Ganapathisubramani *et al*. (2003) was later extended to provide statistical evidence of dominant structure characteristics in the outer region (Ganapathisubramani *et al*., 2005). They used two-point velocity correlation function to quantify the spatial coherence of the large-scaled structures in the flow. They observed that R_{uu} correlation showed significant spatial coherence in the streamwise direction, and this streamwise coherence drops off beyond the logarithm layer. This observation is in accord with their earlier report (Ganapathisubramani *et al*., 2003) that the outer region contains fewer hairpin packets. They suggested that the long streamwise correlations in R_{uu} were dominated by slower streamwise structures. In the logarithm and outer layers, the wall-normal (R_{vv}) and spanwise (R_{ww}) correlations were comparatively compact. This suggests that the spanwise and wall-normal velocity fluctuations are localized and do not have an extended spanwise or streamwise coherence across the boundary layer.

An overview of the effects of Reynolds number (*Re*) on wall-bounded turbulence is provided below. One of the effects of Reynolds number on the mean flow of wall-bounded turbulence is to make the mean velocity more uniform as *Re* increases thereby decreasing the shape factor, *H*. Besides, at relatively low Reynolds number, the logarithm region is very narrow, if it exists at all (Spalart, 1988; Ching *et al*., 1995; Moser *et al*., 1999). DeGraaff and Eaton (2000) observed that for 1430 ≤ Re_θ ≤ 31000, the extent of the logarithm region increases with increasing Reynolds number. It was also observed that the magnitude of the wake formed in the outer region increased rapidly for Re_θ < 6000 but decreased slowly for Re_θ > 6000. The DNS results of a ZPG turbulent boundary layer by Spalart (1988) at $300 \leq Re_\theta \leq 1410$ showed discernible sharp peaks of u^+_{rms} at $y^+ = 15$. The maxima of u^+_{rms}, v^+_{rms}, w^+_{rms} and $-\overline{u^+v^+}$ were found to increase with *Re*. It was observed that the maxima of v^+_{rms}, w^+_{rms} and $-\overline{u^+v^+}$ profiles were broader and y^+ location increased with Re_θ (Ching *et al*., 1995). Similarly, in a fully developed turbulent channel flow, Moser *et al*. (1999) observed that the peak value of u^+_{rms} varied from 2.65 at $Re_\tau = 180$ to 2.77 at $Re_\tau = 590$, and v^+_{rms} and w^+_{rms} were also found to increase with *Re*. Wei and Willmarth (1989) also reported an increase in the turbulence intensities and Reynolds shear stress with *Re* in channel flow for $3000 \leq Re_h \leq 40000$. For example, $-\overline{u^+v^+}_{max}$ was observed to increase from 0.64 to 0.91 as *Re* increases. Andreopoulos *et al*. (1984) reported skewness and flatness factors that showed strong dependence on *Re*. The Reynolds number effects were found to penetrate into the edge of the viscous sublayer and became severe in the outer layer.

As mentioned earlier, Adrian *et al*. (2000a) observed an increase in the number of hairpin vortices in a packet as the Reynolds number increases. It has also been reported by Johansson *et al*. (1987) that the overall size of the structures in viscous units increased slowly with increasing Reynolds number. Additionally, Hutchins *et al*. (2009) observed that large-scale energy in the near-wall region increases with *Re*, but the small-scale energy remains approximately the same. Therefore, the observed increase in u^+_{rms} noted above in the outer layer was attributed to contributions by the large-scale eddies to the flow. In a high Reynolds number boundary layer, Hutchins *et al*. (2009) observed that the large-scale contribution to the flow extended to the walls resulting in a steady increase in $\overline{u^{+2}}$ in the entire y range for $2820 \leq Re_\tau \leq 18830$. Moreover, Purtell *et al*. (1981)

attributed the decrease in u^+_{rms} across most of the boundary layer to suppression of all but the largest turbulence eddies as Reynolds number is decreased.

Some important differences in fully developed channel or pipe flow and zero-pressure gradient turbulent boundary layer are worth mentioning. One of the basic differences between internal flow and ZPG turbulent boundary layer is found in the mean velocity profile. For example, the mean velocity profile of a ZPG turbulent boundary layer in semi-logarithm format shows a stronger wake component compared to that of a channel or pipe flow. This is due to higher entrainment rate in the turbulent boundary layer compared to channel/pipe flows. Monty *et al*. (2009) compared results for channel, pipe and turbulent boundary layer flows at approximately the same Reynolds number (Re_τ = 3000). The measurements were made using hotwire anemometry. The comparison was made using the mean velocity, defect velocity, streamwise component of Reynolds normal stress, skewness and flatness factors, and energy spectra. The mean defect velocity scaled with friction velocity was larger for boundary layer flow than those for the channel/pipe flows. They found close similarity in $\overline{u^{+2}}$ in all the three flows for y up to 0.6δ. Beyond this location, $\overline{u^{+2}}$ for the channel and pipe flows were higher than that obtained for boundary layer. It was also observed that the skewness and flatness factors were independent of the flow type up to $y \approx 0.5\delta$. Beyond $y \approx 0.5\delta$, the boundary layer data increased rapidly due to increasing intermittency. The energy spectra showed that the largest energetic scales were much longer in channel/pipe flow than in turbulent boundary layer. Additionally, the contributions by the large-scales to the energy move to longer wavelengths with distance from the wall in channel/pipe flows. In the boundary layer flow, however, the wavelength of the outer-flow structures decreased very rapidly beyond the logarithm region. Meanwhile, the agreement between channel and pipe flows was very good throughout the entire section. Tomkins and Adrian (2003), and Hutchins and Marusic (2007) compared energy spectra of a channel and turbulent boundary layer flows and observed that the widths of the large-scale structures in channel flow are larger than those in the boundary layer by a factor of about 1.6. Jiménez *et al*. (2009) compared DNS results for channel and turbulent boundary layer for $620 \leq Re_\theta \leq 2140$. Although they observed good agreement for the streamwise turbulence intensity of the two flows, the spanwise and wall-normal turbulence intensities for the boundary layer flow were larger than those for the channel flow. The Reynolds shear stress was found to be larger for the boundary layer than the channel flow. This was attributed to the extra turbulence production in the wake region (and ultimately to the irrotational intermittency) in the outer flow of the boundary layer.

Teitel and Antonia (1991) compared the ratio of the $Q2$ to $Q4$ events (ϕ_0) for turbulent boundary layer and channel flows at a hyperbole hole of $H = 0$. They observed good agreement in ϕ_0 up to $y \approx 0.7h$ for both flows. Beyond $y \approx 0.7h$, ϕ_0 was lower for the channel flow than for the boundary layer, due mainly to an increase in the absolute value of $Q4$ for the channel. This increase was attributed to incursions of relatively high-speed fluid from the opposite side of the centerline. Similarly, Jiménez *et al*. (2010) found that ϕ_0 varied from 1.5 to 2 for channel flow whereas that for the boundary layer exceeded 3 at $y = \delta$. Wu and Christensen (2006) used a PIV to provide salient information on the hairpin vortices of channel and turbulent boundary layer flows. They found that both the logarithm regions of the channel and boundary layer flows were densely populated with hairpin vortices (both prograde and retrograde). They however noted that for $y > 0.45\delta$, both the population density and fraction of retrograde hairpin vortices decreased with wall-normal distance beyond the logarithm layer in the boundary layer. Meanwhile, these quantities increased with y in channel flow near its centreline. These differences were attributed to the influence of the opposing wall in channel flow whereby prograde structures in the reference frame of the upper wall appear as retrograde vortices in the reference frame of the lower wall.

2.2 SMOOTH WALL APG FLOW

In an APG flow, the mean velocity profile in the inner coordinates follows the standard logarithmic law, but the extent of the logarithmic region shrinks as the wake occupies a larger fraction of the boundary layer. As the APG becomes stronger, the wake increases, and the logarithmic region diminishes profoundly. Nickels (2004) defined strong APG as a flow with streamwise non-dimensional pressure gradient, $p_x^+ > 0.005$, where $p_x^+ = \nu/(\rho U_\tau^3)(dP/dx)$, or following Clauser (1954), $p_x^+ = \beta/\delta^{*+}$. Nickels (2004) observed that the effects of pressure gradient are not only limited to the outer layer, but extended to the inner layer. For example, the turbulence intensities and the Reynolds shear stress were larger for the adverse pressure gradient flows than for the zero pressure gradient flows in both the inner and outer regions. Elsberry *et al*. (2000) studied an APG flow maintained on the verge of separation using a hot-wire anemometer. They observed that the APG flow was marked with very little turbulence activity close to the wall although the turbulence level away from the wall was higher. The flow field was highly anisotropic in the sense that the streamwise component of the turbulence intensity was three times as high as the transverse component. Additionally, the Reynolds shear stress correlation coefficient for the APG was found to vary considerable across the flow. This suggests that APG caused considerable reorganization among the energy-containing eddies and the phase relation between u' and v' fluctuations change constantly in the APG flow.

Skåre and Krogstad (1994) studied a turbulent boundary layer that was subjected to a strong APG using a hot-wire anemometer for $25400 \leq Re_\theta \leq 53970$. The measurements were made at pressure gradient parameter that varied from $12.2 \leq \beta \leq 21.4$. It was observed that the normalized mean velocity profiles, Reynolds stresses and their ratios as well as the triple-velocity correlations at different streamwise locations were similar in both the inner and outer layers. A dominant outer peak in the Reynolds stresses at $y = 0.45\delta$ was observed and this was attributed to the strong APG that the flow was subjected to. Skåre and Krogstad (1994) observed significant turbulence production in both the inner and outer regions of the APG boundary layer, suggesting a striking difference in the turbulence structure between ZPG flow (where turbulence production level is only high in the inner region) and APG flow.

Nagano *et al*. (1998) compared APG ($1290 \leq Re_\theta \leq 3350$) and ZPG ($Re_\theta = 1070$ and 1620) flows measured using a hot-wire anemometer. The pressure gradient parameter was varied from $9.12 \times 10^{-3} \leq p_x^+ \leq 2.87 \times 10^{-2}$ and the corresponding Clauser parameter was $0.77 \leq \beta \leq 5.32$. In addition to turbulence statistics, turbulence spectra, and signal traces of u', v' and $u'v'$, fractional contributions to the Reynolds shear stress were computed using quadrant decomposition techniques. They found that in the logarithm region of the ZPG flow, the ejection motion ($Q2$) contributes larger fraction to the Reynolds shear stress, followed by sweep motion ($Q4$). The contributions by interactions ($Q1$ and $Q3$) were fairly small in comparison with those of the active motions ($Q2$ and $Q4$). For example, at $y^+ = 87$, the fractional contributions by the various quadrants to $-\overline{uv}$

were −0.17, 0.71, −0.17 and 0.62, respectively for $Q1$, $Q2$, $Q3$ and $Q4$ motions. Meanwhile, in the logarithm region of the APG flow, the contribution of sweep motions was comparatively larger than ejection motions, but both motions increased towards the wall. At about $y^+ = 84$ (which was in the logarithm region), the fractional contributions by the various quadrants to $-\overline{uv}$ were −0.22, 0.66 −0.19 and 0.73, respectively for $Q1$, $Q2$, $Q3$ and $Q4$ motions. They also reported that APG caused $Q1$ and $Q3$ to increase near the wall, indicating that in APG flows, energy transfer through turbulent diffusion towards the wall becomes dominant thereby increasing inactive motions ($Q1$ and $Q3$). For example, at $y^+ = 23$, the $Q1$ and $Q3$ were −0.17 and −0.21 for ZPG whereas at $y^+ = 21$ the $Q1$ and $Q3$ were −0.40 and −0.35 for the APG. As explained by Krogstad and Skåre (1995), the dominance of turbulent diffusion towards the wall in APG flow, as well as the damping effect of the wall caused the inrushing fluid to squeeze out laterally near the wall and later reflect back to the flow. They also reported that the APG flow was dominated by $Q4$ motions than $Q2$ motions. The observed differences in ejections and sweeps suggest that there are changes in the coherent structure between the ZPG and APG flows. Krogstad and Skåre (1995) also used two-point correlation functions to document structural differences between ZPG and APG flows. The two-point correlation functions in the x-y and x-z planes revealed that the streamwise extent of R_{uu} contour for the ZPG flow was larger than that for the APG flow. However, the lateral extent of R_{uu} contour for the ZPG flow was found to be smaller compared to APG flow, suggesting reduced streamwise stretching of vortices when the boundary layer is subjected to APG. Although the R_{vv} contours were unaffected by pressure gradient, the R_{ww} contours were more elongated for the APG flow than for the ZPG flow.

In recent studies by Lee and Sung (2008 and 2009) and Lee *et al*. (2010) in adverse pressure gradient turbulent boundary layer, it was found that the outer region of the APG boundary layer is populated with streamwise-aligned vortex organizations similar to the vortex packet model proposed by Adrian *et al*. (2000a). The vortical structures induced low-momentum regions in the middle of the boundary layers leading to an outer peak in the Reynolds shear stress. The inclination angles of the vortex packets and the mean streamwise spacing of the vortex heads in the packets were augmented by the APG. They observed that the turbulence level in the APG flow was increased compared to that for ZPG flow, and this was attributed to more active coherent structures in the outer layer of the APG flow than the ZPG flow.

2.3 ROUGH WALL TURBULENCE

Early work on rough wall is credited to Nikuradse (1933) who performed a comprehensive experiments in circular pipes roughened with carefully-graded, closely-packed sand grains for a wide range of relative roughness ($0.002 \leq k_s/R \leq 0.067$), where k_s is the height of sand grains and R is the radius of the pipe. It was found that at low Reynolds number, the friction factor was independent of the wall boundary condition, implying that the sand grains lied utterly within the viscous sublayer. The presence of roughness on wall boundaries increases drag at higher Reynolds numbers, and as a result, the streamwise mean velocity profile over rough walls becomes less uniform compared to a smooth wall profile.

Regarding the effects of wall roughness on the turbulence statistics, two main schools of thoughts exist in near-wall turbulence research community. One group supports the idea that roughness affects only the inner region while the other group supports the idea that roughness affects both the inner and the outer regions. The former group presumed that the turbulence statistics over smooth and rough walls are similar outside the roughness sublayer, as suggested by Townsend (1976) wall similarity hypothesis. They therefore, view wall roughness as a local effect that only affects the inner region up to a distance of $5k$ (Raupach *et al*., 1991). The exact extent of the roughness sublayer, however, depends on the texture (i.e., the size, distribution and shape) of the roughness elements. Inside the roughness sublayer, the roughness elements interact strongly with the streamwise vortices near the walls. As a result, the inner region of a rough wall boundary layer is expected to be severely modified compared to that of a smooth wall boundary layer. The flow in the outer region, is however, expected to be unaffected by the mechanism that produces the turbulence in the inner region and therefore should behave similarly for both smooth and rough walls. In line with classical philosophy, therefore, properly normalized mean velocity and turbulence statistics should be independent of the wall boundary condition outside the roughness sublayer. Jiménez (2004) proposed that in order to eliminate structural differences in the outer regions of smooth wall and rough wall boundary layers, the relative roughness, k/δ (or k/h) should not exceed 2.5%. For larger values of k/δ, the roughness effects may extend well into the outer region because a significant portion of the logarithmic layer may be destroyed by the roughness elements.

Measurements reported by Flack *et al*. (2005), Connelly *et al*. (2006) Schultz and Flack (2007), and Wu and Christensen (2007) over three-dimensional roughness elements such as sandpaper and woven mesh supported the wall similarity hypothesis. Connelly *et al*. (2006) conducted LDV measurements over sandpaper and mesh of varying degree of relative roughness. The principal conclusion of their study was that roughness effects on the mean flow were confined to the inner region. Flack *et al*. (2007) investigated flow over sand grain and woven mesh roughness for a wide range of roughness sizes using LDV. The goal of their study was to document the effects of increasing roughness height on the outer region of turbulence statistics in fully developed turbulent boundary layers. The ratio k/δ was varied from 0.009 to 0.063. The roughness effects were documented using the mean velocity, Reynolds stresses, third order moments as well as quadrant analysis. They observed that roughness effects were confined to the roughness sublayer (within $5k$ or $3k_s$ from the wall), suggesting outer layer similarity with the smooth wall results. Since the sand grain and woven mesh roughness produced similar results, it was conjectured that the shape of the roughness elements does not play a significant role in determining outer layer similarity. Flack *et al*. (2007), however, noted that for larger roughness elements, the region of turbulence modification extends into the outer flow. This observation is consistent with the notion that as the roughness elements are large relative to the boundary layer thickness, the flow does no longer retain the character of a wall-bounded flow as it is dominated by bluff body wakes. Their study was unable to indicate any critical value of k/δ for the breakdown of outer layer similarity.

Similarity in turbulence structure over a smooth wall and a rough wall made from mesh roughness was reported by Volino *et al*. (2007). Both LDA and PIV were used for the measurements, and the Re_θ for the smooth wall and rough wall boundary layers were 6070 and 7660, respectively. The relative roughness for the rough wall was $k/\delta = 0.014$ and the flow was in the fully rough regime ($k_s^+ = 112$). The turbulence structure was documented through Galilean decomposition of the instantaneous velocity fields, turbulence spectra, swirl strength, probability density function and two-point correlation functions. The prominent feature of both rough and smooth walls was hairpin packets. The packets have a characteristic inclination angle and size which scales on boundary layer thickness, and these quantities were the same over both the smooth and rough walls.

Two-dimensional roughness elements such as transverse ribs have been found to interact with the outer layer, thereby severely modifying the flow in the outer region (Krogstad and Antonia, 1999; Keirsbulk *et al*., 2002; Djenidi *et al*., 2008; Lee and Sung, 2007). Krogstad and Antonia (1999) compared flow over woven mesh and smooth wall with a wall roughened with circular ribs (k-type rib). The comparison was made using the Reynolds stresses, third order moments, quadrant analysis and turbulence spectra. They found that the turbulence statistics and structures were modified both in the inner and outer regions, with an increased sweep events for the mesh and rib roughened walls compared to the smooth wall case. However, the observed increased $Q4$ events for the rough walls were more pronounced for the rib roughened wall than for the woven mesh wall. Besides, the wall-normal extent of the $Q4$ events for the rib wall was larger than that for the mesh wall. Differences in the turbulence statistics and coherent structures were also reported by Volino *et al*. (2009) who experimentally studied boundary layers over a smooth wall, a three-dimensional mesh rough wall and a two-dimensional square ribs rough wall. The effects of roughness were documented using Reynolds stresses, Galilean decomposition of the instantaneous velocity vector field, two-point correlation of the fluctuating velocities and the swirling strength, and linear stochastic estimate. They observed good similarity for the normalized Reynolds stresses over the smooth wall and the three-dimensional mesh wall, except near the wall region. No similarity was observed in the outer layer between the normalized Reynolds stresses of the smooth wall or three-dimensional mesh wall and the two-dimensional square ribs. It should be noted that prior results (Volino *et al*. 2007) showed similarity between the coherent structures over the smooth wall and the three-dimensional rough wall. The Galilean decomposition showed that although hairpin packets were present in the flows over both three-dimensional rough wall and two-dimensional rough walls, those over the two-dimensional rough wall were accompanied by distinct larger scale events such as large-scale eruptions of fluid which extended to the edge of the boundary layer. They, however, observed that the dominant feature of the outer flow was hairpin vortex packets which have similar inclination angles of about $10°-15°$ for both wall conditions. The two-point correlations showed that the spatial extent of the hairpin packets was significantly larger for the two-dimensional rough wall, suggesting a more organized motions over the two-dimensional rough wall than over the smooth wall and the three-dimensional rough wall. Further analysis using linear stochastic estimate (LSE) technique conditioned on prograde swirl events, however, indicated an inclination angle of about 13° for all three boundary conditions. Moreover, the LSE results indicated that the extent of the average hairpin packet is about 40% larger in the two-dimensional rough wall than in the other boundary conditions.

The aforementioned studies were conducted for turbulent boundary layers. For rough wall turbulent channel flows, the flow is either through an asymmetric channel that has one wall covered with roughness elements while the other wall is smooth, or through symmetric channel in which case both the upper and lower walls are covered with similar roughness elements. Hanjalic and Launder (1972) were the first researchers to study rough wall, asymmetric turbulent channel flows: one channel wall was roughened with *k*-

type square ribs and the other wall was kept smooth. They found that the mean flow was asymmetric, and there was a remarkable strong interaction between the rough wall boundary layer and the smooth wall boundary layer. This resulted in dissimilar locations for the maximum streamwise mean velocity and the plane at which the Reynolds shear stress changes sign. The location where the Reynolds shear stress changes sign was found to be closer to the smooth wall than the location where the maximum velocity occurred, suggesting that the interaction of the turbulent motions from both sides of the channel occurs nearer to the smooth wall. Recently, Ikeda and Durbin (2007) used both DNS and RANS to corroborate the finding of Hanjalic and Launder (1972) that the location for maximum streamwise mean velocity does not coincide with the location at which the Reynolds shear stress changes sign. Conversely, Burattini *et al*. (2008) studied turbulent channel flow over intermediate type rough wall and found that the location where the maximum velocity occurred was similar to where the Reynolds shear stress changes sign. In a related study in an asymmetrically rib roughened channel, Nagano *et al*. (2004) observed significant modifications by roughness elements to the turbulence intensities, Reynolds shear stress and turbulence kinetic energy.

Examples of two-dimensional rough wall, symmetric channel flows include Ashrafian and Anderson (2006a, 2006b), Krogstad *et al*. (2005), Bakken *et al*. (2005) and Ashrafian *et al*. (2004). In these studies, k-type square ribs with $k/h = 0.034$ were studied both experimentally and numerically. The general conclusion from these studies is that the effects of roughness on the turbulence statistics are limited to the roughness sublayer. Krogstad *et al*. (2005) compared flow over smooth wall and k-type square ribs ($p/k = 8$) using hot-wire anemometry and DNS. They observed good agreement between the experimental and numerical results. The distribution of Reynolds stresses, their ratios and anisotropy tensors over both wall boundary conditions were found to be similar for $y > 5k$ in support of Townsend (1976) similarity hypothesis. Using quadrant decomposition, they however found that the modification to the coherent structures by wall roughness extended beyond $y = 5k$. Their finding contradicted that of Krosgtad and Antonia (1999) who studied rough wall turbulent boundary layer flows and observed significant roughness effects in the outer region. Krogstad *et al*. (2005), therefore, conjectured that the degree to which wall roughness affects the outer layer is controlled by the flow type, for example symmetric channel flow, asymmetric channel flow and turbulent boundary layer. Similarity in second-order moments, third-order moments, budget terms of turbulence kinetic energy equation and Taylor micro-scale beyond $y = 5k$ were also reported by Ashrafian and Anderson (2006a), Bakken *et al*. (2005) and Ashrafian *et al*. (2004).

The above studies on two-dimensional transverse ribs were reported for cases where the ribs were positioned perpendicular (at 90°) to the approach flow. Only a few studies (Bonhoff *et al*., 1999; Gao and Sundén, 2004; Tachie and Shah, 2008; Tachie *et al*., 2009) can be found on two-dimensional transverse ribs that are inclined at an angle other than 90° to the approach flow, as illustrated in Figure 2.4. The motivation for studying flow over inclined rib roughness is partly from the observation from thermal field measurements that inclined ribs augment convective heat transfer enhancement than perpendicular ribs. Additionally, the few velocity field measurements showed that inclined ribs reduce drag significantly compared to the perpendicularly placed ribs. Okamoto *et al*. (1993) measured velocity, pressure and temperature distributions over 90°

ribs spaced at p/k = 2, 3, 4, 5, 7, 9, 13 and 17. They observed that the ribs with $p = 9k$ augments turbulence intensity and heat transfer more than the other pitch ratios. The pressure loss was also found to attain its maximum at p/k = 9. According to Han *et al*. (1978), form drag decreases as the ribs angle of inclination decreased from 90° to 45°. The heat transfer was also found to be highest when ribs were inclined at 45° and p/k = 10. The inclination angle of 45°, therefore, represents angle for optimum thermal-hydraulic performance for ribs.

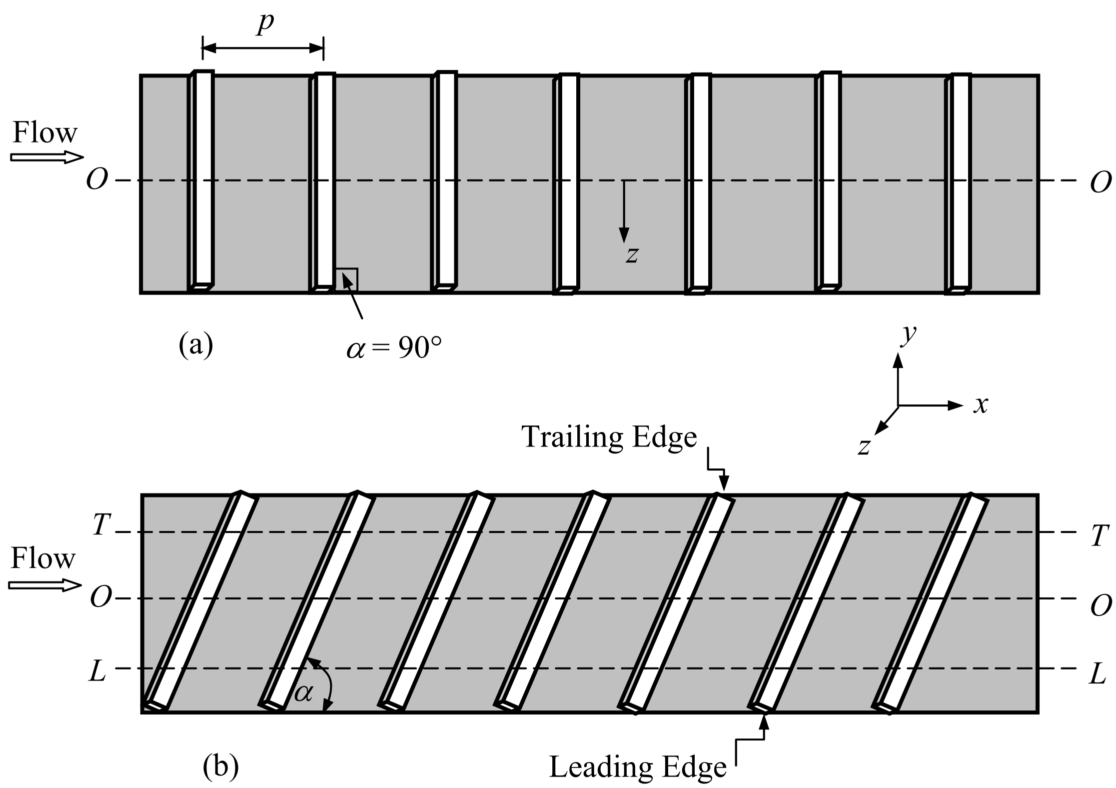

Figure 2.4: Schematic plan views showing (a) ribs perpendicular (α = 90°) to the flow direction and (b) ribs inclined at α to the flow direction.

Bonhoff *et al*. (1999) used both stereoscopic PIV and turbulence models to study flow over two-dimensional transverse square ribs inclined at 45° to the approach flow. The ribs were attached to both walls in a staggered arrangement. They reported only the velocity vectors, mean velocities and turbulence kinetic energy. The study revealed that, rib inclination produces three-dimensional secondary motion where the fluid is driven towards one side wall referred to as the 'trailing wall' and returns towards the opposite side wall called the 'leading wall'. The *U* profiles were found to possess two maxima velocities located close to the rib walls and one minimum velocity at the channel centre. Additionally, they observed low velocity defect along the walls and attributed the enhanced mixing and heat transfer performances by rib inclinations to these low velocity regions. Gao and Sundén (2004) used stereoscopic PIV to measure flow over repeated circular ribs attached to both walls of the channel in a staggered manner. The *k*-type ribs (p/k = 10) were inclined at 30°, 45°, 60° and 90° to the approach flow direction. The measurements were made at a Reynolds number of 5800, based on the mean velocity and hydraulic diameter. They reported only the velocity vector field and mean velocities. The strength of the secondary flow was found to be higher over the inclined ribs than the 90° ribs. The characteristic two secondary vortices were observed to be stronger for the 45° ribs. However, the two maxima velocities and one minimum velocity observed by Bonhoff *et al*. (1999) in the *U* profiles for the 45° ribs were observed for the 30° ribs only.

2.4 ROUGH WALL APG FLOW

As noted earlier, the effects of roughness on zero pressure gradient turbulent boundary layer and fully developed turbulent channel flows as well as the effects of APG on smooth wall have been studied more extensively than the combined effects of roughness and APG. As a result, data from APG flows over smooth wall are used as a guide to predict how rough wall flow might behave under the same condition (Perry and Jourbert, 1963). Perry and Jourbert (1963) reported only mean velocity profiles that were measured over two-dimensional square ribs (p/k = 4) in an APG turbulent boundary layer using Pitot tube. They found that the logarithm law of the wall was still valid. Perry *et al*. (1969) employed both visualization and Pitot tube techniques to study flow over the *d*-type and the *k*-type ribs. The wake component of the mean velocity profile was observed to increase with increasing pressure gradient, and this occurred along with diminishing logarithm region of the mean velocity profile. As the APG increased, the skin-friction coefficient also decreased. Schofield (1975) also reported the mean velocity profiles over *d*-type roughness (p/k = 1.8) in an APG boundary layer, and found that roughness had little effect on the flow.

Recent studies on combined effects of roughness and APG are those by Balachander *et al*. (2002), Pailhas *et al*. (2008), Tachie (2007) and Tay *et al*. (2009). The study by Pailhas *et al*. (2008) was conducted over sanded surfaces using hot-wire anemometry for $3200 \leq Re_\theta \leq 3800$ and $k_s^+ > 70$. They compared their results to smooth wall measurements and found that rough wall modifies the pressure gradient effects on the behaviour of the mean velocity profiles. For example, the wake region of the mean velocity profile over the rough wall was more pronounced than for the smooth wall case. Tay *et al*. (2009) utilized PIV to document the salient features of flow over sand grains and gravels in an APG channel flow. The Reynolds number was varied from $900 \leq Re_\theta \leq 3000$. It was concluded that roughness and APG operate together to augment each other. For example, the combined effects of roughness and APG enhanced production of turbulence as well as turbulence level compared with smooth wall results. Further, APG thickens the boundary layer and the roughness sublayer, and makes the mean velocity profiles less uniform. The roughness function, ΔB was also increased by the joint roughness and APG.

Tachie (2007) utilized PIV system to measure flow over two-dimensional square ribs attached perpendicularly to straight bottom wall of a channel with diverging section. The ribs were spaced to produce pitch-to-height ratios of p/k = 3, 6 and 8. The measurements were made for Reynolds number range of $1020 \leq Re_\theta \leq 5650$. The goal of this study was to document the combined effects of *d*-type and *k*-type rough walls and APG on turbulent flows. The principal finding of this study was that turbulence level over the ribs was more effectively enhanced by adverse pressure gradient than increase observed in the drag characteristics. It was observed that the penetration of the outer flow into the cavity of the ribs was severe for APG flow over *k*-type rough wall.

2.5 SUMMARY OF THE FINDINGS AND PROBLEM DEFINITION

A review of relevant studies on flows over both smooth and rough walls with or without pressure gradient has been conducted. The principal observations from these studies can be summarized as follows:

(*i*) Smooth wall boundary layers with or without pressure gradient have been extensively investigated, and the turbulence statistics and coherent structures associated with smooth wall boundary are relatively well understood.

(*ii*) The zero pressure gradient turbulent boundary layers as well as turbulent channel flows over rough walls have also been extensively studied. This has advanced the understanding of rough wall flows. For example, it is now understood that two-dimensional roughness elements affect the flow in a different way from those of three-dimensional roughness elements. Despite the progress in rough wall flows, there is still the need to investigate the behaviour of the outer layer of a turbulent boundary layer in the presence of roughness compared to that of a rough wall turbulent channel flow.

(*iii*) Adverse pressure gradient flows over rough walls are the least studied in the wall-bounded turbulence research community. As a result, the combined effects of roughness and APG on the turbulence statistics and coherent structures are not well understood.

(*iv*) A few studies have been carried out to advance the knowledge on two-dimensional ribs positioned perpendicular to the approach flow. However, velocity measurements over inclined two-dimensional ribs needed to complement thermal field measurements to aid the understanding of the characteristics of coherent structures over inclined ribs are lacking.

(*v*) Both smooth wall and rough wall turbulent flows contain hairpin vortices in the inner and outer regions. The large-scale events associated with two-dimensional square ribs were found to be more violent and extended into the outer edge of the boundary layer compared to those of three-dimensional roughness elements and smooth wall.

The overall objective of this research is to advance physical understanding of rough wall turbulent flows subjected to adverse pressure gradient and to provide comprehensive experimental data sets that will be useful for validating future turbulence models. The specific objective of this research is to study the combined effects of roughness and adverse pressure gradient as well as rib inclination on the mean and turbulence statistics and coherent structures of wall-bounded turbulent flows. To accomplish this research objective, a high resolution PIV is used to perform velocity measurements over smooth wall and two-dimensional transverse square ribs inclined at 90°, 45° and 30° to the approach flow in a channel that consists of parallel and diverging sections. The velocity field is studied using (*i*) mean velocities, Reynolds stresses, Reynolds stress ratios, mixing length, eddy viscosity, skewness factors, and production terms in the turbulence kinetic energy and Reynolds shear stress equations, (*ii*) Galilean decomposition and contours of swirling strength are used to visualize hairpin vortices, (*iii*) quadrant decomposition is employed to evaluate fractional contributions of the quadrant events to the Reynolds shear stress by coherent structures, (*iv*) two-point velocity correlations are used to study how the turbulence quantities are correlated as well as the length scale and angle of inclination of the hairpin vortex packets, and (*v*) LSE is used to estimate the average velocity field associated with a given conditioning event.

CHAPTER 3

EXPERIMENTAL SET-UP AND MEASUREMENT PROCEDURE

This chapter describes the water tunnel test facility in which the experiments were performed. The design and specifications of the test channel that was inserted into the water tunnel's test section to produce the desired pressure gradients are also presented. The configuration of the ribs is thoroughly described in this chapter. An overview of PIV system and the measurement procedure are also outlined. Furthermore, the notations used to describe the test conditions in the present study as well as the locations of measurement planes are summarized. This is followed by a detailed explanation of the test conditions and how they are grouped to achieve the objectives of the present study. The two-dimensionality of the mean flow is examined, and its implications for the overall flow are discussed. Finally, a summary of estimated measurement uncertainties is presented while detailed uncertainty analysis for PIV is reported in Appendix B.

3.1 THE WATER TUNNEL

The water tunnel was designed and constructed by Engineering Laboratory Design, Inc., Minnesota, USA. The system, which is shown in Figure 3.1, consists of a flow conditioning section, test section, pump, variable speed drive, piping, supporting framework and filtering station. The overall dimensions of the unit are as follows: 5370 mm in length, 1822 mm in height and 1435 mm in width. A settling chamber upstream of the contraction is fitted with perforated steel plates and honeycomb. The settling chamber is designed to ensure quality flow transition from high-speed pipe velocities to low-speed test section velocities, while reducing turbulence and providing flow uniformity. The perforated plates and honeycomb installed in the settling chamber are used to straighten the flow. A 6:1 contraction with a symmetrical cross section is used prior to the working section to further reduce the turbulence level by accelerating the mean flow. The test section of the water tunnel was fabricated using Super Abrasion Resistant® (SAR) clear acrylic to facilitate optical access and flow visualization. The interior dimensions of the test section are 200 mm wide by 200 mm high by 2500 mm long. A 25 hp transistor inverter type variable speed controller regulates the speed of the motor that drives the pump. A filter system is furnished as a means of removing dye concentrations and other contaminants from the system's water. The filtration can be activated at any time, but it was not operated during the present experiments.

Figure 3.1: The water tunnel facility.

3.1.1 THE TEST CHANNEL

In order to produce the desired pressure gradient in the present study, a test channel was designed and fabricated. The test channel consisted of an upstream parallel section to produce a fully developed channel (FDC) flow and a diverging section to produce an adverse pressure gradient (APG) flow. The channel was fabricated from 6 mm thick clear acrylic plates and was inserted into the test section of the water tunnel described in Figure 3.1, hereafter referred to as the main channel. Figure 3.2 shows a three-dimensional view of the test section with the ribs installed on the lower wall. Trips were also installed on both the lower and upper walls at the inlet section of the channel. As shown in the figure, the first 1500 mm of the channel (*OA*) and the last 400 mm of the channel (*BC*) have straight parallel upper and lower walls. The upper wall of the 600 mm section of the channel (*AB*) located between these parallel sections diverges linearly from a height of $2h$ = 55.5 mm to 96.5 mm with an inclination angle of 4°. The internal width of the channel is $2B$ = 186 mm. Therefore, the aspect ratio of the channel (AR = $2B/2h$) varies from 3.35 at the inlet parallel section to 1.93 at the end of the diverging section. These

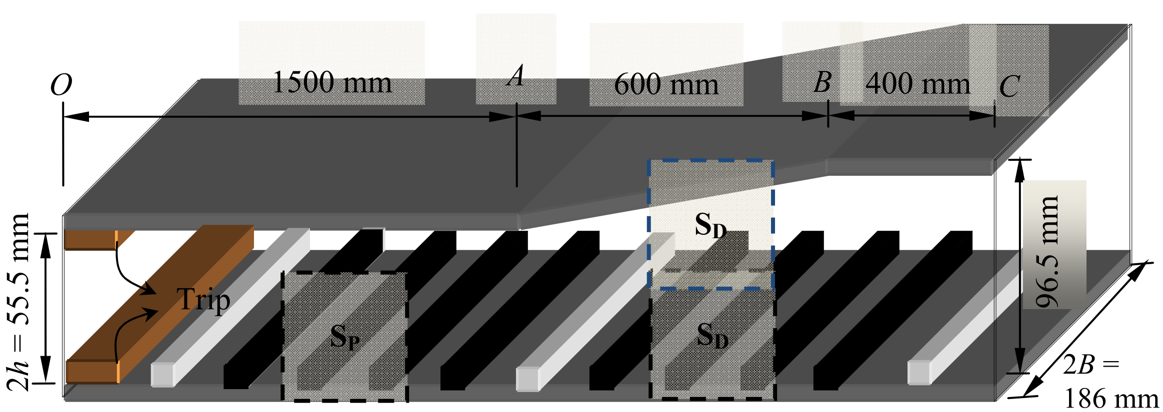

Figure 3.2: Three-dimensional view of the inserted test channel showing ribs oriented perpendicular to the approach flow and measurement planes in the parallel section (S_P) and diverging section (S_D). Not to scale.

aspect ratios are lower than the value of AR ≥ 7 recommended by Dean (1978) to ensure a two-dimensional turbulent channel flow. The effects of the low aspect ratio on the present results will be discussed in Section 3.7.

3.1.2 RIB CONFIGURATION

Two-dimensional transverse square ribs were used as the roughness elements. The transverse square ribs were made of clear acrylic bar and were painted black at the various measurement locations to minimize light reflection. The nominal height of the ribs was k = 3 mm. Digital Vernier calipers were used to measure the height of 50 randomly selected ribs, and it was found that $k = 3.21 \pm 0.21$ mm. The ribs were secured to the straight lower wall of the test channel in both the parallel and diverging sections with a thin double sided tape (Figure 3.2). The rib spanned across the entire width of the channel.

The pitch (p), which is defined as the perpendicular distance between any two adjacent ribs (Figure 3.3) was varied to produce pitch-to-height ratios of p/k = 2, 4 and 8. These values were chosen to, respectively, produce d-type, intermediate type and k-type wall roughness (Perry *et al*., 1969; Tani, 1987). The goal was to study the effects of rib spacing on the flow characteristics. For the k-type rough wall, p/k = 8 was chosen because it produces the largest roughness effects (i.e., roughness shift ΔB) on the mean flow (Furuya *et al*., 1976; Leonardi *et al*., 2003).

As noted in Chapter 2, two-dimensional square ribs are also used in many industrial applications to augment convective heat transfer. In these applications, the two-dimensional transverse ribs are often inclined at an angle to the approach flow. Prior experimental studies of the thermal field demonstrate that inclined two-dimensional

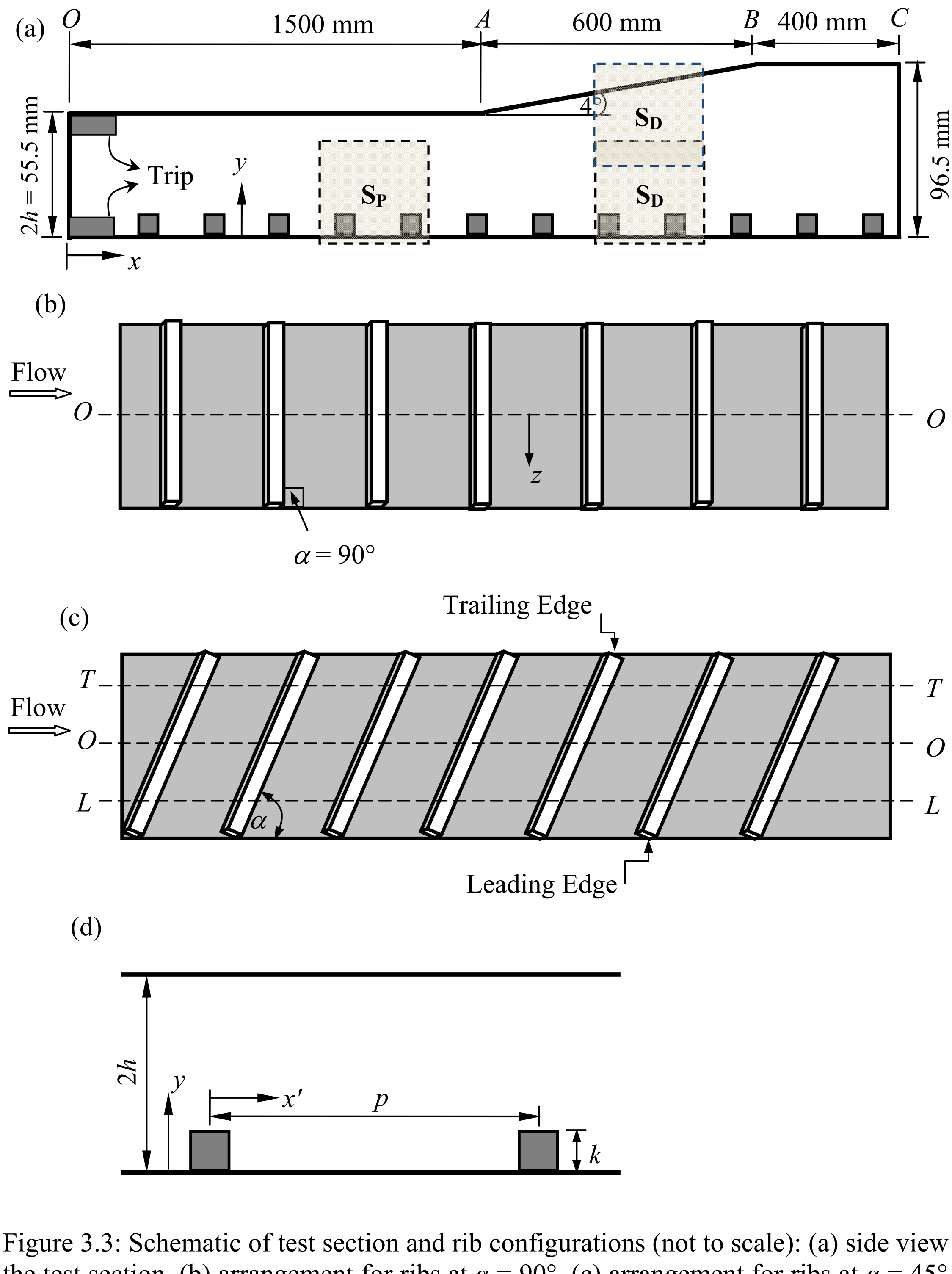

Figure 3.3: Schematic of test section and rib configurations (not to scale): (a) side view of the test section, (b) arrangement for ribs at $\alpha = 90°$, (c) arrangement for ribs at $\alpha = 45°$ or $30°$ (d) typical adjacent square ribs. k is rib height, p is the pitch; LL indicates measurement plane close to the leading edge ($z = +45$ mm), OO at mid-span (i.e. at $z = 0$ mm) and TT is close to the trailing edge ($z = -45$ mm).

square ribs augment convective heat transfer better than ribs positioned perpendicular to the approach flow. Therefore, the ribs were inclined at $\alpha = 90°$, 45° and 30° to the approach flow (Figures 3.3b and 3.3c) for each p/k. Following Bonhoff *et al*. (1999), the edges of the 45° and 30° ribs pointing to the upstream and downstream sections of the channel are referred to as the leading and trailing edges, respectively. The blockage produced by the ribs expressed as the ratio of rib height to the height of the channel, i.e. $k/2h$ decreased from 0.054 in the upstream parallel section to 0.031 in the downstream parallel section.

The streamwise, wall-normal and spanwise directions are along the x, y and z axes, respectively (Figure 3.3): $x = 0$ at the inlet to the 55.5 mm × 186 mm section (denoted by O in Figure 3.3a), $y = 0$ at the floor of the lower wall (Figures 3.3a and 3.3d), and $z = 0$ at the mid-span of the channel (Figure 3.3b). The results presented subsequently in a specific measurement plane focus on flow region around two adjacent ribs in that plane. Therefore, another streamwise coordinate x' (Figure 3.3d) is defined such that $x' = 0$ at the centre of the upstream rib of the two ribs of interest.

3.2 PARTICLE IMAGE VELOCIMETRY (PIV) SYSTEM

A planar particle image velocimetry (PIV) system was used to conduct the velocity measurements. Particle image velocimetry is a non-intrusive optical velocity measurement technique. It provides simultaneous multiple-point instantaneous whole-field velocity measurements in a flow. A PIV is well suited for estimating velocity gradients and derived quantities such as vorticity and the various terms in the transport equations for momentum, turbulence kinetic energy and Reynolds stresses. Due to these attractive features, PIV has been applied in many areas of fluid dynamics research.

A PIV system comprises a laser source used to illuminate the flow field, a camera used to image the flow field, a data acquisition system to acquire and process the flow images. The basic principle of the PIV entails seeding the flow field of interest with small light scattering particles that are presumed to faithfully follow the fluid motion. The flow field is then illuminated by two pulses of laser sheet separated by a time delay, Δt. The light scattered by the seeding particles is recorded as two successive images. The images are divided into grids called interrogation areas. For each interrogation area, a numerical correlation algorithm (cross-correlation) is applied to statistically determine the local displacement vector (Δs) of particles between the first and the second illuminations. The velocity (V) for a particular interrogation area is then obtained from the expression $V = \Delta s/\Delta t$. A velocity vector map over the whole target area is obtained by repeating the correlation for each interrogation area. Since the entire flow field can be analyzed at once, the PIV provides simultaneous whole field measurements.

The present measurements used a PIV system that comprised a neodymium-doped yttrium aluminum garnet (Nd-YAG) laser (120 mJ/pulse) of 532 nm wavelength to illuminate the flow field. A 12 bit HiSense 4 M camera (2048 pixels × 2048 pixels charge-coupled device (CCD) array size and a 7.4 μm pixel pitch) was used to image the flow field. The flow was seeded with 10 μm silver coated hollow glass sphere seeding particles having a specific gravity of 1.4. These particular seeding particles were chosen because they are large enough to scatter sufficient light to be detected by the digital camera and small enough to follow the flow faithfully. Also, particles that have negligible settling velocity are desirable. The settling velocity was estimated from Stokes drag law for flow around a sphere under gravity and is given by (Mei *et al.*, 1991),

$$v_s = \frac{(\rho_p - \rho_f) g d_p^2}{18\mu_f} \tag{3.1}$$

where ρ_p is the particle density, ρ_f is the fluid density, g is the acceleration due to gravity, d_p is the diameter of the particle and μ_f is the viscosity of the fluid. The settling velocity of the particles calculated from Eq. 3.1 was $v_s = 2.18 \times 10^{-5}$ m/s. The settling velocity is, therefore, insignificant compared to the streamwise mean velocity measured (e.g., U is up to 0.385 m/s for the smooth wall test in the upstream parallel section). The ability of a particle to follow the flow is characterized by its response time. The response time, τ_r, for the particle (for Stokes' flow) is (Raffel *et al*., 1998):

$$\tau_r = \rho_p \frac{d_p^2}{18\mu_f} \tag{3.2}$$

For the present measurements, the response time of the particles calculated from Eq. 3.2 is $t_r = 7.78$ μs. The response time is very small compared to the sampling times employed in this study. The negligible settling velocity and response time imply that the seeding particles follow the fluid flow faithfully.

3.3 MEASUREMENT PROCEDURE

The CCD digital camera was positioned perpendicular to the plane of the light sheet for all the test conditions. The laser pulse separation time Δt was found based on the estimation that the particle displacement should be less than one quarter of the interrogation area, using the following expression,

$$\Delta t = \frac{n d_{pp}}{4 M U_m} \tag{3.3}$$

where, n is the interrogation area size, d_{pp} is the pixel pitch, M is the magnification factor and U_m is the maximum velocity of the flow. Before acquiring the 6000 image pairs at any test location, preliminary sample size of 100 image pairs were acquired and processed to ensure that the PIV parameters were correctly chosen and yielded high quality velocity vectors. In all cases, the number of substituted velocity vectors in the main flow domain was always less than 2 percent.

For measurements in the x-y plane, the laser sheet was aligned parallel to the side walls and the laser was shot from the top of the channel. The field of view for these measurements was approximately 49 mm × 49 mm in both the parallel and diverging sections. It should be noted that in the diverging section, the lower and the upper boundary layers were measured separately using a similar field of view (Figure 3.2 and Figure 3.3a). This is necessary to maintain similar vector spacing in the upstream parallel section and diverging section.

Measurements were also made in the x-z planes to examine the turbulence statistics and flow structures in x-z plane over both the smooth and rough walls. For these x-z plane measurements, the laser sheet was aligned parallel to the lower wall and the laser was shot from the side wall of the channel. The x-z plane measurements were made only for the smooth wall and the k-type ribs inclined at α = 90° and 45° in both the parallel and diverging sections. The fields of view for the x-z plane measurements are approximately 100 mm × 100 mm for the smooth wall test and approximately 115 mm × 115 mm for the k-type rough walls. These field of views extend from the side wall (z' = 0 mm) to 7 mm and 22 mm beyond the centerline of the channel (z = 0 mm), respectively for the smooth wall and rough wall measurements.

The instantaneous digital images were post-processed using the adaptive-correlation option of the commercial software developed by Dantec Dynamics (DynamicStudio v2.30). The adaptive-correlation algorithm is an advanced type of the standard cross-correlation. It uses a multi-pass fast Fourier transform (FFT) cross-correlation algorithm to determine the average particle displacement within the interrogation area (IA). The Gaussian window function and the low-pass Gaussian filter that come with the DynamicStudio were used as input and output filters, respectively, to the correlation algorithm. The Gaussian filter eliminates high-frequency noises from the images. The Gaussian window function eliminates particle clipping which tends to bias the average results towards lower velocities. During image acquisition and post-processing, steps were taken to improve the quality and accuracy of the velocity vectors. For example, it was ensured that the maximum particle displacement was less than 1/4 of the IA size of 32 pixels in the main flow direction, and the particle image diameter was $d_p \approx 2.3$ pixels for x-y plane measurements and $d_p \approx 2.0$ pixels for x-z plane measurements. These values of d_p are in good agreement with the recommended value of $d_p = 2.0$ necessary to minimize peak locking and to ensure high signal-to-noise ratio (Raffel *et al.*, 1998). As shown in Appendix B, histograms of typical instantaneous images over smooth wall and rough wall in both the parallel and diverging sections show no discernible peak locking.

In each measurement plane of each test conditions, 6000 pairs of instantaneous images were recorded. Convergence test indicated that 6000 pairs of instantaneous images were sufficient to obtained statistically converged results for one-point statistics and two-point velocity correlation functions.

Two different IA sizes, $\Delta x \times \Delta y$ = 32 pixels × 32 pixels with 50% overlap and $\Delta x \times \Delta y$ = 32 pixels × 16 pixels with 50% overlap were used to process the data. The Δx interval in both cases was kept constant because the resolution required in y-direction is more stringent than required in the x-direction. The average number of particles in an IA varied from 7 (32 pixels × 16 pixels × 50%) to 15 (32 pixels × 32 pixels × 50%) while the total number of vectors per image varied from 16129 (for 32 pixels × 32 pixels × 50%) to 32385 (for 32 pixels × 16 pixels × 50%). Spatial resolution test was performed using IAs of 32 pixels × 32 pixels with 50% overlap and 32 pixels × 16 pixels with 50%. The rationale was to determine any effect of spatial resolution on the mean velocity and turbulence statistics. The results (not shown) indicate that the two IAs provide spatial resolutions that are adequate for the mean velocity and turbulence statistics that are reported in subsequent chapters. Therefore, the results obtained using IA of 32 pixels × 32 pixels with 50% overlap are reported. This interrogation area corresponds to $4.5 \le \Delta y^+ \le 13.8$.

3.4 NOTATIONS

Notation of the form $R_a S_b \alpha_c P_d$ will be used to designate the test conditions for the ribs or rough walls in the present study. The symbol R denotes rib and the subscript a is the pitch-to-height ratio and takes the values of 2, 4 and 8, so that R_2 is for the d-type (p/k = 2) rib roughness. The symbol S denotes channel section and the subscript b is used here to represent parallel (P) or diverging (D) sections, so that S_P is the measurement plane in the parallel section. The symbol α denotes the angle of inclination of the rib to the approach flow and the subscript c = 90°, 45° and 30°, so that α_{45} represents ribs at 45° to the approach flow. The symbol P denotes z-location of the measurement plane and the subscript d is used here to represent O (z = 0 mm, mid-span of the channel), L (z = +45 mm, close to the leading edge of the ribs) and T (z = −45 mm, close to the trailing edge of the ribs), so that P_O is the x-y measurement plane at the mid-span of the channel. Thus, $R_4S_D\alpha_{90}P_O$, represents test condition for p/k = 4 (i.e., R_4, intermediate type ribs) in the diverging section (S_D), ribs at an angle of α = 90° and the measurement plane is at centerline of the channel (i.e., P_O or at z = 0 mm). Similarly, $R_8S_P\alpha_{45}P_L$, represents test condition for p/k = 8 (i.e., R_8, k-type ribs) in the parallel section (S_P), ribs at an angle of α = 45° and the measurement plane is close to the leading edge of the ribs (i.e., P_L or at z = +45 mm). The following notation is adopted for the smooth wall: SMS_P denotes test condition for smooth wall (SM) in the parallel section (S_P) and SMS_D denotes test condition for smooth wall (SM) in the diverging section (S_D).

3.5 MEASUREMENT LOCATIONS

For each of the smooth wall, d-type, intermediate type and k-type ribs configuration, measurements were made in x-y planes located in the upstream parallel section (S_P) and within the diverging section (S_D) of the channel. The middle of the measurement plane or field of view of the camera in the upstream parallel section and diverging section was located, respectively, at $x/h \approx 40$ from the inlet section (designated by O in Figure 3.3a) and $x/h \approx 11$ from the start of divergence (denoted as A in Figure 3.3a). The corresponding channel aspect ratios for the measurement planes in the parallel and diverging sections are 3.35 and 2.40, respectively. For the smooth wall and ribs positioned at 90° to the approach flow, the x-y plane measurements were made only at the mid-span (i.e., z = 0 mm) of the channel. For ribs inclined at 45° and 30° to the approach flow, the x-y plane measurements were made at the mid-span of the channel (z = 0 mm), close to the leading edge of the ribs (z = +45 mm) and close to the trailing edge of the ribs (z = −45 mm). The rationale for these additional measurements was to ascertain how the secondary flow induced by the inclined ribs modified the flow statistics and coherent structures away from the mid-span. The x-y plane measurements over the smooth wall and rough walls are summarized in Table 3.1.

The x-z plane measurements were made at three separate y-locations measured from the lower wall. The specific y-locations for each test are summarized in Table 3.2. These locations were chosen to correspond to typical locations in the logarithm region and outer layer. Besides, these locations were chosen based on the premise that the logarithm region and the outer layer are populated with hairpin vortices (Adrian *et al.*,

Table 3.1: Summary of tests conducted in the x-y plane over smooth wall and rough walls.

	S_P			S_D		
Test	z **= 0 mm**	z **= +45 mm**	z **= −45 mm**	z **= 0 mm**	z **= +45 mm**	z **= −45 mm**
SM	✓	–	–	✓	–	–
$R_2\alpha_{90}$	✓	–	–	✓	–	–
$R_4\alpha_{90}$	✓	–	–	✓	–	–
$R_8\alpha_{90}$	✓	–	–	✓	–	–
$R_2\alpha_{45}$	✓	✓	✓	✓	✓	✓
$R_4\alpha_{45}$	✓	✓	✓	✓	✓	✓
$R_8\alpha_{45}$	✓	✓	✓	✓	✓	✓
$R_2\alpha_{30}$	✓	✓	✓	✓	✓	✓
$R_4\alpha_{30}$	✓	✓	✓	✓	✓	✓
$R_8\alpha_{30}$	✓	✓	✓	✓	✓	✓

Table 3.2: Summary of tests conducted in the x-z plane over smooth and rough walls.

Test		S_P			S_D	
SM	$y^+ = 89$	$y^+ = 156$	$y = 0.75\delta$	$y^+ = 49$	$y^+ = 81$	$y = 0.75\delta$
$R_8\alpha_{90}$	$y^+ = 206$	$y^+ = 305$	$y = 0.75\delta$	$y^+ = 247$	$y^+ = 527$	$y = 0.75\delta$
$R_8\alpha_{45}$	$y^+ = 182$	$y^+ = 338$	$y = 0.75\delta$	$y^+ = 71$	$y^+ = 125$	$y = 0.75\delta$

2000a; Ganapathisubramani *et al*., 2003). As noted earlier, these x-z plane measurements were made only for the smooth wall, and $\alpha = 90°$ and 45° k-type ribs in both the parallel and diverging sections. The k-type ribs were chosen because preliminary analysis of measurements in the x-y plane showed that the effects of roughness are most severe for this rib type. Also the k-type ribs are the geometry which is most relevant for heat transfer augmentation. Furthermore, preliminary analysis of x-y plane measurements indicated that there is no significant variation between the flow characteristics of 45° and 30° k-type ribs. Thus, the test conditions in both the x-y and x-z planes described above are sufficient to thoroughly investigate the effects of pressure gradient, roughness, rib inclinations and spanwise measurement plane location on the flow characteristics.

3.6 TEST CONDITIONS

The specific test conditions for the reference smooth wall (SM) and the transverse ribs experiments are summarized in this section. A 150 mm wide trip made of 6 mm diameter gravels were used on the upper and lower walls of the channel inlet section to ensure a rapid development of the boundary layer. Note that the smooth wall measurements were conducted prior to measurements with the square ribs installed on the channel floor, that is, the smooth wall experiments were conducted without the square ribs secured to the channel floor. The rationale was to understand the effects of adverse pressure gradients on the mean velocities, turbulence statistics and coherent structures in the plain smooth channel. The turbulence level at the core of the channel in the absence of the ribs was $u/U_m = 0.05$. This value is comparable to a turbulence intensity value of 0.04 ± 10% reported by Durst *et al*. (1998) based on a compilation of data from 16 different experiments in fully developed channel flows. For a given wall boundary condition, the volume flow rate was kept constant during all the measurements to maintain the upstream conditions as similar as possible. For each test condition over the ribs, the mean and turbulence statistics were spatially averaged over a pitch ($0 \le x' \le p$). The maximum spatial averaged values for streamwise mean velocity are denoted by U_m. The expression used for the computation of the spatial average results is:

$$f(y) = \frac{1}{N_p} \sum_{i=1}^{N_p} f_i(x', y) \tag{3.4}$$

where $f(y)$ is the spatial average quantity, f_i (x', y) represents any local ensemble average quantity in a particular interrogation region, N_p is the number of data points obtained within a pitch in the streamwsie direction, that is, within the range $0 \le x' \le p$. The streamwise coordinate, x', is measured from the centre of the upstream rib of the two ribs of interest so that $f(y)$ is evaluated over the interval between adjacent ribs at a constant value of y. The computation was repeated for the various interrogation areas in the wall-normal direction.

In all, a total of 62 sets of measurements were performed. The sets of measurements in the x-y plane are 44 in total. These test conditions are grouped based on the objectives of the present study. In the subsequent sections, the maximum velocity is denoted U_m, and Re_h is the Reynolds number based on the maximum velocity and the upstream half channel height (h).

3.6.1 EFFECTS OF ADVERSE PRESSURE GRADIENT AND ROUGHNESS

Table 3.3 provides summary of measurements made in the x-y plane over smooth wall and 90° ribs that are used to study the combined effects of roughness and APG on the flow.

Table 3.3: Summary of test conditions over smooth wall and 90° ribs.

	Test	***p/k***	U_m(m/s)	**Re$_h$**
Smooth Wall	SMS_P	–	0.385	10 690
	SMS_D	–	0.280	7 770
α= 90°	$R_2S_P\alpha_{90}P_O$	2	0.377	10 460
	$R_2S_D\alpha_{90}P_O$	2	0.313	8 690
	$R_4S_P\alpha_{90}P_O$	4	0.394	10 940
	$R_4S_D\alpha_{90}P_O$	4	0.306	8 500
	$R_8S_P\alpha_{90}P_O$	8	0.380	10 560
	$R_8S_D\alpha_{90}P_O$	8	0.300	8 340

3.6.2 EFFECT OF RIB INCLINATION

To study the effects of rib inclination on the flow, the experiments conducted at the mid-span of the channel are grouped by keeping p/k constant and varying α. These test conditions are summarized in Table 3.4.

Table 3.4: Summary of test conditions at the mid-span of ribs at different α.

	Test	α (°)	U_m(m/s)	**Re$_h$**
p/k = 2	$R_2S_P\alpha_{90}P_O$	90	0.377	10 460
	$R_2S_P\alpha_{45}P_O$	45	0.398	11 050
	$R_2S_P\alpha_{30}P_O$	30	0.390	10 830
	$R_2S_D\alpha_{90}P_O$	90	0.313	8 690
	$R_2S_D\alpha_{45}P_O$	45	0.338	9 380
	$R_2S_D\alpha_{30}P_O$	30	0.325	9 020
p/k = 4	$R_4S_P\alpha_{90}P_O$	90	0.394	10 940
	$R_4S_P\alpha_{45}P_O$	45	0.402	11 160
	$R_4S_P\alpha_{30}P_O$	30	0.376	10 430
	$R_4S_D\alpha_{90}P_O$	90	0.306	8 500
	$R_4S_D\alpha_{45}P_O$	45	0.270	7 250
	$R_4S_D\alpha_{30}P_O$	30	0.312	8 670
p/k = 8	$R_8S_P\alpha_{90}P_O$	90	0.380	10 560
	$R_8S_P\alpha_{45}P_O$	45	0.364	10 100
	$R_8S_P\alpha_{30}P_O$	30	0.358	9 950
	$R_8S_D\alpha_{90}P_O$	90	0.300	8 340
	$R_8S_D\alpha_{45}P_O$	45	0.259	8 020
	$R_8S_D\alpha_{30}P_O$	30	0.301	8 350

3.6.3 SPANWISE MEASUREMENT PLANES LOCATIONS

The test conditions that are used to study the variation of the flow across the span of the 45° and 30° ribs are presented in Table 3.5 and Table 3.6, respectively.

Data analysis showed that the spanwise variations of the flow over ribs inclined at 45° and 30° to the approach flow are similar. For this reason, the spanwise variations of the flow are presented for only ribs inclined at 45° to the approach flow in Chapter 5.

Table 3.5: Summary of test conditions at different z-locations over ribs inclined at α = 45° to the approach flow.

	Test	z (mm)	U_m(m/s)	**Re$_h$**
p/k = 2	$R_2S_P\alpha_{45}P_O$	0	0.398	11 050
	$R_2S_P\alpha_{45}P_L$	+45	0.395	10 950
	$R_2S_P\alpha_{45}P_T$	−45	0.369	10 230
	$R_2S_D\alpha_{45}P_O$	0	0.338	9 380
	$R_2S_D\alpha_{45}P_L$	+45	0.362	10 040
	$R_2S_D\alpha_{45}P_T$	−45	0.282	7 810
p/k = 4	$R_4S_P\alpha_{45}P_O$	0	0.402	11 160
	$R_4S_P\alpha_{45}P_L$	+45	0.384	10 660
	$R_4S_P\alpha_{45}P_T$	−45	0.306	8 490
	$R_4S_D\alpha_{45}P_O$	0	0.270	7 250
	$R_4S_D\alpha_{45}P_L$	+45	0.332	9 210
	$R_4S_D\alpha_{45}P_T$	−45	0.209	5 810
p/k = 8	$R_8S_P\alpha_{45}P_O$	0	0.364	10 100
	$R_8S_P\alpha_{45}P_L$	+45	0.402	11 170
	$R_8S_P\alpha_{45}P_T$	−45	0.303	8 400
	$R_8S_D\alpha_{45}P_O$	0	0.259	8 020
	$R_8S_D\alpha_{45}P_L$	+45	0.347	9 630
	$R_8S_D\alpha_{45}P_T$	−45	0.257	7 140

Table 3.6: Summary of test conditions at different z-locations over ribs inclined at α = 30° to the approach flow.

	Test	z (mm)	U_m(m/s)	**Re$_h$**
p/k = 2	$R_2S_P\alpha_{30}P_O$	0	0.390	10 830
	$R_2S_P\alpha_{30}P_L$	+45	0.382	10 600
	$R_2S_P\alpha_{30}P_T$	−45	0.358	9 940
	$R_2S_D\alpha_{30}P_O$	0	0.325	9 020
	$R_2S_D\alpha_{30}P_L$	+45	0.337	9 340
	$R_2S_D\alpha_{30}P_T$	−45	0.295	8 190
p/k = 4	$R_4S_P\alpha_{30}P_O$	0	0.376	10 430
	$R_4S_P\alpha_{30}P_L$	+45	0.387	10 750
	$R_4S_P\alpha_{30}P_T$	−45	0.340	9 440
	$R_4S_D\alpha_{30}P_O$	0	0.312	8 670
	$R_4S_D\alpha_{30}P_L$	+45	0.343	9 530
	$R_4S_D\alpha_{30}P_T$	−45	0.261	7 240
p/k = 8	$R_8S_P\alpha_{30}P_O$	0	0.358	9 950
	$R_8S_P\alpha_{30}P_L$	+45	0.392	10 870
	$R_8S_P\alpha_{30}P_T$	−45	0.328	9 110
	$R_8S_D\alpha_{30}P_O$	0	0.301	8 350
	$R_8S_D\alpha_{30}P_L$	+45	0.345	9 580
	$R_8S_D\alpha_{30}P_T$	−45	0.261	7 230

3.7 FLOW QUALIFICATION

The two-dimensionality of the flow field in the upstream parallel and diverging sections is investigated in this section. Dean (1978) examined forty two references and found that three-dimensional effects are significant near the centerline if the aspect ratio of the channel is less than 7. It was noted that if AR < 7, an apparent increase in U at the centerline results due to low-velocity regions in the corners. According to Dean (1978), true secondary flow reaches the centerline only for AR well below 7. For AR = 12, it was found that the net rise in the centerline values of U was only 2% over a distance of 100 channel heights. For channels having AR of 3 and 1, it was reported that the maximum spanwise velocity was on order of 1.0% to 1.5% of the streamwise centerline velocity (Hoagland, 1960; Brundrett and Baines, 1964). Fujita *et al*. (1989) also studied turbulent flows in channels with AR = 1 and 2, and observed that the secondary flow velocity in the square channel (AR = 1) was more intense than that observed in the rectangular channel. Since the existence of secondary flow velocity is due to the three-dimensionality of the flow, the above observations suggests that as AR decreases, the three-dimensionality of the flow becomes more severe. Fujita *et al*. (1989) observed that the isolines of U across the cross-section of the channel were much more concave in a square channel than in a rectangular channel. This was attributed to the stronger secondary flow velocity in the square channel.

In general, previous studies have shown that if the mean flow is three-dimensional, there is a considerable reduction in the Reynolds shear stress, turbulence kinetic energy and Townsend structural parameter compared to the two-dimensional counterpart (Moin *et al*, 1990; Coleman *et al*., 1990; Sendstad and Moin, 1992). Mean flow three-dimensionality also produces non-alignment of the turbulent shear stress angle and mean velocity gradient angle in planes parallel to the wall. It should be noted that the presence of secondary flow velocity leads to a velocity gradient of the form dW/dy. According to Bradshaw and Pontikos (1985), the streamwise vorticity arises from tilting of spanwise vorticity vector resulting in a gradual decrease in the mean shear dU/dy in x-y plane. The eddies responsible for producing $-\overline{uv}$ are less organized if they are tilted over in the y-z plane by the mean shear dW/dy. Thus, the presence of dW/dy has a significant influence on $-\overline{uv}$, and that $-\overline{uw}$ becomes important in turbulence production. Therefore, if the flow is three-dimensional, the mechanisms responsible for the production of $-\overline{uv}$ are modified.

As noted earlier, the channel aspect ratios in the measurement planes within the upstream parallel section and diverging section are, respectively, 3.35 and 2.40. These values of AR are considerably lower than the minimum value of AR = 7 suggested by Dean (1978) for the flow to be two-dimensional. Figure 3.4 shows the distributions of the streamwise mean velocity $U(z')$, spanwise mean velocity $W(z')$, streamwise Reynolds normal stress $\overline{u^2}(z')$, spanwise Reynolds normal stress $\overline{w^2}(z')$ and Reynolds shear stress $-\overline{uw}(z')$ across the channel in the parallel section. These quantities are normalized with the local mean velocity, U_0 at mid-span of the channel in the respective *x*-*z* measurement plane. The z'-axis (spanwise axis measured from the side wall of the channel) is normalized by the channel half-width, B. The y-locations at which these measurements were made are also indicated. Figure 3.4a demonstrates that U profiles at the three y locations decrease as the centerline of the channel is approached. For example, in the region $0.40 \leq z'/B \leq 0.70$, $U(z')$ is about 4.8%, 2.6% and 5.4%, respectively, at $y = 0.75\delta$ $y^+ = 156$ and $y^+ = 89$ higher than the corresponding value (U_0) at mid-span ($z'/B = 1.0$). The decrease in U near the mid-span of the channel may be due to secondary flow. The iso-contour plots of Fujita *et al*. (1989) also showed a reduction in U at the mid-span of the square and rectangular channels. For $z'/B \leq 0.30$, $U(z')/U_0$ decreases with increasing wall-normal distance. This is due to secondary flow directed toward the corner of the channel along its bisector angle (Leutheusser, 1963) which is a signature of flow in a channel with a low aspect ratio. Beyond $z'/B = 0.30$, U/U_0 at the various y-locations is fairly independent of wall-normal location. The maximum dimensionless mean spanwise velocity (W/U_0) is about 1.7%, 3.6% and 5.0%, respectively at $y = 0.75\delta$, $y^+ = 156$ and $y^+ = 89$ (Figure 3.4b). This suggests that the intensity of the secondary flow is more severe,

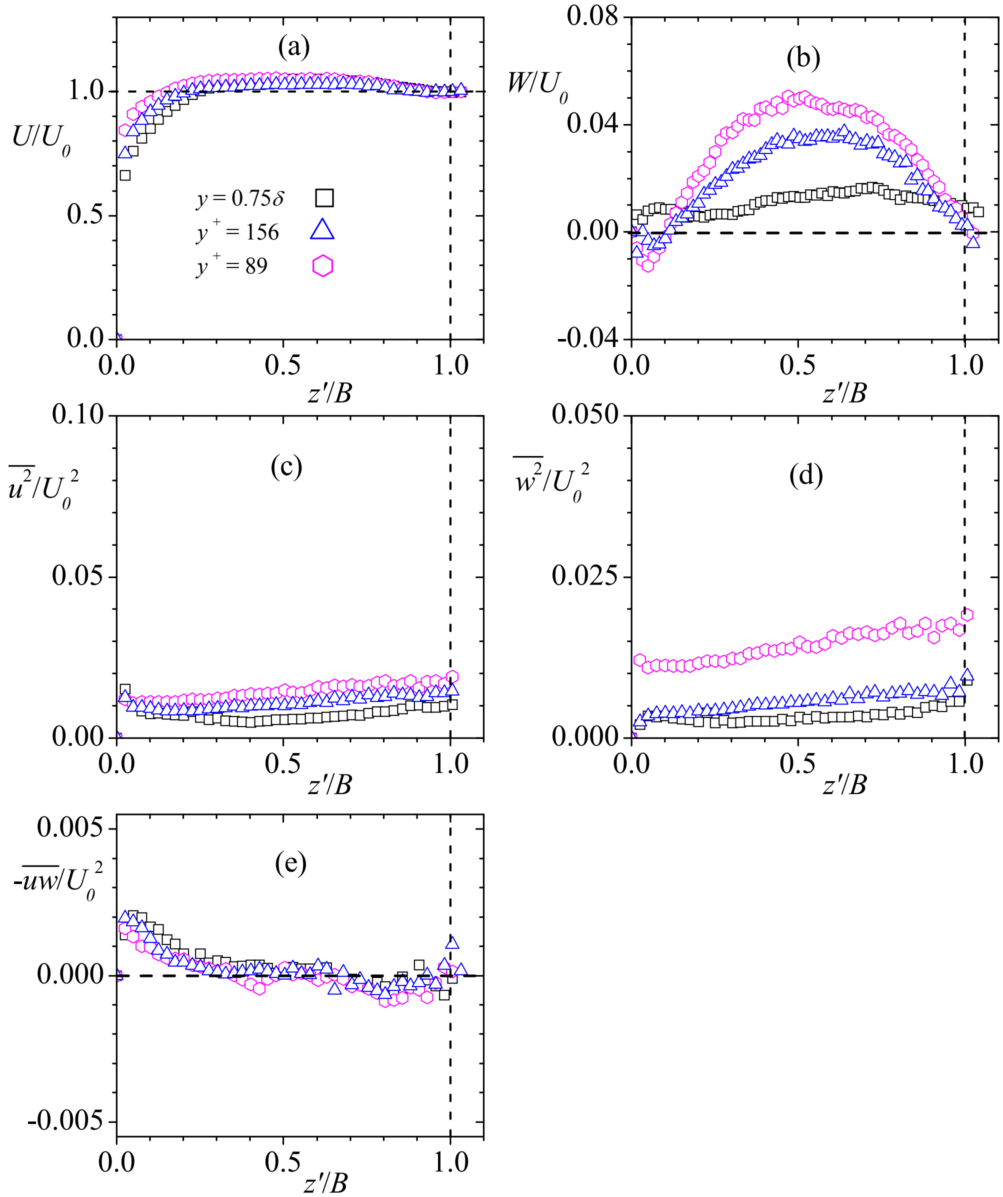

Figure 3.4: Distribution of mean velocities (U/U_0 and W/U_0) Reynolds stresses ($\overline{u^2}/U_0^2$, $\overline{w^2}/U_0^2$and$-\overline{uw}/U_0^2$) over the smooth wall in the upstream parallel section at various y-locations.

near the wall than further away from the wall. Figures 3.4c and 3.4d show that the behaviour of $\overline{u^2}(z')$ and $\overline{w^2}(z')$ are similar. These normal stresses increased towards the channel mid-span, and are higher closer to the channel floor than in the outer layer. The Reynolds shear stress (Figure 3.4e) decreased rapidly away from the wall, and became negligible in the region $0.34 \leq z'/B \leq 0.72$.

Figure 3.5 presents the distributions of U/U_0, W/U_0, $\overline{u^2}/U_0^2$, $\overline{w^2}/U_0^2$ and $-\overline{uw}/U_0^2$ in the diverging section. The distribution of $U(z')$ is more severely distorted especially, at $y = 0.75\delta$ (Figure 3.5a) than observed in the upstream parallel section (Figure 3.4a). This should be expected since the aspect ratio (AR = 2.40) in the diverging section is much lower than in the parallel section (AR = 3.35). At $y = 0.75\delta$, the region of constant U is very narrow compared to those at $y^+ = 81$ and $y^+ = 49$. The maximum value of U/U_0 is 1.15, 1.23 and 1.15, respectively, at $y = 0.75\delta$, $y^+ = 81$ and $y^+ = 49$. As the channel mid-span is approached, U decreases and forms a dent slightly ahead of z'/B = 1.0. The minimum value of U in the core region is about 97%, 98% and 97% of the local streamwise mean velocity at $z'/B = 1.0$, respectively for $y = 0.75\delta$, $y^+ = 81$ and $y^+ = 49$.

Similarly, the maximum spanwise velocity in the diverging section (Figure 3.5b) is about 2.8%, 5.6% and 6.3% of the local streamwise mean velocity at $z'/B = 1.0$, respectively at $y = 0.75\delta$, $y^+ = 81$ and $y^+ = 49$. The present $(W/U_0)_{max}$ in both the parallel and diverging sections are generally higher than the maximum values of 1.0% and 1.5% reported by Hoagland (1960) and Brundrett (1964), respectively. Therefore, three-dimensional effects on the flows investigated in the present study cannot be ignored.

In Figures 3.5c and 3.5d, the behaviour of $\overline{u^2}(z')$ and $\overline{w^2}(z')$ is similar; however $\overline{u^2}(z')$ is more than twice $\overline{w^2}(z')$, indicating that the Reynolds normal stresses are highly anisotropic. Close to the channel floor, these Reynolds normal stresses increase rapidly towards the channel mid-span. Meanwhile, at $y = 0.75\delta$, the normal stresses form an early kink with minimum value at $z'/B = 0.38$. It is also evident that these normal stresses are higher closer to the channel floor than in the outer layer. The Reynolds shear stress (Figure 3.5e) decreased rapidly away from the wall, and it changes sign twice before

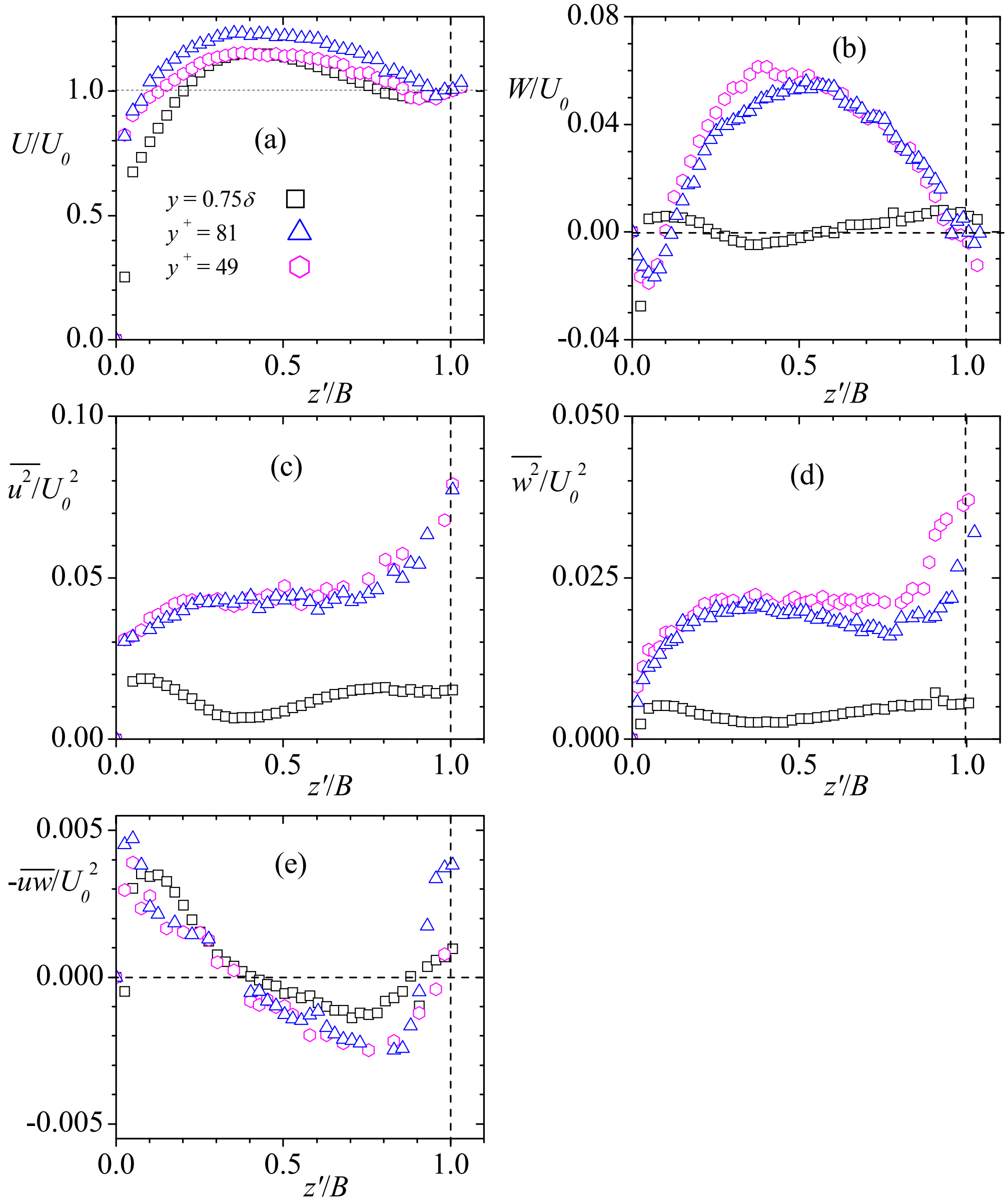

Figure 3.5: Distribution of mean velocities (U/U_0 and W/U_0) Reynolds stresses ($\overline{u^2}/U_0^2$, $\overline{w^2}/U_0^2$ and $-\overline{uw}/U_0^2$) over the smooth wall in the diverging section at various *y*-locations.

reaching z'/B = 1. From the foregoing, the effects of three-dimensionality of the mean flow are likely to be more severe in the diverging section than in the parallel section.

The distribution of Reynolds shear stress ($-\overline{u^+v^+}$) measured in the *x-y* plane in the upstream parallel and diverging sections is show in Figure 3.6. Included in this plot are fully developed turbulent channel flow data from Kim *et al*. (1987) and Moin *et al*.

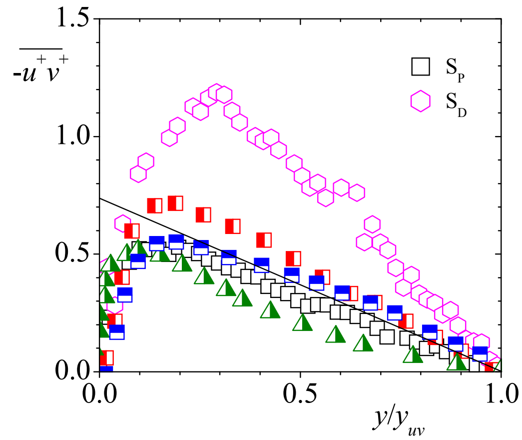

Figure 3.6: Distribution of Reynolds shear stress over the smooth wall in the *x*-*y* plane. Additional symbols: Kim *et al*. (1987): ◧; Coleman *et al*. (1990): ▲, and Moin *et al*. (1990): ⬒. Note: appropriate number of data points is skipped to avoid data congestion.

(1990). The characteristic low Reynolds shear stress in the upstream parallel section is partly due to lack of two-dimensionality of the flow. The DNS results of Spalart (1988), Coleman *et al*. (1990) and Sendstad and Moin (1992) in three-dimensional turbulent boundary layers and channel flow also showed a reduction in the Reynolds shear stress as well as the turbulence kinetic energy. For example, Spalart (1988) observed that the peak of $-\overline{u^+v^+}$ decreased from 0.92 to 0.80, when the aspect ratio of the simulation domain was reduced from 4.0 to 1.9. Moreover, Coleman *et al*. (1990) observed peak value of 0.52 for the $-\overline{u^+v^+}$ in the simulation of Ekman layer over a smooth wall (Figure 3.6). The ratio of the simulation domain in the *y* and *z* directions was 2:1. It was argued that the reduction in $-\overline{u^+v^+}$ was due to the break-up of the streamwise aligned turbulent flow structure by the spanwise directed mean flow. For a three-dimensional fully developed channel flow (AR = 2.1, Re_h = 3000), Moin *et al*. (1990) also reported a decrease in the Reynolds shear stress and turbulence kinetic energy, as well as a misalignment between the shear stress and velocity gradient angles. The peak of $-\overline{u^+v^+}$ was found to be 0.56

(Figure 3.6). The turbulence production was observed to decrease while dissipation increased. Moin *et al*. (1990) attributed the reduction of the Reynolds shear stress and kinetic energy to break-up of near-wall streaks which were weakened as the vortices above them were shifted sideways due to the cross-flow. In the diverging section, however, the maximum $-\overline{u^+v^+}$ exceeds 1. This increase is largely due to enhancement of $-\overline{uv}$ by APG combined with a decrease in U_τ^2 in the presence of APG.

The mean flow three-dimensionality was also analyzed over the $R_8\alpha_{90}$ and $R_8\alpha_{45}$ ribs. These results are presented in Appendix A. The results indicated that $U(z')$ and $W(z')$ were more severely distorted over these rough walls. Also, Fujita *et al*. (1989) observed pronounced concavity in the iso-contours of U over k-type rough wall modeled with square ribs compared to the results over smooth wall. They also found that the secondary flow was more intense over the rough wall.

3.8 MEASUREMENT UNCERTAINTY ANALYSIS

Measurement uncertainty analysis was done following the AIAA standard derived and explained by Coleman and Steele (1995). Analyses of bias and precision errors inherent in the PIV technique are available in Prasad *et al*. (1992) and Forliti *et al*. (2000). In general, a complete uncertainty analysis involves identifying and quantifying both the bias and precision errors in each part of the measurement sequence. In PIV technique, the accuracy of velocity measurement is limited by the accuracy of the sub-pixel interpolation of the displacement correlation peak. Particle response to fluid motion, light sheet positioning, light pulse timing and size of interrogation area are among the other sources of measurement uncertainties. Based on the size of the interrogation area and curve fitting algorithm used to calculate the instantaneous vector maps, and the large number of instantaneous vector maps used to calculate the mean velocity and turbulence quantities, the uncertainty in the mean velocities at 95% confidence level is estimated to be ±1.6% and ±0.7% of the local mean velocity, respectively, for *U* and *V*. The uncertainties in turbulence intensities, Reynolds shear stress and triple velocity correlations are estimated to be ± 4%, ± 8% and ± 12%, respectively. The uncertainties in production terms are estimated to be within ± 12%. Close to the ribs, uncertainties in the mean velocities are estimated to be ±2.3% and ±1.7% of the local mean velocity, respectively, for *U* and *V*. For the Reynolds stresses uncertainty close to the ribs is estimated to be ±10%. Detailed uncertainty analyses in this study are presented in Appendix B.

CHAPTER 4

TURBULENCE STATISTICS AND STRUCTURES OVER SMOOTH WALL AND RIBS AT 90° TO APPROACH FLOW

This chapter presents the data sets obtained in the *x*-*y* plane in both the parallel and diverging sections of the smooth wall and rough walls modeled with ribs at 90° to the approach flow. As noted in earlier chapters, the ribs (of nominal height, k = 3 mm) were attached to the lower wall of the channel. They were spaced to produce pitch-to-height ratios of p/k = 2, 4 and 8 corresponding to *d*-type, intermediate type and *k*-type rough walls, respectively. Both one point statistics and multi-point statistics were obtained to examine the effects of adverse pressure gradient (APG), roughness, and combined effects of roughness and APG on the flow. The data sets presented include the streamlines, mean velocities, Reynolds stresses and their ratios, eddy viscosity, mixing length, skewness factors, and production terms for turbulence kinetic energy and Reynolds shear stress. The structure analysis was performed using techniques such as Galilean decomposition of the instantaneous velocity fields, swirling strength, quadrant decomposition, two-point correlations and linear stochastic estimate. These techniques will provide additional insight to unravel the cause of the differences observed in the distributions of turbulence statistics due to roughness and pressure gradient.

The chapter is divided into two main sections. The flow characteristics such as boundary layer and drag parameters, and the flow patterns of some selected quantities are presented in Section 4.1. The combined effect of roughness and APG is considered in Section 4.2.

4.1 GENERAL FLOW CHARACTERISTICS

4.1.1 BOUNDARY LAYER CHARACTERISTICS

The boundary layer thickness (δ), displacement thickness (δ^*), momentum thickness (θ) and shape parameter (H) adjacent to the lower wall in the upstream parallel section (S_P) and diverging section (S_D) of the test channel over the smooth and rough walls are presented in Table 4.1. In the estimation of these boundary layer parameters and subsequent plots in this chapter, the wall-normal axis is made zero at the floor of the straight lower wall. The table also includes the maximum velocity (U_m), deceleration/acceleration parameter (K), Clauser pressure gradient parameter (β), Reynolds number based on the maximum velocity and momentum thickness ($Re_\theta = U_m\theta/\nu$), and the Reynolds number based on the friction velocity and boundary layer thickness ($Re_\tau = U_\tau\delta/\nu$). In the diverging section, the flow expands and spreads towards the upper diverging wall, thereby making the flow asymmetric and reducing the mean velocity drastically. Therefore, one of the effects of an adverse pressure gradient on the mean flow is to decrease the maximum velocity (U_m). This reduction is largely explained by a 41% increase in cross-sectional area in the diverging section relative to the upstream parallel section for the smooth wall test condition.

Table 4.1 revealed that adverse pressure gradient thickens the boundary layer thereby increasing the values of δ, δ^*, θ and H over both the smooth and rough walls. The increase in δ, δ^*, θ and H in the diverging section are 54%, 162%, 145% and 7%, respectively for the smooth wall. Similarly, over the *d*-type rough wall, δ, δ^*, θ and H increased by 73%, 137%, 118% and 8.5%, respectively, compared to the upstream values. A similar behaviour of δ, δ^*, θ and H with APG is observed over the intermediate type and *k*-type rough walls. The larger δ, δ^* and θ in the diverging section is attributed to

Table 4.1: Summary of boundary layer parameters over smooth wall and 90° ribs.

Test	***p/k***	U_m m/s	δ mm	δ^* mm	θ mm	H	k/δ	K $\times 10^{-7}$	β	Re_θ	Re_τ
SMS_P	–	0.385	24.0	2.9	2.0	1.45	-	1.21	−0.05	750	470
R_2S_P	2	0.377	28.2	6.8	3.4	2.00	0.106	1.41	−0.07	1300	750
R_4S_P	4	0.394	35.5	10.6	4.9	2.17	0.085	1.29	−0.09	1930	1100
R_8S_P	8	0.380	39.6	12.7	5.6	2.29	0.076	1.93	−0.10	2120	1440
SMS_D	–	0.280	37.5	7.6	4.9	1.56	-	−24.49	2.93	1370	440
R_2S_D	2	0.313	48.8	16.1	7.4	2.17	0.061	−23.95	2.56	2320	1050
R_4S_D	4	0.306	53.2	20.7	8.6	2.39	0.056	−20.67	2.42	2650	1200
R_8S_D	8	0.300	57.8	22.7	9.4	2.41	0.052	−26.59	2.18	2820	1580

the reduction in U by APG across a significant portion of the boundary layer. Prior studies also reported an increase in δ, δ^*, θ and H with an APG (Spalart and Watmuff, 1993; Tay *et al*., 2009). The observed increase in δ^* and θ within the diverging section is an indicative of the characteristic higher mass and momentum flux deficits associated with an APG flow. This observation is consistent with the less uniform distribution of the mean velocity profiles in the diverging section. Meanwhile, Table 4.1 also demonstrates that δ, δ^*, θ and H are enhanced over the rough walls, irrespective of the pressure gradient. The enhancement increases as p/k increases. This is due to a considerable reduction in U by the ribs across a significant portion of the boundary layer as p/k increases. Similarly, the increase in the values of δ^* and θ suggests that the ribs are effective in enhancing mass and momentum flux deficits. Connelly *et al*. (2006) and Tachie (2007) also observed that δ, δ^*, θ and H increase with increasing roughness. Besides, the larger values observed for δ, δ^* and θ and H over the ribs in the diverging section imply that APG acts jointly with roughness to enhance the effects of wall roughness on the boundary layer parameters. As will be seen subsequently, the closeness of the values of H for the intermediate type and the k-type rough walls suggests that their U-profiles are not significantly different in shape. The relative roughness, k/δ in the parallel section ($7.6\% \leq k/\delta \leq 10.6\%$) and diverging section ($5.2\% \leq k/\delta \leq 6.1\%$) exceed the maximum value of $k/\delta = 0.025$ suggested by Jimenez (2004) for the effects of roughness to be limited to the roughness sublayer.

The deceleration parameter (K) and Clauser pressure gradient parameter (β) were estimated as follows: the streamwise mean velocity profiles across the channel were obtained at several x-locations at four vector spacing intervals, i.e., $4\Delta x$, and the local maximum velocity ($U_{l,m}$) for each profile was determined and subsequently plotted versus x (Figure 4.1). A least-square linear fit to $U_{l,m}$ versus x' was made to obtain the local flow deceleration $dU_{l,m}/dx$, and this value was subsequently used to calculate K (Eq. 1.6) and β (Eq. 1.7). Table 4.1 demonstrates that K is positive in the upstream parallel section, suggesting a modest acceleration of the approach flow over both smooth and rough walls. As expected, K is negative over the smooth and rough walls in the diverging section.

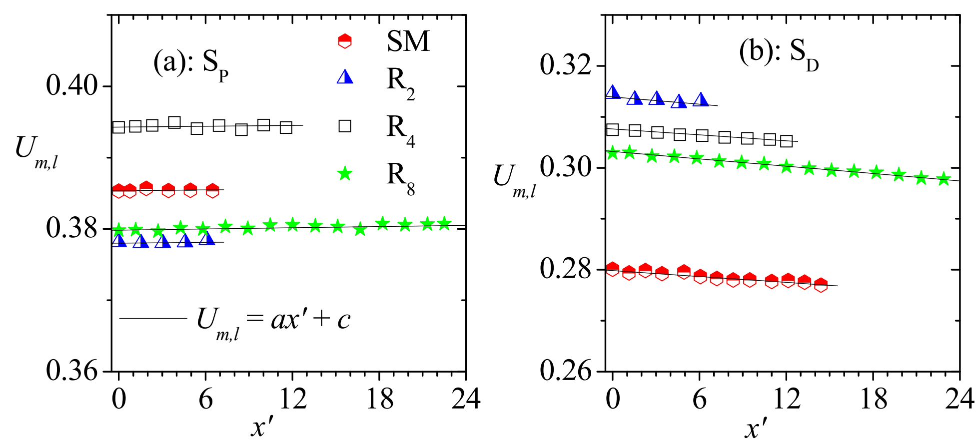

Figure 4.1: The distribution of the local maximum velocity over smooth and rough walls in the parallel section (a), and diverging section (b). Equation $U_{m,l} = ax' + c$ is the least-square linear fit to the data, where $a = dU_{l,m}/dx$ and c is a constant.

4.1.2 ISO-CONTOURS OF MEAN STREAMLINES

Figure 4.2 shows the streamlines associated with the ensemble averaged mean flow (U and V) in the parallel and diverging sections over the rough walls with the streamwise mean velocity superimposed at the background. The relative positions of the two adjacent ribs are indicated. The cavities of the *d*-type ribs are filled with a recirculation bubble (Figures 4.2a and 4.2b), and the focal points of the recirculation bubbles are located approximately at the centre of the cavity, i.e. $(x'/k, y/k) = (1.0, 0.50)$ for R_2S_P, and $(x'/k, y/k) = (1.0, 0.40)$ for R_2S_D. Compared to the *d*-type ribs, the recirculation bubbles for the intermediate type ribs are no longer circular in shape, but they are elongated in the streamwise direction (Figures 4.2c and 4.2d). The focal point is shifted towards the leading face of the downstream ribs, approximately at (2.6, 0.5) for R_4S_P and (2.6, 0.6) for R_4S_D. Since the recirculation bubble occupies the entire cavities of the *d*-type and the

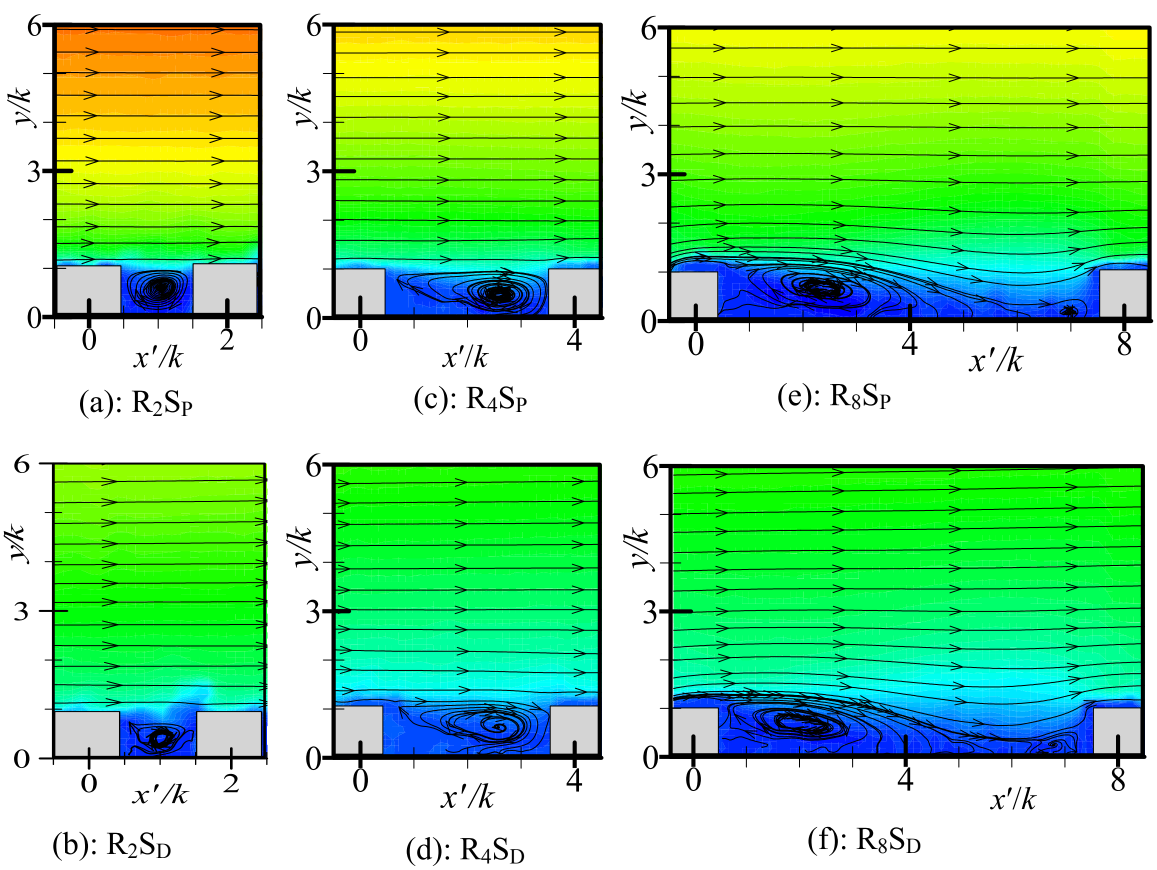

Figure 4.2: Mean streamlines with contour of the streamwise mean velocity superimposed at the background.

intermediate type ribs, the overlying boundary layer did not reattach onto the cavity floor. This observation is in good agreement with previous studies over *d*-type ribs (Cui *et al*., 2003; Tachie, 2007) and intermediate ribs (Leonardi *et al*., 2003; Nagano *et al*., 2004; Tachie *et al*., 2007). This would suggest that the flow within the cavity does not interact intensely with the overlying shear layer. The acute mutual sheltering produced by the *d*-type rib roughness is responsible for isolating the outer flow from the rib cavity (Jimenez, 2004).

Over the *k*-type ribs, two recirculation zones consisting of primary and secondary recirculation bubbles rotating at the same clockwise direction are observed (Figures 4.2e and 4.2f). In the parallel section (Figure 4.2e), the focal point of the primary recirculation bubble is at (2.4, 0.71) and that for the secondary recirculation bubble is at (6.9, 0.21). The focal points reported by Lee and Sung (2007) are (2.2, 0.75) and (6.5, 0.3) for the primary and secondary recirculation bubbles, respectively. In the diverging section (Figure 4.2f), the focal point of the primary and secondary recirculation bubbles are located at (2.0, 0.68) and (6.8, 0.27), respectively. The present focal point for the primary recirculation bubble is similar to (2.0, 0.62) reported by Tachie (2007) in an APG channel flow. Furthermore, Figures 4.2e and 4.2f revealed that the separated flows did not reattach onto the floor of the cavities, owing to a weak cavity-penetration of the inrushing fluid. The DNS results of Lee and Sung (2007), Ashrafian *et al*. (2004) and the DNS and PIV results of Lee *et al*. (2008) for $p/k = 8$ also indicated that the separated flows did not reattach to the floor of the cavities. Conversely, Leonardi *et al*. (2003) observed that for $p/k = 8$, the flow reattached onto the cavity floor at $x' = 4.8k$ and formed a short recovery region before the flow separated again. The flow visualization results of Liu *et al*. (1966)

revealed a value of $5k$ for the reattachment length for $p/k = 8$ and 12. Ikeda and Durbin (2007) suggested that the above differences in the behaviour of the *k*-type rough wall are due to Reynolds number dependence of the flow structure within the roughness sublayer. However, Ashrafian *et al*. (2004) attributed the inability of the flow to reattach to the cavity floor to low turbulence intensities and low turbulence diffusivity downstream of the trailing corner of the ribs. Although, the present Reynolds numbers (*Re*) over the *k*-type ribs are higher than the *Re* for the aforementioned studies, the level of turbulence intensities in the vicinity of the ribs is lower compared to the data of Ashrafian *et al*. (2004). Unlike the *d*-type and intermediate type ribs, the fluid in the cavities of *k*-type ribs established a remarkably strong interaction with the flow above the ribs because of the long streamwise spacing between the consecutive ribs. This is evident in the inward curving of the streamlines close to the upstream face of the downstream ribs up to $y \approx 4k$. This is also indicative of a more severe flow inhomogeneity near the *k*-type ribs. The severe curvature of the streamlines for the *k*-type ribs (Figures 4.2e and 4.2f) would also produce intense vertical transport of the streamwsie momentum (ρU) by the wall-normal velocity (V). According to Kameda *et al*. (2004), the mean momentum flux (UV) is produced by the curvature of the mean streamline so that the significant curvature associated with the *k*-type ribs increased the magnitude of UV. The high UV will undoubtedly argument momentum transport across the interface, and hence a stronger interaction between the cavities and the overlying boundary layer.

In the parallel section, the streamlines are nearly parallel to the rib crest at $y > k$ (Figures 4.2a and 4.2c) and for $y > 4k$ (Figure 4.2e). Thus, beyond these locations, the flow is nearly homogeneous in the streamwise direction. On the contrary, the tilting of the streamlines beyond the cavity height (i.e., $y > k$ in Figures 4.2b and 4.2d, and $y > 3k$ in Figure 4.2f) in the diverging section upward towards the upper diverging wall implies that the flow inhomogeneity in the streamwise direction is not limited to the vicinity of the ribs. Since the severity of the streamlines inclination in the diverging section increases with p/k, so does the level of flow inhomogeneity. The inclination of the streamlines in the diverging section was also observed by Tachie (2007).

4.1.3 ISO-CONTOURS OF MEAN VELOCITIES

The iso-contours of the streamwise mean velocity (U) and the wall-normal mean velocity (V) are plotted to visualize the global variation of U and V over a pitch. The above quantities were normalized using the spatial averaged maximum streamwise mean velocity (U_m), and the rib height (k) is used to normalize the x and y axes. Figure 4.3 shows the plots for the normalized streamwise mean velocity (U/U_m). For all the test cases, negative values of U/U_m are found in the cavity, confirming the observed flow reversal in the cavity. The strength of the reverse flow is nearly similar for all the test cases, except for R_4S_P (Figure 4.3c) where the strength of the reverse flow is about twice the values observed for R_4S_D (Figure 4.3d) and other flow conditions. The contraction produced by the ribs created a region of strong flow acceleration in the immediate vicinity of the ribs followed by a region of flow deceleration. The contraction produced by the ribs also results in a large mean shear ($\partial U/\partial y$) immediately above the crest of the ribs. As a result, the production of the turbulence kinetic energy will be high in the vicinity of the ribs. Previous study by Ashrafian *et al*. (2004), indeed, indicated that maximum production of the turbulence kinetic energy occurred upstream and on the crest of the ribs. The least magnitude for the production of the kinetic energy was observed

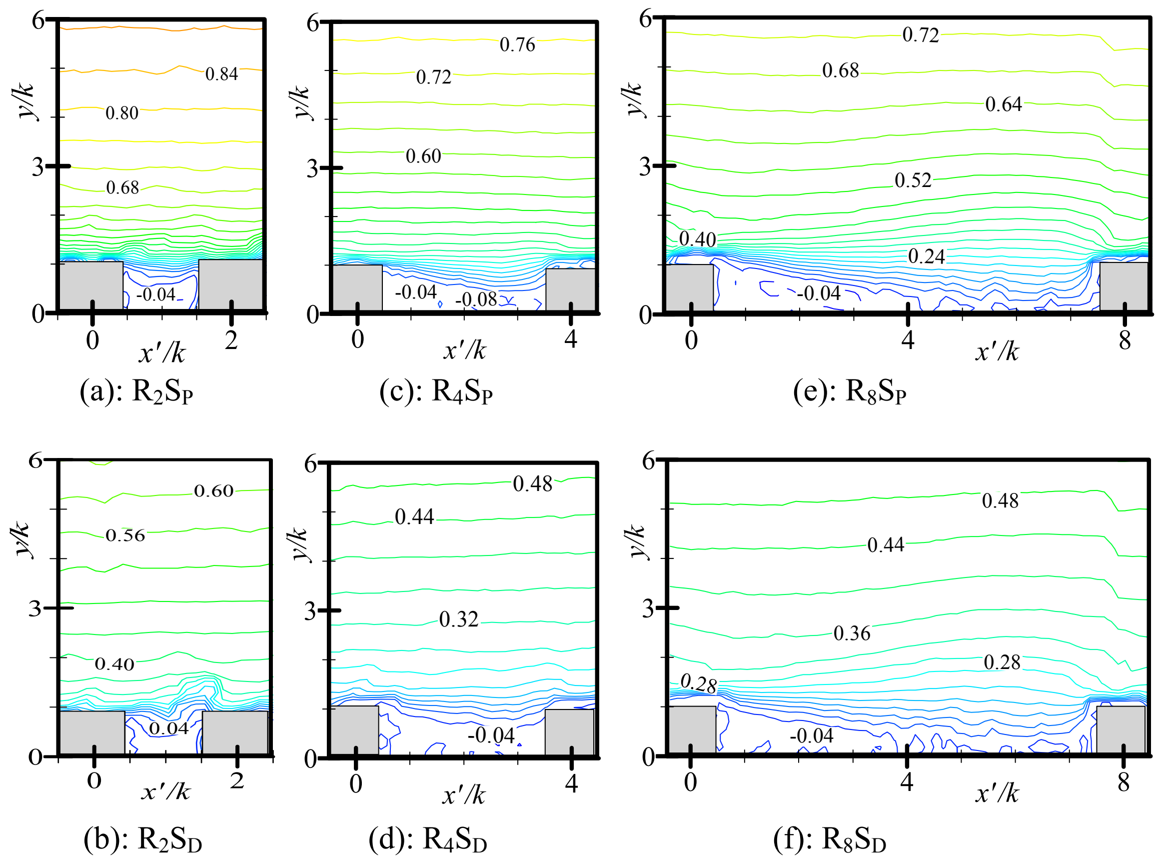

Figure 4.3: Iso-contours of the streamwise mean velocity component (U/U_m) in the parallel section: (a), (c) and (e) and diverging section: (b), (d) and (f).

within the cavity. In general, the values of U/U_m increases monotonically with y/k from the rib crest. The streamwise mean velocity is spatially inhomogeneous close to the ribs. The extent of the region of inhomogeneity in U increases with APG. Figures 4.3a, 4.3c and 4.3e show that the iso-lines above the rib become nearly parallel to the rib crest in the region $y/k > 1.5$ for R_2S_P (Figure 4.3a), $y/k > 2$ for R_4S_P (Figure 4.3c), and $y/k > 6$ for R_8S_P (Figure 4.3e). Figures 4.3b, 4.3d and 4.3f demonstrate that the isolines of U/U_m above the rib are not parallel to the rib crest in the diverging section, instead they are tilted upward towards the upper diverging wall. The tilting of the isolines of U/U_m is most severe for R_8S_D.

The corresponding iso-contours of the wall-normal mean velocity, V/U_m are shown in Figure 4.4. For p/k = 8 (Figures 4.4e and 4.4f), the plot for the wall-normal mean velocity is qualitatively similar to the DNS results of Lee and Sung (2007) and Ashrafian *et al*. (2004). In general, the plots show that there is periodically alternating flows towards the wall (inflow, i.e. negative V) and away from the wall (outflow, i.e. positive V) in the near-wall region. Noticeable differences exist in V/U_m for the various p/k. For p/k = 2 (Figures 4.4a and 4.4b), the region of negative V occurs near the upstream face of the downstream rib and it extends from the cavity floor to about 0.75k of the rib. The negative V is due to the inflow of the fluid from the downstream edge of

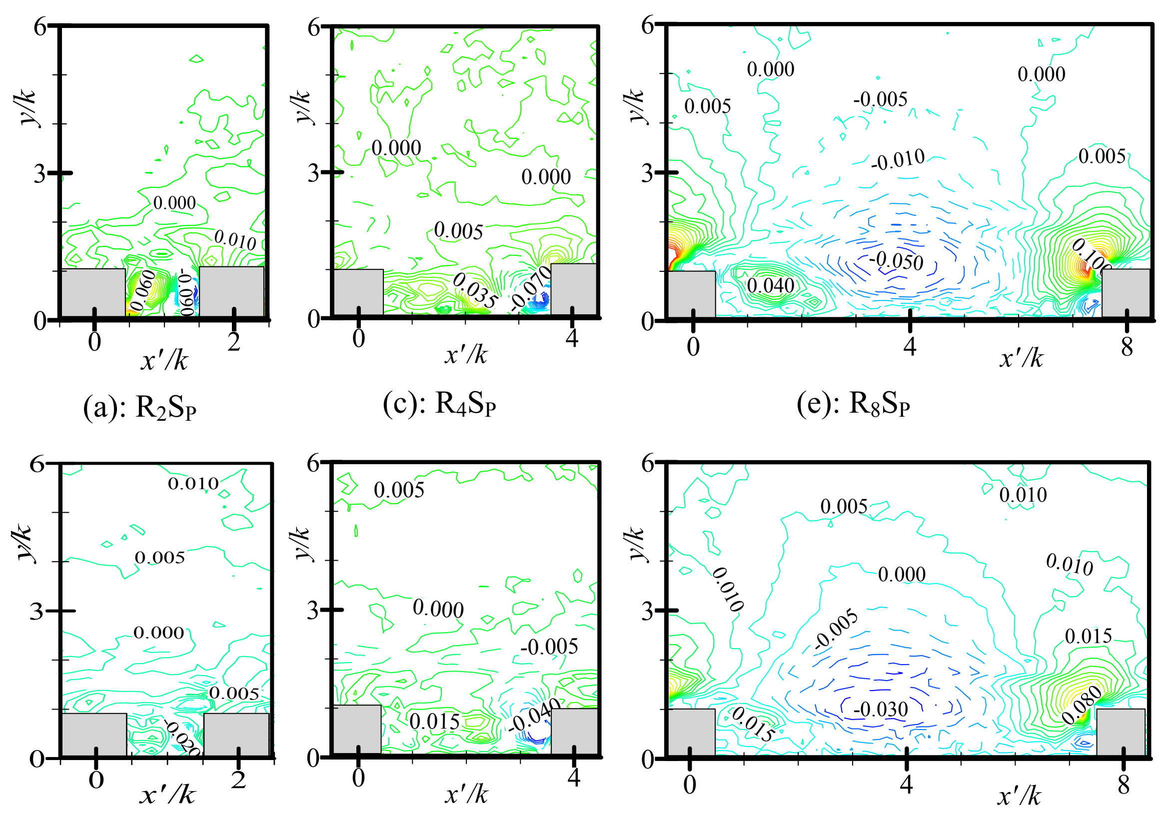

(a): R_2S_P (c): R_4S_P (e): R_8S_P

(b): R_2S_D (d): R_4S_D (f): R_8S_D

Figure 4.4: Iso-contours of the wall-normal mean velocity component (V/U_m) in the parallel section: (a), (c) and (e) and diverging section: (b), (d) and (f).

the cavity. Kameda *et al*. (2007) suggested that the inflows are associated with the formation of eddies in the cavity, whereas the outflows are accompanied by the disappearance of the spanwise vorticity in the cavity. Note that the region of negative V near the upstream face of the downstream rib diminishes with increasing p/k. At the leading edge of the downstream rib, V is mostly positive and both the magnitude and extent of the positive region increase with p/k. Thus, the diminishing of the negative V region near the upstream face of the downstream rib is due to the suppression of the observed negative flows by the positive flows. At the downstream face of the upstream rib, V is positive, covering about 87%, 71% and 31% of the cavity size, respectively for R_2S_P, R_4S_P, and R_8S_P. Similarly, the extent of positive V formed in the cavity at the downstream face of the upstream rib diminished to about 58%, 69% and 25% of the cavity size, respectively for R_2S_D, R_4S_D, and R_8S_D. This suggests that a larger portion of the *d*-type and intermediate type cavities are mainly outflow fluid. The sudden drop in the x extent of the positive V close to the downstream face of the upstream rib for $p/k = 8$ (Figures 4.4e and 4.4f) is due to the large concomitant negative V resulting from flow entrainment that occupies a larger portion of the cavity. The maximum of this negative V occurs at the centre of the cavity, and the negative V extends radially out towards the two adjacent ribs, thereby suppressing the outflow fluid (positive V). However, the flow entrainments that occur in the cavities of *k*-type ribs are less distinct for the *d*-type and intermediate type rough walls.

4.1.4 ISO-CONTOURS OF REYNOLDS STRESSES

The iso-contours of Reynolds stresses are also plotted to visualize the global variation of the turbulence motions over a pitch (Figure 4.5 and Figure 4.6). The Reynolds stresses were normalized using ${U_m}^2$ and the x and y axes were normalized by the rib height, k. The $\overline{u^2}$ and $-\overline{uv}$ contours for R_2S_P and R_8S_P are qualitatively similar to the results reported over d-type ribs by Cui *et al*. (2003), and k-type ribs by Lee and Sung (2007) and Lee *et al*. (2008). It should be noted that the streamwise Reynolds normal stress, $\overline{u^2}/U_m^2$ (Figure 4.5) is least within the cavity, but grows quickly to a maximum near the overlying layer of the cavity (i.e., just above $y = k$) in the parallel section. This is followed by a reduction with increasing y, for y greater than $1.4k$ in the parallel section. Meanwhile, in the diverging section, $\overline{u^2}/U_m^2$ increases monotonically with increasing y/k right from the floor of the cavity. Thus, the maximum $\overline{u^2}/U_m^2$ occurs farther away from the wall in the

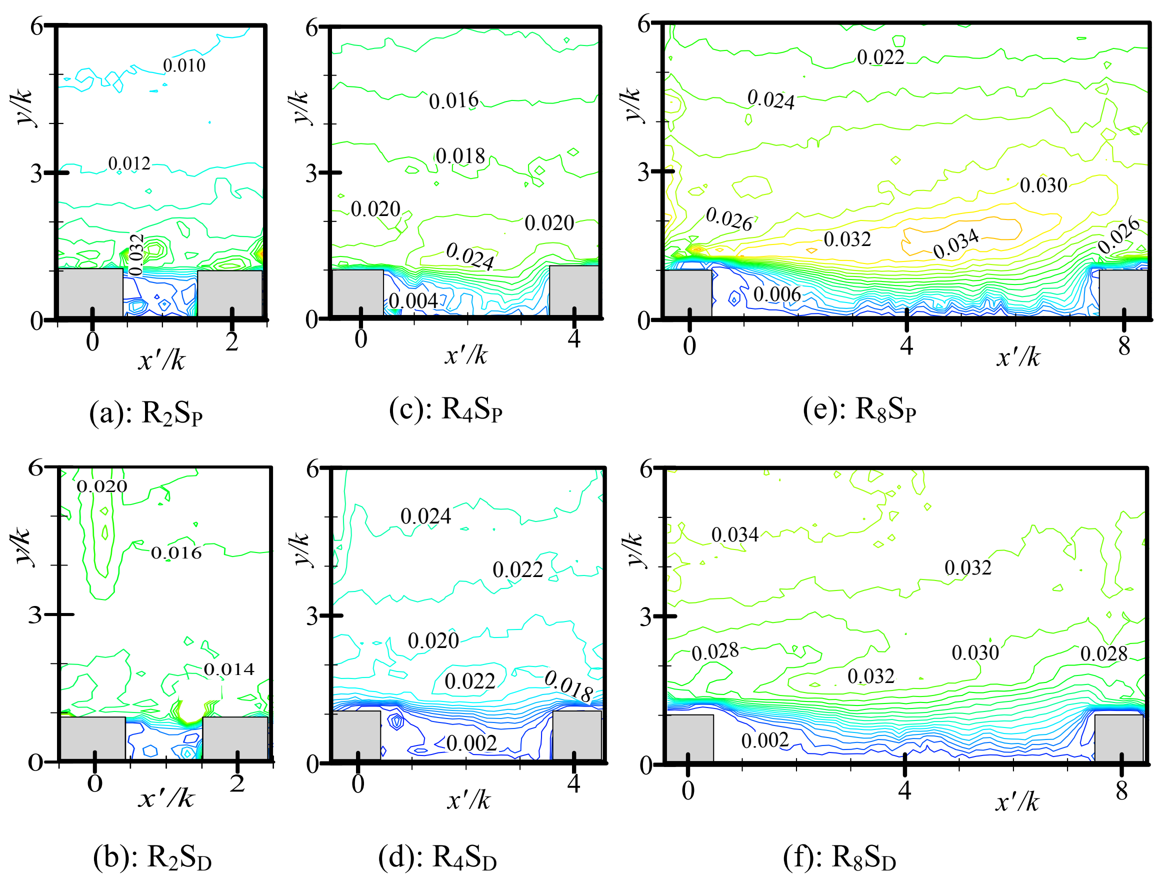

Figure 4.5: Iso-contours of the streamwise Reynolds normal stress ($\overline{u^2}/U_m^2$) in the parallel section: (a), (c) and (e) and diverging section: (b), (d) and (f).

diverging section. This is caused by the imposed APG which spreads the inactive motions outward.

The Reynolds shear stress provides insight into the vertical turbulent momentum flux. The contours of $-\overline{uv}/U_m^2$ in the parallel and diverging sections are shown in Figure 4.6. Similar to the previous results, $-\overline{uv}$ in the cavity of the *d*-type rough wall is practically negligible (Figures 4.6a and 4.6b). Meanwhile, the intermediate type and the *k*-type ribs (Figure 4.6c-Figure 4.6f) show that $-\overline{uv}$ in the cavity is significantly larger than observed in the *d*-type ribs. Also, small regions of negative values of the Reynolds shear stress are observed near the crest of the ribs. As observed in the previous results in

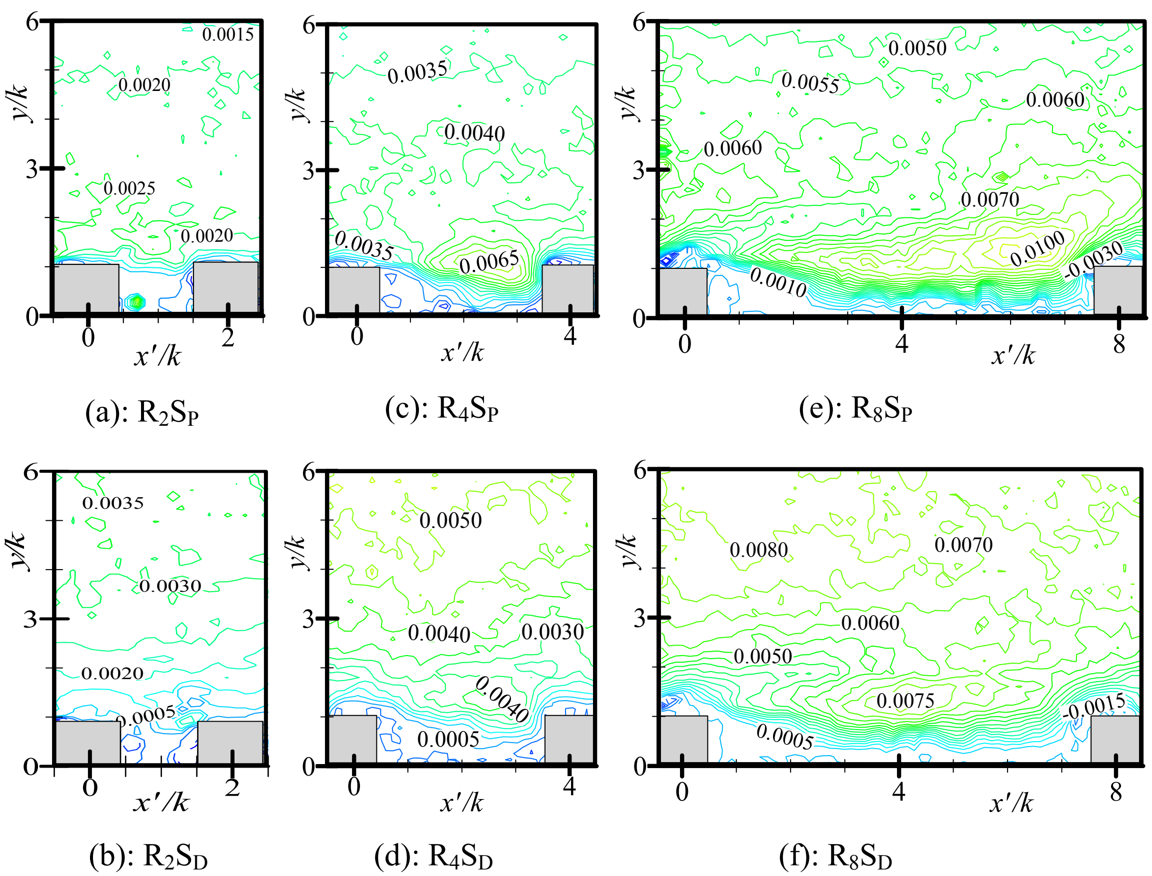

Figure 4.6: Iso-contours of the Reynolds shear stress ($-\overline{uv}/U_m^2$) in the parallel section: (a), (c) and (e) and diverging section: (b), (d) and (f).

Figure 4.5, $-\overline{uv}/U_m^2$ in the parallel section increased to a maximum near the interface of the cavity and the overlying flows. This region corresponds to where the mean velocity gradient is steep (Figure 4.3). According to Lee and Sung (2007), this region also corresponds to the location where ejection and sweep events are very active. However, in the diverging section, the maximum $-\overline{uv}/U_m^2$ occurred further away from the wall as a result of the imposed APG. Besides, the magnitude of $-\overline{uv}/U_m^2$ increases in the presence of an adverse pressure gradient. It should be noted that, in all cases, the location of the maximum $-\overline{uv}/U_m^2$ corresponds to the location of the maximum streamwise and wall-normal turbulence motions. These observations are also in good agreement with the DNS and PIV results of Lee *et al*. (2008), and Ashrafian and Andersson (2006b).

4.1.5 MEAN VELOCITY PROFILES IN INNER COORDINATES AND DRAG CHARACTERISTICS

As noted earlier, prior studies have indicated that the logarithm law is also valid for mild and moderate APG (Samuel and Jourbert, 1974; Cutler and Johnston, 1989; Aubertine and Eaton, 2006). Furthermore, prior experimental and numerical simulations results over rough walls modeled with ribs demonstrated that the overlap region of the mean velocity is well described by the classical logarithm law (Leonardi *et al*., 2003; Cui *et al*., 2003). However, an accurate determination of the friction velocity over the rough walls remains a challenging task because the virtual origin (d_o) and roughness function (ΔB) are not known *a priori*. The logarithm law has also been used for turbulent flows over rough wall with mild and moderate APG (Samuel and Jourbert, 1974). Recently, Monty *et al*. (2011) employed both the Clauser chart method and oil-film interferometry method to independently estimate the skin friction velocity in APG flows over smooth wall for $0 \leq \beta$

≤ 4.75. They observed good agreement between the two methods for zero and mild adverse pressure gradient. However, for $\beta > 2.0$, it was observed that the C_f determined from the Clauser chart technique decreased by 10% from the C_f obtained from oil-film interferometry technique. In the present study, the friction velocity (U_τ) was determined using two methods: (i) the Clauser chart technique which involves fitting the measured mean velocity data to the logarithm law and (ii) by fitting the power law proposed by George and Castillo (1997) to the mean velocity data. The implementation of the two methods is described below.

The Logarithm Law: For the rough walls, the mean velocity profiles from the parallel and diverging sections were first fitted to Eq. 1.20 (Figure 4.7a-c) to estimate the friction velocity (U_τ) and virtual origin (d_o). These values were used to re-plot the mean velocity profiles in the classical logarithm law format (Eq. 1.17) in Figure 4.7d-f. The present data in the parallel section of the *k*-type rough wall agrees fairly well in the logarithm region with prior hotwire (Hanjalic and Launder, 1972) and DNS (Ikeda and Durbin, 2007) data sets obtained in fully developed channel flows (Figure 4.7c). The deviation of the data of Hanjalic and Launder (1972) from the present and DNS data of Ikeda and Durbin (2007) close to the wall is likely due to the fact that the hotwire measurements were obtained at a fixed streamwise location on the rib crest while the present PIV and previous DNS data sets were spatially averaged over a pitch. In general, Figure 4.7a-c indicates that the U^+ profiles in the diverging section of the rough walls are displaced downward relative to the profiles in the parallel section, irrespective of the specific surface condition. The values of the additive constant E for the various rough walls are summarized in Table 4.2. It is observed that the value of E (= 3.2) in the parallel section of the *k*-type ribs ($R_8S_P\alpha_{90}P_O$) is the same as reported in the previous studies (Hanjalic and Launder, 1972; Ikeda and

Durbin, 2007). In the diverging section, however, E decreased to 1.2 over the k-type ribs. Similarly, the values of E for the d-type and intermediate-type rough walls are higher in the parallel section than in the diverging section. The table also revealed that in both the parallel and diverging sections, the additive constant, E tends to be larger as p/k is reduced.

Perry *et al.* (1969) pointed out that d_o is a measure of interaction between the overlying flow and the cavities. As noted earlier, the interaction between the outer flow and the cavity flow should vary with pressure gradient and p/k. Table 4.2 demonstrates that, indeed, ratio d_o/k increases with APG and p/k which is consistent with the observation by Tachie (2007) and Leonardi *et al.* (2003).

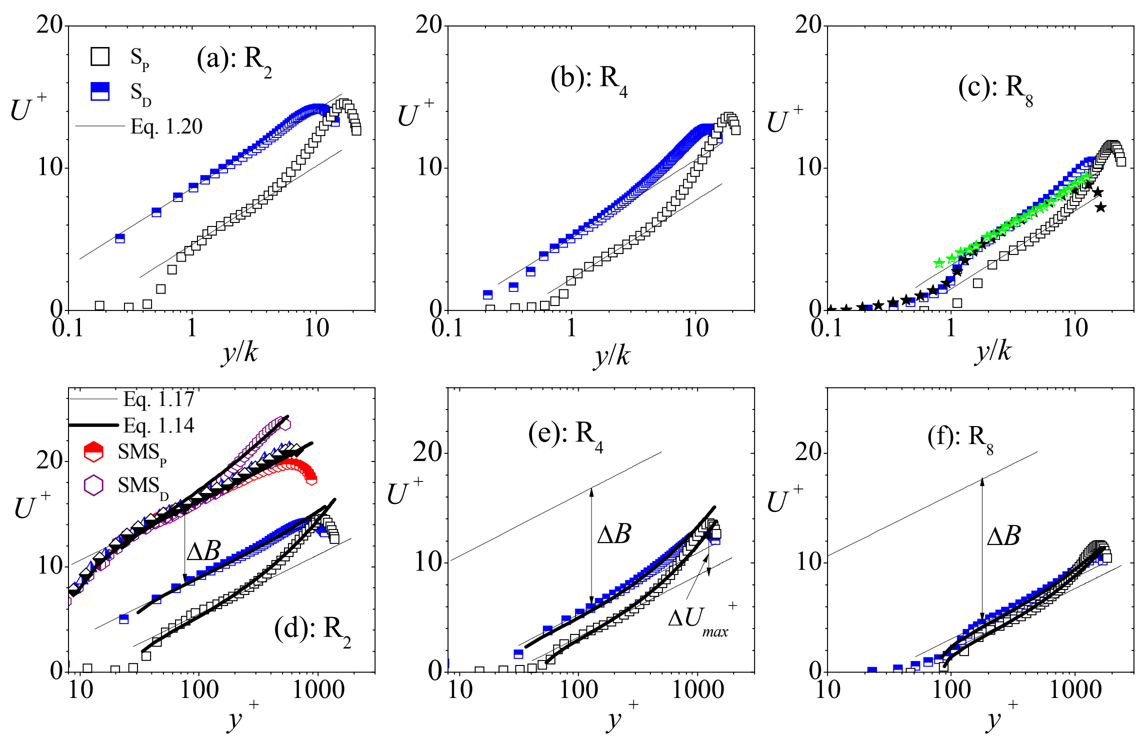

Figure 4.7: The distributions of the streamwise mean velocity profiles in inner coordinates in the parallel and diverging sections of the smooth and rough walls. Additional symbols: smooth wall: Moser *et al.* (1999): ⬢ ($Re_\tau = 395$), ▲($Re_\tau = 590$) and Krogstad *et al.* (2005): ◆ ($Re_\tau = 670$); k-type ribs: Hanjalic and Launder (1972): ☆; Ikeda and Durbin (2007): ★.

Table 4.2: Drag and wake parameters over smooth wall and 90° ribs.

Test	$U_{\tau,\,log}$ cm/s	C_f $\times 10^{-2}$	d_o/k	k^+	E	ΔB	k_s^+	k_s/k	k_s/δ	Π	C_o	C_i	a^+	γ	$U_{\tau,\,pow}$ cm/s	ΔU_τ (%)
SMS_P	1.95	0.51	-	-	-	-	-	-	-	−0.254	1.00	9.34	−16	0.125	1.96	0.51
R_2S_P	2.66	1.00	0.13	80	8.60	7.01	74	0.9	0.099	0.000	1.00	3.60	−22	0.210	2.68	0.75
R_4S_P	3.08	1.22	0.47	92	5.10	11.05	390	4.2	0.357	0.316	1.02	0.96	−26	0.382	3.12	1.30
R_8S_P	3.63	1.82	0.60	109	3.20	13.13	914	8.4	0.637	0.199	1.02	0.75	−79	0.370	3.61	−0.55
SMS_D	1.18	0.36	-	-	-	-	-	-	-	0.732	1.00	7.15	−16	0.192	1.21	2.54
R_2S_D	2.15	0.94	0.43	65	4.65	10.75	345	5.3	0.328	0.664	1.01	1.01	−28	0.387	2.20	2.33
R_4S_D	2.25	1.08	0.73	68	2.25	13.13	914	13.5	0.763	0.863	1.01	0.48	−50	0.464	2.32	3.11
R_8S_D	2.58	1.48	0.87	74	1.52	14.19	1412	18.2	0.947	0.586	1.02	0.43	−86	0.442	2.51	−2.71

The classical logarithm law plots for the smooth wall and rough walls data sets in both the parallel and diverging sections are shown in Figure 4.7d-f. The DNS data from Moser *et al*. (1999) and hotwire data from Krogstad *et al*. (2005) obtained over a smooth wall in a fully developed channel are included in Figure 4.7d for comparison. The present smooth wall data show an excellent agreement with the prior results in the logarithm region. Although the present U^+-profiles over the smooth and rough walls show a substantial logarithm region, the extent of this region diminished in the presence of APG and as p/k becomes larger. Due to the high drag characteristics associated with the ribs, the U^+-profiles in the parallel and diverging sections are shifted downward relative to the classical logarithm law plots for the smooth wall (Figure 4.7d-f). The downward shift produced by the rough wall is intensified by APG and increasing p/k.

In the upstream parallel section of the smooth wall, the U^+-profile demonstrates a negative wake component whereas in the diverging section, there is a strong positive wake component. Even though the U^+-profiles over the rough walls in the parallel and diverging sections exhibit positive wake components, the strength of the wake component is more pronounced in the diverging section than in the upstream parallel section. Thus, the reduction in the extent of the logarithm region for the U^+-profile in the diverging section is caused by the formation of the large wake component. To quantify the strength of the wake observed in the U^+ profiles (Figure 4.7), the value of the wake parameter (Π) was computed from the following relation: $\Delta U^+_{max} = 2\Pi/\kappa$, where $\kappa = 0.41$. The values of ΔU^+_{max} and Π in the parallel and diverging sections are summarized in Table 4.2. The present value of Π (= –0.25) for SMS_P is comparable to the value of –0.27 reported by Tay *et al*. (2009). Krogstad *et al*. (1992) reported $\Pi = 0.51$ for their smooth wall ZPG turbulent boundary layer measurements and attributed the higher value of Π to a higher entrainment rate. Osaka and Mochizuchi (1988) reported a value of Π = 0.68 at Re_θ = 5300 over a *d*-type rough wall turbulent boundary layer and remarked that the higher value reflects a high entrainment rate over a rough wall. The large positive value of Π in the diverging section of the smooth and rough walls can be attributed to a higher growth rate of the shear layer in the diverging section. As noted earlier, the upper diverging wall allows the flow in the diverging section to expand enabling significant entrainment of the slow-moving fluid into the outer layer, which yielded the observed dominant wake region in the profiles within the diverging section (Figures 4.7).

The Power Law: As noted above, the power law proposed by George and Castillo (1997) was also used to model the mean velocity profiles and to provide an independent estimate of the friction velocity. In applying the power law to estimate U_τ, Eq. (1.15) was first fitted to the measured data to determine the values of C_o and γ. Subsequently, Eq. 1.14 and Eq. 1.16 were used iteratively to determine C_i and U_τ. During the fitting process, the values of a^+ were adjusted for the various test conditions until a good agreement between the lower portion of the measured data and the power law was achieved. The values of C_o, C_i, γ, a^+ and U_τ are summarized in Table 4.2 and the optimized power law fits in inner coordinates are shown in Figure 4.7d-f as thick solid lines. It is immediately obvious that, in each case, the power law describes the entire logarithmic region and a significant portion of the outer layer. The implication of this salient feature is that more measured data points are available for fitting the power law than for the logarithm law. This is particularly beneficial in flows with characteristic narrow logarithmic region, for example, the low Reynolds number boundary layers, rough wall boundary layers and APG boundary layers investigated in the present study.

Table 4.2 reveals that the power law constant, C_o is nearly independent of roughness and pressure gradient. It is observed that C_i diminishes with both roughness and APG while a^+ increases with roughness and APG. The lower C_i value over the rougher surface is necessary to mimic the reduced mean velocity produced by roughness. The increase in a^+ demonstrates that as the mean velocity profiles become more asymmetric in the presence of roughness and APG, the roughness sublayer extends deeper into the outer layer of the mean flow. The power law exponent, γ, also increases in the presence of APG due to the characteristic higher wake component associated with turbulent flow subjected to APG. In both parallel and diverging sections, however, γ attained maximum over the intermediate type ribs consistent with the intense wake component observed in the U^+-profiles. Table 4.2 also shows the percentage difference between the U_τ values determined from the Clauser chart and power law. It is observed that differences between the two methods are relatively larger in the diverging section than in the parallel section. In all cases, however, the differences ΔU_τ are within ± 3.11%. It should be noted that these differences are smaller than measurement uncertainty of 10% in estimating the friction velocity, U_τ.

The Drag Parameter: The drag parameters evaluated from the Clauser method for all the four surface conditions in the parallel and diverging sections are summarized in Table 4.2. The friction velocity, U_τ, as well as the skin friction coefficient, C_f (= $2[U_\tau/U_m]^2$) decreased with APG, irrespective of the boundary condition. For example, APG diminished U_τ by 40%, 19%, 33% and 25%, respectively, over the smooth wall, *d*-type, intermediate type and k-type rough walls in the diverging section compared to the corresponding values in the upstream parallel section. Similarly, APG reduced C_f over the smooth wall and rough walls in the diverging section compared to the values in the upstream parallel section. These results imply that APG causes a larger reduction in U_τ than in U_m. Previous studies over smooth wall (Nagano *et al*., 1998; Aubertine and Eaton, 2005) and rough walls (Tachie, 2007; Tay *et al*., 2009) also reported a decrease in C_f by APG. However, both U_τ and C_f were amplified as p/k increases confirming that the k-type rough wall creates higher flow resistance than the other rough wall types in the present study. The DNS results by Leonardi *et al*. (2003) also demonstrated that C_f increase with p/k over the range of p/k considered here.

The roughness shift (ΔB) was estimated from Figure 4.7d-f, by measuring the vertical distance between the logarithm law for the case of smooth wall and the logarithm region of the U^+ profile over the rough walls. An alternate ΔB estimate was made for p/k = 8 in the parallel section using $\Delta B = \kappa^{-1} \ln k^+ + F$ proposed by Krogstad and Antonia (1999) for k-type rough walls. F = 1.2 in ZPG boundary layer flows, but Bakken and Krogstad (2003) suggested 1.9 in a rib-roughened channel flow. The calculated values for ΔB are 12.64 (for F = 1.2) and 13.34 (for F = 1.9). The latter value for ΔB (= 13.34) compares very well with ΔB = 13.13 (Table 4.2) obtained from the logarithm law plot. The roughness shift, ΔB in the diverging section increased by 53%, 13% and 13% compared to the corresponding upstream values, respectively, over the d-type, intermediate type and k-type rough walls. Earlier studies by Tachie (2007) and Tay *et al*. (2009) also indicated that APG enhances the downward shifts of the mean velocity profiles. The increase in ΔB in the diverging section compared to the upstream parallel section is due to a considerable reduction in the values of U by the ribs and APG. For the same reason, ΔB increases as p/k increases in agreement with prior studies.

The non-dimensional equivalent sand grain roughness height or roughness Reynolds number, k_s^+ was determined from Eq. 1.19 and these values are also summarized in Table 4.2. As noted in Chapter 1, the roughness regime is hydraulically smooth if $k_s^+ < 5$, transitionally rough if $5 \leq k_s^+ \leq 70$ and fully rough if $k_s^+ > 70$ (Schlichting, 1979). This classification has been used widely for both two-dimensional and three-dimensional roughness elements; however, variations to these demarcations have also been used. For example, on a closely packed spheres, Ligrani and Moffat (1986) adopted $k_s^+ \approx 15$ for the onset of the transitionally rough regime and $k_s^+ \geq 55$ for fully rough regime whereas Schultz and Flack (2007) used a much lower value of $k_s^+ \geq 26$ for fully rough regime for flow over sandpaper roughness. These support Hama (1954) assertion that the upper limit of the transition regime does not have a universal value. Based on the above classification, the present measurements over the rough walls are in the fully rough regime. It should be noted that the $k_s^+ = 74$ in the parallel section of the *d*-type ribs is just at the onset for the fully rough regime.

Bandyopadhyay (1987) argued that $k_s^+ = 55$ or 70 often used as the onset of the fully rough regime is valid for sand grain roughness only. Bandyopadhyay (1987) recast the stability chart of Furuya and Miyata (1972) and showed that for two-dimensional roughness elements with infinite aspect ratio, $k^+ = 10$ is sufficient for the onset of the fully rough regime. This also presupposes that the roughness shift depends only on k^+ and not on the Reynolds number. The values of k^+ summarized in Table 4.2 also demonstrate that all the three ribs in both the parallel and diverging sections are in the fully rough regime. Moreover, the k_s^+ is increased as the rib spacing increases and also in the presence of APG. For example, k_s^+ obtained in the diverging section is about 5-folds, 2-folds and 2-folds higher than the corresponding values obtained in the upstream parallel section, respectively, over the *d*-type, intermediate type and *k*-type ribs. Nakayama and Yokota (2002), Tachie (2007) and Tay *et al*. (2009) also reported an increase in k_s^+ in the presence of APG. On the other hand, Pailhas *et al*. (2008) reported a reduction in the non-dimensional equivalent sand grain roughness height in the presence of adverse pressure gradient. As explained by Tachie (2007), the increased values of ΔB and k_s^+ in the diverging section are consistent with the observation that APG modifies a greater extent of the inner layer of the streamwise mean velocity (Figure 4.8).

The ratio k_s/k expresses the diameter of the mono disperse equivalent sand grains that will be needed to produce the same amount of flow resistance over a particular type of roughness. Except in the parallel section of the *d*-type ribs, the values of the ratio of the equivalent sand grains roughness height to rib height (k_s/k) indicate that the ribs are much more effective in generating resistance than uniform sand grain roughness. In the parallel section of the *k*-type ribs for instance, sand grains of height 8.4k covering the entire lower wall of the channel would be required to produce this resistance generated by ribs of height k. Moreover, Table 4.2 shows that k_s/k increased with APG and p/k. Such an increase with adverse pressure gradient suggests that the size of the mono disperse equivalent sand grains required to provide the same amount of flow resistance should be larger if the flow is subjected to an APG. For example, the diameter of mono disperse equivalent sand grains required to produce the same amount of flow resistance over the ribs should be approximately 0.9k and 5.3k, respectively for $R_2S_P\alpha_{90}P_O$ and $R_2S_D\alpha_{90}P_O$.

The present values of k_s for the *d*-type rough wall are close to the values of $0.9k$ and $4.9k$ reported by Tachie (2007) over *d*-type rough wall in parallel and diverging sections, respectively. However, the present values of k_s over the *k*-type rough wall are remarkably higher than $k_s = 4.3k$ and $12.2k$, respectively for the parallel and diverging sections reported by Tachie (2007). Tay *et al*. (2009) also reported higher values of k_s/k over sanded wall and gravelled wall in the presence of APG. The ratio k_s/δ which represents a more appropriate measure of the relative roughness than k/δ is very large compared to the limit of $k/\delta = 0.025$ recommended by Jimenez (2004) for the effect of roughness to be limited to the roughness sublayer. As noted earlier, Raupach *et al*. (1991) suggested that the roughness sublayer should extend from the wall to $y = 5k$, and this recommendation is adopted for this study. The roughness sublayer, therefore, extends from the wall to $y = 0.48y_{uv}$ (0.51δ), $0.38y_{uv}$ (0.42δ) and $0.41y_{uv}$ (0.46δ) in the parallel section, respectively for *d*-type, intermediate type and the *k*-type rough walls. Note that y_{uv} corresponds to *y*-location where the Reynolds shear stress changes sign. The corresponding values in the diverging section are $0.30y_{uv}$ (0.30δ), $0.26y_{uv}$ (0.28δ) and $0.23y_{uv}$ (0.26δ), respectively, for the *d*-type, intermediate type and the *k*-type rough walls.

4.2 COMBINED EFFECTS OF ROUGHNESS AND ADVERSE PRESSURE GRADIENT

4.2.1 MEAN FLOW AND TURBULENCE STATISTICS

In order to study the combined effects of roughness and adverse pressure gradient on the flow, the profiles of mean velocity and selected turbulence statistics in the parallel section of each type of ribs are compared to the profiles in the parallel section of the smooth wall and later to the profiles in the diverging section of the corresponding rough wall. However, in order to understand the nature of APG effects over the rough walls, it is worth considering the effects of APG on the smooth wall results first. For this reason, the profiles of smooth wall data sets in both the parallel and diverging sections are always shown together with the results over the *d*-type ribs.

4.2.1.1 Mean Velocity Profiles in Outer Coordinates

Figure 4.8 shows the streamwise mean velocity profiles in outer coordinates along with some previous results for comparison. Figure 4.8a shows that the *U*-profile in the upstream parallel section of the smooth wall is in good agreement with the DNS data from Moser *et al*. (1999) obtained at $Re_\tau = 395$ in a fully developed turbulent channel flow. The plots clearly show that one of the effects of APG on the mean flow is to reduce the values of *U*, irrespective of the surface condition, and make the profiles less uniform compared to the profiles obtained in the upstream parallel section. For example, at $y/\delta = 0.5$ the value of U/U_m decreased from 0.93 in the upstream parallel section to 0.84 in the diverging section of the smooth wall (Figure 4.8a). The distribution of the *U*-profiles in the diverging section is consistent with the observed higher values of the shape factor in the diverging section compared to the parallel section.

The *U*-profile in the parallel section of the *d*-type rough wall in Figure 4.8a is compared with the large eddy simulation (LES) data in a fully developed channel (Cui *et al*., 2003). The present profile in the parallel section shows good agreement with the data from Cui *et al*. (2003) for $y/\delta > 0.1$. The difference in these profiles near the wall ($y/\delta < 0.1$) may be due to fact that the data from Cui *et al*. (2003) was obtained by performing spatial average in both streamwise and spanwise directions, whereas the present data is a spatial averaged result obtained over a pitch in the streamwise direction only. In Figure 4.8b-c, the present *U*-profiles in the upstream parallel section compared well with the

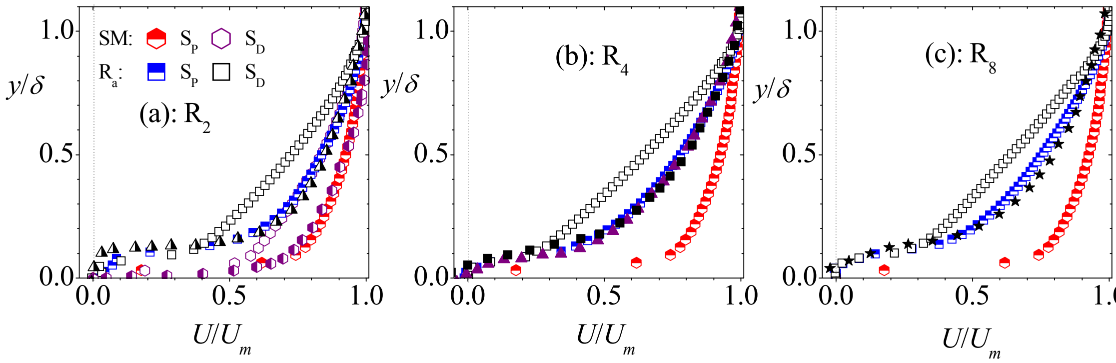

Figure 4.8: The distributions of the streamwise mean velocity profiles in outer coordinates in the parallel and diverging sections of the smooth and rough walls. Additional symbols: smooth wall: Moser *et al*. (1999), ⬢ ($Re_\tau = 395$); *d*-type ribs: Cui *et al*. (2003), ▲; intermediate type ribs: Leonardi *et al*. (2004), ▲ and Nagano *et al*. (2004), ■, and *k*-type ribs: Ikeda and Durbin (2007), ★.

DNS data from Leonardi *et al*. (2004) and Nagano *et al*. (2004) over the intermediate type rough wall (Figure 4.8b) and DNS data from Ikeda and Durbin (2007) over the *k*-type rough wall (Figure 4.8c). In Figure 4.8, negative values of U/U_m are observed over the rough walls, as a consequence of the observed flow reversal in the cavities (Figure 4.2). Due to the higher resistance generated by the ribs, the velocity profiles over the rough walls are 'less uniform' compared to the smooth wall profile in the parallel section. The *k*-type rough wall profile shows the greatest deviation from the smooth wall profile due to its higher drag characteristics.

The combined effects of APG and roughness are to further reduce *U* and make the profile even less uniform than observed in the parallel section. The more profound flow retarding observed over the rough walls in the diverging section compared to those in the parallel section can be explained by an upward spreading of the fluid towards the upper diverging wall and subsequent deceleration of the flow near the straight lower wall (Shah and Tachie, 2008).

4.2.1.2 Mean Velocity Defect Profiles

The outer layer similarity of the mean flow is often evaluated using the mean velocity defect profiles. Figure 4.9 shows the defect velocity profiles obtained in the upstream parallel and diverging sections. The defect velocity is normalized using two different velocity scales, namely friction velocity U_τ (Figure 4.9a-c) and mixed velocity scale $U_m\delta^*/\delta$ (Figure 4.9d-f) proposed by von Karman (1938), and Zagarola and Smits (1998), respectively. The wall-normal axis is normalized using the boundary layer thickness, δ. In these (Figure 4.9) and subsequent plots, the vertical dashed and the solid lines are used to mark the extent of the roughness sublayer ($y = 5k$) in the parallel and diverging sections, respectively. In Figure 4.9a, the defect profile obtained in the diverging section of the smooth wall drops less rapidly compared to the corresponding upstream profile. However, Skåre and Krogstad (1994) used U_τ and δ to collapse their mean velocity defect

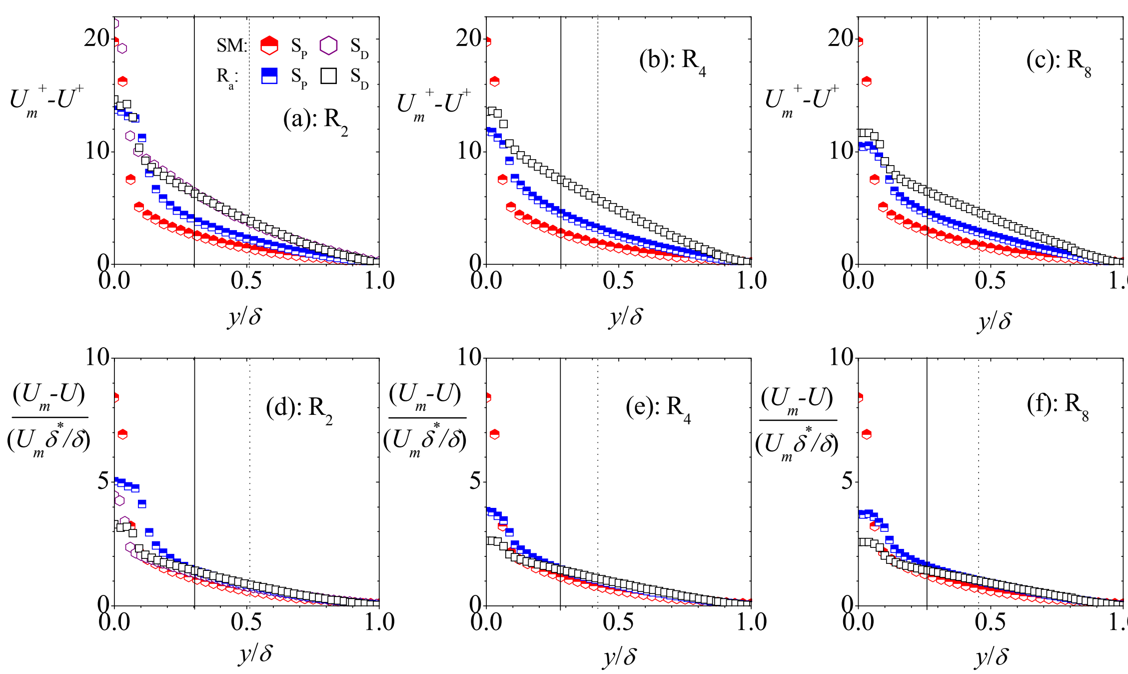

Figure 4.9: The distributions of the mean defect profiles over smooth and rough walls normalized by friction velocity, (a)-(c) and mixed outer velocity scale, (d)-(f).

profiles obtained in an equilibrium boundary layer subjected to a strong adverse pressure gradient. The rough wall defect profiles in Figure 4.9a-c also deviates from the smooth data. The friction velocity and the boundary layer thickness were used by Schultz and Flack (2007), Wu and Christensen (2007) and Connelly *et al*. (2006) to collapse the defect profiles obtained over smooth wall and rough walls with low relative roughness height. The lack of collapse for the present defect profiles is not surprising since the roughness sublayer covers 26%-51% of the boundary layer. In the presence of APG, the rough wall defect profiles further deviate from the smooth wall results in the parallel section, supporting the observation that combined effects of roughness and APG enhance momentum deficit. This also presupposes that in the diverging section of the rough walls, the defect profile also drops less rapidly compared to the corresponding upstream profile. Similar observations were made by Tachie (2007) and Tay *et al*. (2009) for profiles obtained over various rough walls in the presence of APG.

Figure 4.9d-f shows the defect velocity profiles normalized by the mixed outer velocity scale. Except for $y < 0.07\delta$ where there is a rapid variation, Figure 4.9d exhibits an improved collapse in the defect profiles in the parallel and diverging sections of the smooth wall. The collapse of the smooth and rough walls defect profiles is also better when $(U_m\delta^*/\delta)$ is used to normalize the mean defect velocity (Figures 4.9d-f) than when U_τ was used (Figure 4.9a-c). However, significant differences are observed in the regions $y < 0.11\delta$, $y < 0.16\delta$, $y < 0.26\delta$, respectively, for the *d*-type, intermediate type and *k*-type rough walls. Meanwhile, excellent agreement is observed among the defect profiles in the parallel and diverging sections of the rough walls, except for $y < 0.22\delta$, $y < 0.19\delta$, $y < 0.26\delta$, respectively, for the *d*-type, intermediate type and *k*-type rough walls. The relative success of the mixed outer scale over both smooth and rough walls with APG was also reported by Tay *et al*. (2009). Since the rough wall defect profiles deviate from that of the smooth wall beyond the roughness sublayer, the notion that the roughness affects the mean velocity only in the inner layer is not supported by the present results. This is due to large k/δ compared to the limit of k/δ = 0.025 recommended by Jimenez (2004) for the effect of roughness to be limited to the roughness sublayer.

4.2.1.3 Reynolds Stresses

The Reynolds stresses ($\overline{u^2}$, $\overline{v^2}$ and $-\overline{uv}$) are plotted to examine the behaviour of large-scale turbulence motions in the presence of roughness and APG. The stresses are normalized using the following two different sets of scales: U_m^2 and δ, and U_τ^2 and y_{uv}. It should be recalled that y_{uv} corresponds to the y-location where the Reynolds shear stress ($-\overline{uv}$) changes sign. The distributions of $\overline{u^2}$, $\overline{v^2}$ and $-\overline{uv}$ normalized using U_m^2 and the y-axis scaled with δ are shown in Figure 4.10. Over the smooth wall, APG augments the stresses considerably (Figure 4.10a-c) in agreement with previous studies. The increase in $\overline{u^2}$ is likely caused by enhanced production ($-\overline{uv}\partial U/\partial y$) by APG. The large distribution of $\overline{v^2}$ in the diverging section may be due to larger angular excursions of the wall-normal instantaneous velocity vectors in the presence of APG. Besides, the increase in $-\overline{uv}$ resulted from elevated $\overline{v^2}$ which contributed to production ($\overline{v^2}\partial U/\partial y$) as APG is applied to the flow. However, over the smooth wall (Figure 4.10a) the near-wall peak value of $\overline{u^2}/U_m^2$ (caused by increasing mean shear ($\partial U/\partial y$) as the wall is approached) in the parallel section is 1.75% compared to 1.56% in the diverging section. Besides, $(\overline{u^2}/U_m^2)_{max}$ in the parallel section occurs closer to the wall (at $y \approx 0.03\delta$) than in the

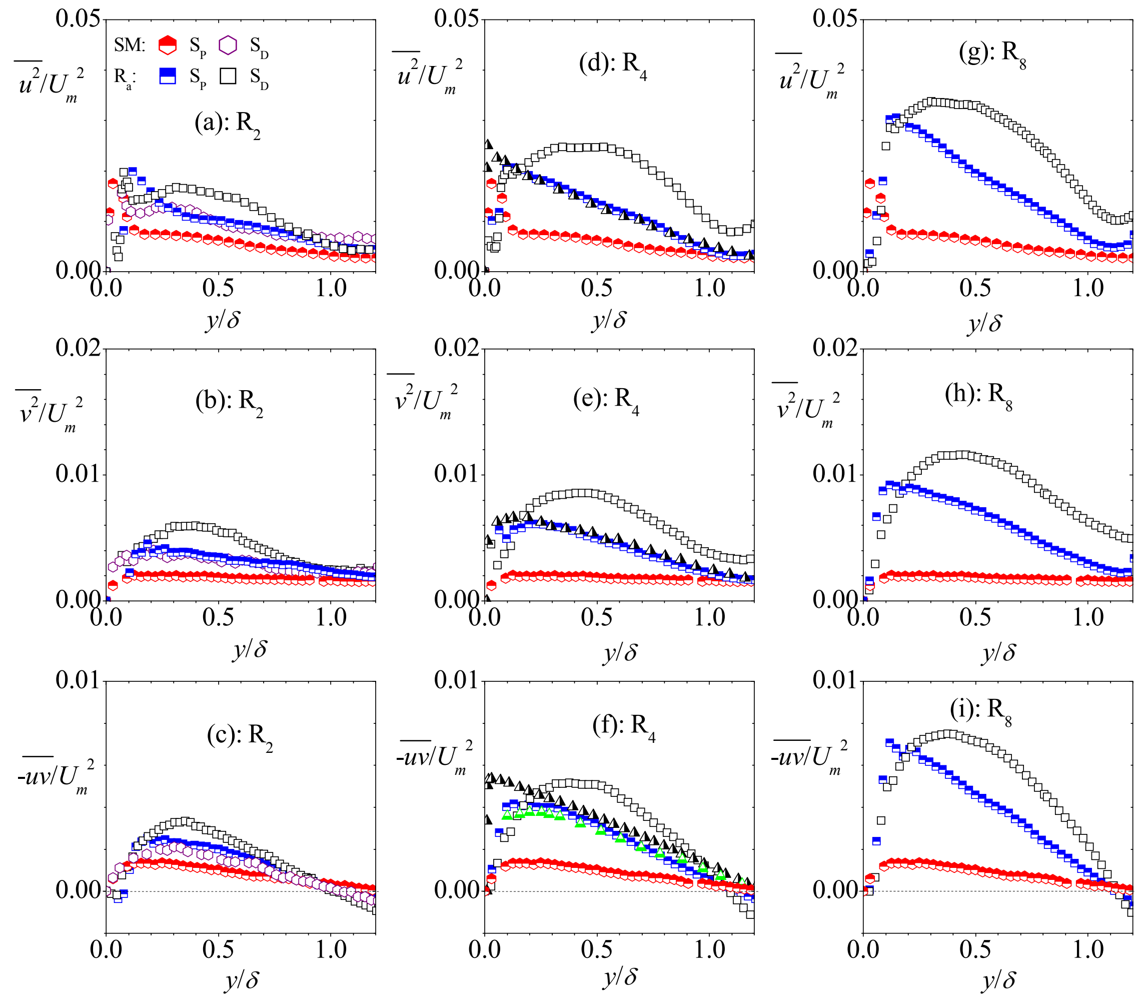

Figure 4.10: Distribution of Reynolds normal stresses and Reynolds shear stress over the smooth and rough walls normalized by: $U_m^{\ 2}$. Additional symbols: intermediate type rough wall: Burattini *et al*. (2008): ▲ (DNS, $Re_b = 2800$); △(Experiment, $Re_b = 3600$).

diverging section (at $y \approx 0.07\delta$). The $\overline{u^2}$-profile in the diverging section of the smooth wall shows a second peak ($\overline{u^2}/U_m^2$ = 1.28%) further from the wall (i.e., at about $y \approx 0.30\delta$). This outer peak is broad and flat. The formation of a peak in outer region is a salient feature of an APG flow. It should be noted that the outer peak in $\overline{u^2}$ profile was also reported by Skåre and Krogstad (1994) at $y \approx 0.45\delta$ for a smooth wall APG turbulent boundary layer. The location of maximum $\overline{v^2}/U_m^2$ and $-\overline{uv}/U_m^2$ is also shifted away from the wall in the presence of APG, and it coincides with the outer peak of $\overline{u^2}$ obtained over the smooth wall. However, $-\overline{uv}/U_m^2$ in the diverging section diminishes more rapidly with y/δ than in the parallel section (Figure 4.10c).

In Figure 4.10d-e, the present $\overline{u^2}/U_m^2$ and $\overline{v^2}/U_m^2$ profile obtained in the parallel section over the intermediate type rough wall are in very good agreement with the data from Burattini *et al*. (2008), except in the region $y < 0.16\delta$. However, some differences are seen in $-\overline{uv}/U_m^2$ (Figure 4.10f). With the outer velocity scale, the stresses are substantially larger over the rough walls than the smooth wall. The increase in the Reynolds stresses suggests that wall roughness intensifies the motion of the large-scale eddies, and hence, increased their contributions to $\overline{u^2}$, $\overline{v^2}$ and $-\overline{uv}$. Previous studies have also demonstrated that the Reynolds stresses are enhanced in the presence of roughness and the level of enhancement increases with p/k (Cui *et al*., 2003; Tachie, 2007). Furthermore, the locations of maximum values of $\overline{u^2}$, $\overline{v^2}$ and $-\overline{uv}$ over the rough walls are shifted away from the wall compared to the locations for the smooth wall value.

The effects of roughness on the Reynolds stresses are more pronounced in the diverging section than in the parallel section. Moreover, the stresses in the diverging section of the rough walls also formed a broad and flat hump in the outer layer. The hump observed in the stresses in the diverging section widen with increasing roughness. The distribution of $\overline{u^2}$ over the *d*-type ribs in the parallel and diverging sections exhibits a near-wall peak each (Figure 4.10a), notwithstanding the fact that the roughness is in fully rough regime. In the diverging section of the *d*-type and intermediate type ribs, two distinct peaks are observed for $\overline{u^2}$ just as reported for the smooth wall data. As noted earlier, the formation of a peak in outer region is a salient feature of an APG flow but the presence of roughness intensified it. Over the *d*-type ribs (Figure 4.10a), the near-wall peak ($\overline{u^2}/U_m^2$ = 1.97% at y/δ = 0.08) in the diverging section is only marginally different from that in the parallel section ($\overline{u^2}/U_m^2$ = 2.14% at y/δ = 0.13). The outer peak of $\overline{u^2}/U_m^2$ in the diverging section is about 1.67%, at y/δ = 0.31 (Figure 4.10a). In Figure 4.10d, the peak of $\overline{u^2}/U_m^2$ in the parallel section is about 0.021 (at y/δ = 0.10) which is similar to the inner peak of 0.020 at y/δ = 0.1 in the diverging section. The outer peak in the diverging section is about 0.025, which is about 19% larger than the inner peak. Thus, the inner peak gradually merges with the outer peak as p/k increases. The transition is obvious over the intermediate type rough wall where the outer peak is enhanced compared to the inner peak (Figure 4.10d). For p/k = 8, the near-wall peak is completely annihilated by the joint effects of roughness and APG, however, the broad and flat hump persists (Figure 4.10g). The broad and flat hump observed in $\overline{u^2}$ profiles is the region where production of the longitudinal turbulence energy is very important (Ligrani and Moffat, 1986). Grass (1971) argued that the hump in $\overline{u^2}$ is due to low-momentum fluid entrainment following an inrush stage. The broad flat hump in $\overline{v^2}$ may be attributed to the transport of high-speed fluid from a region further away from the wall towards the wall during the sweep-ejection cycle of events.

Figure 4.11 shows the distributions of the Reynolds stresses in the inner coordinates. In Figure 4.11a-b, the distributions of $\overline{u^{+2}}$ and $\overline{v^{+2}}$ in the parallel section of the smooth wall are in excellent agreement with the results of Bhaganagar *et al*. (2004) and Miyake *et al*. (2002). The sharp peak value of $\overline{u^2} \approx$ 6.8, is not significantly different from 6.9 and 7.0 reported by Bhaganagar *et al*. (2004) and Miyake *et al*. (2002), respectively. The near-wall peak of $\overline{u^{+2}}$ in the diverging section is about 8.8, and the outer peak is 7.2. As noted earlier in Chapter 3, the distribution of $-\overline{u^+v^+}$ in the parallel section of the smooth wall is significantly lower than the data reported by Kim *et al*. (1987) in a fully developed turbulent channel flow but comparable to $-\overline{u^+v^+}$ reported by Moin *et al*. (1990) in a fully developed turbulent channel and Coleman *et al*. (1990) in an Ekman layer (Figure 4.11c). It was also remarked that the characteristic low $-\overline{u^+v^+}$ in the upstream parallel section may be due to lack of two-dimensionality of the mean flow. The peak of $-\overline{u^+v^+}$ in the upstream section is 0.53 compared to 0.71 reported by Kim *et al*. (1987), Moser *et al*. (1999), and Alfonsi and Primavera (2007). As noted in Chapter 3, three-dimensionality of the mean flow arises from the presence of secondary flow which leads to spanwise velocity gradient. The presence of dW/dy results in the tilting of the hairpin vortices. Since the low-speed fluids which are ejected resides between the legs of the hairpin vortices, the tilting of the vortices results in the ejected fluid being directed at an angle in the spanwise direction, instead of the fluid being lifted vertically up as in the case of a two-dimensional turbulent boundary layer or fully developed channel flow. The tilting of the vortices, therefore, weakens the production of the Reynolds shear stress from the ejection-sweep cycle. Sendstad and Moin (1992) studied three-dimensional fully developed channel flow and observed that the ejections associated with vortices were weakened. They reported that the fluid closer to the wall is convected in the spanwise direction instead of being lifted, and the ejected fluid experienced more viscous dissipation due to convection of low-speed fluid on top of high-speed fluid in the three-dimensional flow. It was also noted that during sweep motion, the vortices generate less intense velocity fluctuations in three-dimensional flows. In this case, when the vortices are submerged in the spanwise boundary layer, the fluid swept toward the wall is simultaneously swept away from the vortex and will not reach as close to the wall

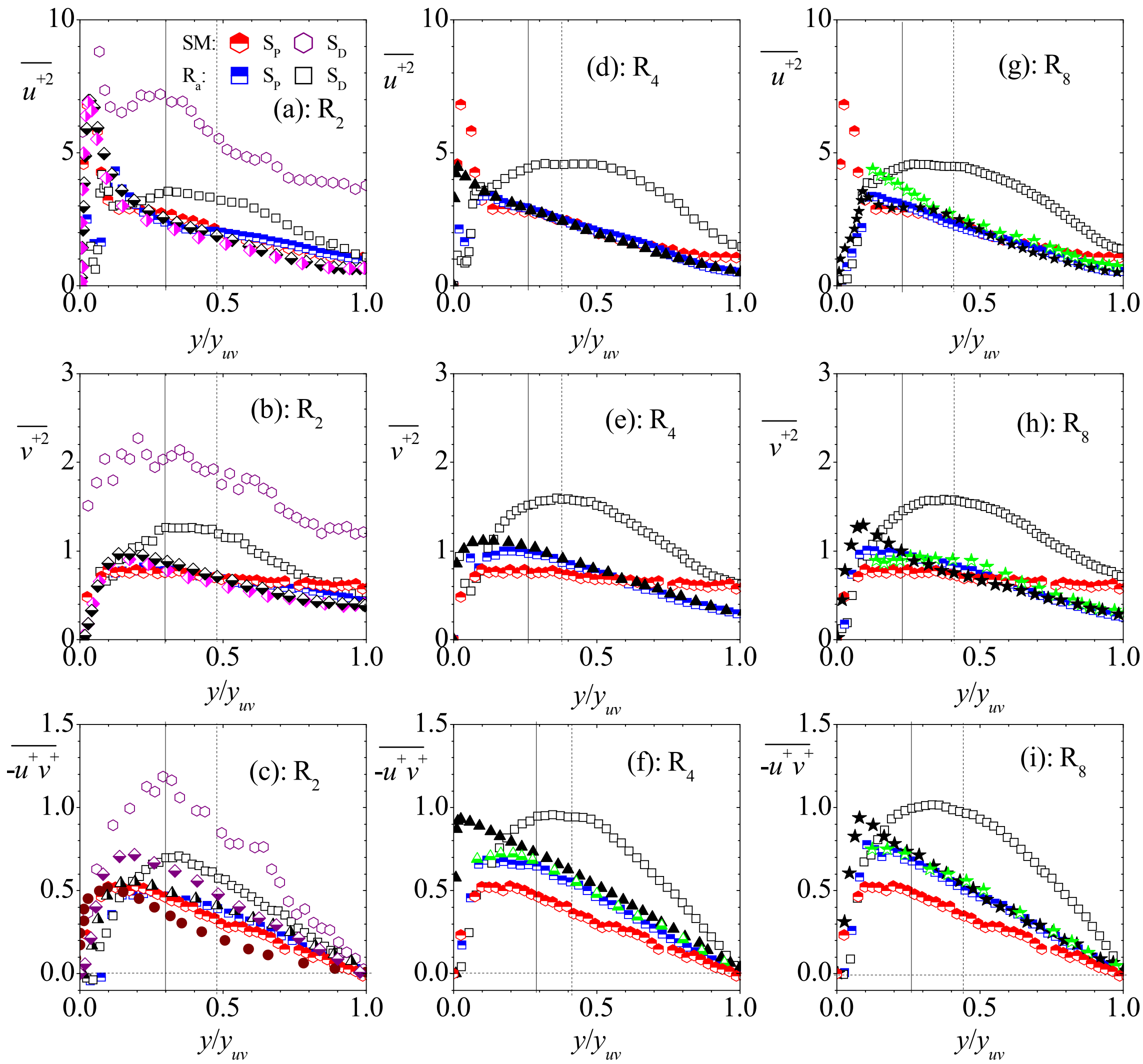

Figure 4.11: Distribution of Reynolds normal stresses and Reynolds shear stress over the smooth and rough walls normalized by U_τ^2. Additional symbols: smooth wall: Bhaganagar *et al*. (2004): ◇; Miyake *et al*. (2002): ⬙; Kim *et al*. (1987): ⬙. Coleman *et al*. (1990): ●; Moin *et al*. (1990): ◭; intermediate type rough wall: Burattini *et al*. (2008): ▲ (DNS, Re_b = 2800); △(Experiment, Re_b = 3600); *k*-type rough wall: Hanjalic and Launder (1972): ☆; Ikeda and Durbin (2007): ★.

(Sendstad and Moin, 1992). These alterations in the ejection-sweep events were linked to the reduction in the Reynolds shear stress. Meanwhile, in the diverging section, the peak of $-\overline{u^+v^+}$ is approximately 1.2. This finding is consistent with observation by Skåre and Krogstad (1994) that in the presence of APG, the maximum in the Reynolds shear stress distribution may be considerable higher than the wall shear stress. Moreover, due to the low wall shear stress associated with APG flow in general, $\overline{u^{+2}}$, $\overline{v^{+2}}$ and $-\overline{u^{+}v^{+}}$ over the smooth wall are significantly amplified in the diverging section for most of the y range. Previous studies (e.g. Lee and Sung, 2008) also revealed that APG enhances $-\overline{u^{+}v^{+}}$ over a smooth wall.

Over the rough walls, a reasonable agreement is observed between the present profiles over the intermediate type ribs and the corresponding data sets of Burattini *et al.* (2008), except that the DNS data tends to be larger as the wall is approached for $y/y_{uv} < 0.30$ (Figure 4.11d-f). It is, however, worth noting that the DNS data were spatially averaged in the streamwise and spanwise directions, i.e., over a pitch and across the channel width. The present stresses over the k-type ribs collapsed reasonably well with the data from Hanjalic and Launder (1972), and Ikeda and Durbin (2007) in Figure 4.11g-i, with only subtle differences close to the wall. For example, the peak value ($\overline{u^{+2}}_{peak}$ = 3.4) for the present k-type data set is similar to $\overline{u^{+2}}_{peak}$ = 3.6 reported by Ikeda and Durbin (2007), but 23% lower than $\overline{u^{+2}}_{peak}$ = 4.4 reported by Hanjalic and Launder (1972). The disparity in the peak values and their locations may be a manifestation that the DNS and the present data sets are spatial averaged results over a pitch whereas the data by Hanjalic and Launder (1972) was obtained above the rib crest.

As demonstrated in the preceding sections, roughness increases the Reynolds stresses and wall shear stress compared with the corresponding smooth wall values. Thus, the Reynolds stresses normalized by U_τ^2 would provide an insight into the relative effectiveness of roughness in enhancing the Reynolds stresses and wall shear stress. For example, if $-\overline{u^{+}v^{+}}$ is higher for a rough wall than the corresponding distribution over the smooth wall, it will suggest that the increase in the Reynolds shear stress caused by the ribs exceeds the increase in the wall shear stress. Figures 4.11a, 4.11d and 4.11g demonstrate that in the parallel section, $\overline{u^{+2}}$ profiles are virtually unaffected by roughness for $y > 0.26y_{uv}$. This implies that the increase in the streamwise Reynolds normal stress caused by the ribs is proportional to the increase in the wall shear stress such that their ratio ($\overline{u^{+2}}$) remains relatively similar to that over a smooth wall. As the wall is approached, however, distinct differences are observed between the smooth wall and the rough wall data sets. For example, $\overline{u^{+2}}$ over the smooth wall has a very distinct sharp peak near the wall at $y = 0.025y_{uv}$. According to Grass (1971) and Krogstad *et al*. (1992), the spike in the smooth wall $\overline{u^{+2}}$-profile is primarily due to viscous effects. Within the buffer region, there is an intense mean shear ($\partial U/\partial y$) and from the transport equation for $\overline{u^2}$, $-\overline{uv}\partial U/\partial y$ becomes the dominant production term, leading to the sharp peak in $\overline{u^2}$. For example, as roughness intensity increases, the peak in $\overline{u^{+2}}$ over the rough wall diminished. Since large-scale streamwise vortical structures play vital roles in the formation of the peak and turbulence production, the reduced peak for the rough wall profiles may be attributed to breakup of streamwise vortices by the ribs. Close to the wall, i.e., $y \leq 0.11y_{uv}$, the reduction in $\overline{u^{+2}}$ over the rough walls is likely due to an obstruction of the longitudinal motion of inrushing fluid during the ejection-sweep cycle. This resistance to the longitudinal turbulence motion increases with increasing k_s^+ (Ligrani and Moffat, 1986). It should be noted that as k_s^+ increases, a larger percentage of the ribs is exposed to interact with the inrushing fluid. In this case, the form drag generated by the ribs acts as a much more effective arrest mechanism than when the fast-moving fluid near the wall is slowed only by viscous forces, as in the case near the smooth wall (Ligrani and Moffat, 1986). In contrast to $\overline{u^{+2}}$, no distinct peaks are observed in $\overline{v^{+2}}$ profiles over the smooth and rough walls (Figures 4.11b, 4.11e and 4.11h). The absence of a peak in $\overline{v^2}$ is due to wall damping effects on the wall-normal velocity fluctuations. Over the *d*-type ribs, $\overline{v^{+2}}$ is identical to the data over the smooth wall in the parallel section (Figure 4.11b). Figures 4.11e and 4.11h demonstrate that the level of $\overline{v^{+2}}$ is more intense over the rough walls in the region $y/y_{uv} \leq 0.50$ than over the smooth wall in the parallel section. The higher values of $\overline{v^{+2}}$ near the rough walls compared to the smooth wall indicate that there is an enhanced redistribution of turbulence kinetic energy and/or an increased production of $\overline{v^2}$ following the intensification of the wall-normal turbulence motion of the large-scale eddies by the ribs. However, $\overline{v^{+2}}$ decays more rapidly over the rough walls than the smooth wall as the edge of the boundary layer is approached. For example, for $y/y_{uv} > 0.50$, the wall-normal turbulence motion over the intermediate type and *k*-type ribs is reduced considerably relative to the smooth wall data. The distribution of $-\overline{u^+v^+}$ in the parallel section is remarkably enhanced over the rough walls (Figures 4.11c, 4.11f and 4.11i). Figure 4.11i shows that the most pronounced effects of roughness on $-\overline{u^+v^+}$ in the parallel section is exhibited by the *k*-type rough wall, where $-\overline{u^+v^+}$ is significantly larger in both the inner and outer regions than the Reynolds shear stress over the smooth wall. Clearly, Figure 11 shows that the effects of roughness on $\overline{v^{+2}}$ and $-\overline{u^+v^+}$ in the parallel section persist beyond the roughness sublayer.

It is clear from Figure 4.11 that, across most of the boundary layer, the levels of the Reynolds stresses in the diverging section are significantly higher than observed in the parallel section. Thus, APG reinforces roughness in augmenting $\overline{u^{+2}}$, $\overline{v^{+2}}$ and $-\overline{u^+v^+}$ with the exception of the region $y/y_{uv} < 0.16$, where $-\overline{u^+v^+}$ (Figure 4.11c) is slightly larger over the smooth wall than the data over the *d*-type rough walls. These results are consistent with the observations made in previous study of combined effects of roughness and APG by Tachie (2007) and Tay *et al*. (2009). Over the *d*-type ribs (Figure 4.11a), for example, the near-wall peak ($\overline{u^{+2}}_{peak}$ = 4.2 at y/y_{uv} = 0.07) in the diverging section is only marginally different from that in the parallel section ($\overline{u^{+2}}_{peak}$ = 4.9 at y/y_{uv} = 0.12) but the outer peak of $\overline{u^{+2}}$ in the diverging section is about 3.5 (Figure 4.11a). Similarly, the peak of $\overline{u^{+2}}$ = 3.4 in the parallel section of the intermediate type ribs is weaker than 3.7 and 4.6 found in the diverging section, respectively for inner and outer peaks (Figure 4.11d). The observed higher Reynolds stresses in the diverging section may also be partly attributed to significant transverse motion, V in the diverging section. The large positive variation of V with y (Appendix C) coupled with the more intense $\partial U/\partial y$ in the diverging section implies that V may play a significant dynamic role in the transport of momentum and the production of $\overline{v^2}$, $-\overline{uv}$ and turbulence kinetic energy, q. Townsend (1961) argued that positive $\partial V/\partial y$ tends to enlarge the large eddies and increase their contribution to the Reynolds stresses.

The asymmetry produced by roughness and APG causes the location (y_U) where the maximum value of U occurs to move closer to the upper smooth wall of the channel. More importantly, y_U increases with increasing roughness and in the presence of APG. Besides, y_U does not necessarily correspond to the location (y_{uv}) where the Reynolds shear stress changes sign over the various rough walls. As noted earlier, Hanjalic and Launder (1972) observed that over the *k*-type rough wall, y_{uv} is closer to the smooth wall than y_U. Similar observation was made most recently by Leonardi *et al*. (2005), and Ikeda and Durbin (2007) over *k*-type rough wall. Nagano *et al*. (2004) reported that the difference between y_U and y_{uv} was 2.0%, 2.8% and 0.8% of the channel height, respectively, for p/k = 4, 8 and 16. They attributed the small variations between y_U and y_{uv} to the low Reynolds number of their study. Hanjalic and Launder (1972) argued that the non-coincidence of y_U and y_{uv} would result in extraction of energy by the mean flow field from the turbulent field and lead to a region of negative energy production and negative eddy viscosity. In contrast to these observations, Burattini *et al*. (2008) observed that y_U coincides with y_{uv} over intermediate type rough wall. Table 4.3 shows a summary of y_U and y_{uv} for the present results and those reported by Hanjalic and Launder (1972), and Ikeda and Durbin (2007). In the parallel section, the present smooth-wall results indicate that y_U is similar to y_{uv}. This is expected since both upper and lower smooth walls represent a symmetric boundary condition. For R_2S_P, y_U is closer to the upper smooth wall than y_{uv}. The difference in these locations is about 5.0% of the channel height. For R_4S_P, y_U and y_{uv} coincide, which is in agreement with the finding of Burattini *et al*. (2008), but at variance with Nagano *et al*. (2004). The results for R_8S_P show that y_{uv} is closer to the upper smooth wall than y_U. This is consistent with the results by Hanjalic and Launder (1972), and Ikeda and Durbin (2007), however, the difference in the present

Table 4.3: Summary of y_U and y_{uv} over smooth wall and 90° ribs.

Test	p/k	$y_U/2h$	$y_{uv}/2h$	Re_h
SMS_P	-	0.51	0.51	10 690
R_2S_P	2	0.61	0.56	10 460
R_4S_P	4	0.72	0.72	10 940
R_8S_P	8	0.77	0.80	10 560
Ikeda &Durbin (2007)	10	0.76	0.81	8 200
Hanjalic & Launder (1972)	10	0.70	0.79	18 500
SMS_D	-	0.52	0.49	7 770
R_2S_D	2	0.67	0.64	8 690
R_4S_D	4	0.73	0.75	8 500
R_8S_D	8	0.79	0.84	8 340

locations is about 3.0% of the channel height compared to 9% and 5% reported by Hanjalic and Launder (1972), and Ikeda and Durbin (2007), respectively. This variation may be due to differences in the Reynolds number of the flow and the blockage ratio, k/h. In the diverging section, the table indicates that y_U is closer to the upper diverging wall than y_{uv} for SMS_D and R_2S_D. The difference between these two locations is about 3.0% of the channel height in the measurement plane location for the SMS_D and R_2S_D. However, for R_4S_D and R_8S_D, y_{uv} occurs closer to the upper diverging wall than y_U. In this case, the differences between the two locations are 2% and 5% of the channel height in the measurement plane location, respectively, for R_4S_D and R_8S_D. The non-coincident of y_{uv} and y_U is an indication that there exist a strong interaction between the rough wall boundary layer and upper smooth wall boundary layer (Hanjalic and Launder, 1972). The present results clearly demonstrate that the interaction between the lower and upper boundary layer depends strongly on the roughness and pressure gradient. Table 4.3 demonstrates that both y_U and y_{uv} increases with p/k due to shifting of the interaction of the turbulent motions from both sides of the channel nearer to the smooth upper wall. This is consistent with the increasing relative roughness, k_s/δ (Table 4.2). The implication is that the effect of roughness extends further into the outer layer as p/k increases.

4.2.1.4 Anisotropy of Reynolds Stresses

The ratios of the Reynolds stresses as well as the correlation coefficient (ρ_{uv}) for the Reynolds shear stress and the Townsend structure parameter (a_1) are plotted in Figure 4.12 to examine the effects of roughness and APG on large-scale anisotropy. Figure 4.12a shows that the ratio $-\overline{uv}/\overline{u^2}$ over the smooth wall is nearly independent of APG, except for the slight bulge in $-\overline{uv}/\overline{u^2}$ for $0.1 < y/y_{uv} < 0.29$ in the parallel section. The lower

$-\overline{uv}/\overline{u^2}$ in the region 0.1 < y/y_{uv} < 0.29 within the diverging section is due to a rapid increase in $\overline{u^2}$ near the wall compared to $-\overline{uv}$. This is in agreement with the notion that APG intensifies inactive motions, and these motions do not contribute to $-\overline{uv}$ (Bradshaw, 1967). For this reason, $-\overline{uv}$ decreases near the wall whereas $\overline{u^2}$ increases in an APG flow. More importantly, the similarity in the ratio of the Reynolds shear stress and the normal stress for most of the y range over the smooth wall is an indication that the Reynolds shear stress and the streamwise Reynolds normal stress are distributed in the same manner regardless of pressure gradient (Figures 4.12a). Figures 4.12b shows that, except for the region y/y_{uv} < 0.6, the distribution of $\overline{v^2}/\overline{u^2}$ in the parallel and diverging sections of the smooth wall exhibits consistent disagreement in the outer region. The rapid rise in $\overline{v^2}/\overline{u^2}$ in the parallel section beyond y/y_{uv} = 0.6 is an indication that the flow in the parallel section tends to be more isotropic than in the diverging section. This behaviour of $\overline{v^2}/\overline{u^2}$ is consistent with the data of Tay *et al*. (2009), but at variance with that of Skåre and Krogstad (1994). Skåre and Krogstad (1994) observed similarity in $\overline{v^2}/\overline{u^2}$ for the entire boundary layer. The general increase in $\overline{v^2}/\overline{u^2}$ with y in both the parallel and diverging sections is due to slower decays of $\overline{v^2}$ compared to $\overline{u^2}$ as the outer layer is approached. This is also an indication that in the core region, the flow tends to be more isotropic than near the wall. Besides, the similarity in the ratio $\overline{v^2}/\overline{u^2}$ in both the parallel and diverging sections for y/y_{uv} < 0.6 suggests that the mechanism for redistributing the turbulence kinetic energy between the different Reynolds normal stresses is independent of adverse pressure gradient. Furthermore, the rapid variation of $\overline{v^2}/\overline{u^2}$ across the channel in addition to the low values of $\overline{v^2}/\overline{u^2}$ imply that turbulence models which employ isotropic assumptions across the shear layer will not be able to predict these flows accurately.

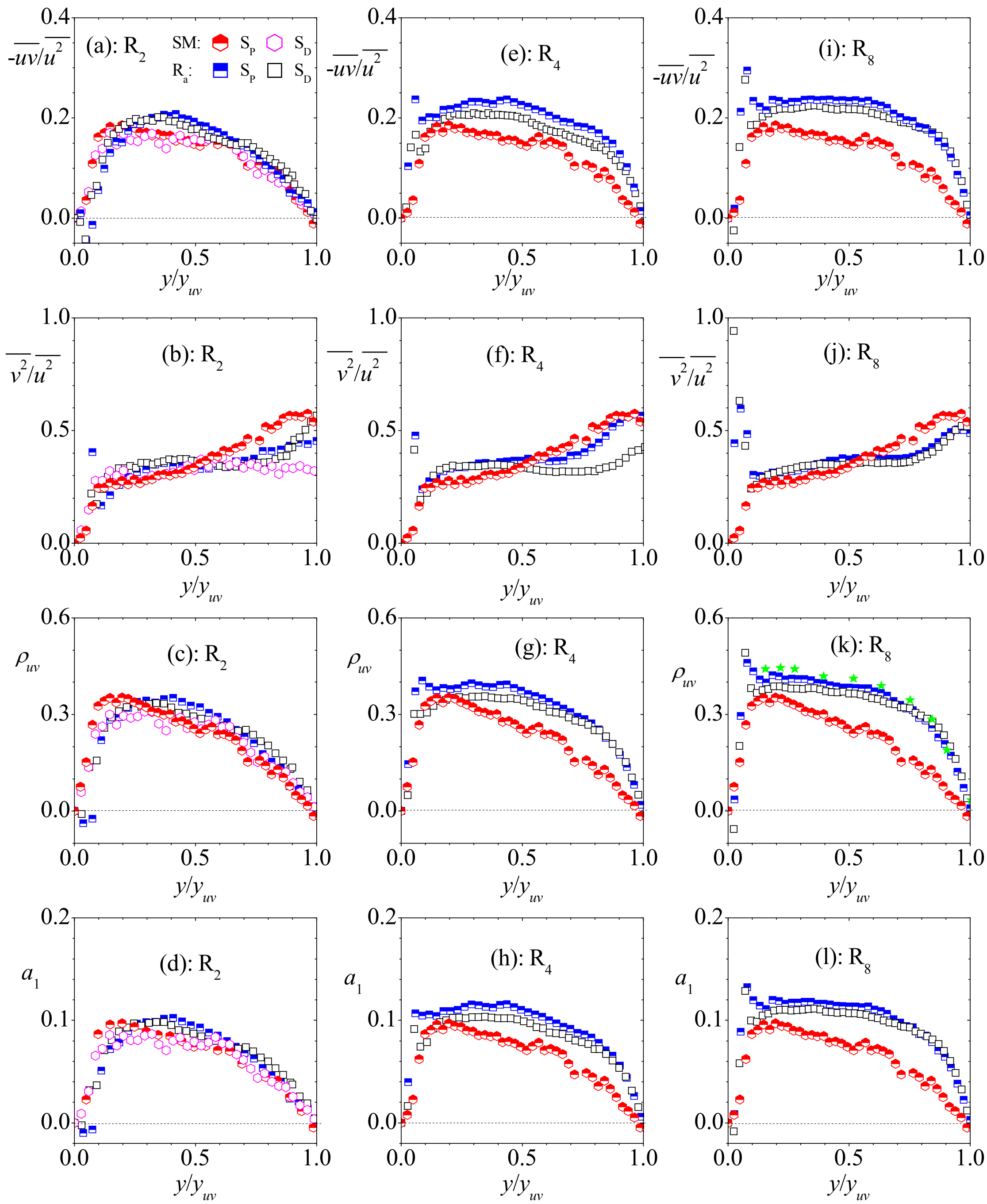

Figure 4.12: Distribution of Reynolds stress ratios ($-\overline{uv}/\overline{u^2}$ and $\overline{v^2}/\overline{u^2}$), Reynolds shear stress correlation coefficient (ρ_{uv}) and Townsend structure parameter (a_1) over smooth and rough walls. Additional symbol: *k*-type rough wall: Hanjalic and Launder (1972), ★.

The present maximum value for ρ_{uv} (= 0.35) in the parallel section of the smooth wall (Figure 4.12c) is lower than typical values of 0.40 to 0.43 found in ZPG flows. For a fully developed turbulent channel flow, Alfredsson and Johansson (1984) found that ρ_{uv} = 0.40 in the logarithm region. Similarly, the present maximum values for ρ_{uv} (= 0.31) in the diverging section of the smooth wall (Figure 4.12d) is considerable lower than a typical value of 0.42 reported by Skåre and Krogstad (1994). Although the maximum ρ_{uv} in the parallel section is larger than in the diverging section, the y extent of the maximum or constant ρ_{uv} in the parallel section is narrower than in the diverging section. For $y/y_{uv} \geq$ 0.3, ρ_{uv} in the parallel and diverging sections collapsed fairly well. The effects of APG on the turbulence motions are also studied using Townsend structure parameter. The Townsend structure parameter was computed from $a_1 = -\overline{uv}/2q$, and the turbulence kinetic energy was estimated from $q = 0.75(\overline{u^2} + \overline{v^2})$, since the spanwise component of the velocity fluctuation was not measured in the present study. Bradshaw (1967) reported a value of a_1 = 0.15 for a turbulent boundary layer, and this is the value adopted in most turbulence models. The structure parameter (Figure 4.12d) is substantially lower than the typical value of a_1 = 0.15 reported in a turbulent boundary layer by Bradshaw (1967). In the present study, the maximum value of a_1 over the smooth wall is 0.10 in the parallel section and 0.09 in the diverging section, indicating 33% and 40% reduction in a_1. Moin *et al*. (1990) also reported a 25% reduction in a_1 for a three-dimensional channel flow. They argued that the reduction in a_1 was due to three-dimensionality of the mean flow. Except for a narrow region $0.09y_{uv} < y < 0.29y_{uv}$, the Townsend structure parameter in both the parallel and diverging sections collapsed fairly well. The observed agreement in the distribution of a_1 in most part of the smooth wall boundary layers in the parallel and diverging section suggests that the type of mechanism resulting in the production and redistribution of turbulence is independent of pressure gradient, even though changes in the intensity and distribution of this mechanism may occur. For the region $0.09 < y/y_{uv} < 0.29$, the lower a_1 in the diverging section is due to the reduction in $-\overline{uv}$ near the wall by APG as opposed to the increase in the normal stresses. Spalart and Watmuff (1993) also observed a reduction in a_1 in a two-dimensional boundary layer subjected to APG. Moreover, the observed lower values for a_1 in the present study may suggest that the extraction of the Reynolds shear stress from the mean flow is less efficient compared to the extraction of the turbulence kinetic energy (Schwarz and Bradshaw, 1994).

Figure 4.12 shows that the distribution of $-\overline{uv}/\overline{u^2}$ in the parallel section of the rough walls are often larger than those in the parallel section of the smooth wall, except for $y < 0.23y_{uv}$ for $-\overline{uv}/\overline{u^2}$ (Figure 4.12a) over the *d*-type rough walls. It is noticeable that the reduction in smooth wall $-\overline{uv}/\overline{u^2}$ is primarily due to the decrease in $-\overline{uv}$. The ratio $-\overline{uv}/\overline{u^2}$ generally increases near the wall, and becomes approximately constant in the logarithm region before decaying in the outer layer. In the outer layer, $-\overline{uv}/\overline{u^2}$ vanishes at a faster rate because $\overline{u^2}$ decays at a slower rate more than $-\overline{uv}$ does. Figures 4.12b, 4.12f and 4.12j show that the distribution of $\overline{v^2}/\overline{u^2}$ is only enhanced over the rough walls for $y/y_{uv} < 0.50$. This suggests that the observed reduction in $\overline{u^2}$ close to the ribs is associated with an increase in $\overline{v^2}$. Beyond $y/y_{uv} = 0.50$, $\overline{v^2}/\overline{u^2}$ over smooth wall rises rapidly above the data for the rough walls. This is an indication that the flow is more isotropic in the outer region of the smooth wall than observed for the rough walls. Mazouz *et al*. (1998) compared the anisotropy invariants of the Reynolds stress tensor and found that, unlike the turbulent boundary layer, roughness increases anisotropy in the channel flow. However, Krogstad and Antonia (1994) showed that roughness tends to reduce the overall anisotropy of the large-scale motions in a ZPG boundary layer over a

k-type rough wall. This observation was corroborated by Antonia and Krogstad (2001) using mesh and rib-roughened walls and Keirsbulck *et al*. (2002) using rib-roughened wall, in a ZPG boundary layer. They found that, although the Reynolds stress anisotropy was larger for the smooth wall, it was smaller over mesh than the rib. These mixed observations suggest that anisotropy may depend on the flow type. Besides, the significant difference in $\overline{v^2}/\overline{u^2}$ over the smooth wall and the rough walls suggests that the mechanism for redistributing the turbulence kinetic energy between the different Reynolds normal stresses is dependent on boundary condition.

The maximum values of ρ_{uv} in the parallel section of the intermediate type and k-type ribs, and in the diverging section of k-type ribs exceed 0.40 (Figures 4.12g and 4.12k). The present ρ_{uv} over the k-type ribs is only marginally lower than ρ_{uv} from Hanjalic and Launder (1972). In general, the distributions of ρ_{uv} over the three rough walls are larger than the correlation coefficient over the smooth wall. Near the wall of the d-type ribs (y/y_{uv} < 0.25), however, ρ_{uv} is diminished relative to the smooth wall data (Figure 4.12c). Although the structure parameter is lower than the reported value of a_1 = 0.15 for a turbulent boundary layer, a_1 over the rough walls are typically larger than the smooth wall value. However, in a narrow region of y/y_{uv} < 0.23, a_1 is increased over the smooth wall relative to the d-type ribs. This is in sharp contrast with the findings of Lagrani and Moffat (1986) who observed negligible variation in ρ_{uv} and a_1, from transitionally rough to fully rough boundary layer.

Figure 4.12 demonstrates that the combined effects of roughness and adverse pressure gradient reduce the ratios of the stresses as well as the correlation coefficient and the Townsend structure parameter in the diverging section compared to the parallel section of the rough walls. However, the distributions remain relatively larger than those observed over the smooth wall. Exception is however observed over the d-type ribs where $-\overline{uv}/\overline{u^2}$ and $\overline{v^2}/\overline{u^2}$ as well as ρ_{uv} and a_1 are almost independent of APG, and over the k-type ribs where $\overline{v^2}/\overline{u^2}$ in the parallel and diverging sections collapsed fairly well. More importantly, the similarity in $-\overline{uv}/\overline{u^2}$ for most of the y range over the d-type rough wall is an indication that the Reynolds shear stress and the streamwise Reynolds normal stress are distributed in the same manner regardless of pressure gradient. The reduction in $-\overline{uv}/\overline{u^2}$ in the diverging section of the intermediate type and k-type rough walls is caused by the excessive increase in the inactive motions by APG relative to the active motions.

4.2.1.5 Distribution of Eddy Viscosity and Mixing Length

Eddy viscosity turbulence models such as the mixing length and two-equation models are often employed to predict turbulent flows of practical importance. In this section, the effects of rib roughness and APG on the distributions of the eddy viscosity and mixing length are presented and discussed. The eddy viscosity (ν_t) and the mixing length (l) are related to the Reynolds shear stress and the mean velocity gradient as follows:

$$\nu_t = -\overline{uv}/(\partial U/\partial y) \qquad 4.1$$

$$l = (-\overline{uv})^{0.5}/(\partial U/\partial y) \qquad 4.2$$

Figure 4.13 shows the distributions of the dimensionless eddy viscosity ($\nu_t/U_\tau\delta$) and mixing length (l/δ). In these plots, the wall-normal axis is made zero at the virtual origin. In contrast to the dramatic effects of APG on both $\partial U/\partial y$ (Figure 4.8) and $-\overline{uv}$

(Figures 4.10 and 4.11), it is clear from Figure 4.13a that APG does not affect the distribution of the eddy viscosity over the smooth wall. It is also evident from Figure 4.13a-c that the variation of the eddy viscosity over the rough walls compared to the smooth wall data is not significant, notwithstanding the remarkable effects of roughness and APG on both $\partial U/\partial y$ (Figure 4.8) and $-\overline{uv}$ (Figures 4.10 and 4.11). Over the intermediate type and *k*-type rough walls, the eddy viscosity in the parallel section compares fairly well with the data over the smooth wall in the region $y < 0.32\delta$ and $y < 0.45\delta$, respectively. Beyond these locations, the smooth wall data tends to be larger partly due to the low values of $\partial U/\partial y$ produced by the nearly uniform velocity profile in the outer layer. Meanwhile, the reduction of the eddy viscosity over the rough walls relative to the smooth wall is felt across the entire layer of the *d*-type ribs in the parallel section (Figure 4.13a). APG enhanced the eddy viscosity over the rough walls, however, the

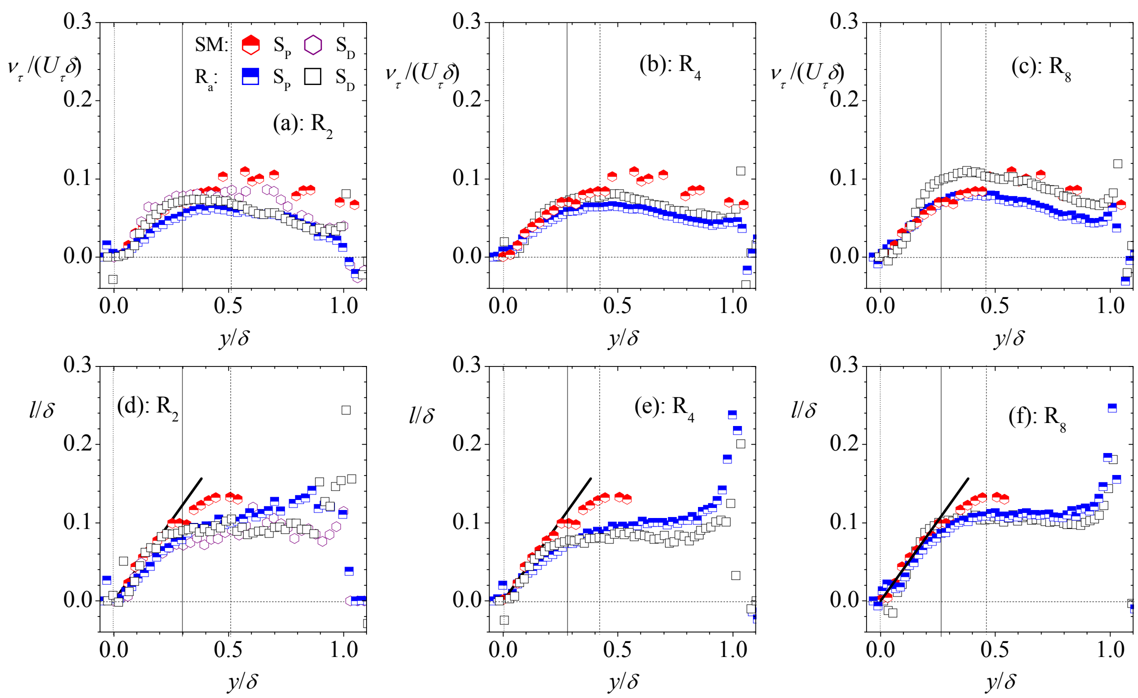

Figure 4.13: Distributions of eddy viscosity and mixing length over the smooth and rough walls.

enhancement is significant for $y > 0.16\delta$ over the k-type ribs (Figure 4.13c).

The distributions of the mixing length are compared in Figure 4.13d-f. The slope of l/δ in the region $y < 0.25\delta$ matches $\kappa = 0.41$ reasonably well. Unlike the similarity observed in the distribution of the eddy viscosity in the parallel and diverging sections of the smooth wall, the mixing length is strongly modified by APG, except in a narrow region of $y < 0.19\delta$ (Figure 4.13d). Skåre and Krogstad (1994) reported a modest reduction in l/δ in a strong adverse pressure gradient compared to the zero pressure gradient values in the region $0.15\delta < y < 0.9\delta$. In the regions $y > 0.21\delta$, $y > 0.11\delta$ and $y > 0.25\delta$, respectively for the d-type, intermediate type and k-type ribs, the mixing length for the smooth wall is larger than the values obtained over the rough walls in the parallel section. Krogstad and Antonia (1999) observed similarity in the mixing length over smooth wall and wire mesh roughness but reported higher l/δ values in the outer layer over circular ribs. The distributions of l/δ over the rough walls is nearly unaffected by APG for $y < 0.45\delta$, $y < 0.4\delta$ and $y < 0.65\delta$, respectively over the d-type, intermediate type and k-type ribs. Beyond these locations, APG combined with roughness to enhance the reduction of the values of l/δ in the diverging section of the rough walls compared to those in the parallel section. It should be noted that unlike $\nu_t/U_\tau\delta$, the variation in l/δ in the parallel and diverging sections diminishes with increasing p/k. Meanwhile, the modifications to the eddy viscosity and mixing length by roughness extend beyond the roughness sublayer.

4.2.1.6 Production of Turbulence Kinetic Energy and Reynolds Shear Stress

The production terms (P_q and P_{-uv}) in the turbulence kinetic energy (q) and Reynolds shear stress ($-\overline{uv}$) transport equations were computed to explain the high turbulence levels observed in the diverging section of the smooth wall, and over the ribs in both the parallel and diverging sections compared with the smooth wall data. The production terms for the turbulence kinetic energy and Reynolds shear stress was approximated using the data obtained in the *x*-*y* plane as follows:

$$P_q \approx -\overline{uv}\left(\frac{\partial U}{\partial y}+\frac{\partial V}{\partial x}\right)-\left(\overline{u^2}\frac{\partial U}{\partial x}+\overline{v^2}\frac{\partial V}{\partial y}\right) \tag{4.3}$$

$$P_{-uv} \approx \overline{v^2}\frac{\partial U}{\partial y} \tag{4.4}$$

Figure 4.14 shows the P_q and P_{-uv} normalized with δ/U_τ^3. It should be noted that the peak values of P_q and P_{-uv}, especially over the smooth wall exceeds the values where the abscissas were terminated. This termination of the abscissas was necessary to better reveal the trends in the production terms. Clearly APG enhanced both P_q (Figure 4.14a) and P_{-uv} (Figure 4.14d) over the smooth wall. The hump that was observed at $y = 0.3y_{uv}$ in the stresses in the diverging section of the smooth walls is also imprinted in the production terms for q and $-\overline{uv}$. The double peaks in P_q and P_{-uv} were also observed by Skåre and Krogstad (1994) and Krogstad and Skåre (1995) in an APG flow over smooth wall. The larger distributions of P_q and P_{-uv} in the diverging section of smooth wall are consistent with the higher level of the Reynolds stresses observed in the diverging section relative to the parallel section.

In the parallel section, the normalized P_q and P_{-uv} (except for P_q over the *d*-type ribs where only a subtle increase is observed) are significantly larger over the rough walls than over the smooth wall for $y < 0.7\delta$. However, as noted earlier the inner peaks in P_q and P_{-uv} over the smooth wall exceed the near-wall peaks in P_q and P_{-uv} over the rough

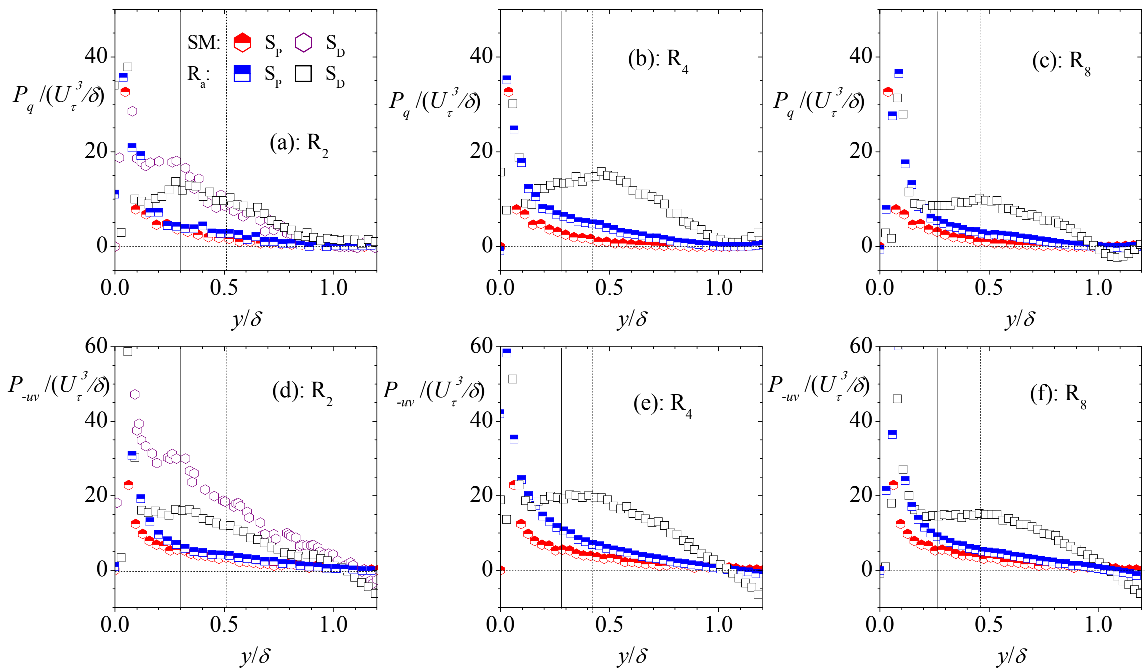

Figure 4.14: Production terms for turbulence kinetic energy and Reynolds shear stress over smooth and rough walls.

walls. The larger values of P_q and P_{-uv} over the rough walls are consistent with the higher level of the Reynolds stresses observed over the rough walls compared to the smooth wall. Beyond $y = 0.7\delta$, no significant increase in P_q and P_{-uv} are observed over the rough walls. However, APG significantly augments the production of the turbulence kinetic energy and Reynolds shear stress throughout the entire boundary layer over the rough walls except for a modest reduction as the wall is approached. The double peaks that were observed in the stresses over the rough walls in the diverging section are also present in the P_q and P_{-uv}. The inner peak conforms to the peak observed in $\overline{u^2}$ near the ribs in the diverging section. The outer peak of P_q and P_{-uv} is broad consistent with hump in the Reynolds stresses.

Over the k-type ribs (Figure 4.14c), P_q tends to be negative in the regions $0.99\delta \leq y \leq 1.15\delta$ and $0.99\delta \leq y \leq 1.18\delta$, respectively in the parallel and diverging sections. In these regions, therefore, the turbulence field is actually feeding the mean flow. This is in agreement with the earlier observation that the non-coincidence of y_U and y_{uv} will result in the production of negative P_q. Conversely, no negative P_q was observed over the d-type ribs (Figure 4.14a) and intermediate type ribs (Figure 4.14b), despite the non-coincidence of y_U and y_{uv} (except for parallel section of the intermediate type ribs where y_U = y_{uv}). It was observed that the sum of the shear production terms ($-\overline{uv}[\partial U/\partial y + \partial V/\partial x]$) in Eq. 4.3 was negative in the region between y_U and y_{uv} for these surfaces but the normal production terms ($-[\overline{v^2}\partial V/\partial y + \overline{u^2}\partial U/\partial x]$) in Eq. 4.3 was positive due to the large positive values of $-\overline{u^2}\partial U/\partial x$ near y_{uv}. Thus, the disappearance of the expected negative values in P_q over the d-type ribs and in the diverging section of the intermediate type ribs was due to the large positive net normal production relative to the smaller net negative shear production in the region between y_U and y_{uv}.

4.2.2 TURBULENCE STRUCTURE

As noted in Chapter 1, coherent structures affect flow dynamics such as turbulence production, turbulence mixing, and transport of heat and momentum. In this section, Galilean decomposition of the instantaneous velocity fields, quadrant decomposition, two-point correlations and linear stochastic estimate are used to provide additional physical insight into the effects of roughness and APG on the boundary layer.

4.2.2.1 Instantaneous Velocity Fields

As noted earlier in Chapter 1, the Galilean decomposition is one of the simplest vortex identification techniques for construing instantaneous velocity fields. Following Kline and Robinson (1989), a vortex is defined as a region of concentrated vorticity around which the pattern of streamlines is roughly circular when viewed in a frame moving with the centre of the vortex. The Galilean decomposition of the instantaneous vector field requires that the convection velocity of the vortex is removed from the velocity field to reveal velocity vector patterns in the form of closed streamlines. The cores of the vortex can also be identified by vorticity or swirling strength. However in this study, the swirling strength, λ_{ci} is used jointly with the Galilean decomposition as a vortex core marker. The swirling strength is the imaginary part of the complex eigenvalue of the local velocity gradient tensor and it is an explicit measure of rotation (Zhou *et al*., 1999). According to Zhou *et al*., (1999) and Adrian *et al*. (2000a), swirling strength does not emphasize regions of intense shear. Instead, λ_{ci} captures the local swirling character of a region without contamination from shear. On the other hand, vorticity highlights regions of intense shear and swirling that are non-vortical (Adrian *et al*., 2000b). The Galilean decomposition and the swirling strength have been applied extensively in the recent past to analyse the organisation of vortices in both the inner and outer layers of turbulent flows.

Selected instantaneous velocity fields in the parallel and diverging sections over the smooth wall, intermediate type and *k*-type rough walls are shown in Figure 4.15-4.17. A Galilean decomposition is applied by removing a constant convection velocity, U_c from each field to reveal those vortex structures whose cores are advecting at this particular speed. It should be noted that the closed streamlines of the velocity vectors can only be revealed if the convection velocity matches with that of the vortex cores. Contours of $\lambda_{ci}\omega_z/|\omega_z|$ are also superimposed in the background to highlight the locations of the vortex cores. λ_{ci} is multiplied by the sign of the spanwise vorticity to capture the direction of the swirl at each location. In these plots, the blue colour contours correspond to prograde (negative or $\omega_z < 0$) swirling strength, i.e., clockwise rotating vortices. The red colour contours correspond to retrograde (positive or $\omega_z > 0$) swirling strength, representing anti-clockwise rotating vortices. In general, the plots show that each velocity field contains vortex cores that are associated with heads of hairpin vortices advecting in the longitudinal direction.

Figure 4.15 shows the Galilean decomposed velocity vector fields in the parallel and diverging sections of the smooth wall. Uniform convection velocities of $U_c = 0.85U_m$ and $U_c = 0.80U_m$ were subtracted, respectively, from the vector fields in the parallel and diverging sections to reveal the heads of hairpin vortices that are advecting at these speeds. In both the parallel and diverging sections, the vector fields reveal examples of vortex cores that are construed to be associated with the heads of hairpin vortices. However, it appears that there are fewer hairpin vortices in the parallel section of the smooth wall compared to the diverging section. This observation is consistent with the finding of Lee and Sung (2009) and Lee *et al*. (2010) who also observed more swirling motions in an APG boundary layer compared to ZPG boundary layer. The vortex generates a low-momentum fluid at its upstream by backward induction of the legs and vortex head. This low-momentum fluid formed under the upstream of the head of each hairpin vortex is lifted away from the wall leading to $Q2$ events ($u' < 0$, $v' > 0$). This feature is one of the hairpin vortex signatures reported by Zhou *et al*. (1999) and Adrian *et al*. (2000b). The vortices in both the parallel and diverging sections are aligned to each other (shown by dashed line) to form a single train of hairpin packet. The hairpin packet in the parallel section is inclined relatively to the wall at an inclination angle of 14.8° (Figure 4.15a). In the diverging section, the vortices in the packet are regularly spaced

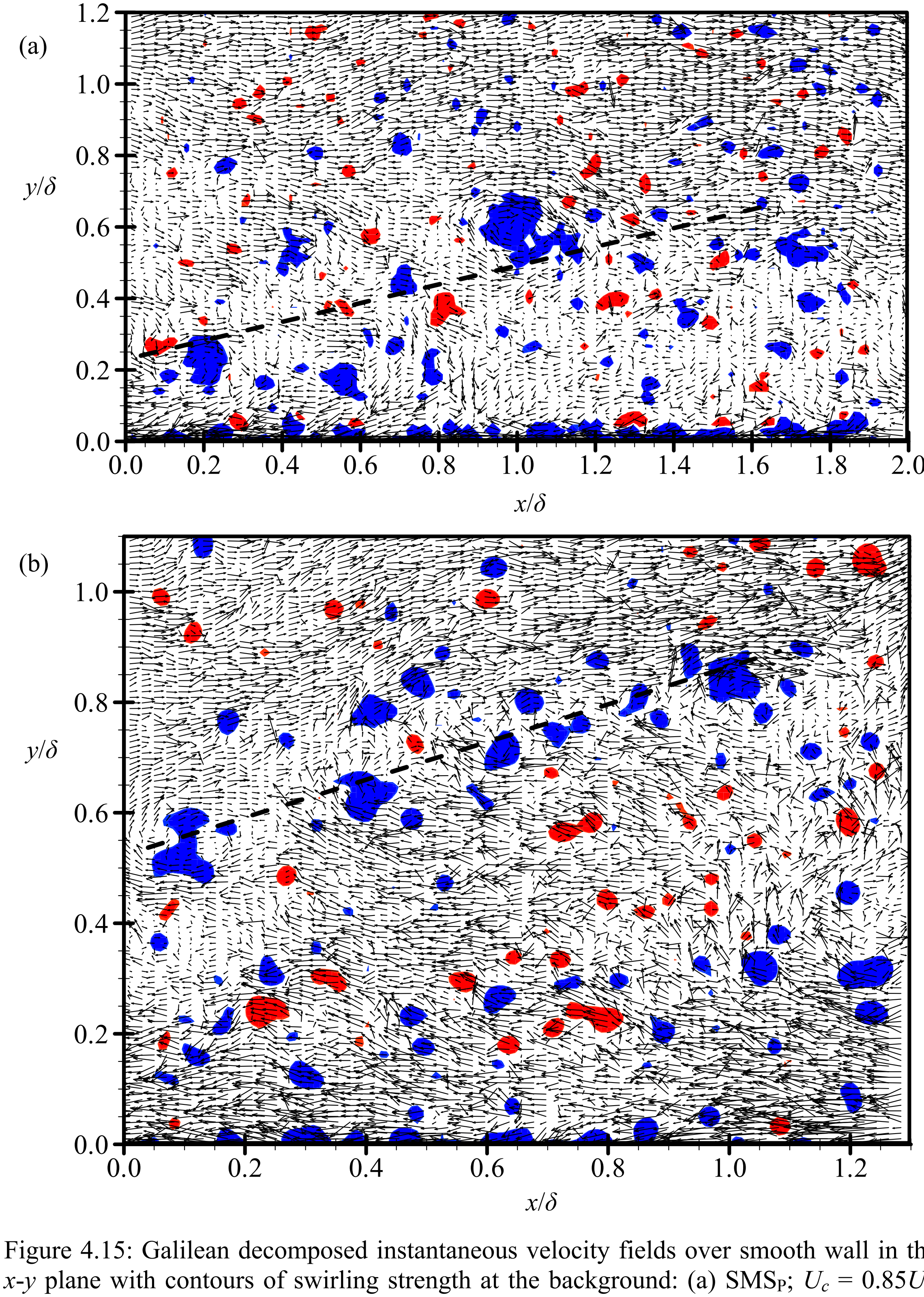

Figure 4.15: Galilean decomposed instantaneous velocity fields over smooth wall in the *x*-*y* plane with contours of swirling strength at the background: (a) $\mathrm{SMS_P}$; $U_c = 0.85U_m$ and (b) $\mathrm{SMS_D}$; $U_c = 0.8U_m$.

and the packet is inclined at a slightly higher angle of 18.8° (Figure 4.15b). Lee and Sung (2009) observed inclination angles of 13° and 18°, respectively, for ZPG and APG turbulent boundary layers. Meanwhile, the less defined circular path traced by vectors in the diverging section of the smooth wall is likely due to a non-matching convection velocity. However, the swirling strength unambiguously identified the presence of a group of vortices. Figure 4.15 demonstrates that the influence of hairpin vortices in the parallel section is limited to $y < 0.75\delta$ whereas in the diverging section, it extends to $y = 0.9\delta$.

The Galilean decomposed velocity fields over the intermediate type ribs are shown in Figure 4.16. For this rough wall, the uniform convection velocities subtracted from the flow fields are $U_c = 0.78U_m$ (Figure 4.16a) and $U_c = 0.55U_m$ (Figure 4.16b), respectively in the parallel and diverging sections. Clearly, the flow fields over the intermediate type rough wall also reveal the presence of hairpin vortices advecting at the above convection velocities. A single hairpin packet can be identified in the parallel and the diverging sections. In the diverging section, the packet contains fewer (about four) vortex cores while about ten hairpin vortices are found in the hairpin packet in the parallel section. Apparently, more violent eruption of low-momentum fluid is observed in the parallel section compared to the diverging section. However, this does not produce larger stresses in the parallel section compared to the diverging section. Meanwhile, in both sections the contour size of the retrograde vortices although still smaller and fewer than the prograde vortices is relatively increased. The packet in the parallel and diverging sections are inclined at angles of 23.1° and 22.8°, respectively.

Figure 4.17 shows examples of the decomposed vector fields in the parallel and

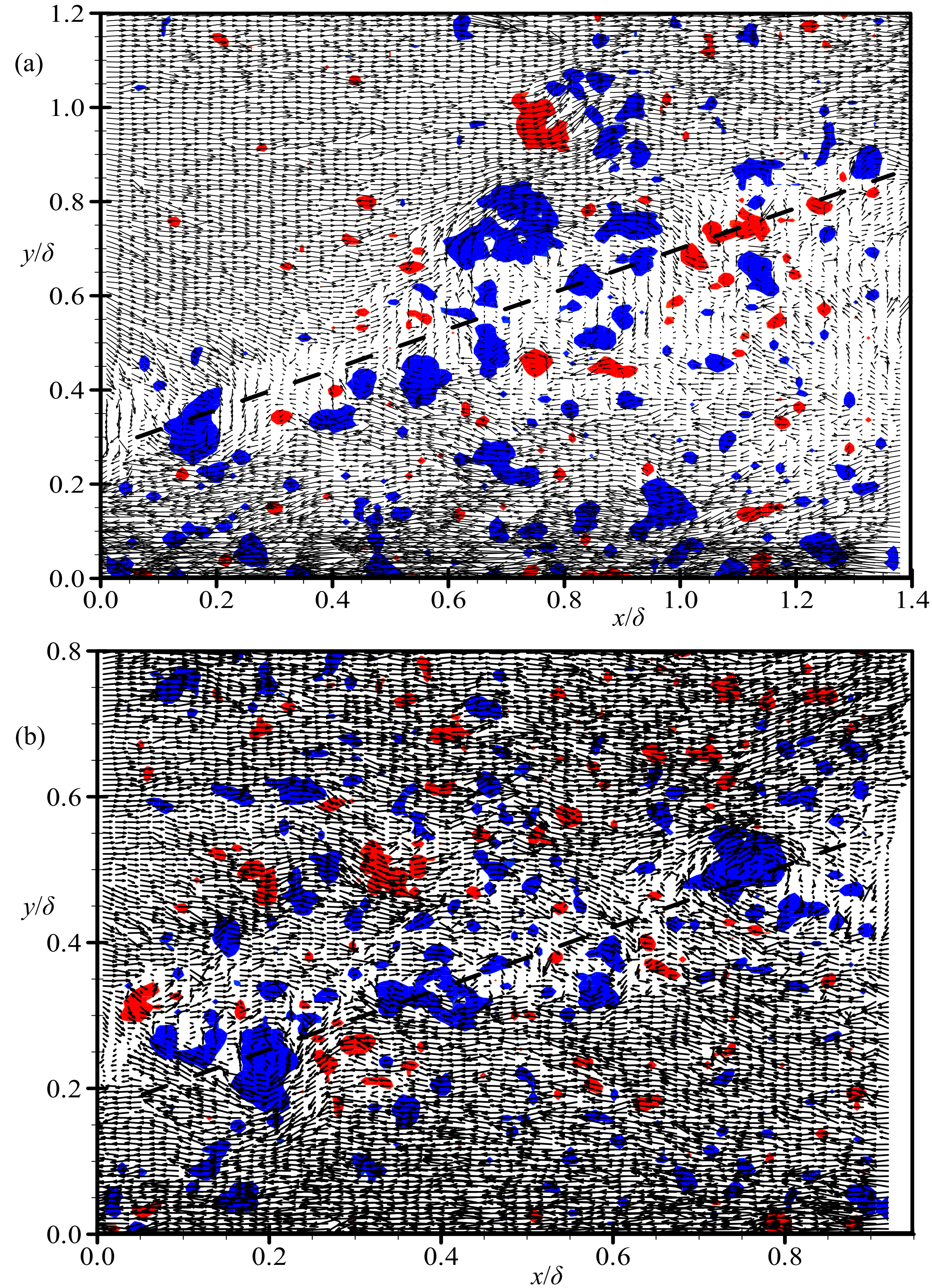

Figure 4.16: Galilean decomposed instantaneous velocity fields over intermediate type rough wall in the *x*-*y* plane with contours of swirling strength at the background: (a) R_4S_P; $U_c = 0.78U_m$ and (b) R_4S_D; $U_c = 0.55U_m$.

diverging sections of the k-type rough wall. In this case, the uniform convection velocities applied to the fields are $U_c = 0.70U_m$ (Figure 4.17a) for the parallel section and $U_c = 0.72U_m$ (Figure 4.17b) for the diverging section. In Figure 4.17, a further increase in the size of the contours of retrograde vortices is observed, especially in the parallel section where the retrograde vortices are relatively more distinct. In fact, in the parallel section, the size of the retrograde is similar to that of the prograde with a remarkable character. The retrograde reveals a clear circular streamlines, rotating in the counter-clockwise direction, suggesting that the translation velocity matches that for the prograde rotating in the clockwise direction. At the upstream of the retrograde in the parallel section, high-speed fluid ($Q4$) is pumped from the above and upstream of the hairpin head towards the wall. The fields shown over the k-type ribs exhibit more intense activities that extend to the outer edge of the instantaneous boundary layer. Thus, roughness alters the coherent structure size and its activities beyond the roughness sublayer. Over the k-type rough wall, one hairpin packet is revealed in the parallel section and diverging section. The hairpin packets are inclined at 17.5° and 17.4°, respectively in the parallel and diverging sections. Figure 4.17a demonstrates that in the parallel section, the head of a mature packet can extend to y/δ = 0.95, for example at x/δ = 1.05. Apparently, there are fewer vortices in the diverging section compared to the parallel section. However, these fewer vortices associated with APG are accompanied by a more intense momentum transport that resulted in the dramatic increase in the Reynolds stresses in the diverging section compared to the stresses in the parallel section. Moreover, the near lack of the vortices near the wall of the rough walls is in agreement with the annihilation of the peak in $\overline{u^2}$ profile. Furthermore, the fields reveal uniform

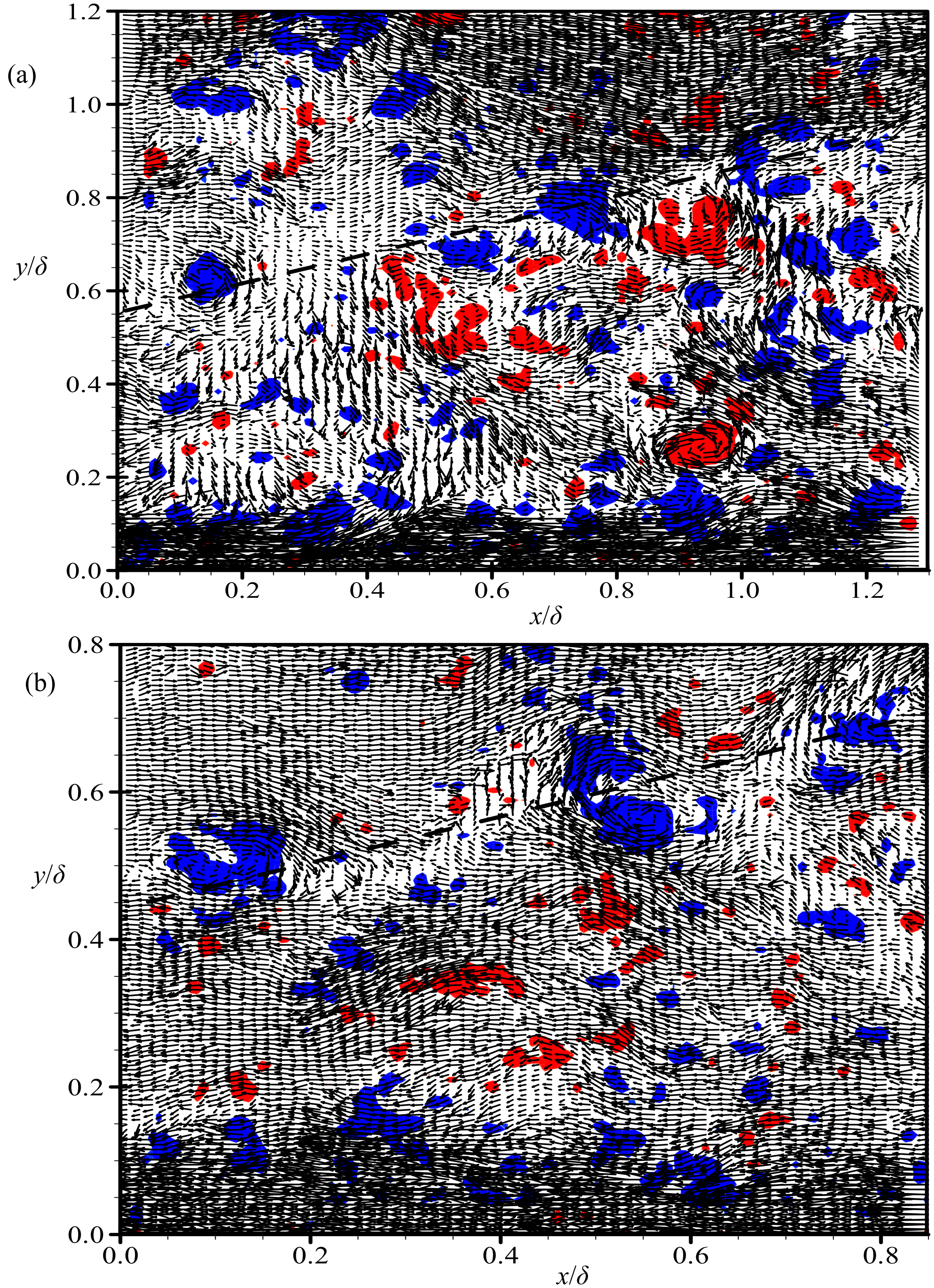

Figure 4.17: Galilean decomposed instantaneous velocity fields over k-type rough wall in the x-y plane with contours of swirling strength at the background: (a) R_8S_P; $U_c = 0.70U_m$ and (b) R_8S_D; $U_c = 0.72U_m$.

momentum zones similar to those observed by Meinhart and Adrian (1995) and Adrian *et al*. (2000b). Usually three zones are identified. The zone close to the wall has streamwise component of the instantaneous velocity lower than U_c whereas the zone with $U_i > U_c$ generally occurs further away from the wall. In-between these zones, is the third zone characterized with small velocity vectors due to their $U_i \approx U_c$. Similar features of the vortices were observed over *d*-type, the size of the contours of λ_{ci} being larger in the diverging section than parallel section (Appendix D). In this case, the packets were inclined at inclination angles of 14.8° and 19.9°, respectively in the parallel and diverging sections of the *d*-type rough wall.

From the foregoing, the flow fields over the ribs revealed several larger size vortex cores than over the smooth wall in both the parallel and diverging sections. Over the rough walls, vortices are observed close to the edge of the boundary layer, and these vortices are accompanied by larger scale events similar to the large-scale eruptions of fluid observed by Volino *et al*. (2009). In fact, the vortices over the rough walls induced larger low-speed region in comparison to flow over smooth wall. The induced $Q2$ and $Q4$ events are vigorous over the rough walls than over the smooth wall. The relative importance of this low-momentum region is manifested as an enhancement of the turbulent stresses. The large-scale events originate from the ribs and extend into the outer layer. These disparities in the organisation of the hairpin packets over the smooth wall and rough walls are likely responsible for the observed differences in the Reynolds stresses and transport velocities of the turbulence kinetic energy and Reynolds stresses (Tsikata and Tachie, 2012). Although the present observations over the rough walls are consistent with the results of Volino *et al*. (2009) and Lee *et al*. (2009) over two-dimensional ribs, Volino *et al*. (2007) observed common features in the instantaneous velocity fields over their mesh surface and smooth wall. Such differences demonstrate the effectiveness of transverse ribs in the generation of larger scale turbulent activities than three-dimensional roughness elements.

4.2.2.2 Quadrant Decomposition

The quadrant decomposition is often used to provide insight into the role of coherent structures on the Reynolds stress producing events. Since $-\overline{uv}\partial U/\partial y$ is the main contributing term in the turbulence production term, such an analysis will also improve our understanding of the effects of surface roughness and APG on near-wall turbulence production. In this technique, the contributions of the various quadrant events to the overall Reynolds shear stress are easily quantified. In the implementation of the quadrant decomposition, the overall Reynolds shear stress at each measurement location is decomposed into the individual contributions from the four quadrants of the u'-v' plane excluding a hyperbolic hole of size H as given in Eq. 1.22, following Lu and Willmarth (1973). This excludes the smaller fluctuations corresponding to more quiescent periods in the hole. It should be noted that the value of H depicts a threshold on the strength of the Reynolds shear stress producing events. For a hyperbole hole of size $H = 0$, all $u'v'$ events are included in the decomposition whereas for increasing values of H only increasingly strong Reynolds shear stress producing events are included. Although, the quadrant results are presented for $H = 0$, an analysis was conducted to study the effects of H on quadrant events. Preliminary analysis shows that a threshold of $H = 2$ characterizes instantaneous Reynolds shear stress producing events stronger than $5.7\overline{uv}$ in the parallel section of the smooth wall.

As noted earlier, the ejection ($Q2$) and sweep ($Q4$) events are the most important events that contribute significantly to $-\overline{uv}$. The inward ($Q3$) and outward ($Q1$) interaction motions, on the other hand, do not contribute to $-\overline{uv}$. The fractional contributions of the various quadrant events to the Reynolds shear stress over the smooth wall and rough walls are shown in Figure 4.18 and Figure 4.19 for a threshold of $H = 0$. The present results in the parallel section of the smooth wall and *k*-type rough wall are compared with the DNS data of Krogstad *et al*. (2005) in the inserts in Figure 4.18 and Figure 4.19. Except in the region $0.07y_{uv} \leq y \leq 0.27y_{uv}$ for $Q2$, the smooth wall data sets exhibit consistent disagreement with the DNS data sets. However, over the *k*-type rough walls, excellent agreement is observed between the present data sets and the DNS data sets, notwithstanding the fact that the latter data sets were obtained in a symmetrically roughened channel.

As expected, the contributions from $Q1$ (Figure 4.18a-c) and $Q3$ (Figure 4.18d-f) to $-\overline{uv}$ are always negative, and they are fairly small compared to $Q2$ (Figure 4.19a-c) and $Q4$ (Figure 4.19d-f). Figure 4.18a and Figure 4.18d demonstrate that over the smooth wall the outward ($Q1$) and inward ($Q3$) interaction motions are stronger in the diverging section than in the parallel section. The influence of APG on these motions manifests across the entire layer. Krogstad and Skåre (1995), and Nagano *et al*. (1998) also observed an increased $Q1$ and $Q3$ events in an APG boundary layer compared to ZPG boundary layer. The large distribution of $Q1$ and $Q3$ caused by flow retardation is consistent with enhanced wall-normal turbulence diffusion of kinetic energy in the diverging section (Tsikata and Tachie, 2012). It was also remarked by Bradshaw (1967) and Nagano *et al*. (1998) that in an APG flow, energy transfer via turbulence diffusion is

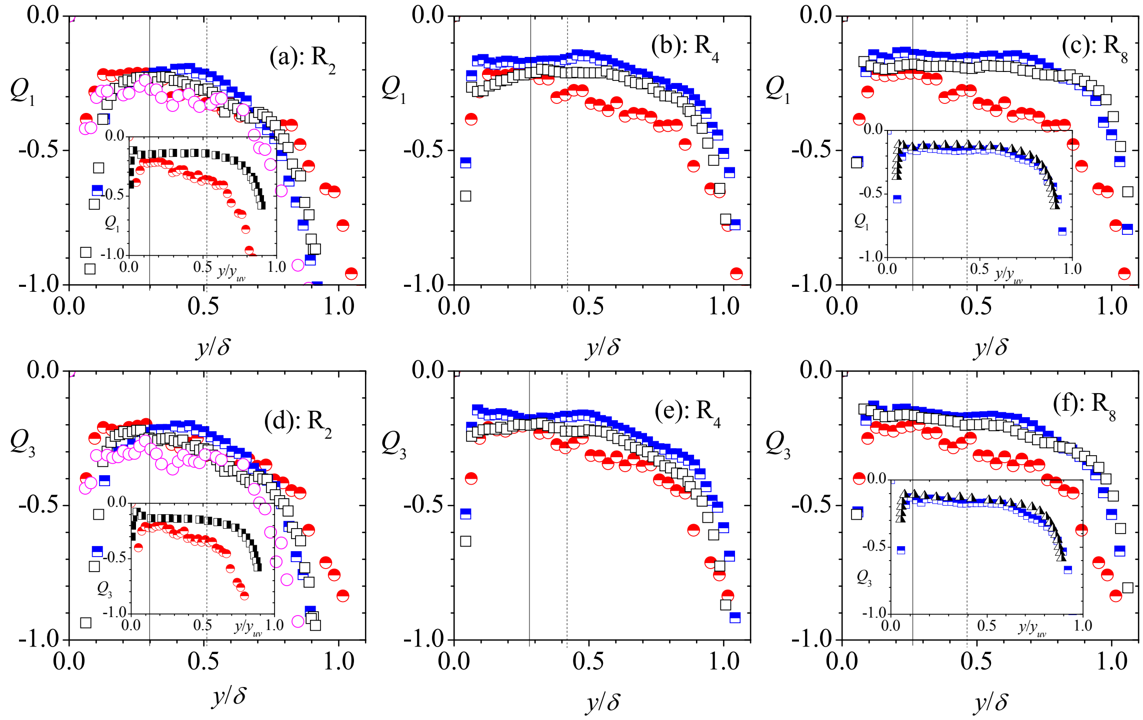

Figure 4.18: Fractional contributions to $-\overline{uv}$ by first and third quadrants for H = 0. Symbols: smooth wall: parallel section ◓ and diverging section ○; rough walls: parallel section ⬒ and diverging section □: inserted figure: Krogstad *et al*. (2005): smooth wall ◨ and *k*-type ribs ▲.

dominant than ZPG boundary layer. Besides, APG strengthened the corresponding ejections (Figure 4.19a) and sweeps (Figure 4.19d). This observation is also consistent with the finding of Krogstad and Skåre (1995), and Nagano *et al*. (1998) who observed an increased $Q2$ and $Q4$ events in an APG boundary layer compared to ZPG boundary layer. Thus, the enhanced $-\overline{uv}$ as well as P_q and P_{-uv} in the diverging section of the smooth wall are due to aggressive ejection ($Q2$) and sweep ($Q4$) events. The near-wall spike in $Q4$ in the diverging section is likely due to dominant turbulence transport towards the wall. Previous studies also show that APG enhanced sweeps in the wall region in comparison to ZPG flow over smooth wall. Nagano *et al*. (1998) observed an increased $Q1$ and $Q3$ events as the wall is approached in an APG boundary layer compared to ZPG boundary layer and remarked that in APG flow energy transfer via turbulence diffusion is dominant. In general, the rapid rise in $Q2$ is due to more intense transport of low-momentum fluid from the wall region towards the outer region.

Figure 4.18 revealed that the inward and outward interaction motions in the parallel section are weaker in the presence of roughness, although $Q1$ and $Q3$ over rough walls are peaky at the wall. However, over the *d*-type ribs stronger inward and outward motions are observed near the wall, $y \leq 0.3\delta$ and in the wake region, $y \geq 0.7\delta$ compared to those in the parallel section of the smooth wall. The DNS results of Krogstad *et al*. (2005) also indicate a reduction in $Q1$ and $Q3$ across the entire layer of the *k*-type ribs relative to the smooth wall data. Contrarily to these results are the $Q1$ and $Q3$ motions reported by Krogstad and Antonia (1999). Their results show that roughness augmented both $Q1$ and $Q3$ over mesh and rib roughness compared to smooth wall due to the large relative roughness used. On the other hand, Wu and Christensen (2007) observed similarity in the outer layer for both $Q1$ and $Q3$ over smooth wall and rough walls with $k_s/\delta = 0.0062$ and 0.0208. It should be noted that these motions are altered by roughness in both the inner and the outer layers.

Figure 4.19 demonstrates that except for the *d*-type ribs, ejections of the low-speed fluid are consistently more intense over the smooth wall than rough walls. Compared to the *d*-type rough wall, ejection event over the smooth wall is only strengthened in the region $0.35\delta < y < 0.72\delta$; beyond this region $Q2$ is stronger over *d*-type ribs (Figure 4.19a). It is believed that the reduction of $Q2$ over the rough walls, especially the intermediate type and *k*-type ribs, is due to trapping of low-momentum fluid between roughness elements, as explained by Grass (1971). This effect extends beyond the end of the logarithm region since effective lifting of the low-momentum fluid

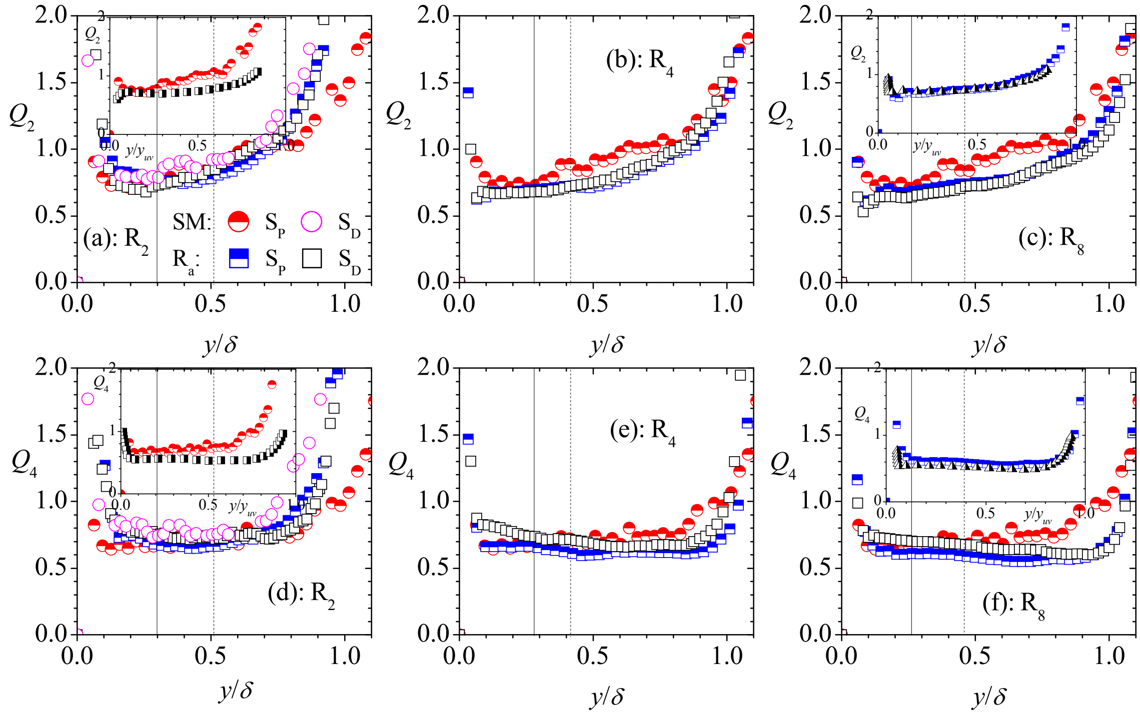

Figure 4.19: Fractional contribution to $-\overline{uv}$ by second and fourth quadrants for H = 0. Symbols for inserted figure: Krogstad *et al*. (2005): smooth wall ◨ and k-type ribs ▲.

is mitigated. Figure 4.19 also revealed that apart from the d-type ribs, there is enhanced transport of high-speed fluid ($u' > 0$, $v' < 0$) towards the smooth wall compared to the rough walls. In the case of the d-type ribs, $Q4$ events over this type of ribs and smooth wall are similar for $0.26\delta < y < 0.67\delta$, and beyond this region, intense transport of high-speed fluid towards the wall of the d-type ribs is evident. Moreover, the distribution of $Q4$ over the intermediate type ribs agrees with the smooth wall result for $0.09\delta < y < 0.34\delta$. The increase in $Q2$ and $Q4$ over the d-type ribs may be an indication of higher level of intermittency in the wake region and near the wall. The flatness factors (not shown) were indeed larger near the wall and in the wake region over the d-type ribs. It should however be noted that as the ribs are approached a strong spike is observed in $Q4$. As noted earlier, this spike is caused by enhanced transport of turbulence kinetic energy towards the wall. However, Krogstad *et al*. (1992) attributed this intense sweep event near the rough wall relative to the smooth wall as a consequence of reduced damping due to the open nature of the rough wall. The DNS results of Krogstad *et al*. (2005) also indicated strong reduction in $Q2$ for $y < 0.2h$ and throughout the entire layer for $Q4$. However, the reduction in the contributions from the second and fourth quadrants over the rough walls is at variance with results of Krogstad *et al*. (1992). Krogstad *et al*. (1992) observed stronger contributions from $Q2$ and $Q4$ to Reynolds shear stress over the mesh rough wall ($k_s/\delta = 0.067$) than over the smooth wall. Krogstad and Antonia (1999) also observed more intense $Q4$ events near the mesh and the rod roughness ($k_s/\delta = 0.125$), but observed a reduction in $Q2$. Similarly, stronger $Q2$ and $Q4$ events were detected over a packed sphere bed than smooth wall (Schultz and Flack, 2005). On the contrary, Schultz and Flack (2007), Flack *et al*. (2007), and Wu and Christensen (2007) observed similarity in the outer layer for both $Q2$ and $Q4$ over smooth wall and rough walls. Since the scale separation between k_s and δ employed in the above studies varies, the different observations may be due to dissimilarity in k_s/δ.

The present data were also analyzed using a hole size of $H = 2$. When only strong events ($H = 2$) was considered, the results (not shown) exhibited only modest variations with roughness. This suggests that the large distributions of Q_i ($H = 0$) over the smooth wall relative to the rough walls in Figure 4.18 and Figure 4.19 were due to the dominant contributions to $-\overline{uv}$ by smaller turbulence fluctuations over the smooth wall.

Similarly, APG augments the interaction motions over the rough walls. Thus, the combined effects of roughness and APG are expected to enhance the turbulence transport via turbulence diffusion. Indeed, the vertical transport velocity for the turbulence kinetic energy (V_q^+) in the diverging section of these rough walls (Tsikata and Tachie, 2012) was enhanced by APG compared to V_q^+ in the parallel section. In the vicinity of the rough walls, $Q1$ is stronger than $Q3$, indicating that there is a strong transfer of high-speed fluid directed towards the wall (i.e., $Q4$) away from the ribs into the outer region. Figure 4.19a-c demonstrates that the contribution from $Q2$ to the Reynolds shear stress is less sensitive to APG over the rough walls. Unlike ejections, the $Q4$ events are stronger in the diverging section of the rough walls compared to the parallel section. This means that the increased Reynolds stresses observed in the diverging section of the rough walls is primarily caused by the stronger sweep events.

The ratio of the ejection to sweep events ($\phi_H = Q2/Q4$) is often used to measure the relative importance of $Q2$ and $Q4$ events (Lu and Willmarth, 1973; Krogstad *et al*., 1992; Krogstad *et al*., 2005; Schultz and Flack, 2007; Wu and Christensen, 2007). The fractional difference in the ejection and sweep events i.e., $\Delta Q_H = Q4 - Q2$, is also a useful way of quantifying the relative importance of ejection and sweep events, for example, Raupach (1981) and Krogstad *et al*. (1992) used ΔQ_H to highlight relative importance of ejections and sweeps over smooth and rough walls. For $H = 0$, ϕ_H and ΔQ_H become ϕ_0 and ΔQ_0. Figure 4.20 and shows plots of both ϕ_0 and ΔQ_0. It is observed that $Q4$ dominates in a narrow region close to the wall while $Q2$ dominates a wide region that extends from the wall region into the outer layer. This is consistent with strong turbulence diffusion of kinetic energy from the wall region to the outer layer. For example, in the parallel section, sweep events dominate (i.e., $\phi_0 < 1$ or $\Delta Q_0 > 0$) for $y < 0.06\delta$, $y < 0.14\delta$, $y < 0.11\delta$ and $y < 0.15\delta$, respectively for the smooth wall, *d*-type, intermediate type and *k*-type rough walls. In the diverging section, sweep events dominate for $y < 0.27\delta$, $y < 0.35\delta$, $y < 0.43\delta$ and $y < 0.4\delta$, respectively for the smooth wall, *d*-type, intermediate type

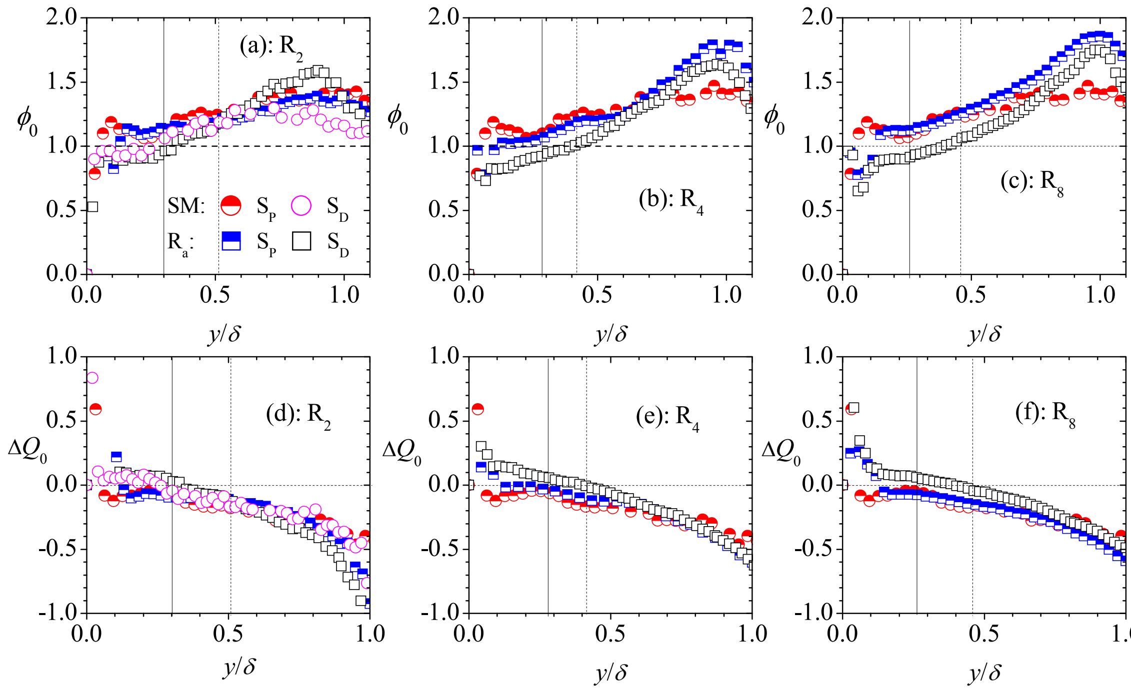

Figure 4.20: Ratio of contributions to the Reynolds shear stress from $Q2$ and $Q4$ events and their difference for $H = 0$.

and k-type rough walls. Beyond these regions, ejection events are more important (i.e., $\phi_0 > 1$ or $\Delta Q_0 < 0$) than the sweep events. Thus, in the presence of roughness and/or APG the region where sweep events are importance is broadened. Moreover, these regions correspond closely to regions beneath the peak in the Reynolds stresses. The implication is that, there is enhanced diffusion of turbulence kinetic energy towards the wall. Whereas ϕ_0 is more sensitive to roughness and APG, ΔQ_0 tends to be less sensitive to roughness for $y > 0.15\delta$. ΔQ_0 is however affected by APG in most part of the layer. The general reduction in ϕ_0 throughout the layer in the diverging section of the smooth wall and rough walls is also an indication of relative dominance of $Q4$ events in an APG flow compared to fully developed channel flow as well as ZPG boundary layers. This observation is consistent with previous studies (Krogstad and Skåre, 1995; Nagano *et al.*, 1998). Schultz and Flack (2007) observed consistency in ϕ_0 over smooth and rough walls due to the low relative roughness used. Raupach (1981) also observed that ΔQ_0 is independent of roughness beyond the roughness sublayer although the relative roughness was in the range $0.048 \leq k/\delta \leq 0.113$. Conversely, Krogstad *et al*. (1992) observed effects of roughness on ΔQ_0 in both the inner and outer regions for $k/\delta = 0.021$.

Raupach (1981) established a close correlation between ΔQ_H and skewness factors using the cumulant-discard method (Antonia and Atkinson, 1973; Nakagawa and Nezu, 1977) given a third-order Gram-Charlier probability distribution of the two variables u' and v'. According to Raupach (1981), the existence of a linear relationship between ΔQ_0 and skewness factors provides an avenue for a good description of the ejection-sweep character of the boundary layer by considering third-order moments of u' and v'. This indeed means that the third-order moments are linked to ejection and sweep events. In Figure 4.21, the normalized third-order moments or skewness factors ($M_{ij} = \overline{u^i v^j}/{u_{rms}}^i {v_{rms}}^j$, where $i + j = 3$, $i, j \geq 0$) are plotted against ΔQ_0 for all the test conditions. Figure 4.21 demonstrates that ΔQ_0 and each skewness factor are linearly related irrespective of the wall condition or pressure gradient. In the parallel section, the relationship that exists between ΔQ_0 and the four skewness factors is given as:

$$\Delta Q_0 = 0.57M_{30} = -1.14M_{21} = 0.85M_{12} = -0.56M_{03} \tag{4.5}$$

and in the diverging section the relationship is given by:

$$\Delta Q_0 = 0.75M_{30} = -1.55M_{21} = 0.91M_{12} = -0.61M_{03} \tag{4.6}$$

Similar plots for ΔQ_0 and M_{30} over smooth wall and surfaces with different roughness were made by Raupach (1981) who found the constant of proportionality to be 0.37. Balachandar and Bhuiyan (2007) reported a value of 0.60 for the constant of

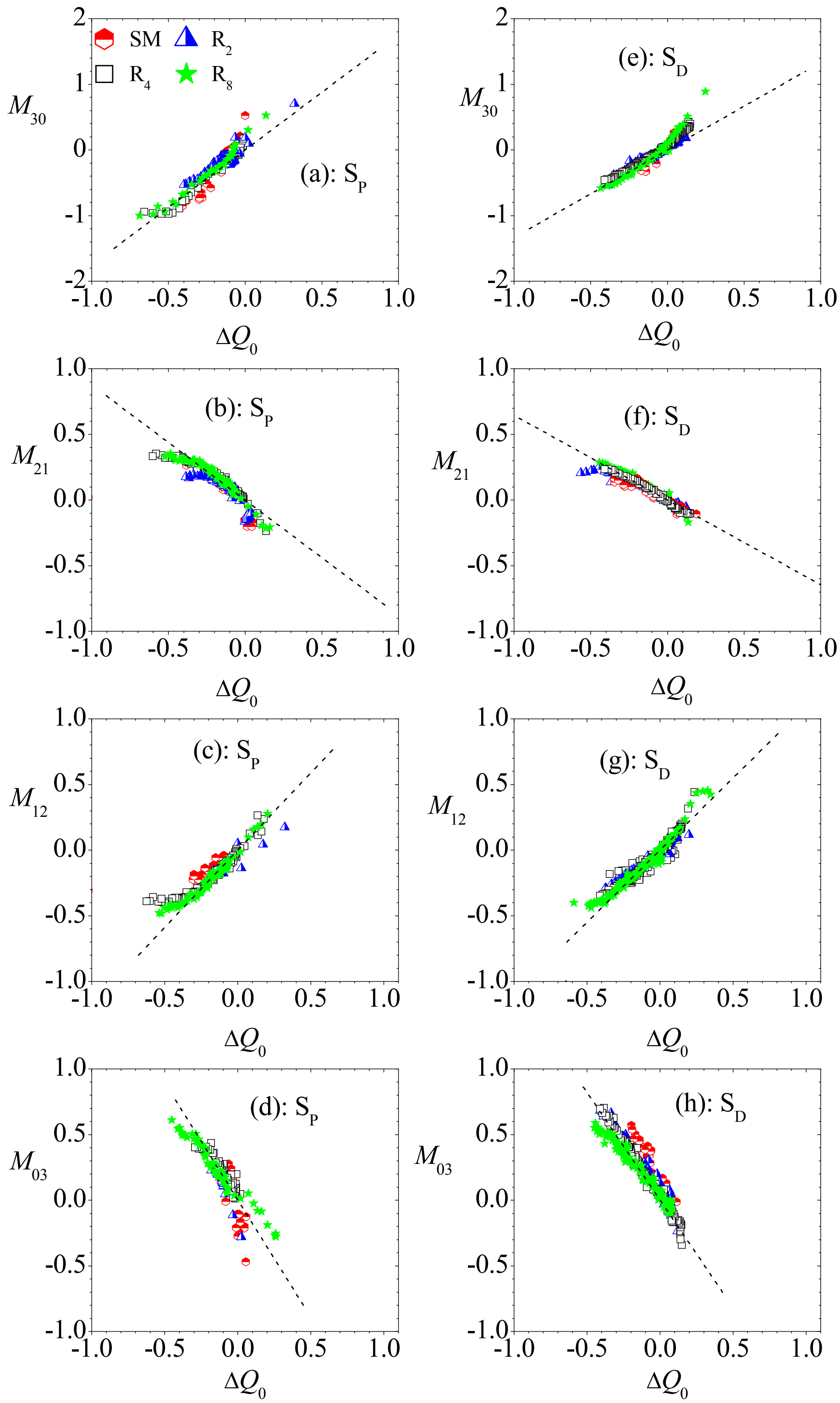

Figure 4.21: Relation between ΔQ_0 and skewness factors, M_{ij} over the smooth wall and rough walls.

proportionality between ΔQ_0 and M_{30}. Raupach's (1981) data sets also showed that ΔQ_0 is connected to M_{21}, M_{12} and M_{03} by proportionality constants of −0.75, 0.73 and −0.63, respectively (Raupach *et al*., 1991). From the foregoing, the present values of constant of proportionality are larger than those reported by Raupach (1981). The observed differences in these constants may be attributed to the difference in the flow type. For example, the previous constants were obtained for measurements in a zero pressure gradient turbulent boundary layer (Raupach, 1981) and a turbulent open-channel flow (Balachandar and Bhuiyan, 2007). The present results clearly show that these constants of proportionality are independent of roughness in spite of the observed dependence of the turbulence structure on roughness. However, these constants depend strongly on APG as demonstrated by the present results.

Consideration is now turned to the effects of roughness and APG on the number of times an event is detected in a given quadrant. The relative number of each type of event (N_i) was computed from the following relation:

$$N_i(y;H) = \frac{1}{N}\sum I_{i,H}(y) \tag{4.7}$$

where N is the total number of samples and $I_{i,\,H}$ is an indicator function defined in Eq. 1.23. Figure 4.22 and Figure 4.23 show the fractions of the number of each type of event detected in the four quadrants for H = 0. The distribution of N_1 and N_3 over the smooth wall is independent of APG in the lower half of the boundary layer (Figures 4.22a and 4.22d). For $y > 0.10\delta$, the number of detection in the first quadrant drops in the diverging section while the number of detection in the third quadrant rises. This suggests that in the first quadrant only few but stronger outward interaction motions were induced by APG to

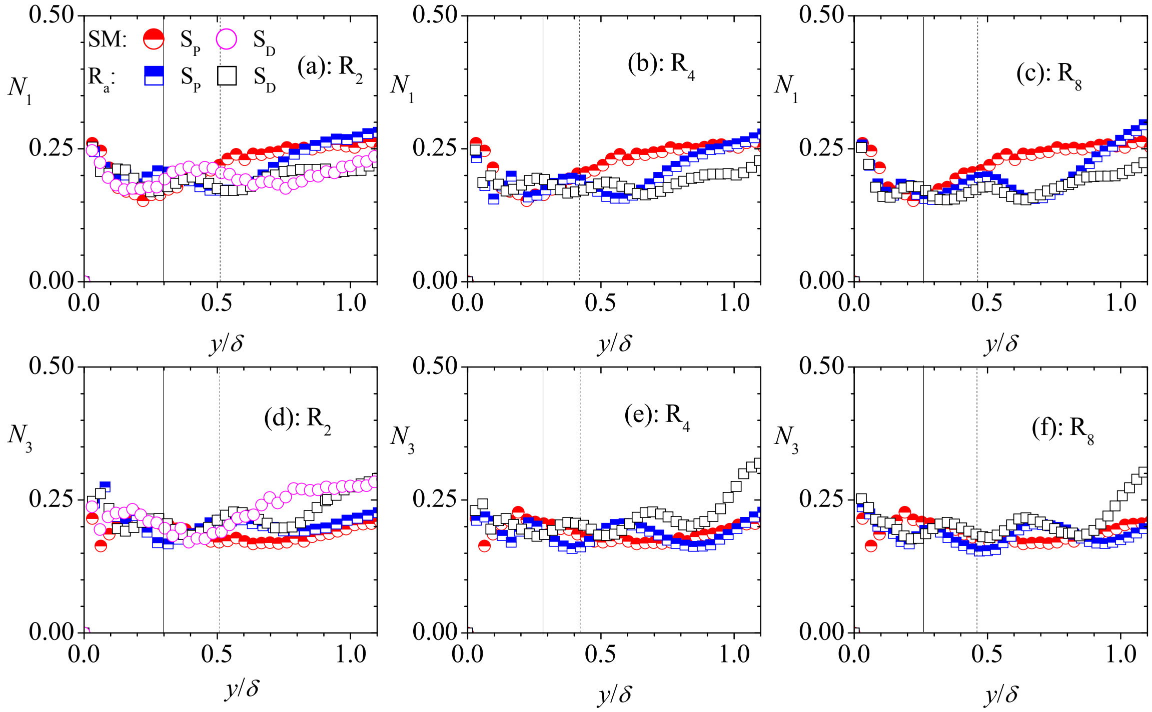

Figure 4.22: Fractions of the number of events detected in the first and third quadrants at $H = 0$.

augment $Q1$. In Figures 4.23a and 4.23d, both N_2 and N_4 are altered by APG for $y > 0.56\delta$, but is less sensitive to pressure gradient near the wall. Since N_2 is only marginally increased while N_4 is significantly reduced in the outer layer in the diverging section, Figures 4.23a and 4.23d would imply that APG does not produce more Reynolds shear stress producing events but it intensifies the strength of these events compared to the flow in the parallel section.

In spite of the strong effects of roughness on the quadrant contributions to the Reynolds shear stress in the roughness and outer layers, the relative number of detections in the various quadrants (except N_1) demonstrates a weak dependence on roughness. Figure4.22a-c, however, revealed that more first quadrant events were detected over the smooth wall compared to the rough walls in the regions $0.38\delta < y < 0.82\delta$, $0.41\delta < y < 0.96\delta$ and $0.26\delta < y < 0.98\delta$, respectively for the d-type, intermediate type and k-type ribs

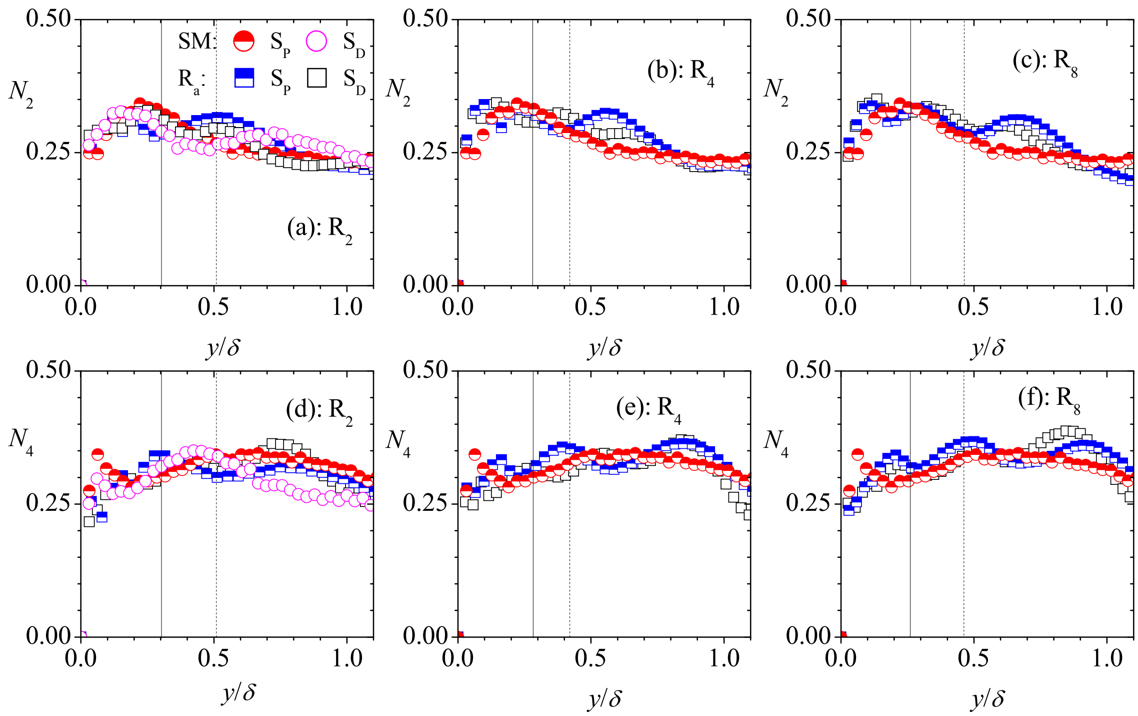

Figure 4.23: Fractions of the number of events detected in the second and fourth quadrants for $H = 0$.

in the parallel section. The modest dependence of N_2 and N_4 (as well as N_3) on roughness may imply that the smooth wall does not produce large amount of Reynolds shear stress producing events, yet there is intensification of Q_2 and Q4 events (as well as $Q1$ and $Q3$ motions) over the smooth wall compared to the rough walls. The observed less sensitive of relative number of detections to roughness is consistent with results of Wu and Christensen (2007), and Mejia-Alvarez and Christensen (2010) who observed good agreement in N_i over smooth wall and various rough walls for $H = 0$.

Over the rough walls, APG did not significantly alter the number of detections of each type of quadrant event. However, in the wake region $y > 0.72\delta$, $y > 0.62\delta$ and $y > 0.83\delta$, respectively for d-type, intermediate type and k-type ribs, APG strongly modified N_1 (decrease) and N_3 (increase) over the rough walls compared to the data in the parallel section. The less sensitivity of N_4 throughout the entire layer as well as N_1 and N_3 in the wall region and the lower part of outer layer suggests that only few events were detected to enhance $Q1$, $Q3$ and $Q4$ in the diverging section compared to parallel section. Meanwhile, the similarity in N_2 in the parallel and diverging sections of the rough wall is consistent with the observed agreement in $Q2$.

4.2.2.3 Two-Point Correlation

In the previous sections, it was demonstrated that roughness and APG affect coherent structures in both the inner and outer regions. It is therefore prudent to quantify the size and inclination angle of these structures with respect to roughness and APG. The two-point correlations of the fluctuating velocities are often used to quantify the average size and inclination angle as well as to describe the shape of the hairpin packets.

Figure 4.24 shows the contours of streamwise two-point velocity auto-correlations R_{uu} in the x-y plane centred at $y_{ref} = 0.4\delta$ over the smooth and rough walls in both the parallel and diverging sections. Similar to previous studies, the present R_{uu} contours are elliptical in shape and they are elongated in the streamwise direction, irrespective of the boundary condition and the pressure gradient. The long streamwise correlation in R_{uu} is dominated by elongated low-speed fluid regions within the vortex packets. Besides, the R_{uu} contours are inclined obliquely in the flow direction. It should be noted that the streamwise and wall-normal sizes, and the inclination angle of R_{uu} depend on the reference location, boundary condition and pressure gradient.

The streamwise and wall-normal one-dimensional profiles of R_{uu} correlations obtained by taking horizontal and vertical slices passing through the self-correlation peaks of the R_{uu} contours in Figure 4.24 are shown in Figure 4.25. In particular, the one-dimensional profiles of R_{uu} ($\Delta x/\delta$) and R_{uu} (y/δ) provide insight into the streamwise and

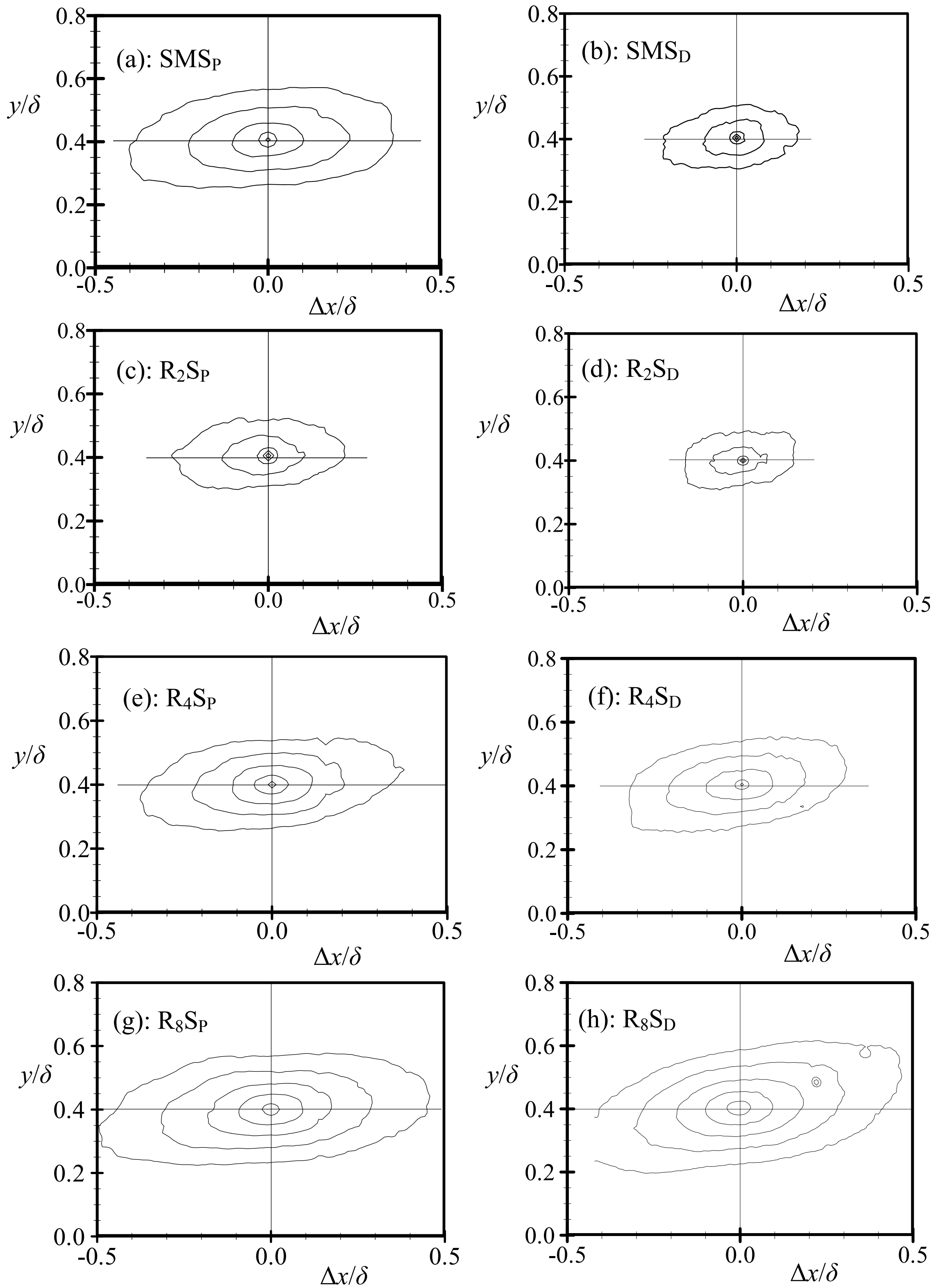

Figure 4.24: Contours of R_{uu} centered at $y_{ref} = 0.4\delta$, outermost contour level of $R_{uu} = 0.5$, contour spacing is 0.1.

wall-normal extents of the hairpin packets. Due to the small field of view used for the measurements, the long streamwise tail of R_{uu} is not captured. Over the smooth wall, APG diminished R_{uu} profiles (Figures 4.25a and 4.25d). This will imply that the characteristic streamwise and wall-normal sizes of the spatial structure embodied in R_{uu} are diminished by APG over the smooth wall.

In Figure 4.25a-b and Figure 4.25d-e, roughness reduced R_{uu} correlation, however, the difference is small over the intermediate type ribs. The reduction is severe over the *d*-type rough walls. Conversely, the *k*-type rough wall enhanced the values of R_{uu} correlation compared to the smooth wall values, (Figures 4.25c and 4.25f). Volino *et al*. (2007) observed similarity in streamwise slices of R_{uu} contours obtained at $y_{ref}/\delta = 0.40$ over their wire-mesh rough wall and smooth wall. The combined effects of roughness and APG only reveal modest modifications to the R_{uu} correlation. APG tends to reduce the

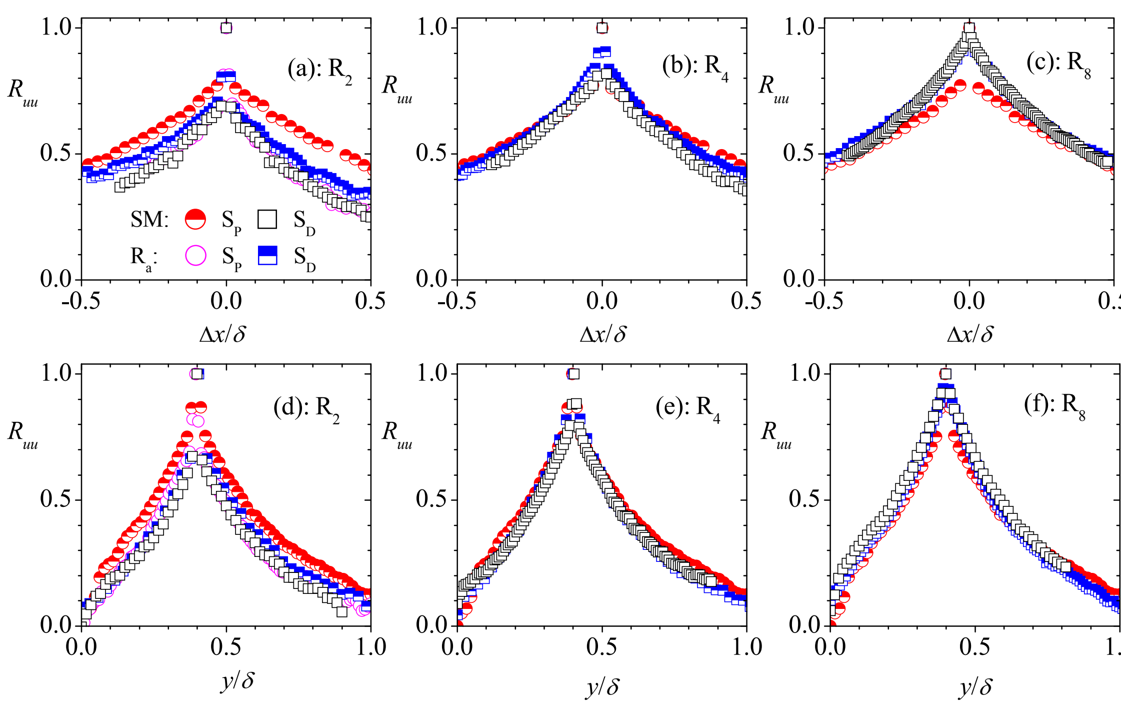

Figure 4.25: Streamwise and wall-normal one-dimensional profiles of R_{uu} at $y_{ref} = 0.40\delta$.

R_{uu} profiles over the *d*-type ribs (Figures 4.25a and 4.25d), and the streamwise profile over the intermediate type ribs (Figure 4.25b). The collapse of R_{uu} profiles in the parallel and diverging sections of the *k*-type ribs signifies that the spatial structures of the flow are insensitive to APG over this rough wall (Figures 4.25c and 4.25f). Similarly, the vertical profiles of R_{uu} correlation in the parallel and diverging sections of the intermediate type ribs collapsed (Figure 4.25e). From the foregoing, the weak effects of APG on R_{uu} over the rough walls in general, suggest that APG does not produce dramatic changes on the spatial structures embodied in R_{uu} correlation (unlike smooth wall) even though there may be changes in the dynamics of these structures due to combined effects of roughness and APG.

The average inclination angle, β of the vortex packets was estimated using the procedures employed by Christensen and Wu (2005) and Volino *et al*. (2007). In this approach, the R_{uu} contours were modelled as ellipses so that the major axis of each ellipse coincides with the self-correlation peak at each y_{ref}. Ellipses were fitted to five different contour levels: 0.9, 0.8, 0.7, 0.6 and 0.5 using the least-square methods. The points (x, y) farthest away from the self-correlation peak (i.e., Δx = 0, $y = y_{ref}$) on the five contour levels at both the upstream and downstream of the self-correlation peak were extracted for each contour level. A linear fit of these points facilitate the determination of inclination angle of the contours relative to the wall. The procedure was repeated for each contour map corresponding to a different y_{ref} for all surfaces in both the parallel and diverging sections. Figure 4.26 demonstrates that the average inclination angle, β of the vortex packets generally varies with y_{ref}/δ. The dependence of the hairpin packet inclination on both roughness and adverse pressure gradient is also revealed. For $0.1\delta \leq y$

$\leq 0.7\delta$, the average values of β are 8.6° ± 2.4°, 9.8° ± 0.8°, 11.6° ± 2.7° and 10.8° ± 1.2°, in the parallel section of the smooth wall, *d*-type, intermediate type and *k*-type rough walls, respectively. The corresponding values in the diverging section are 15.1° ± 4.9°, 12.3° ± 2.5°, 13.1° ± 1.2° and 12.3° ± 0.9°, for the smooth wall, *d*-type, intermediate type and *k*-type rough walls, respectively. Christensen and Wu (2005) reported β value of 11° for a fully developed flow over smooth wall. In a strong APG boundary layer flow, Krogstad and Skåre (1995) reported an inclination angle of 45° for the hairpin packet. For $0.2\delta \leq y \leq 0.5\delta$, Volino *et al*. (2009) reported 10.6° ± 2.7°, 11.3° ± 2.2° and 10.6° ± 1.2° for the average values of β, respectively over smooth wall, woven mesh rough wall and *k*-type rough wall.

In the absence of the long streamwise tail of R_{uu} correlation, Christensen and Wu (2005) defined average streamwise length scale, Lx_{uu} of R_{uu} as twice the distance from self-correlation peak to the most downstream location on the $R_{uu} = 0.5$ contour. Similar definition for Lx_{uu} was used by Volino *et al*. (2007) and Volino *et al*. (2009). The wall-normal length scale, Ly_{uu} of R_{uu} was estimated as the wall-normal distance between the points closest and farthest from the wall on the $R_{uu} = 0.5$ contour level (Volino *et al*., 2007). The estimated distances Lx_{uu}/δ and Ly_{uu}/δ are shown in Figure 4.27. In general,

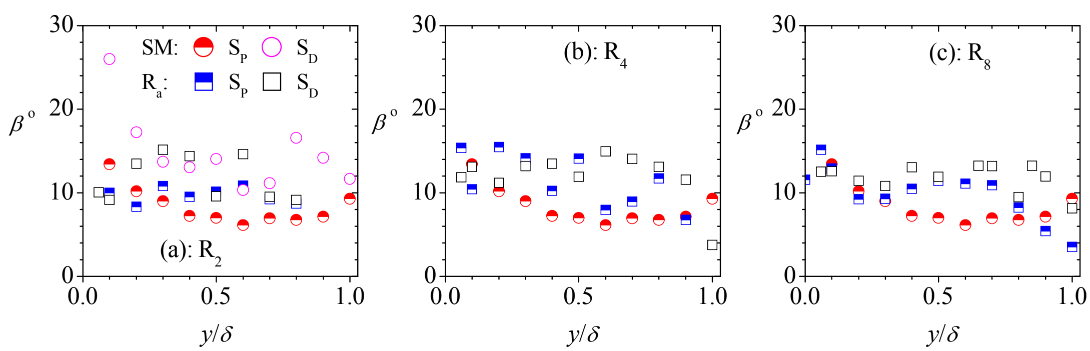

Figure 4.26: Average inclination angle of R_{uu} contours as a function of y/δ.

both Lx_{uu}/δ and Ly_{uu}/δ grow with y/δ near the wall, but they decrease rapidly as the edge of the boundary layer is approached. This behaviour of the characteristics length scales is consistent with the notion that the building-blocks of the hairpin packets are born within the near-wall and logarithm layers where the mean shear is strongest (Christensen and Wu, 2005). The packets then grow and mature beyond the logarithm layer. The decrease in Ly_{uu}/δ as the wall is approached is an artefact of the merging of the contours with the wall. The reduction of the streamwise extent as the centreline of the channel is approached was also observed by Christensen and Wu (2005). Such a reduction is attributed to the breakdown of the vortex organization due to strong interactions of the packets with the flow on the opposing wall. Over the smooth wall, APG diminished Lx_{uu}/δ and Ly_{uu}/δ (Figures 4.27a and 4.27d) in agreement with the results of Krogstad and Skåre (1995). They observed that APG reduced Lx_{uu}/δ all the way to the wall. Krogstad and Skåre (1995) argued that when the flow is subjected to APG, the streamwise vortex stretching becomes less effective, resulting in reduction of Lx_{uu}/δ. Christensen and Wu (2005) observed a rise in the Lx_{uu}/δ with increasing Reynolds number and attributed it to an increase in the average number of vortices per packet with Reynolds number as well as an increase in the average streamwise spacing of consecutive vortices within a packet with Reynolds number. It is evident that the vortices observed in the instantaneous velocity field in the diverging section are less spaced compared to the parallel section over the smooth wall. This together with ineffective stretching of the vortices by APG is likely the cause of the lower values of Lx_{uu}/δ in the diverging section. Meanwhile, the maximum value for Lx_{uu}/δ and Ly_{uu}/δ in the diverging section of the smooth wall occurred at y = 0.30δ, which corresponds to the location of the outer peak in $-\overline{u^2}$. Since the larger value of Lx_{uu}/δ and Ly_{uu}/δ also means the presence of a long and wide low-momentum region, the result for Lx_{uu}/δ indeed confirmed that the low-momentum fluid plays a role in the formation of the hump in the $-\overline{u^2}$ as well as other stresses.

Roughness strongly influenced Lx_{uu}/δ and Ly_{uu}/δ (Figure 4.27). The smooth wall Lx_{uu}/δ and Ly_{uu}/δ are respectively, 55% and 46% larger than the length-scales obtained over the *d*-type ribs (Figures 4.27a and 4.27d), but they are almost similar to Lx_{uu}/δ and Ly_{uu}/δ over the intermediate type ribs (Figures 4.27b and 4.27e). Krogstad and Antonia (1994) also observed 50% reduction in the streamwise size of R_{uu} over rough wall in comparison to the smooth wall Lx_{uu}/δ. Volino *et al*. (2007), and Wu and Christensen (2007) observed that the Lx_{uu}/δ and Ly_{uu}/δ were independent of roughness. On the contrary, a dramatic increase in Lx_{uu}/δ and Ly_{uu}/δ over the *k*-type ribs relative to the smooth wall is observed in Figures 4.27c and 4.27d. In this case, both Lx_{uu}/δ and Ly_{uu}/δ

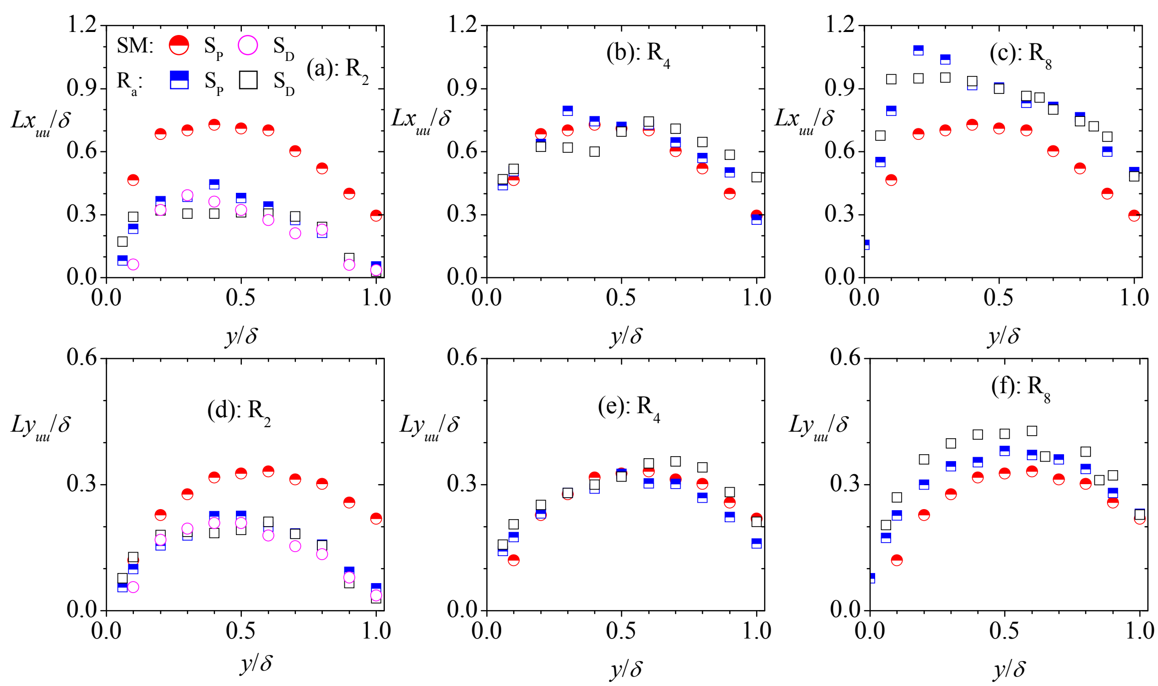

Figure 4.27: Average streamwise and wall-normal sizes of R_{uu} contours as a function of y/δ.

are 26% and 16% larger over the k-type rough wall. The larger distributions of Lx_{uu}/δ and Ly_{uu}/δ over k-type ribs are in agreement with the observation by Volino *et al*. (2009) who also observed that Lx_{uu}/δ and Ly_{uu}/δ are 42% and 39% larger over k-type ribs compared to smooth wall (and woven mesh rough wall). The implication is that the physical sizes of the hairpin packets are smaller over the d-type ribs but, they are larger over the k-type ribs relative to the smooth wall. On the contrary, the sizes of the packets are similar over the intermediate type rough wall and smooth wall.

Adverse pressure gradient did not significantly modify the physical size of the packets over the rough wall. In a region of $0.2\delta \leq y \leq 0.6\delta$ over the d-type ribs, and $0.2\delta < y < 0.5\delta$ over the intermediate type ribs APG somewhat diminished both Lx_{uu}/δ (Figure 4.27a-b). For $y \geq 0.6\delta$, over the intermediate type ribs however, Lx_{uu}/δ and Ly_{uu}/δ in the diverging sections were fairly augmented by APG. Over the k-type ribs, Lx_{uu}/δ is almost similar in the parallel and diverging sections, except for the spike in Lx_{uu}/δ at $0.2\delta \leq y \leq 0.3\delta$ in the parallel section (Figure 4.78c). On the other hand, APG combined with roughness to enhance Ly_{uu}/δ in the diverging section of the k-type ribs (Figure 4.27f).

The wall-normal auto-correlation, R_{vv} contours centred at $y_{ref} = 0.4\delta$ over the four surfaces in both the parallel and diverging sections are shown in Figure 4.28. In general, the R_{vv} contours are compact in both the streamwise and wall-normal directions in comparison with R_{uu}. This is likely due to the damping effects of the wall on v'. The R_{vv} contour was found to be even more compact near the wall than it is away from the wall. This implies that the wall-normal fluctuating velocity is localized and does not have an extended streamwise coherence across the boundary layer (Ganapathisubramani *et al*., 2005). Moreover, unlike R_{uu} contour, the R_{vv} contour is aligned to the y-axis which is

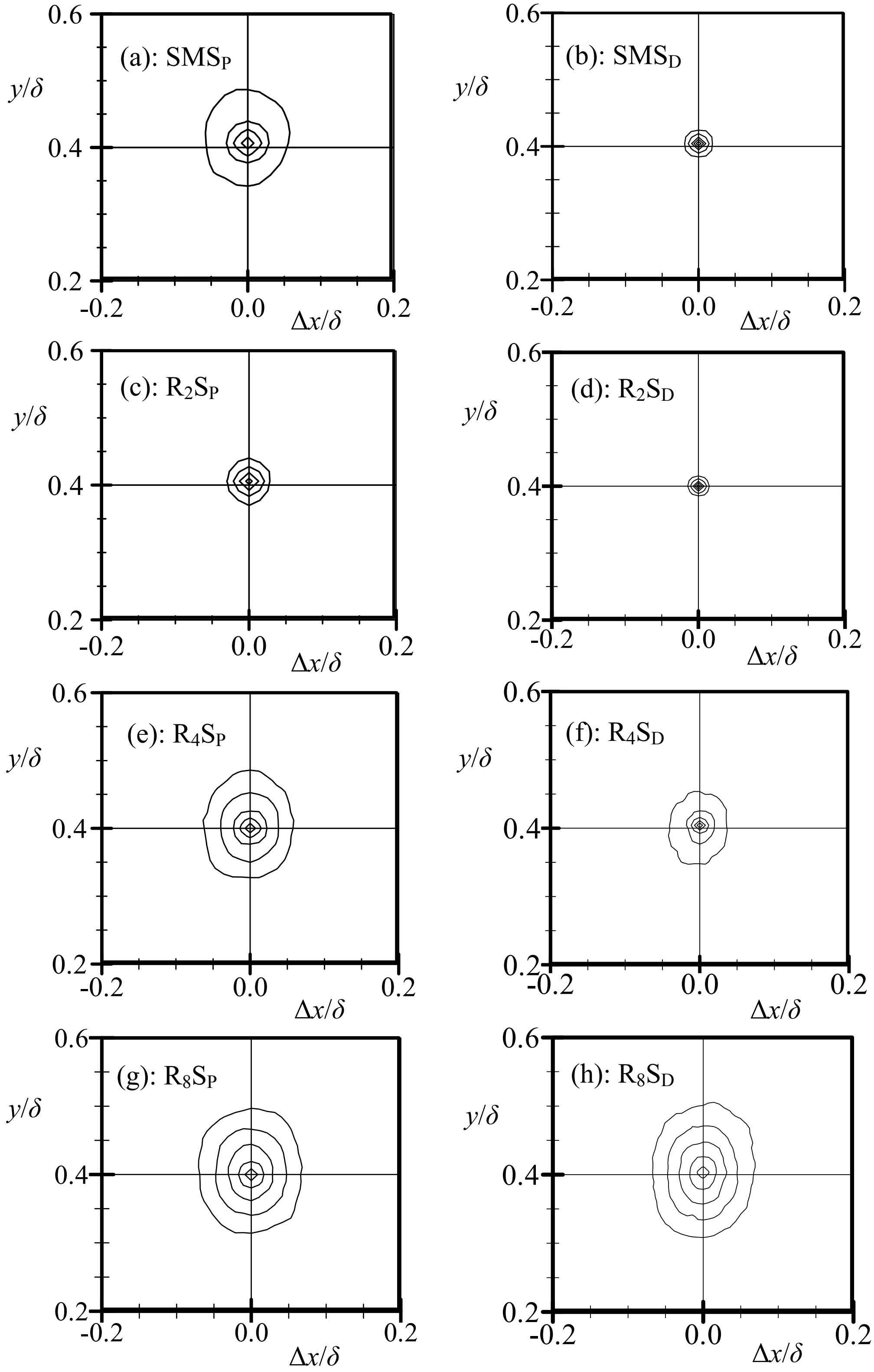

Figure 4.28: Contours of R_{vv} centered at $y_{ref} = 0.4\delta$, outermost contour level of $R_{uu} = 0.5$, contour spacing is 0.1.

consistent with some of the previous results (Volino *et al*., 2007; Volino *et al*., 2009). However, Krogstad and Skåre (1995) reported R_{vv} contour which is inclined slightly towards the streamwise direction. The one-dimensional profiles obtained from the streamwise and the wall-normal slices of R_{vv} contours centred at $y_{ref} = 0.4\delta$ (Figure 4.28) are shown in Figure 4.29. The figure revealed that the R_{vv} correlation in the diverging section of the smooth wall is diminished by APG relative to the correlation in the parallel section. The implication is that APG reduce the size of the domain over which the hairpin vortex exerts its influence.

Roughness affects the distributions of the one-dimensional profiles of R_{vv}. For the case of the *d*-type and intermediate type rough walls, roughness diminished the values of R_{vv} correlation (Figure 4.29a-b and Figure 4.29d-e). In contrast, the streamwise profile of R_{vv} over the *k*-type rough wall collapsed fairly well with the smooth wall data (Figure 4.29c). Meanwhile, the wall-normal profile of R_{vv} over the smooth wall tends to drop slightly relative to that of the *k*-type ribs for $0.28\delta \leq y < 0.4\delta$ and $0.4\delta < y \leq 0.52\delta$ (Figure 4.29f). Wu and Christensen (2005), Mejia-Alvarez and Christensen (2010) observed differences in the streamwise one-dimensional profiles of R_{vv} for y_{ref}/δ within the roughness sublayer, but reported collapse of R_{vv} as y_{ref}/δ increases (outside the roughness sublayer). Volino *et al*. (2009) observed a large variation in the streamwise and wall-normal one-dimensional profiles of R_{vv} over their mesh-wire despite the similarity reported in the R_{uu} profiles.

Figure 4.29a-b and Figure 4.29d-e revealed that APG produced a drop in the streamwise and wall-normal distributions of R_{vv} correlation in the diverging section of the *d*-type and intermediate type ribs compared to parallel section. Conversely, the

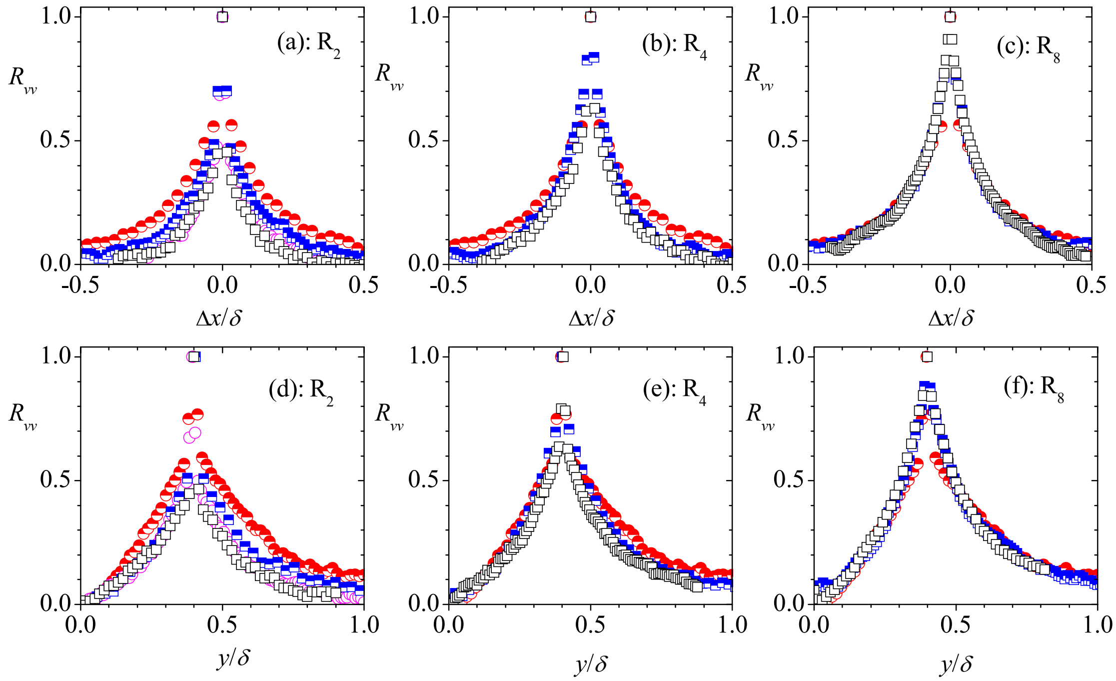

Figure 4.29: Streamwise and wall-normal one-dimensional profiles of R_{vv} at $y_{ref} = 0.4\delta$. Symbols are as in Figure 4.27.

distributions of R_{vv} correlation over the *k*-type ribs collapsed in the presence of APG (Figures 4.29c and 4.29f). The collapse may imply that roughness and APG produced opposing influence which only resulted in similar spatial size of the structures.

The streamwise (Lx_{vv}) and wall-normal (Ly_{vv}) length scales of R_{vv} are shown Figure 4.30. The Lx_{vv} is defined as the length of the streamwise distance between the most upstream and downstream points on the $R_{vv} = 0.5$ contour level following Volino *et al*. (2007) and Volino *et al*. (2009). The Ly_{vv} of R_{vv} was estimated as the wall-normal distance between the points closest and farthest from the wall on the $R_{vv} = 0.5$ contour level. It should be noted that both the streamwise and wall-normal sizes of R_{vv} contour are significantly less than those of R_{uu} correlation The disparity is due to the fact that R_{uu} correlation is directly associated with the convection velocity of each hairpin packet in addition to the restrain imposed by the wall on the v'. Over the smooth wall, APG reduced both Lx_{vv}/δ and Ly_{vv}/δ in comparison with the results in the parallel section (Figures 4.30a and 4.30d). This observation is also consistent with the results of Krogstad and Skåre (1995) who observed larger sizes of R_{vv} for a ZPG flow compared to an APG flow. Both the Lx_{vv}/δ and Ly_{vv} over the smooth wall are larger than the length scales over the *d*-type ribs (Figures 4.30a and 4.30d). Volino *et al*. (2007) reported 20% reduction in the sizes of R_{vv} contours over the rough wall compared to the smooth wall. Conversely, over the *k*-type ribs, roughness clearly magnified the Lx_{vv}/δ and Ly_{vv}/δ throughout the boundary layer (Figures 4.30c and 4.30f) and for $y \leq 0.40\delta$ over intermediate type ribs (Figures 4.30b and 4.30e) compared to the smooth wall. This is consistent with the results of Volino *et al*. (2009) who reported 35% and 40% increased in Lx_{vv}/δ and Ly_{vv}/δ over the *k*-type ribs. In Figure 4.30, except in the region of $0.6\delta \leq y \leq 0.8\delta$ over the *d*-type ribs and $y \geq 0.8\delta$ over intermediate type ribs, adverse pressure gradient diminishes Lx_{vv}/δ and

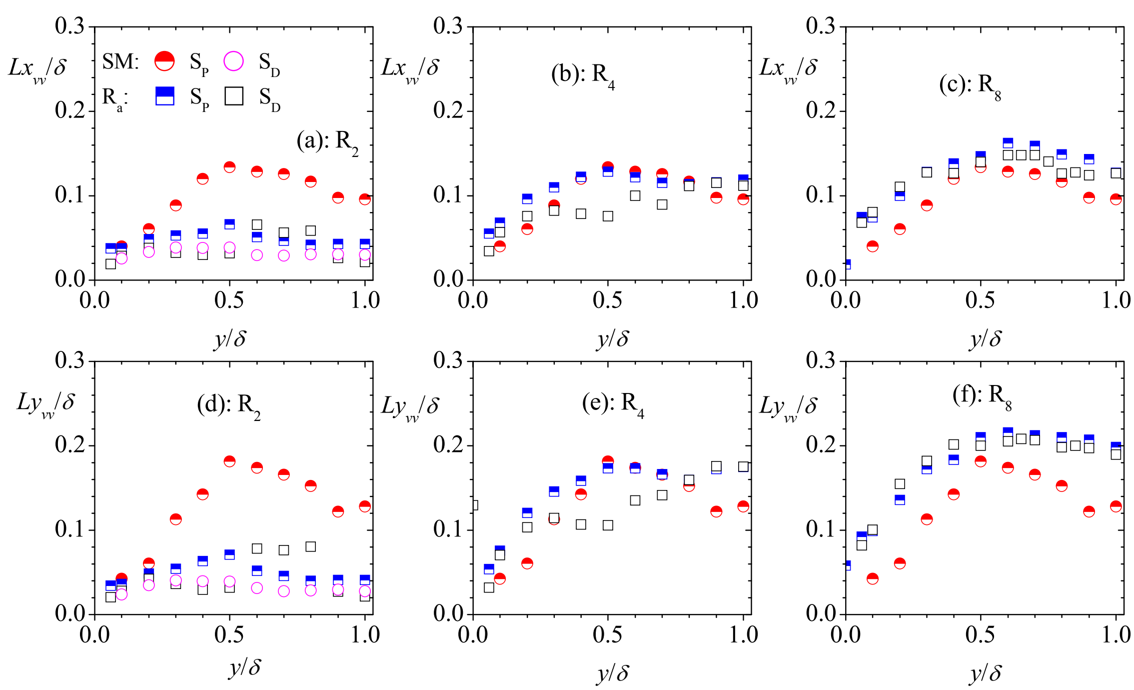

Figure 4.30: Average streamwise and wall-normal sizes of R_{vv} contours as a function of y/δ.

Ly_{vv}/δ over these rough walls. Conversely, the length scales of R_{vv} correlation over the *k*-type ribs are independent of pressure gradient. The weak dependence of Lx_{vv}/δ and Ly_{vv}/δ on APG over the rough walls in general is in contrast to the dramatic increase in $\overline{v^2}$ by APG.

The contours of the cross-correlation R_{uv} are reported in Figure 4.31. In Figure 4.31, the shape of the R_{uv} contours are similar, irrespective of the boundary condition and pressure gradient. The R_{uv} contours are tilted backward to the flow direction. Variation in the spatial extents of R_{uv} contours due to roughness and APG can be discerned. In the parallel section, the streamwise and the wall-normal sizes of R_{uv} over smooth wall are larger than those over *d*-type and intermediate type ribs. On the other hand, the streamwise and wall-normal extents of R_{uv} over the *k*-type ribs are larger compared to those over smooth wall. However, in the diverging section the size of the turbulence structure embodied in R_{uv} shows consistent increase with roughness. Irrespective of the boundary condition, APG diminished the spatial extents of R_{uv} contours.

The streamwise and the wall-normal one-dimensional profiles of the cross-correlation, R_{uv} obtained by taking horizontal and vertical slices passing through the self-correlation peak of R_{uv} contours in Figure 4.31 are shown in Figure 4.32. As with the R_{uu} and R_{vv} correlations, APG reduced the values of R_{uv} correlation over the smooth wall (Figures 4.32a and 4.32d).

Over the *d*-type ribs, roughness reduces the values of R_{uv} correlation (Figures 4.32a and 4.32d). Conversely, roughness augments R_{uv} correlation over the *k*-type rough wall (Figures 4.32c and 4.32f), hence, the increased size of R_{uv} contour compared to the smooth wall. For the intermediate type rough wall, roughness enhanced R_{uv} correlation

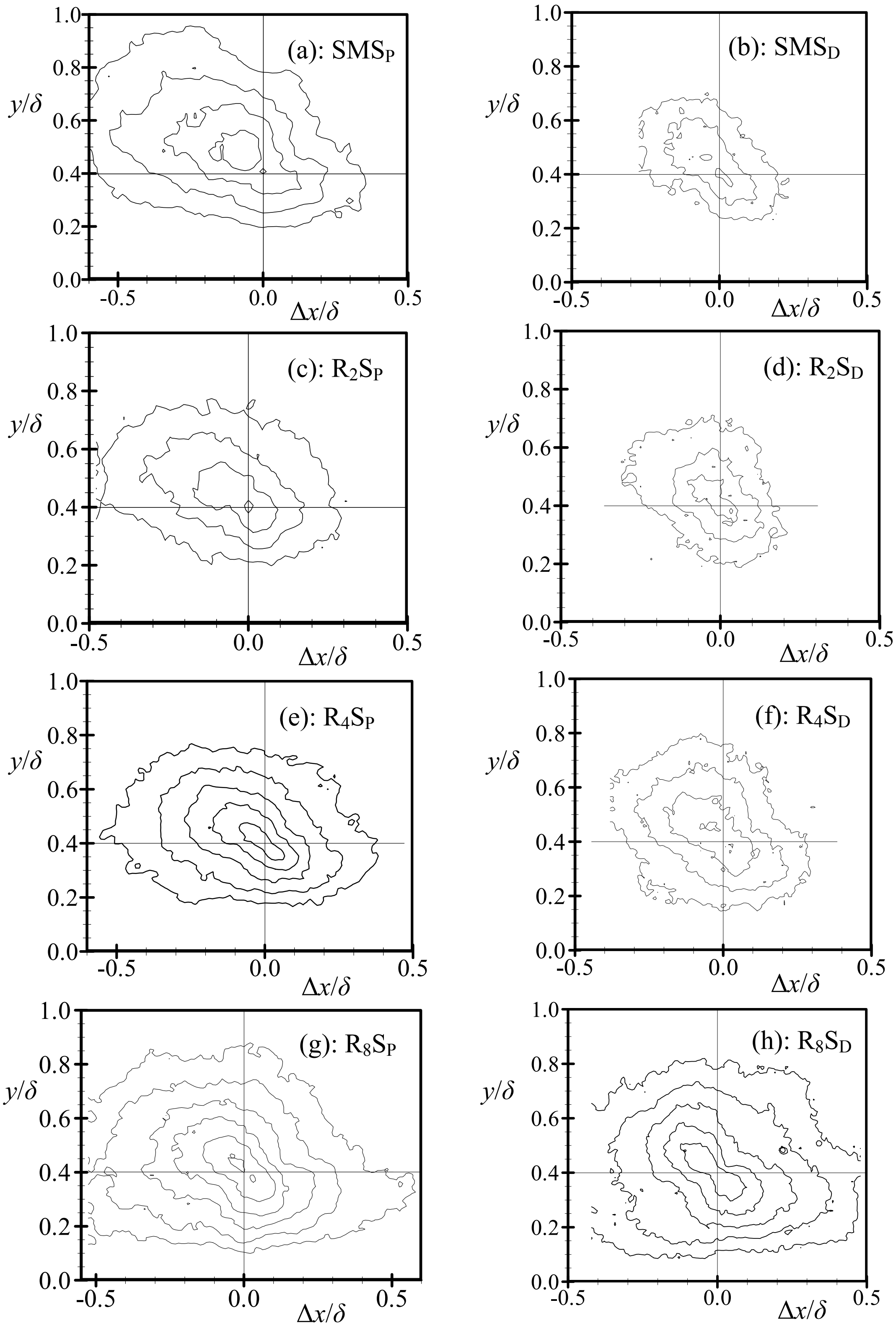

Figure 4.31: Contours of R_{uv} centered at $y_{ref} = 0.40\delta$, outermost contour level of $R_{uv} = -0.15$, contour spacing is 0.05.

only at small $\Delta x/\delta$ and at y/δ-distance close to the self-correlation peak (Figures 4.32b and 4.32e). However, R_{uv} correlation over the intermediate type rough wall decays very rapidly so that at larger $\Delta x/\delta$ and y/δ-distance further away from the self-correlation peak, R_{uv} correlation over the smooth wall is amplified. As a result, the spatial extents of R_{uv} contour are larger over the smooth wall compared to the intermediate type rough wall. This implies that although *d*-type and intermediate type ribs reduced the physical spatial size of the structure based on the cross-correlation, the *k*-type ribs enlarged the physical size of the structure relative to the smooth wall. The combined roughness and APG generally diminished the values of R_{uv} correlation.

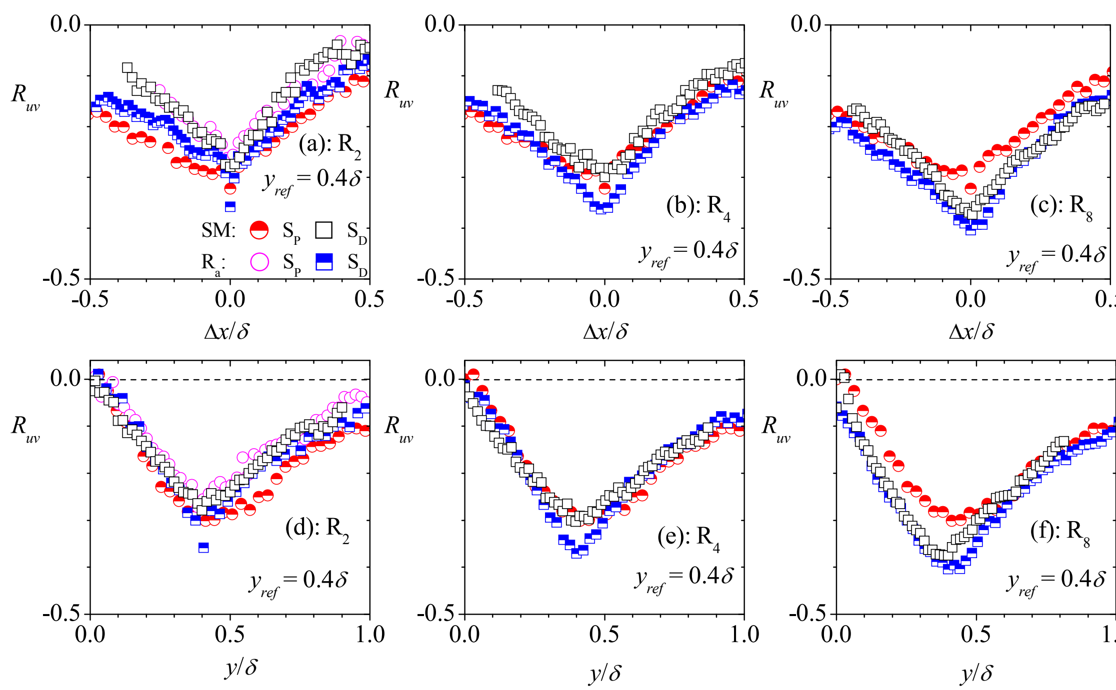

Figure 4.32: Streamwise and wall-normal one-dimensional profiles of R_{uv} at $y_{ref} = 0.4\delta$.

4.2.2.4 Linear Stochastic Estimation (LSE)

The LSE average velocity fields presented here are those computed based on the negative component of the swirling strength λ_{ci}, i.e., conditioning the event on the prograde, although other conditioning events such as retrograde, swirl and $u'v' < 0$ were also explored. Figure 4.33-4.35 shows the average velocity field results for the LSE at y_{ref} = 0.4 over the smooth and rough walls in both the parallel and diverging sections. The length of each vector was normalized by its magnitude thereby forcing it to unity. In doing so, the arrows of the vectors associated with each average velocity field are all the same length and indicate only the average flow direction. This permits clear visualization of weaker motions away from the event location since stochastically estimated velocity field is strongest around the event location. The strength of this motion tends to obscure the weaker motions away from the event location (Christensen and Adrian, 2001).

Over each surface, irrespective of the pressure gradient, a strong prograde swirling motion in the clockwise direction is induced at the event location. The centre of the swirling motion is indicated by a solid circle in each figure. The swirling motion formed closed streamlines which is consistent with the head of the vortex core. This is more obvious in the close-up view obtained in the vicinity of the event location which also featured the conditionally averaged streamwise velocity associated with the LSE at the background. This swirling motion observed at the event location is also consistent with those observed by Christensen and Adrian (2001), Hambleton *et al*. (2006), Volino *et al*. (2009), and Lee and Sung (2009). Just at the upstream and below the vortex core at the event location, low-speed fluid is lifted upward, corresponding to *Q*2 event. It is also evident that the high-speed fluid just at the back of the vortex core is pumped downward resulting in a *Q*4 event. As shown in the close-up view, the conditionally averaged streamwise velocity exhibits strong positive (red colour) and negative (blue colour) values near the conditioning event location. The magnitude of the conditionally averaged streamwise velocity as well as the conditionally averaged wall-normal velocity (not shown) is lower over *k*-type ribs compared to smooth wall and intermediate type ribs in the parallel section. For the smooth wall and intermediate type ribs, the magnitude of the average velocities is less influenced by APG, but over the *k*-type ribs, APG enhanced the

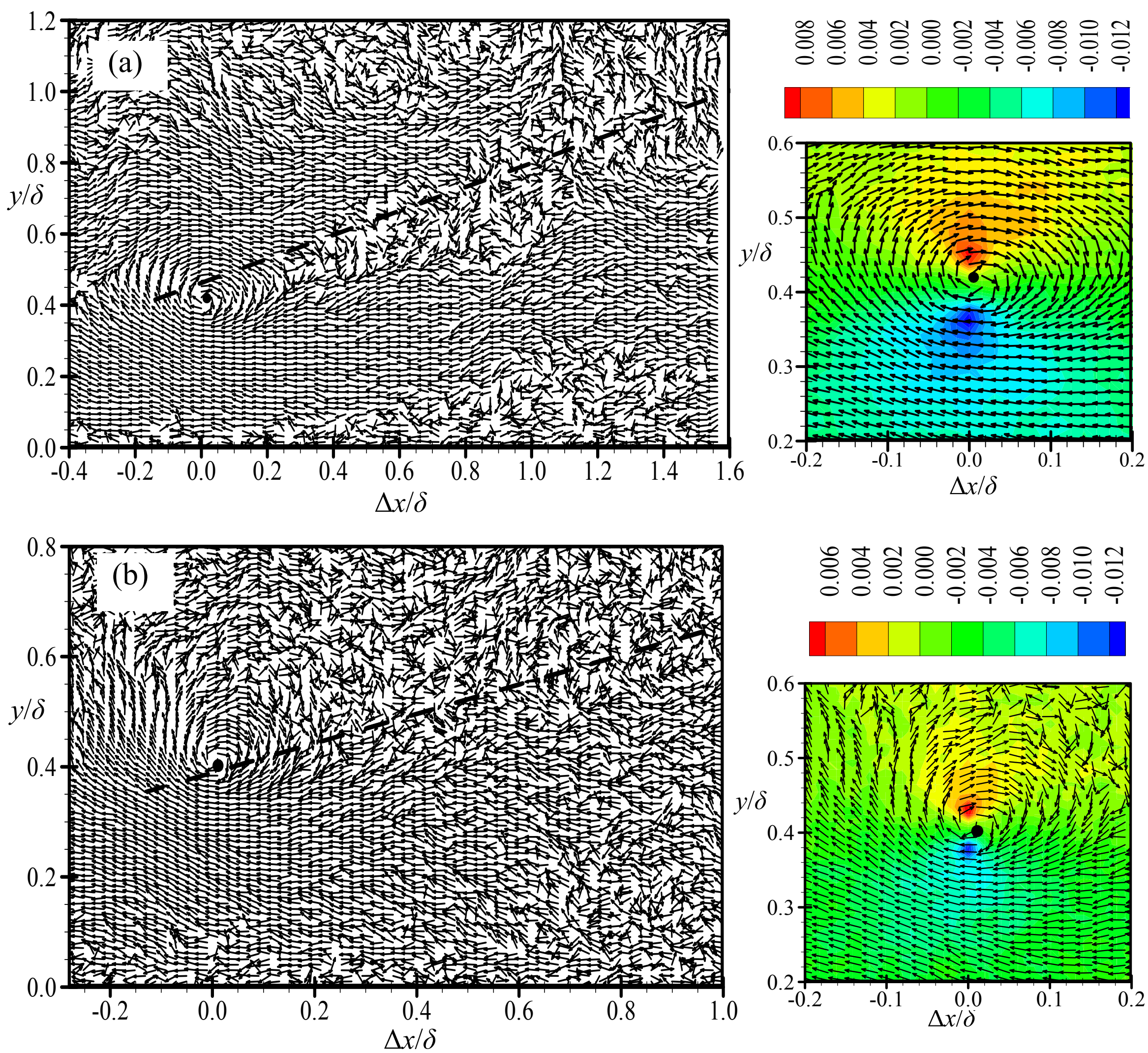

Figure 4.33: Linear stochastic estimation conditioned on prograde swirl event at $y/\delta = 0.4$ over smooth wall: (a) parallel section and (b) diverging section. Shown at the side is the corresponding close-up view with the contour of conditionally averaged streamwise velocity at the background.

average velocities. Lee *et al*. (2010) reported larger values in APG flow compared to ZPG flow over a smooth wall. Over each surface, the lifting of the low-speed fluid occurred at where the conditionally averaged streamwise velocity is negative, consistent with the observation of Lee *et al*. (2010). Conversely, the downward motions corresponding to the transport of high-speed fluid towards the wall occurred at the location where the conditionally averaged streamwise velocity is positive. These occurrences are $Q2$ and $Q4$ events that are associated with vortices or hairpin packet.

In fact, the prograde swirling motion formed a crease similar to those observed by Christensen and Adrian (2001), Hambleton *et al*. (2006), Volino *et al*. (2009), and Lee and Sung (2009). The crease propagates toward the downstream and upstream of the event location. However, the manner of the propagation of the vortical motions away from the event location depends on the surface condition and pressure gradient. For example, the crease is inclined at an angle that varies with roughness and APG. The estimated average inclination angles of the crease are 10.6°, 16.1, 19.7° and 17.3°, respectively, for the smooth wall, *d*-type, intermediate type and *k*-type ribs in the parallel section. In the diverging section, the crease is inclined at average inclination angles of 15.5°, 16.2, 12.7° and 15.5°, respectively, for the smooth wall, *d*-type, intermediate type and *k*-type ribs. These angles deviate about 2°-8° and 0°-2° from the average values estimated from R_{uu} contour in the parallel and diverging sections, respectively. The crease angles are also about 0°-4° and 2°-8° lower than the values estimated from the instantaneous Galilean decomposed vector fields in the parallel and diverging sections, respectively. Volino *et al*. (2009) also observed variation of 3° relative to the R_{uu} inclination angle. Lee and Sung (2009) found the crease inclination associated with APG flow to be 18.5° compared to 13° for the ZPG flow. It should be noted that the crease formed over the rough walls, especially *k*-type ribs (Figure 4.35) is very distinct compared to those observed over other surfaces. This is likely due to the presence of intense prograde swirling motion as revealed in the instantaneous fields (Figure 4.17).

Organized motion similar to that observed by Volino *et al*. (2009), and Christensen and Adrian (2001) can be seen above and below the crease over each surface. The vectors below the crease are generally pointing upstream and directed towards the crease. On the other hand, the vectors above the crease are generally pointing downstream towards the crease. Also evident is a region where the vector orientation

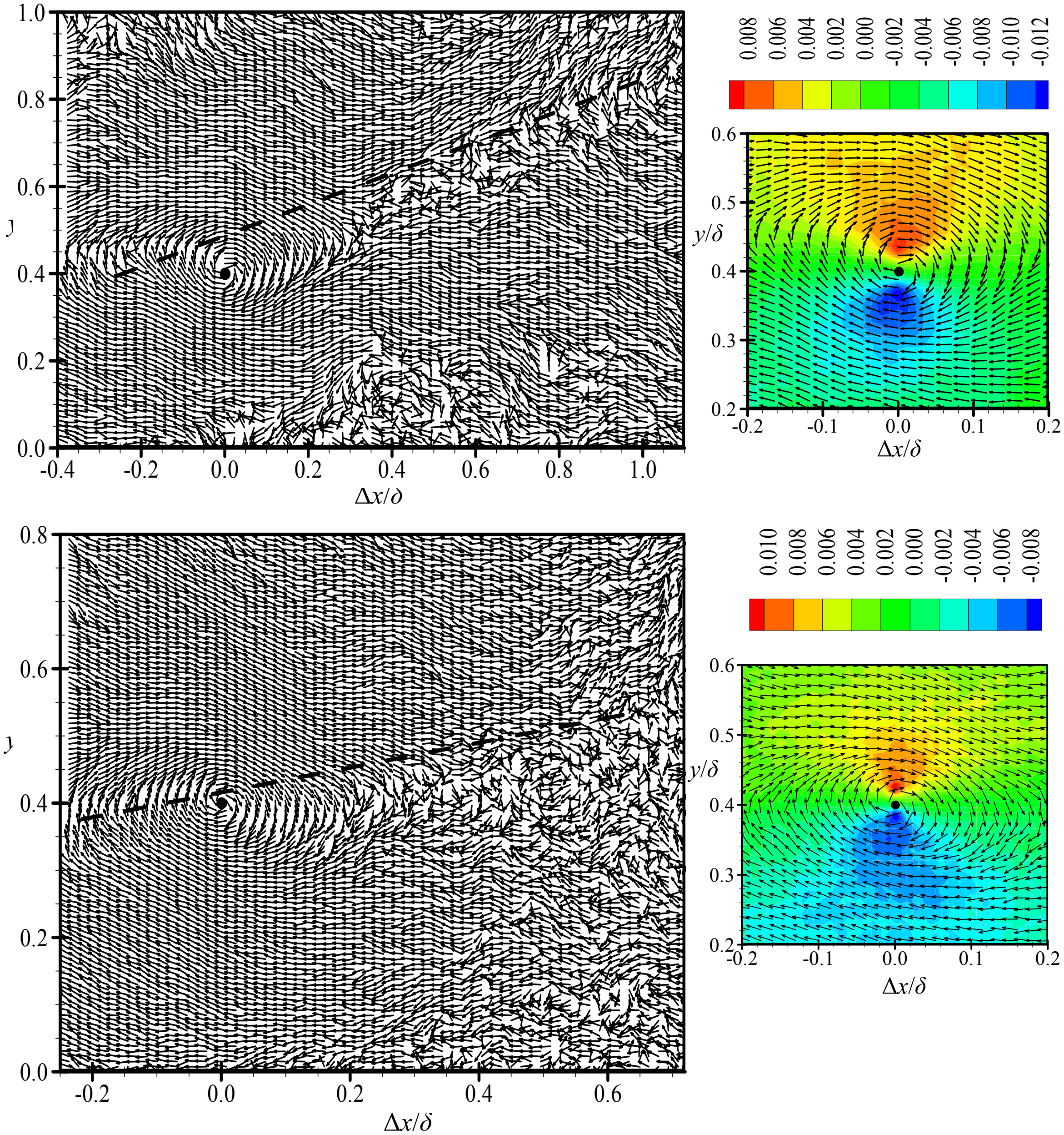

Figure 4.34: Linear stochastic estimation conditioned on prograde swirl events at y/δ = 0.4 over intermediate type rough wall: (a) parallel section and (b) diverging section. Shown at the side is the corresponding close-up view with the contour of conditionally averaged streamwise velocity at the background.

appears random, usually outside the region of the organized motion, consistent with the results of Volino *et al*. (2009). The extent of the region where the vectors appeared random varied with boundary condition and APG. It turns out that the random vectors are more associated with smooth wall (Figure 4.33) and APG flows at small p/k than in fully developed flow. As p/k increases, fewer random vectors are observed.

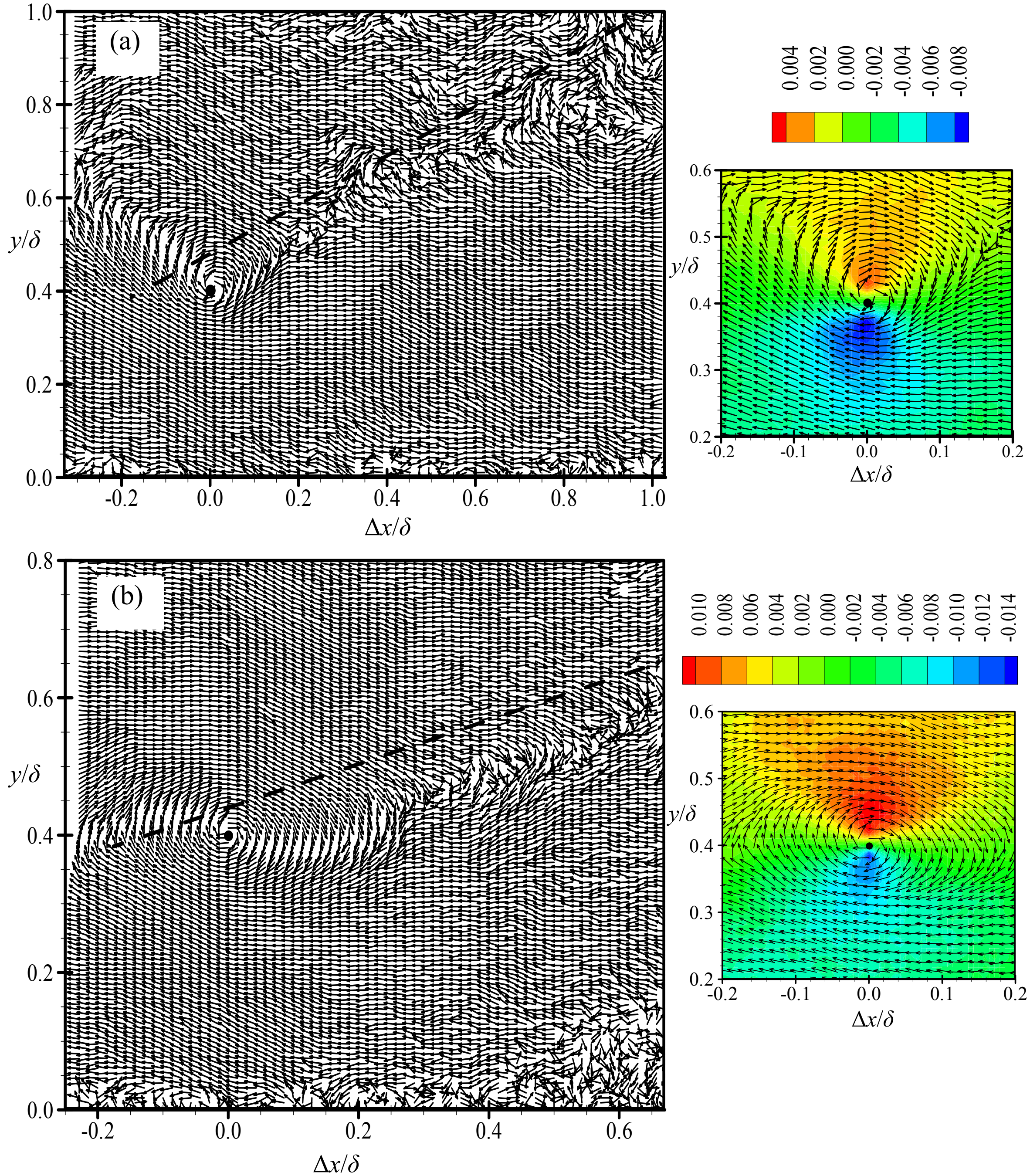

Figure 4.35: Linear stochastic estimation conditioned on prograde swirl events at y/δ = 0.4 over k-type rough wall: (a) parallel section and (b) diverging section. Shown at the side is the corresponding close-up view with the contour of conditionally averaged streamwise velocity at the background.

CHAPTER 5

EFFECTS OF RIB INCLINATION ON TURBULENCE STATISTICS AND STRUCTURES

The aim of this chapter is to evaluate the effects of rib inclination on the flow characteristics. The chapter is therefore divided into two main sections. Section 5.1 presents the variation of the flow characteristics across the span of the ribs inclined at 45° to the approach flow and Section 5.2 examines the effects of rib inclination angle on the flow statistics at the mid-span of the channel.

5.1 EXAMINATION OF TURBULENCE STATISTICS AND STRUCTURES ACROSS THE SPAN OF RIBS INCLINED AT 45°

In this section, both the mean and turbulence statistics obtained in the x-y plane at three spanwise-offsets or z-locations over each type of ribs are compared. The goal is to examine how the rib inclination modifies the flow characteristics at various spanwise locations relative to the flow properties at the mid-span of each type of the inclined ribs. It will be recalled that for 45° ribs, measurements were made at the mid-span (z = 0 mm), close to the leading edge of the ribs (z = +45 mm) and close to the trailing edge of the ribs (z = −45 mm) in both parallel and diverging sections. In this and subsequent section, the wall-normal axis is made zero at the crest of the ribs. This is necessary because the ribs attached to the lower wall blocked the camera view near the wall, thereby contaminating the data in the region $y < k$.

5.1.1 MEAN AND TURBULENCE STATISTICS

5.1.1.1 Boundary Layer Characteristics

The boundary layer characteristics over ribs inclined at 45° to the approach flow are presented in Table 5.1. In the upstream parallel section of the d-type and intermediate type rib, the maximum mean velocity, U_m close to the leading edge is higher than U_m close to the trailing edge but somewhat lower than the U_m at the mid-span. For example, in the upstream parallel section of the intermediate type ribs, the maximum mean velocity, U_m close to the leading edge ($R_4S_P\alpha_{45}P_L$) and trailing edge ($R_4S_P\alpha_{45}P_T$) of the ribs decreased by 4% and 24%, respectively compared to the U_m at the mid-span ($R_4S_P\alpha_{45}P_O$). However, in the upstream parallel section of the *k*-type ribs, the U_m close to the leading edge of the 45^o rib ($R_8S_P\alpha_{45}P_L$) is increased by 10% compared to the value of U_m at the mid-span ($R_8S_P\alpha_{45}P_O$) while the U_m close to the trailing edge ($R_8S_P\alpha_{45}P_T$) is reduced by 17% of the U_m value at the mid-span ($R_8S_P\alpha_{45}P_O$). These behaviours of the flow close to the leading and trailing edges, and at the mid-span of *k*-type ribs were also reported by Tachie and Shah (2008). The disparities in the U_m at these three *z*-locations over a particular type of ribs were caused by the secondary flow induced by the inclined

Table 5.1: Boundary layer characteristics over ribs at 45° to approach flow

Test	p/k	U_m m/s	δ mm	δ^* mm	θ mm	H	k/δ	K $\times 10^{-7}$	β	Re_θ	Re_τ
$R_2S_P\alpha_{45}P_O$	2	0.398	25.7	4.8	3.0	1.59	0.117	0.88	−0.04	1200	630
$R_2S_P\alpha_{45}P_L$	2	0.395	24.0	4.2	2.7	1.35	0.125	4.37	−0.19	1050	580
$R_2S_P\alpha_{45}P_T$	2	0.369	29.3	6.1	3.9	1.56	0.102	8.68	−0.43	1450	730
$R_4S_P\alpha_{45}P_O$	4	0.402	28.2	5.9	3.8	1.56	0.106	1.79	−0.10	1530	750
$R_4S_P\alpha_{45}P_L$	4	0.384	29.7	4.6	3.0	1.29	0.101	3.19	−0.17	1150	660
$R_4S_P\alpha_{45}P_T$	4	0.306	18.9	3.2	2.1	1.58	0.159	6.52	−0.11	630	440
$R_8S_P\alpha_{45}P_O$	8	0.364	25.1	3.2	2.4	1.33	0.120	1.51	−0.05	880	530
$R_8S_P\alpha_{45}P_L$	8	0.402	23.6	4.0	2.2	1.26	0.127	4.45	−0.19	880	580
$R_8S_P\alpha_{45}P_T$	8	0.303	15.4	2.5	1.6	1.55	0.195	1.31	−0.02	490	350
$R_2S_D\alpha_{45}P_O$	2	0.338	45.4	12.3	7.1	1.73	0.066	−17.49	1.85	2410	960
$R_2S_D\alpha_{45}P_L$	2	0.362	40.0	9.7	5.7	1.62	0.075	−9.16	1.04	2080	810
$R_2S_D\alpha_{45}P_T$	2	0.282	49.5	17.3	8.6	2.00	0.061	−25.23	1.88	2430	1130
$R_4S_D\alpha_{45}P_O$	4	0.261	35.5	8.6	5.5	1.55	0.085	−24.45	1.08	1440	660
$R_4S_D\alpha_{45}P_L$	4	0.332	29.0	3.1	2.0	1.25	0.104	−9.99	0.40	670	490
$R_4S_D\alpha_{45}P_T$	4	0.209	30.5	9.2	5.1	1.82	0.098	−88.94	1.85	1070	620
$R_8S_D\alpha_{45}P_O$	8	0.289	13.9	2.8	1.7	1.62	0.216	−30.88	0.66	490	250
$R_8S_D\alpha_{45}P_L$	8	0.347	9.1	1.4	1.0	1.43	0.330	−19.53	0.31	340	180
$R_8S_D\alpha_{45}P_T$	8	0.257	15.8	2.7	1.8	1.46	0.190	−36.37	0.57	470	270

ribs. According to Bonhoff *et al*. (2004), ribs inclined at 45° to the approach flow produce three-dimensional secondary motion where the fluid is driven towards the trailing edge close to one sidewall of the channel and returns towards the leading edge close to the opposite sidewall of the channel. It was argued that the enhancement of heat transfer performance by the inclined ribs is caused by this secondary motion. As the flow evolves in the diverging section of the *d*-type, intermediate type and *k*-type ribs, the U_m close to the leading edge of these three ribs is higher than the U_m at the mid-span whereas the U_m close to the trailing edge is lower than the U_m at the mid-span. For example, in the diverging section of the intermediate type rough wall, the U_m close to the leading edge of the 45° rib ($R_4S_D\alpha_{45}P_L$) is 23% larger than the U_m at the mid-span ($R_4S_D\alpha_{45}P_O$) while the U_m close to the trailing edge ($R_4S_D\alpha_{45}P_T$) is 23% lower than the U_m at the mid-span ($R_4S_D\alpha_{45}P_O$). In this case, the fluid close to the trailing edge tends to experience a larger deceleration than at the mid-span and close to the leading edge of the ribs. Therefore, in the diverging section the least deceleration is encounter by the fluid close to the leading edge of the ribs.

The boundary layer thickness, displacement thickness, momentum thickness and the shape factor also vary across the span of the channel for each rib type. For example, for $R_2S_P\alpha_{45}$, $R_2S_D\alpha_{45}$ and $R_8S_D\alpha_{45}$, δ, δ^*, θ and H are least close to the leading edge of the ribs, but they attain maximum close to the trailing edge of the ribs. The distributions of δ^*, θ and H in the parallel section of the *k*-type ribs ($R_8S_P\alpha_{45}$) is consistent with those of Tachie and Shah (2008). They observed maximum values for δ^* and θ, but minimum value for H close to the leading edge of the ribs. The minimum values for δ^* and θ, and the maximum value for H were observed close to the trailing edge of the ribs. The pressure gradient parameter, K or the Clauser pressure gradient parameter, β is not similar across the span of the channel over a particular rib in either parallel section or diverging section. The values of K indeed, indicate that the deceleration of the flow in the diverging section of each type of ribs is stronger close to the trailing edge and least close to the leading edge. Since the flow over inclined ribs is driven towards the trailing edge and later returned to the leading edge of the ribs, the returning fluid is weakened by the three-dimensional secondary motion at the leading edge, hence the lower value for K. In the parallel section, however, K is magnified closed to the trailing edge, but is least at the mid-span for the d-type and intermediate type ribs. For $R_8S_P\alpha_{45}$, the value of K is however largest close to the leading edge and is least close to the trailing edge. The variation of Reynolds numbers (Re_θ and Re_τ) across the channel for a particular type of rib are consistent with the variations of the length and velocity scales used in their computation.

5.1.1.2 Mean Velocity Profiles in Outer Coordinates

Figure 5.1 reports the mean velocity scaled with U_m in the parallel and diverging sections over the d-type, intermediate type and k-type ribs. The plots are used to highlight the variation of the mean flow across the span of the inclined ribs. As noted earlier, as the fluid is driven towards the trailing edge and returned towards the leading edge, the magnitude of U_m close to the edges is enhanced or reduced relative to the value of U_m at mid-span (except for R_2S_P and R_4S_P). In both the parallel and diverging sections of the d-type and intermediate type ribs, the U/U_m profiles close to the leading edge are more uniform compared to the profiles at mid-span and close to the trailing edge. Except for R_4S_P where the U/U_m profile at the mid-span is least uniform, the U/U_m profiles close to

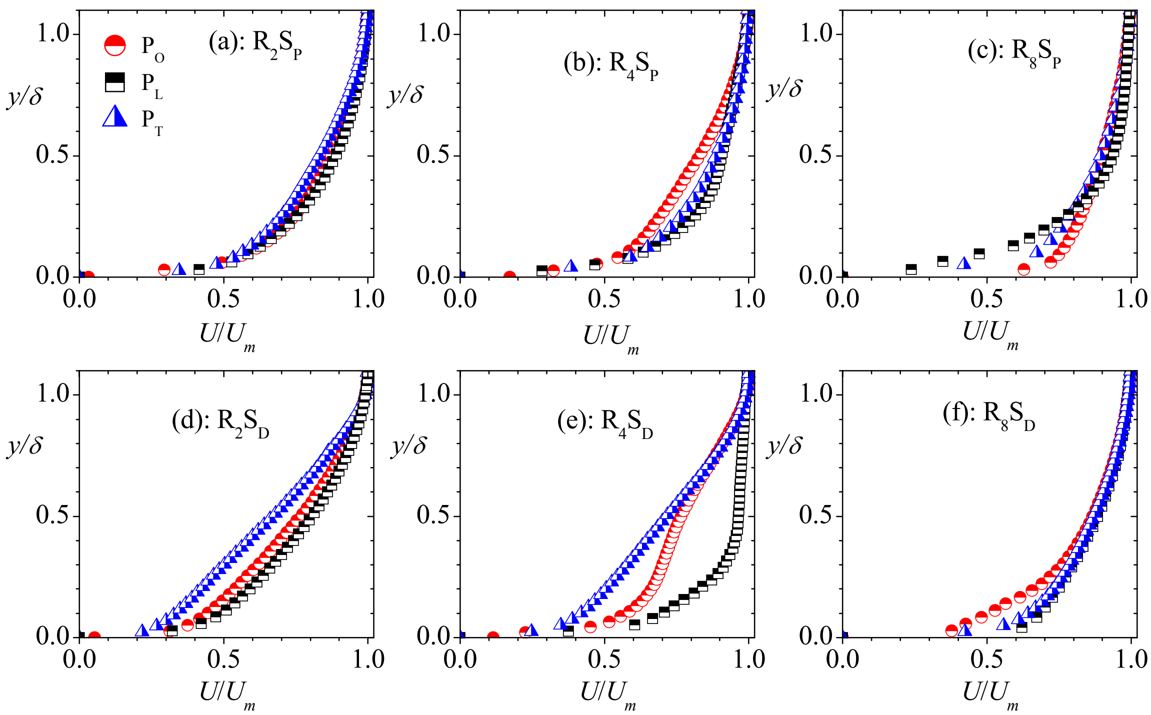

Figure 5.1: The distributions of the streamwise mean velocity profiles in outer coordinates over ribs at 45° to approach flow: (a)-(c), parallel section and (d)-(f), diverging section.

the trailing edge of the R_2S_P, R_2S_D and R_4S_D are the least uniform among the profiles obtained in the three measurement locations over these ribs. This may be due to additional resistance and/or deceleration encountered by mean flow close to the trailing edge of R_2S_P, R_2S_D and R_4S_D as the flow is driven towards the trailing edge by the secondary motions. The difference in these profiles is more dramatic in the diverging section of the intermediate type ribs. Meanwhile, in the diverging section of the *d*-type (Figure 5.1d) and intermediate type (Figure 5.1e) ribs, the less uniformity of the profiles close to the trailing edge is consistent with the larger negative K values (Table 5.1) observed close to the trailing edge. In the parallel section of the *k*-type ribs, there is a remarkable reduction in U/U_m close to the leading edge of the ribs for $y/\delta < 0.4$ compared to the profiles close to the trailing edge and at the mid-span. Beyond $y/\delta = 0.4$, the profile close to the leading edge becomes more uniform. Figure 5.1f demonstrates that the U/U_m profiles close to the leading edge and trailing edge of the ribs are identical throughout the boundary layer. However, the higher resistance encountered by the mean flow at the mid-span diminished the values of U/U_m for $y/\delta < 0.4$ compared to the data close to the leading edge and trailing edge of the ribs. Figure 5.1, therefore, demonstrates that the mean flow over the ribs at 45° to the approach flow is highly three-dimensional, and the variation in the profiles across the span of each type of ribs is due to the secondary motions induced by inclined ribs. The mean profiles indicate that the strength of the secondary motions is more intense in the diverging section of the intermediate type ribs. The secondary motion is apparently weaker in the diverging section of the *k*-type ribs.

5.1.1.3 Mean Velocity Profiles in the Inner Coordinates and Drag Characteristics

Figure 5.2 shows the mean velocity profiles plotted in the semi-logarithm formats. Although the figure demonstrates the existence of logarithm region, the size of the logarithm region varies across the span of the channel for each type of rib. Moreover, the profiles are shifted relative to each other, indicating that roughness effects on the flow are not identical across the ribs. Note that the U^+-profile close to the leading edge of the intermediate type ribs in the diverging section almost coincides with Eq. 1.12 (Figure 5.2e), a behaviour known for smooth wall profile. The wake parameter is also not similar in the three measurement locations for each type of rib in either the parallel or diverging section. For example, in the parallel section of the intermediate type ribs, the Π values at the mid-span and close to the leading edge are positive, but the Π value close to the trailing edge is negative (Table 5.2).

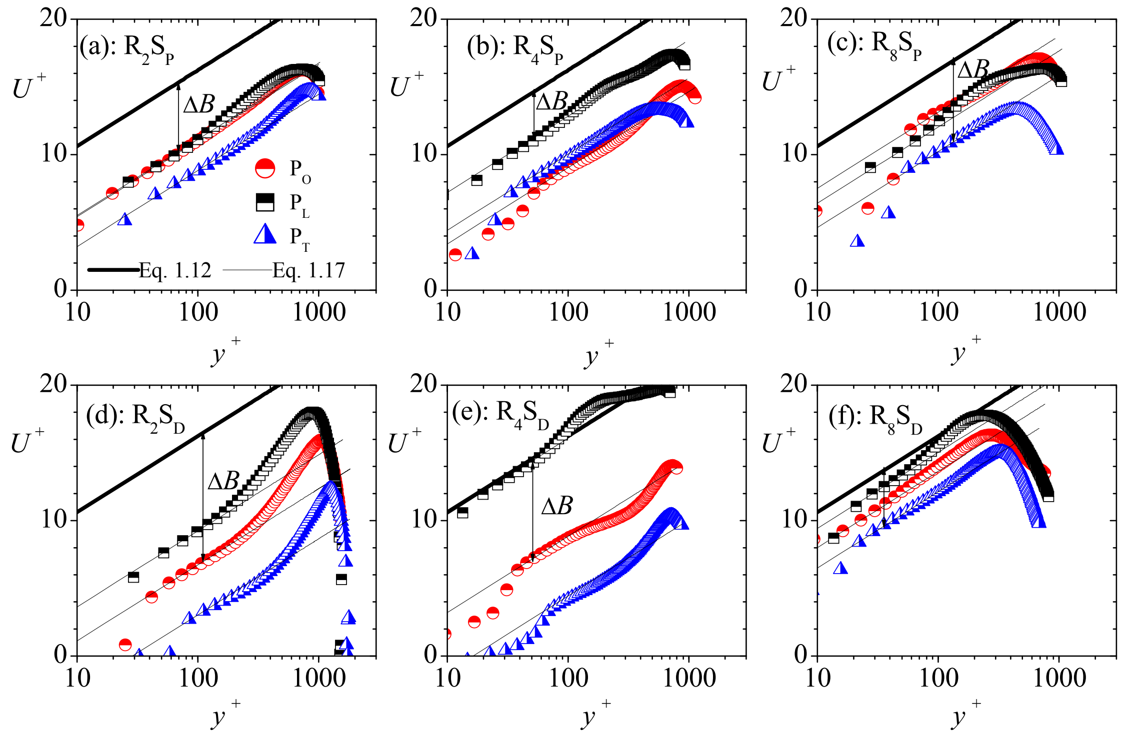

Figure 5.2: The distributions of the streamwise mean velocity profiles in inner coordinates over ribs at 45° to approach flow: (a)-(c), parallel section and (d)-(f), diverging section.

The higher values of C_f close to the trailing edge of each type of ribs in both parallel and diverging sections, indeed indicate that the flow encountered higher level of resistance close to the trailing edge than at the mid-span and close to the leading edge (Table 5.2). Except at the mid-span of *k*-type ribs in the parallel section where C_f is least, the friction coefficient is generally lower close to the leading edge of the ribs. Earlier, Tachie and Shah (2008) observed that the resistance to the flow is higher at the mid-span and least close to the leading edge of the ribs. With the exception of the measurement at the mid-span of the intermediate type ribs in the parallel section where the roughness shift function attained maximum, Table 5.2 and Figure 5.2 demonstrate that the relative displacement of U^+-profiles over the ribs from the classical logarithm law (Eq. 1.12) is larger close to the trailing edge of the ribs. The corresponding values for the equivalent roughness Reynolds number are also higher close to the trailing edge of the ribs, except for R_4S_P where k_s^+ is higher at $R_4S_P\alpha_{45}P_O$. The results for k_s^+ demonstrate that $R_2S_P\alpha_{45}P_T$, $R_4S_P\alpha_{45}P_O$, $R_2S_D\alpha_{45}P_O$, $R_2S_D\alpha_{45}P_T$, $R_4S_D\alpha_{45}P_O$ and $R_4S_D\alpha_{45}P_T$ are in the fully rough regime ($k_s^+ > 70$) whereas the remaining measurements locations are in transitionally rough regime. The ratio k_s/k also changes across the width of the channel.

Table 5.2: Drag and wake characteristics over ribs at 45° to approach flow

Test	U_τ cm/s	U_τ/U_m	C_f	E	ΔB	k_s^+	k_s/k	ΔU^+_{max}	Π
$R_2S_P\alpha_{45}P_O$	2.45	0.0615	0.0076	10.20	5.20	35	0.5	0.90	0.185
$R_2S_P\alpha_{45}P_L$	2.42	0.0613	0.0075	10.10	5.11	34	0.5	1.08	0.221
$R_2S_P\alpha_{45}P_T$	2.50	0.0678	0.0092	8.10	7.45	89	1.2	0.94	0.193
$R_4S_P\alpha_{45}P_O$	2.67	0.0664	0.0088	8.30	7.25	82	1.0	1.17	0.245
$R_4S_P\alpha_{45}P_L$	2.21	0.0575	0.0066	11.65	3.46	17	0.3	0.70	0.144
$R_4S_P\alpha_{45}P_T$	2.30	0.0752	0.0113	8.90	6.32	56	0.8	−1.69	−0.346
$R_8S_P\alpha_{45}P_O$	2.13	0.0585	0.0068	12.10	3.00	14	0.2	−0.75	−0.154
$R_8S_P\alpha_{45}P_L$	2.46	0.0611	0.0075	11.30	4.22	24	0.3	1.07	0.219
$R_8S_P\alpha_{45}P_T$	2.27	0.0750	0.0112	9.40	6.01	49	0.7	−0.90	−0.185
$R_2S_D\alpha_{45}P_O$	2.12	0.0627	0.0079	5.60	9.55	211	3.3	3.71	0.761
$R_2S_D\alpha_{45}P_L$	2.01	0.0555	0.0062	7.90	7.03	75	1.2	3.65	0.748
$R_2S_D\alpha_{45}P_T$	2.28	0.0810	0.0131	2.10	13.25	961	14.0	3.32	0.681
$R_4S_D\alpha_{45}P_O$	1.86	0.0712	0.0101	7.36	7.49	91	1.6	0.60	0.123
$R_4S_D\alpha_{45}P_L$	1.68	0.0506	0.0051	14.20	0.42	5	0.1	1.59	0.326
$R_4S_D\alpha_{45}P_T$	2.02	0.0965	0.0186	3.00	12.08	595	9.8	1.46	0.299
$R_8S_D\alpha_{45}P_O$	1.77	0.0612	0.0075	12.15	2.56	12	0.2	0.56	0.115
$R_8S_D\alpha_{45}P_L$	1.95	0.0562	0.0063	13.65	1.21	7	0.1	1.06	0.217
$R_8S_D\alpha_{45}P_T$	1.71	0.0664	0.0088	10.50	4.11	23	0.4	0.38	−0.078

5.1.1.4 Reynolds Stresses

The Reynolds stresses in the outer coordinates are shown Figure 5.3-Figure 5.5. It was observed earlier in Figure 5.1 that the velocity profiles are more uniform close to the leading edge and less uniform close to the trailing edge of the ribs. This uniform mean velocity distribution coupled with weak shear rate ($\partial U/\partial y$) close to the leading edge of the ribs would diminish $-\overline{uv}\partial U/\partial y$ as the main turbulence production term and reduce the turbulence levels compared to the levels at the mid-span. Conversely, the stronger shear rate close to the trailing edge of the ribs would augment production of turbulence and increase turbulence levels. Figure 5.3-Figure 5.5**,** indeed demonstrates that the Reynolds stresses are enhanced close to the trailing edge of the ribs than at the mid-span and close to the leading edge of the ribs. The plateau formed in $\overline{u^2}$, $\overline{v^2}$ and $-\overline{uv}$ in the diverging section is more pronounced close to the trailing edge of the ribs. This may also provide support for the higher level of turbulence production close to the trailing edge of the ribs. In the diverging section of the intermediate type ribs, $\overline{u^2}$ close to the trailing edge rose to a maximum value away from the wall and tends to be independent of y/δ, but close to the leading edge $\overline{u^2}$ decays with y/δ. The corresponding $\overline{v^2}$ at mid-span and close

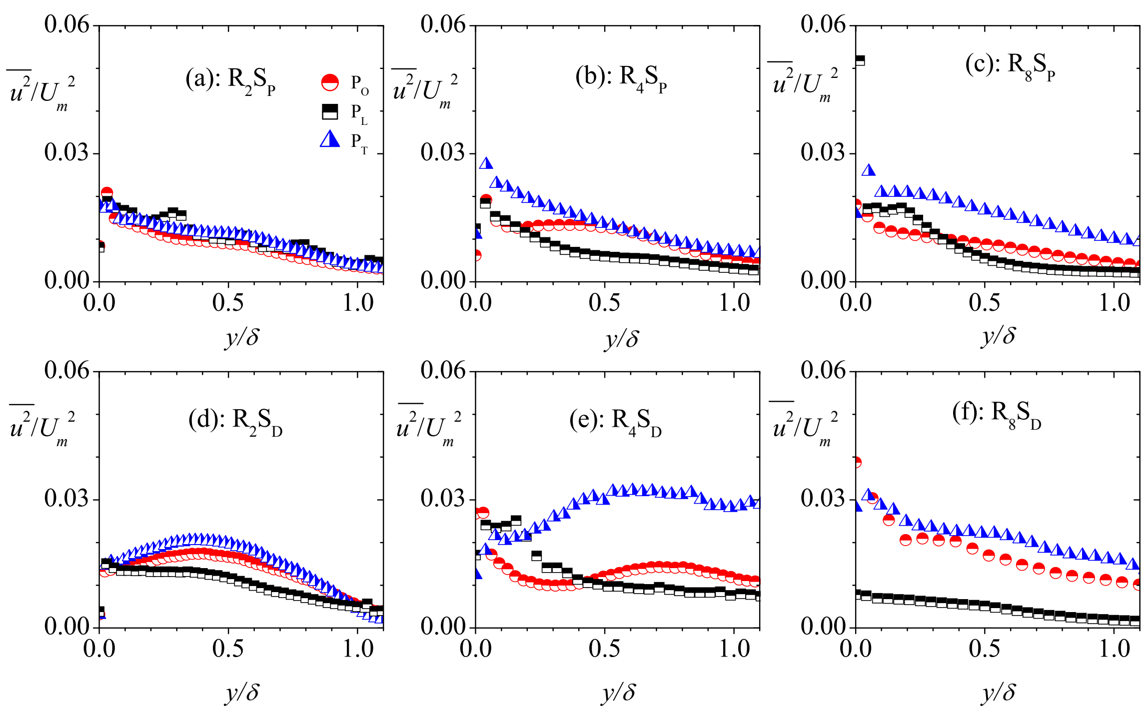

Figure 5.3: The distributions of the streamwise Reynolds normal stress scaled with U_m^2 over ribs at 45° to approach flow: (a)-(c), parallel section and (d)-(f), diverging section.

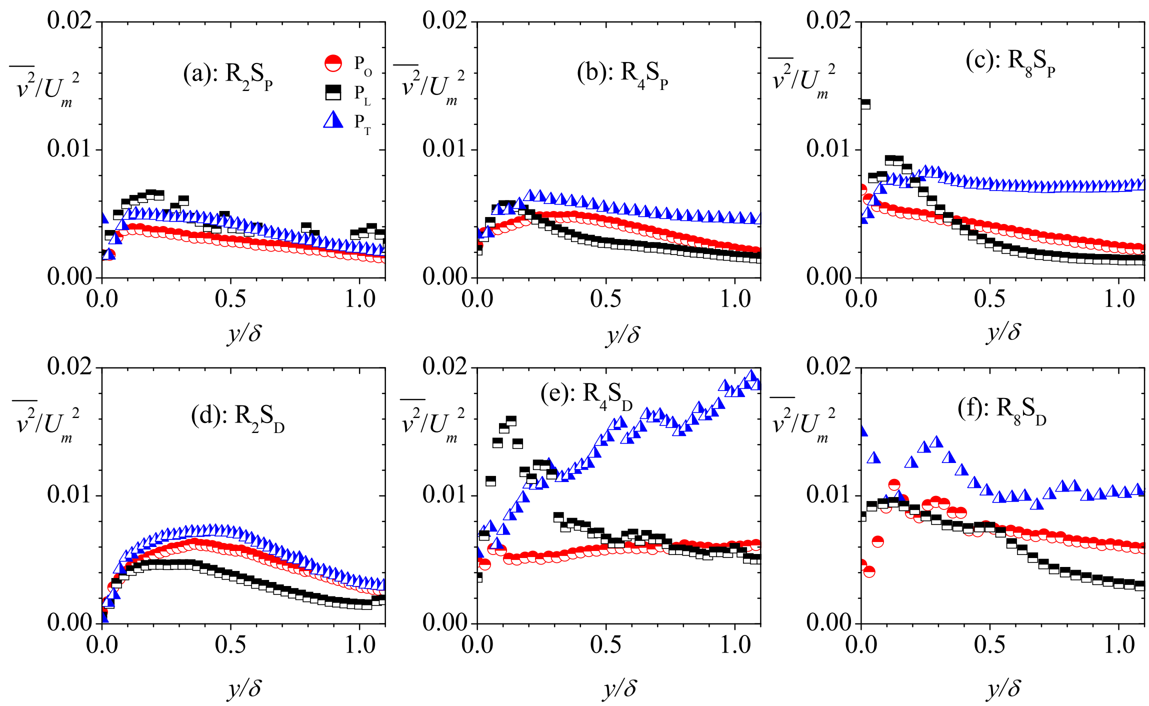

Figure 5.4: The distributions of the wall-normal Reynolds normal stress scaled with U_m^2 over ribs at 45° to approach flow: (a)-(c), parallel section (S_P) and (d)-(f) diverging section (S_D).

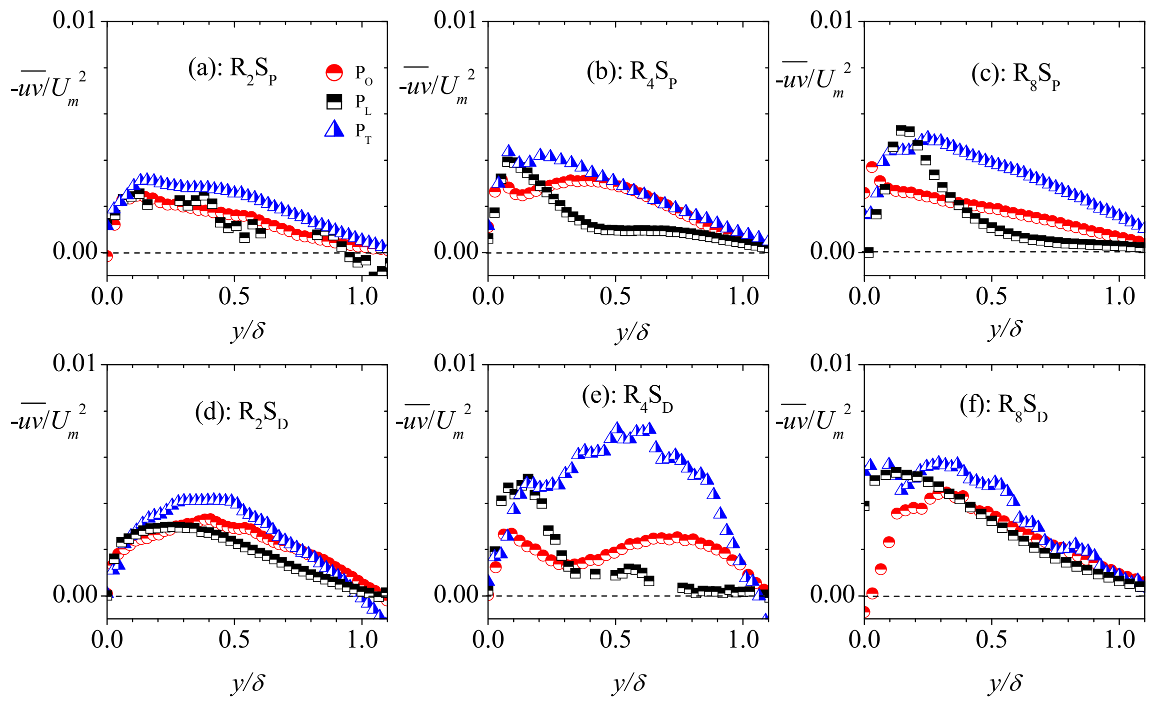

Figure 5.5: The distributions of the Reynolds shear stress scaled with U_m^2 over ribs at 45° to approach flow: (a)-(c), parallel section and (d)-(f), diverging section.

to the trailing edge grows with *y*, but close to the leading edge the profile decays rapidly with *y* (Figure 5.4e). Further, in the parallel section of the *k*-type ribs, $\overline{v^2}$ close to the trailing edge is relatively independent of *y*.

The distributions of the Reynolds stresses in inner coordinates are presented in Figure 5.6-Figure 5.8. Due to the dissimilar variation of wall shear stress per unit density (i.e., U_τ^2) across the span of each type of ribs with respect to the Reynolds stresses, the distributions of $\overline{u^{+2}}$, $\overline{v^{+2}}$ and $-\overline{u^+v^+}$ in Figure 5.6-Figure 5.8 are not consistent with those presented in Figure 5.3-Figure 5.5. For example, in the parallel section the increase in $\overline{u^{+2}}$ close to the leading edge of the *d*-type ribs is due to low wall shear stress relative to $\overline{u^2}$, while the data close to the leading edge of the *k*-type ribs decreased dramatically. In the diverging section of the *d*-type and intermediate type ribs, the effects of secondary

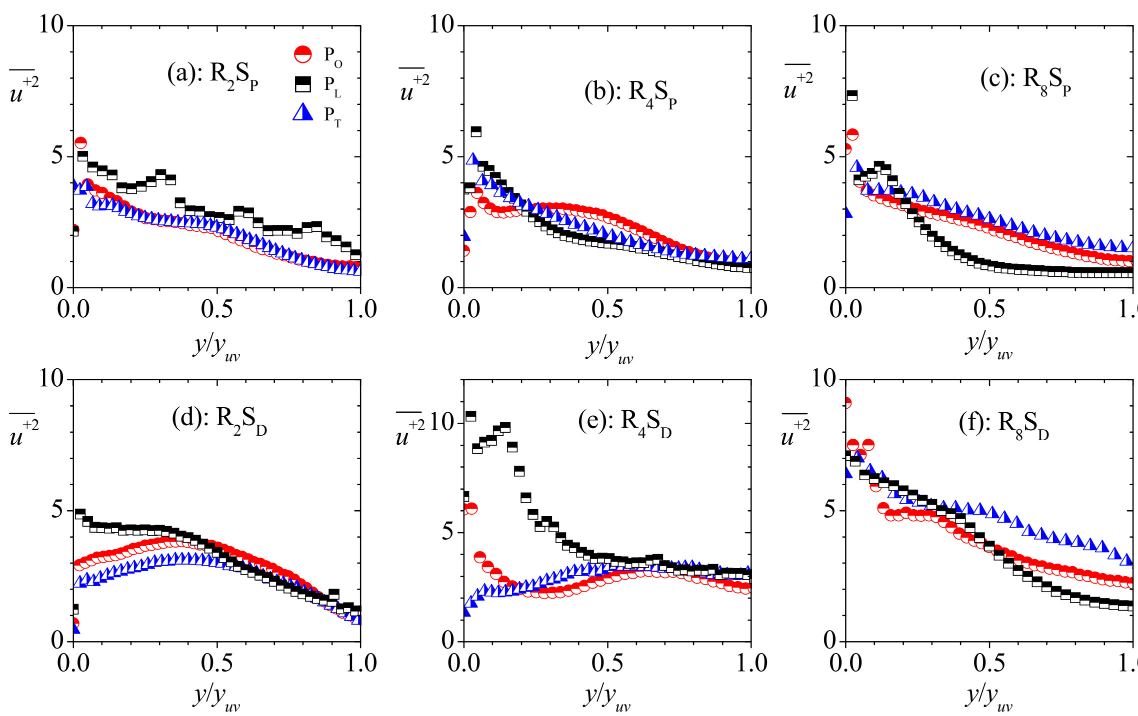

Figure 5.6: The distributions of the streamwise Reynolds normal stress scaled with U_τ^2 over ribs at 45° to approach flow: (a)-(c), parallel section and (d)-(f), diverging section.

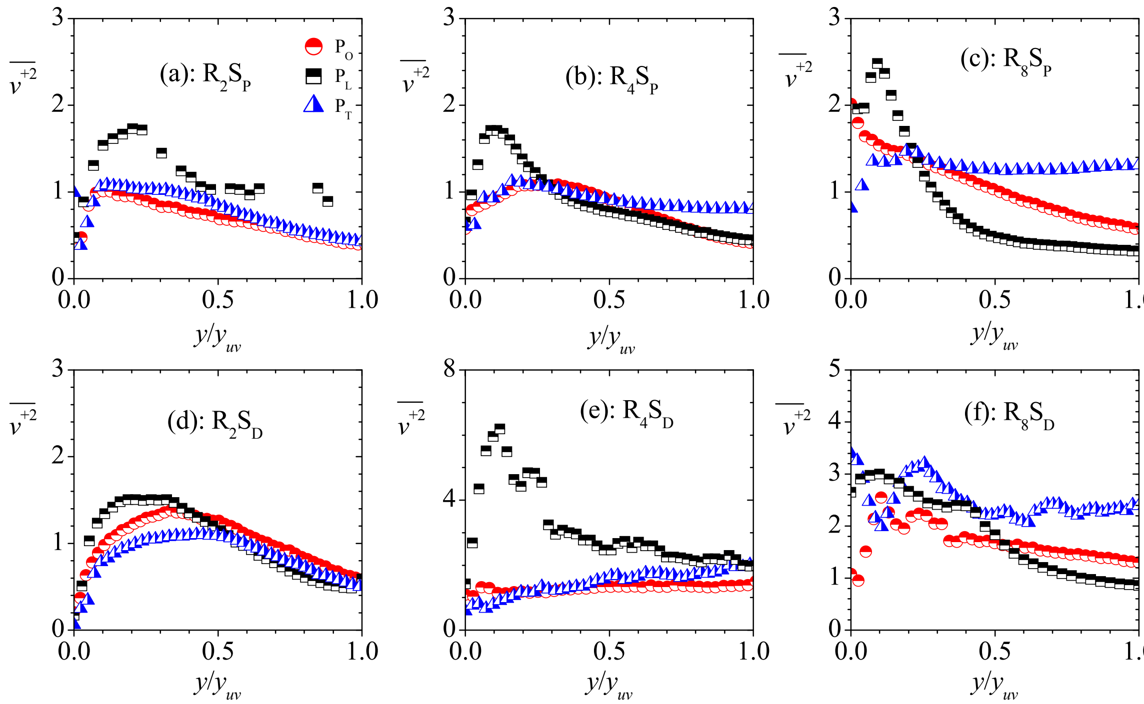

Figure 5.7: The distributions of the wall-normal Reynolds normal stress scaled with U_τ^2 over ribs at 45° to approach flow: (a)-(c), parallel section and (d)-(f), diverging section.

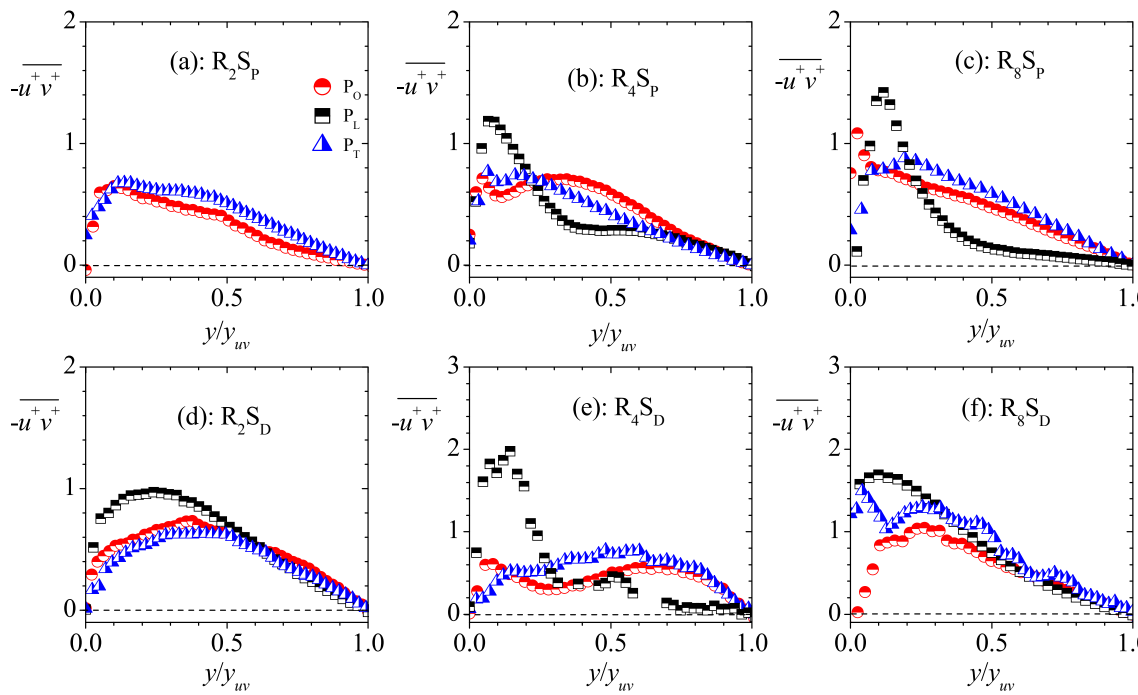

Figure 5.8: The distributions of the Reynolds shear stress scaled with U_τ^2 over ribs at 45° to approach flow: (a)-(c), parallel section and (d)-(f), diverging section.

motion on $\overline{u^{+2}}$ are dominant for $y < 0.6y_{uv}$. Conversely, the drop in $\overline{u^{+2}}$ close to the trailing edge of the d-type and intermediate type ribs for $y < 0.6y_{uv}$ is presumed to be an imprint of severe obstruction of the streamwise turbulence motion coupled with enhanced level of U_τ^2 relative to $\overline{u^2}$ close to the trailing edge of the ribs. The behaviour of $\overline{v^{+2}}$ and $-\overline{u^+v^+}$ across the span of these ribs are similar to $\overline{u^{+2}}$.

5.1.2 TURBULENCE STRUCTURE

5.1.2.1 Quadrant Decomposition

The quadrant decomposition is used to examine the effects of the secondary motions on the contributions by each quadrant to $-\overline{uv}$ across the span of the 45° ribs. The fractional contributions from each quadrant in the parallel section are shown in Figure 5.9 and Figure 5.10. The strong outward and inward interaction motions close to the leading edge

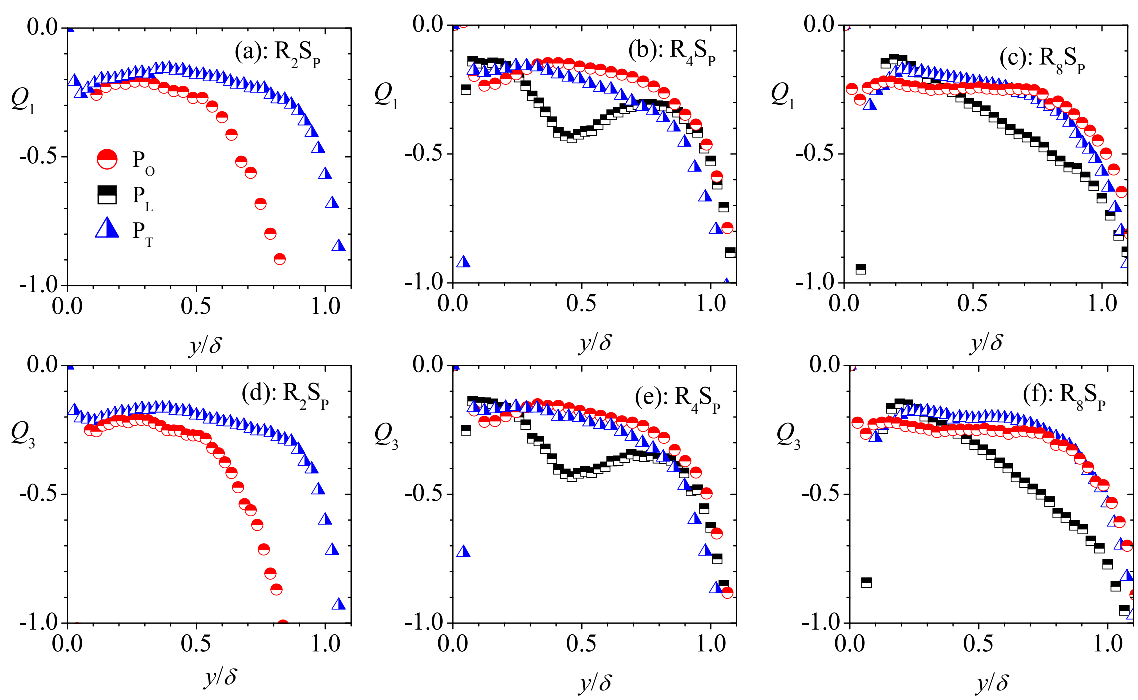

Figure 5.9: The distributions of the fractional contributions to $-\overline{uv}$ from first and third quadrants in the parallel section of ribs at 45° to approach flow for $H = 0$.

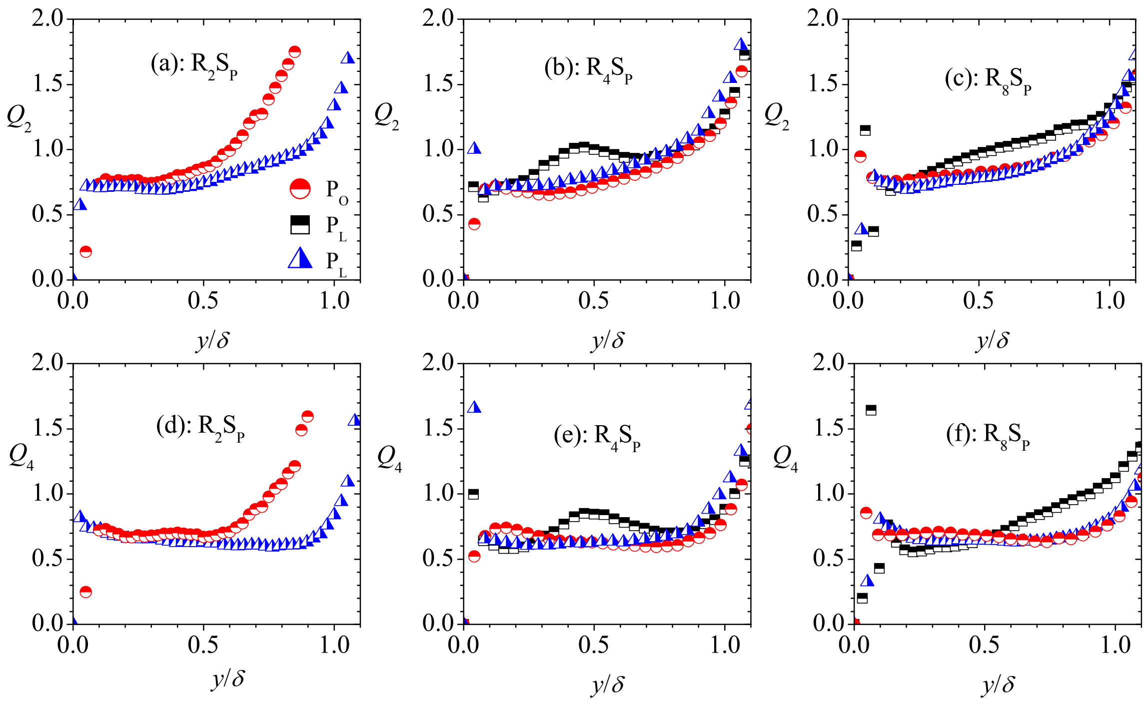

Figure 5.10: The distributions of the fractional contributions to $-\overline{uv}$ from second and fourth quadrants in the parallel section of ribs at 45° to approach flow for $H = 0$.

of the intermediate type and k-type ribs is due to intense diffusion of turbulence energy in the wall-normal direction. The distributions of $Q1$ and $Q3$ over the d-type ribs are more intense at the mid-span as the edge of the boundary layer is approached. The general variation of interaction motions across the span of the ribs implied that secondary flow influenced the activities of turbulence structures over inclined ribs.

In Figures 5.10a and 5.10d, strong ejection and sweep events are observed at the mid-span of the d-type ribs for $y > 0.1\delta$ and $y > 0.3\delta$. This is caused by simultaneous violence lift-up of low-speed fluid away from the wall and pumping of high-speed fluid towards the wall by the hairpin vortices. In the case of the k-type ribs, both ejection and sweep events are however stronger close to the leading edge of the ribs whereas $Q2$ and $Q4$ at the mid-span and close to the trailing edge collapsed fairly well. Thus, in the region $0.16\delta \leq y \leq 0.85\delta$, the hairpin packets close to the leading edge are engaged in strong pumping of the low-momentum fluid that reside in the legs of the vortices away from the wall. Similarly, there is an intensive pumping of high-speed fluid from the outer region towards the wall as depicted by the high level of $Q4$ close to the leading edge for $y > 0.55\delta$ (Figure 5.10f). Close to the leading edge, $Q2$ decreased rapidly for $y < 0.16\delta$ while there is a rapid rise in $Q4$ as the wall is approached ($y < 0.16\delta$), relative to those at the mid-span and close to the trailing edge. Furthermore, it should be noted that the contributions from $Q1$ which is a reflection of the high-speed away from the wall, also increased rapidly in this region for the contributions close to the leading edge. Figures 5.10b and 5.10e demonstrate that, except in region $0.11\delta \leq y \leq 0.62\delta$, both $Q2$ and $Q4$ are less affected by secondary motion across the span of intermediate type ribs.

The distributions of the quadrant events in the diverging section are shown in Figure 5.11 and Figure 5.12. It is clear from Figure 5.11 that the interaction motions in the diverging section of the *d*-type, intermediate type and *k*-type ribs are also altered by the secondary motion across the span of the channel. The variation is stronger over the intermediate type and *k*-type ribs than the *d*-type ribs. In Figures 5.12a and 5.12d, both $Q2$ and $Q4$ are in good agreement across the channel over the *d*-type ribs. The implication is that the contribution by the second and fourth quadrant to the stresses is independent of the spanwise location at which the measurements were made, and ejections and sweeps produced by the hairpin packets are nearly uniformly distributed across the channel. Except for $y < 0.3\delta$, the distribution of the fractional contributions from ejections to $-\overline{uv}$ is similar over the *k*-type ribs (Figure 5.12c). A drop in $Q4$ close to the leading edge relative to $Q4$ close to the trailing edge and at the mid-span is seen in Figure 5.12f. Over the intermediate type ribs, intense ejection and sweep events are

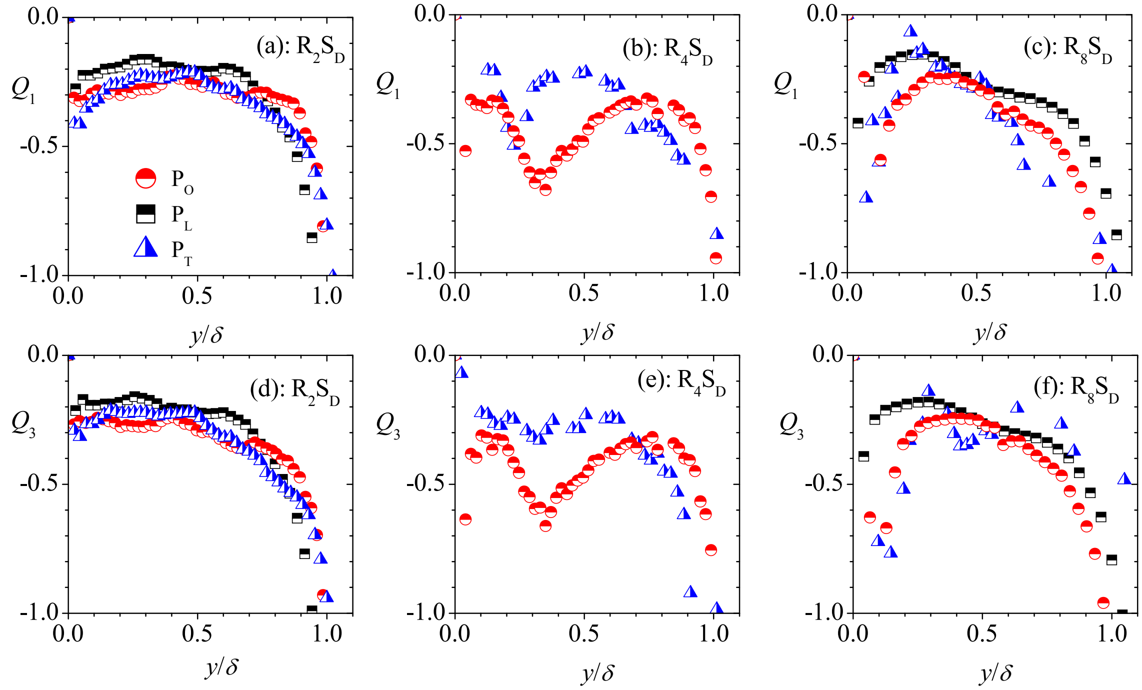

Figure 5.11: The distributions of the fractional contributions to $-\overline{uv}$ from first and third quadrants in the diverging section of ribs at 45° to approach flow for $H = 0$.

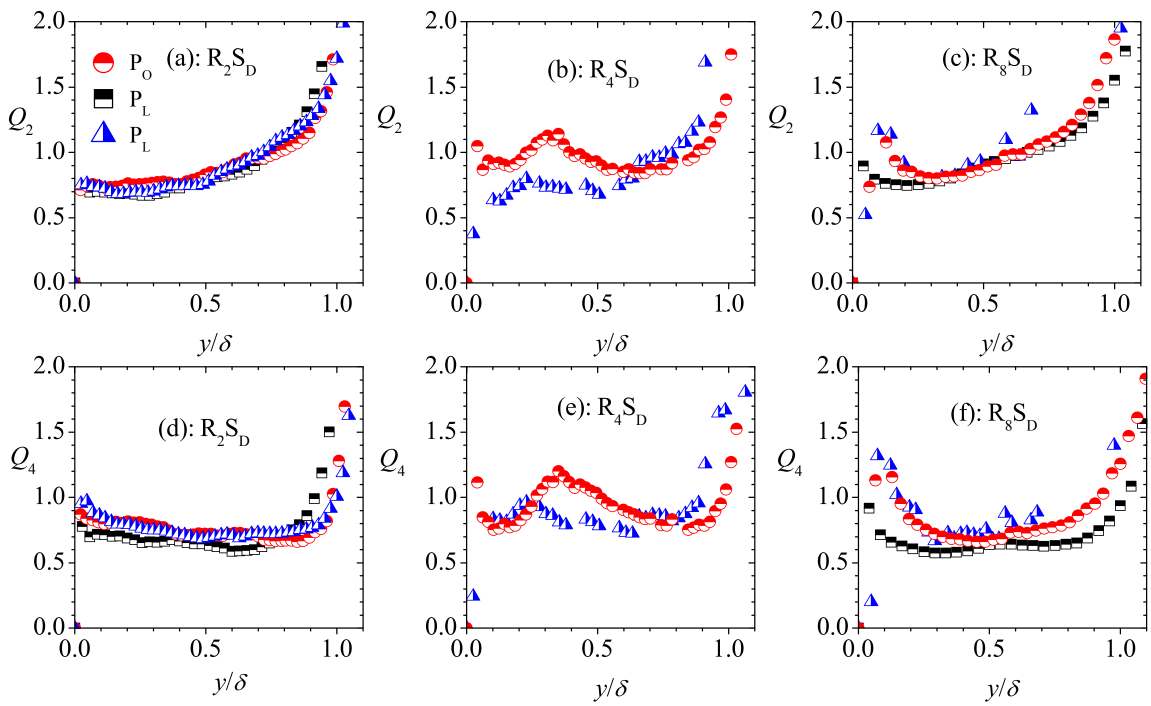

Figure 5.12: The distributions of the fractional contributions to $-\overline{uv}$ from second and fourth quadrants in the diverging section of ribs at 45° to approach flow for $H = 0$.

observed at the mid-span of the ribs for $y < 0.65\delta$ (Figures 5.12b and 5.12e). Beyond this location, the transport of low-velocity and high-velocity fluid is stronger close to the trailing edge of the ribs. However, the Reynolds shear stress at the mid-span is lower relative to the shear stress obtained close to the trailing edge (Figure 5.5e and Figure 5.8e). The foregoing results for the quadrant decomposition indicate that the secondary flow induced by inclining the ribs to an angle of 45° to the approach flow alters the activities of the turbulence structures thereby modifying the turbulence statistics across the span of the ribs.

5.1.2.2 Two-Point Velocity Correlations

Further insight into the variation of the turbulence structure across the span of each type of ribs is provided using the two-point velocity correlation functions. In general, it was observed that the shape of R_{uu}, R_{vv} and R_{uv} contours (not shown) at various measurement locations over 45° ribs is similar to those obtained over the smooth wall and 90° ribs.

The streamwise and wall-normal one-dimensional profiles of R_{uu} in the parallel section are shown in Figure 5.13. Figure 5.13a demonstrates that the streamwise profiles of R_{uu} over the *d*-type ribs is slightly enhanced close to the edges of the ribs compared to the data at the mid-span while the wall-normal profile close to the trailing edge is nearly similar to the R_{uu} correlation at the mid-span (Figure 5.13d). Conversely, both the streamwise and wall-normal one-dimensional profiles of R_{uu} over the intermediate type and *k*-type ribs show distinct differences across the span of the channel. In this case, the profiles of R_{uu} at the mid-span of these ribs are higher than those close to the leading edge of the ribs but lower than the data close to the trailing edge of the ribs. The present results demonstrate that the secondary flow driven to the trailing edge formed larger spatial

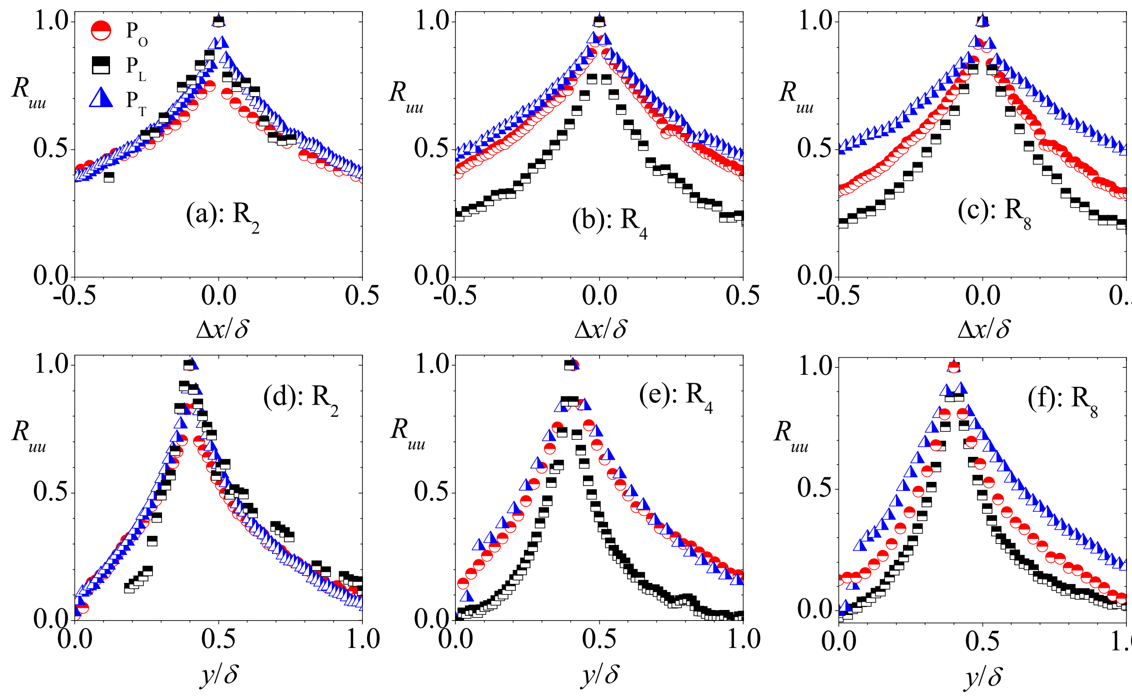

Figure 5.13: Streamwise and wall-normal one-dimensional profiles of R_{uu} at $y_{ref} = 0.4\delta$ in the parallel section of ribs at 45° to approach flow.

structures, but as the secondary flow returned to the leading edge, the structure is gradually attenuated via the mid-span to the leading edge of the ribs.

Figure 5.14 shows that the average inclination angle, β of the vortex packets generally varies with y_{ref}/δ. Over the *d*-type ribs, β is similar across the span of the channel. The values of β are however modified across the span of the intermediate type and *k*-type ribs. For example, β is negative at the mid-span and close to the leading edge of the *k*-type ribs for $0.3\delta \leq y \leq 0.7\delta$. In the same range, β is positive close to the trailing edge. Thus, the induced secondary motion modified the orientation of the structure as the flow is driven in the quasi-streamwise-spanwise direction.

The estimated characteristics length-scales of R_{uu} contours in the parallel section are shown in Figure 5.15. Figure 5.15 revealed that both Lx_{uu}/δ and Ly_{uu}/δ are larger close to the trailing edge of the ribs and are usually least near the leading edge of the ribs.

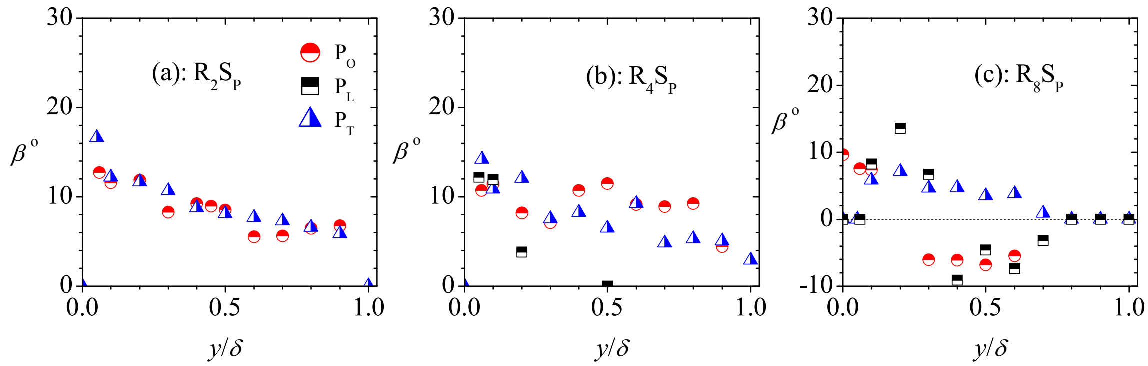

Figure 5.14: Average inclination angle of R_{uu} contours as a function of y/δ in the parallel section of ribs at 45° to approach flow.

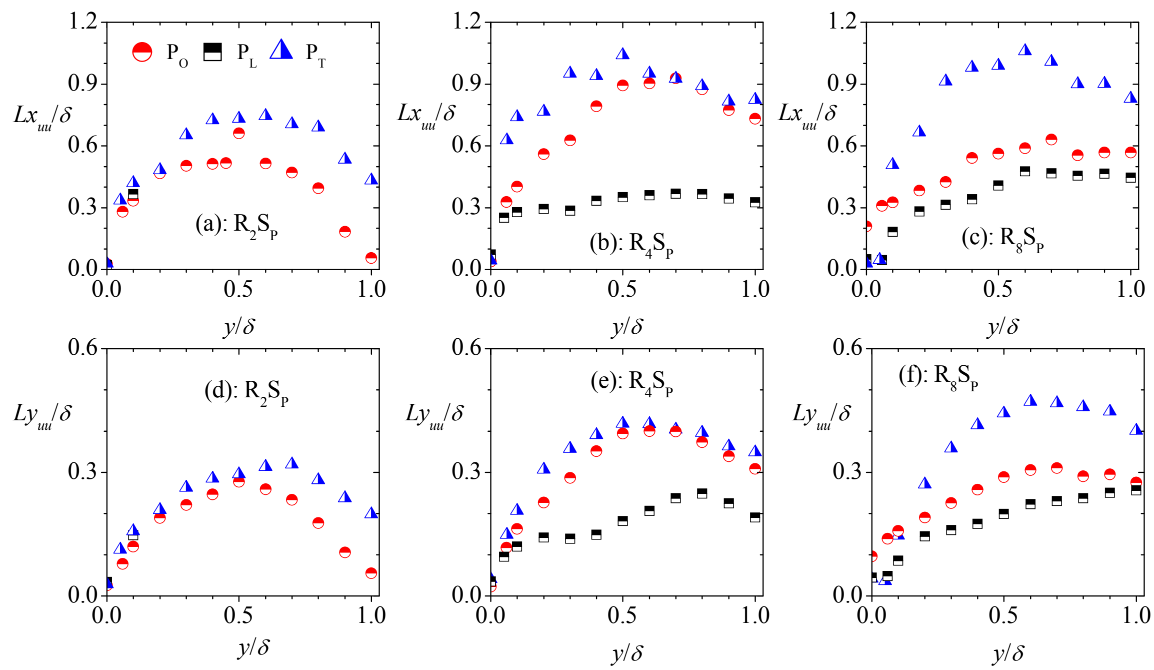

Figure 5.15: Average streamwise and wall-normal sizes of R_{uu} contours as a function of y/δ in the parallel section of ribs at 45° to approach flow.

Figure 5.16 presents the plots for the one-dimensional profiles of R_{uu} in the diverging section. The distribution of both the streamwise and the wall-normal profiles of R_{uu} in the diverging section of the *d*-type ribs collapsed well across the span of the ribs. This may suggest that the spatial structure in the diverging section of the *d*-type ribs is similar across the span of the channel. However, the distributions of R_{uu} profiles over the

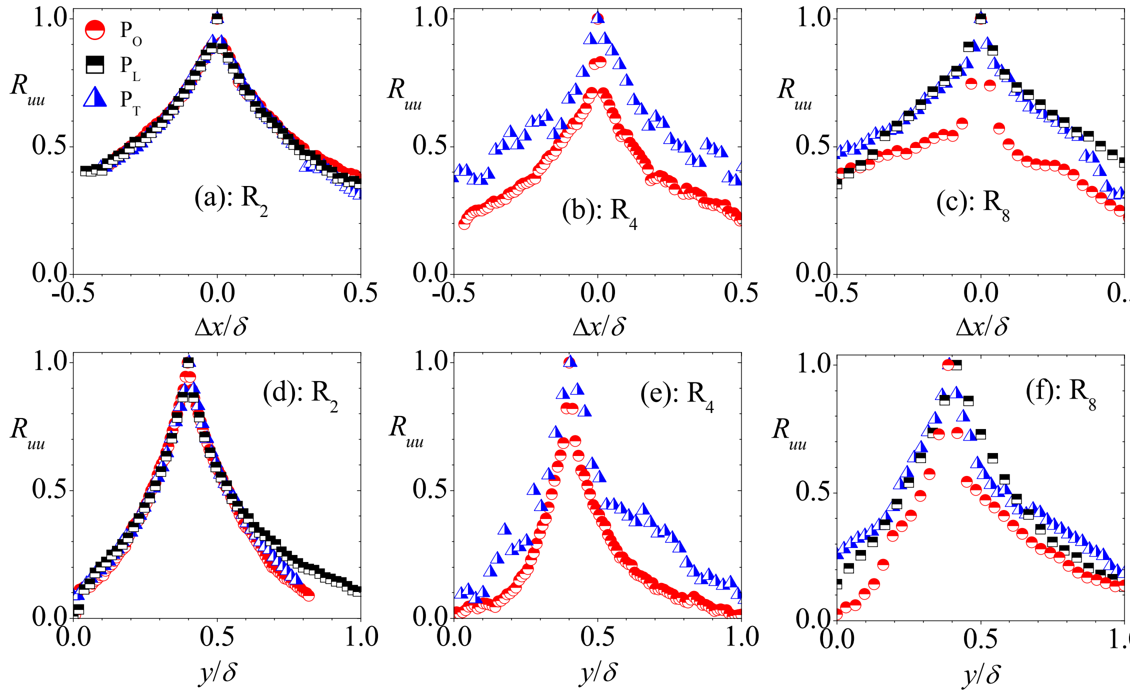

Figure 5.16: Streamwise and wall-normal one-dimensional profiles of R_{uu} at $y_{ref} = 0.4\delta$ in the diverging section of ribs at 45° to approach flow.

intermediate type and *k*-type ribs are larger close to the edges of the ribs than at the mid-span. Figure 5.17 shows that the average inclination angle of the vortex packets generally varies across the span of the ribs and with y_{ref}/δ. Over the *d*-type and intermediate type ribs, β is larger close to the trailing edge than at the mid-span and close to the leading edge. Meanwhile, the distribution of β is somewhat similar across the span of the *k*-type ribs.

The characteristics length-scales of R_{uu} contours in the streamwise and the wall-normal directions are shown in Figure 5.18. Both the streamwise and wall-normal sizes of R_{uu} contours over the *d*-type ribs are nearly equal across the span of the channel. It is evident from the figure that both Lx_{uu}/δ and Ly_{uu}/δ are augmented close to the trailing edge of the intermediate type and *k*-type ribs. However, the variations of both Lx_{uu}/δ and Ly_{uu}/δ close to the trailing and leading edges of the *k*-type ribs are small. This resulted in the higher level of turbulence close to the trailing edge of the ribs as seen in the stresses.

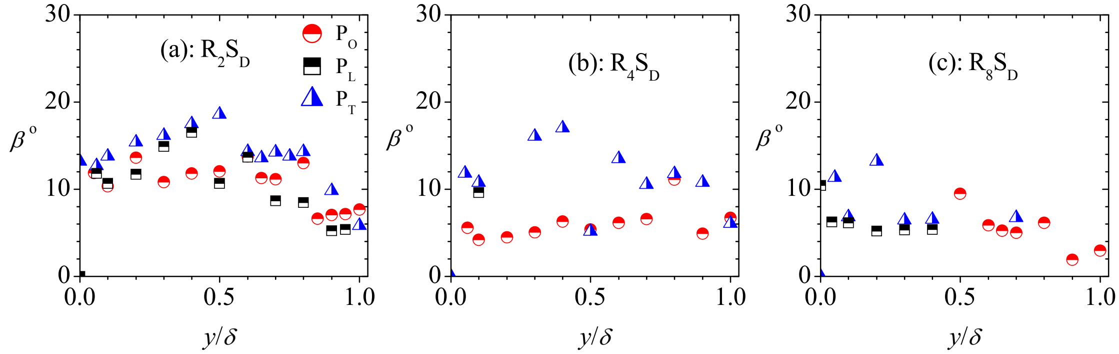

Figure 5.17: Average inclination angle of R_{uu} contours as a function of y/δ in the diverging section of ribs at 45° to approach flow.

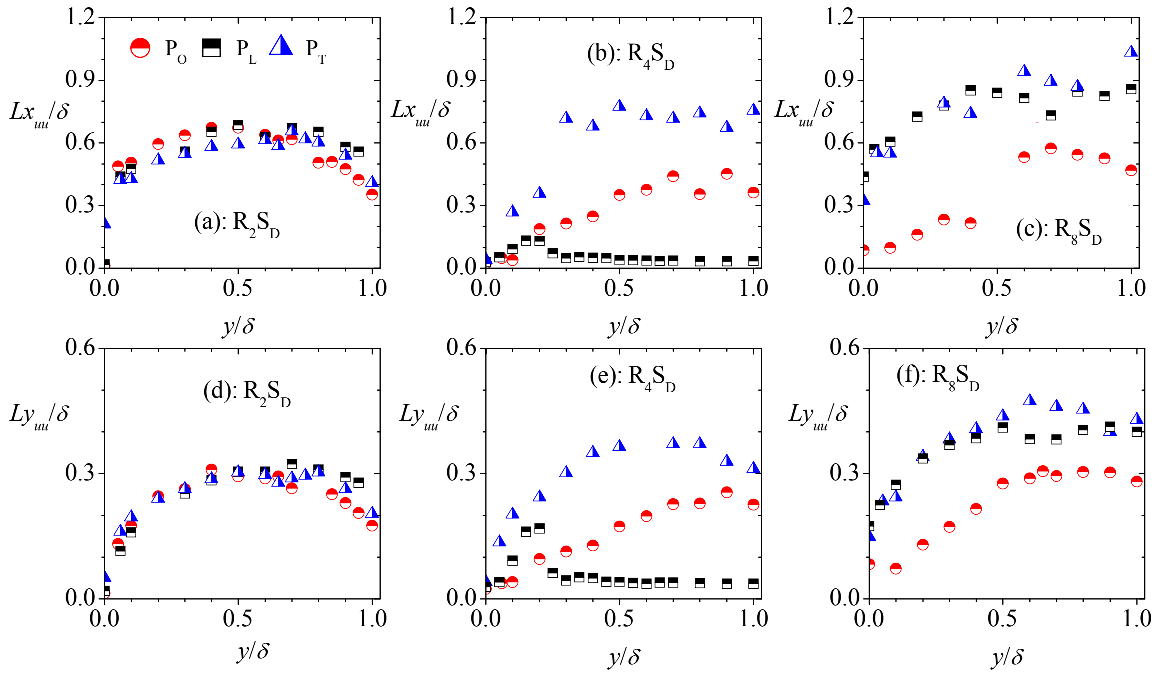

Figure 5.18: Average streamwise and wall-normal sizes of R_{uu} contours as a function of y/δ in the diverging section of ribs at 45° to approach flow.

Figure 5.19 demonstrates that both the streamwise and the wall-normal profiles of R_{vv} in the parallel section of the *d*-type, intermediate type and *k*-type ribs are also enhanced close to the trailing edge of the ribs. The R_{vv} correlation is however lower close to the leading edge of the intermediate type and *k*-type ribs, and at the mid-span of *d*-type ribs, suggesting that the spatial extent of the structure associated with R_{vv} is diminished close to the leading edge and mid-span, respectively. The estimated length-scales of R_{vv}

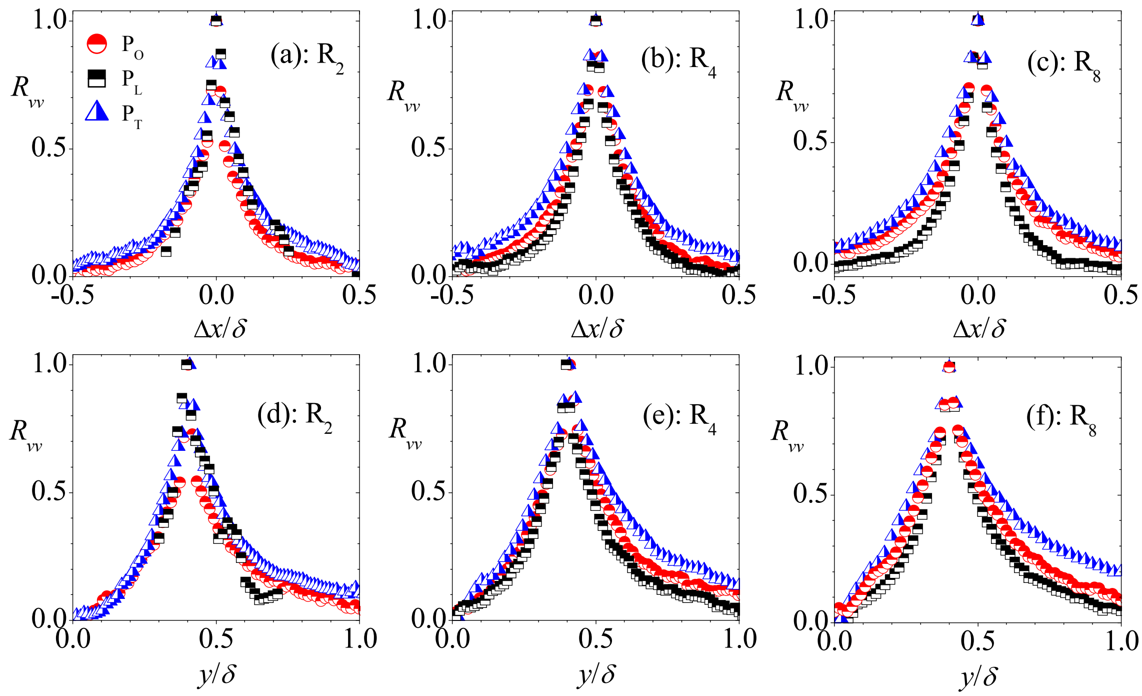

Figure 5.19: Streamwise one-dimensional profiles of R_{vv} at y_{ref} = 0.4δ in the parallel section of ribs at 45° to approach flow.

shown in Figure 5.20 are larger close to the trailing edge of the ribs. This may be due to stretching of R_{vv} close to the trailing edge of the ribs in both the longitudinal and vertical directions.

Figure 5.21 shows the one-dimensional profiles of R_{vv} centred at y_{ref} = 0.4δ in the diverging section. The streamwise and the wall-normal profiles of R_{vv} at the different spanwise locations collapsed reasonably well over the *d*-type ribs. However, significant variations in the profiles of R_{vv} are observed over the intermediate type and *k*-type ribs. In general, both the streamwise and wall-normal profiles of R_{vv} correlations over the intermediate type ribs are enhanced close to the trailing edge, an indication of formation of larger spatial structures close to the trailing edge compared to the structures at mid-span. In the case of the *k*-type ribs, the increase in the R_{vv} correlations close to the leading edge is an indication of formation of larger spatial structure close to the leading edge

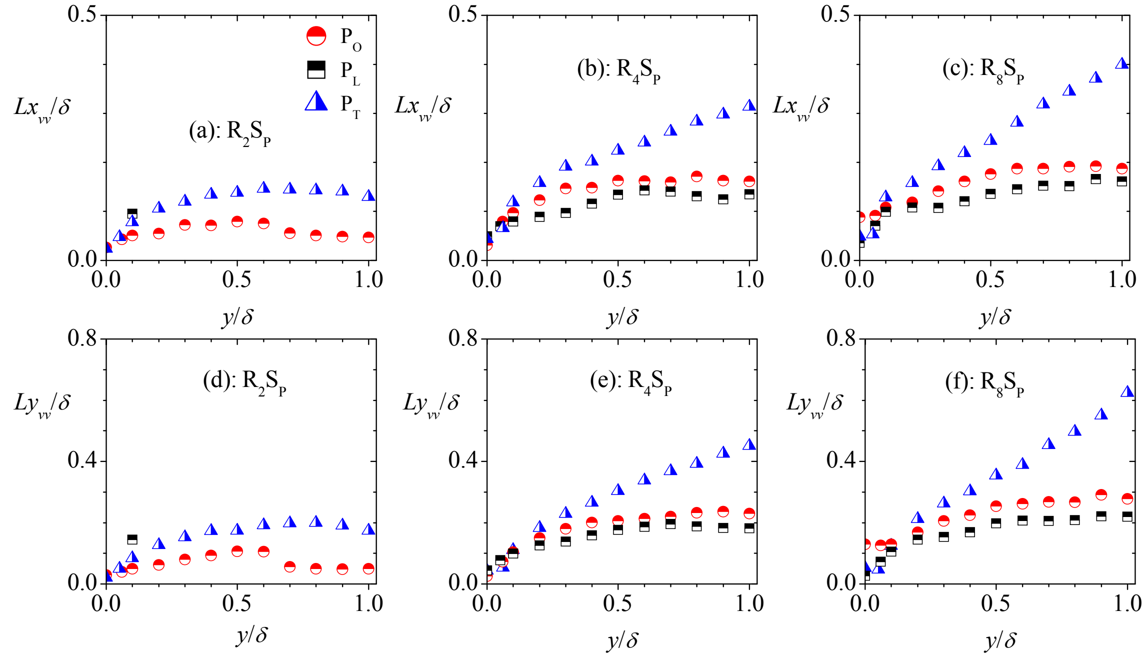

Figure 5.20: Average streamwise and wall-normal sizes of R_{vv} contours as a function of y/δ in the parallel section of ribs at 45° to approach flow.

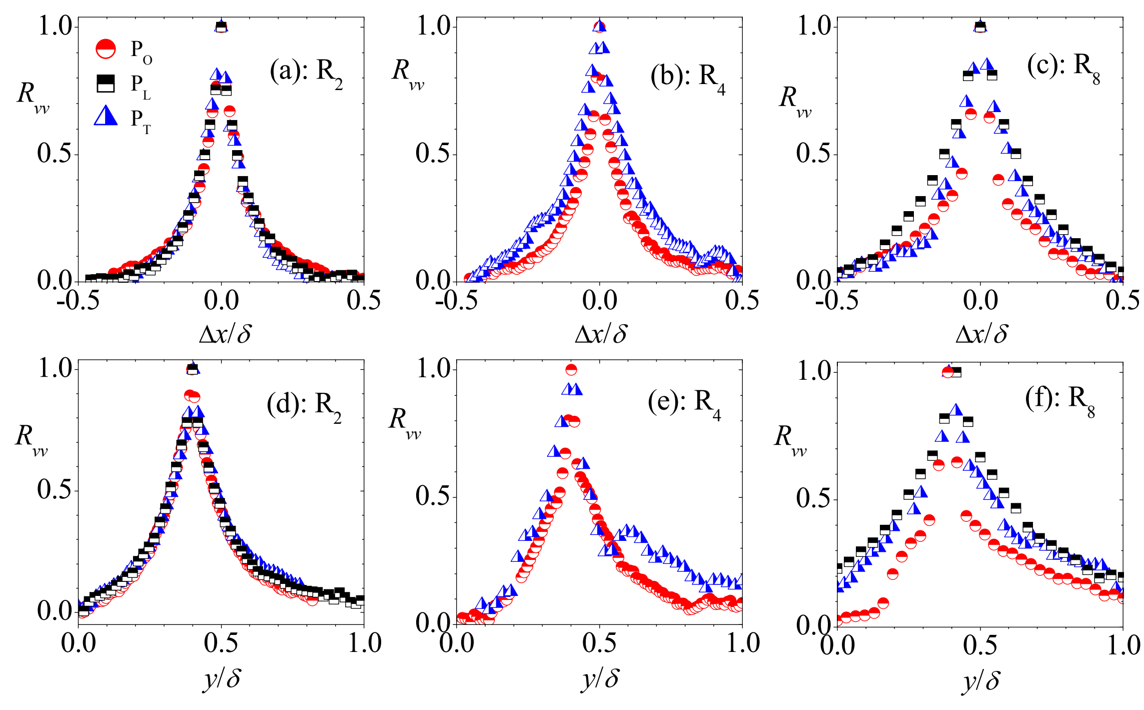

Figure 5.21: Streamwise and wall-normal one-dimensional profiles of R_{vv} at $y_{ref} = 0.4\delta$ in the diverging section of ribs at 45° to approach flow.

compared to the mid-span and close to the trailing edge of the ribs. The distributions of the streamwise and the vertical length-scales of R_{vv} in the diverging section are reported in Figure 5.22. Both Lx_{vv}/δ and Ly_{vv}/δ in the diverging section of the *d*-type ribs are in good agreement across the channel. Conversely, Lx_{vv}/δ and Ly_{vv}/δ over the intermediate type and *k*-type ribs exhibit significant variation across the span of the ribs. Over the intermediate type ribs, for example, the Lx_{vv}/δ and Ly_{vv}/δ tend to be larger close to the trailing edge of the ribs than at the mid-span and close to the leading edge of ribs. They are however least close to the leading edge of the ribs. For the case of the *k*-type ribs, both Lx_{vv}/δ and Ly_{vv}/δ are lower at the mid-span of the channel.

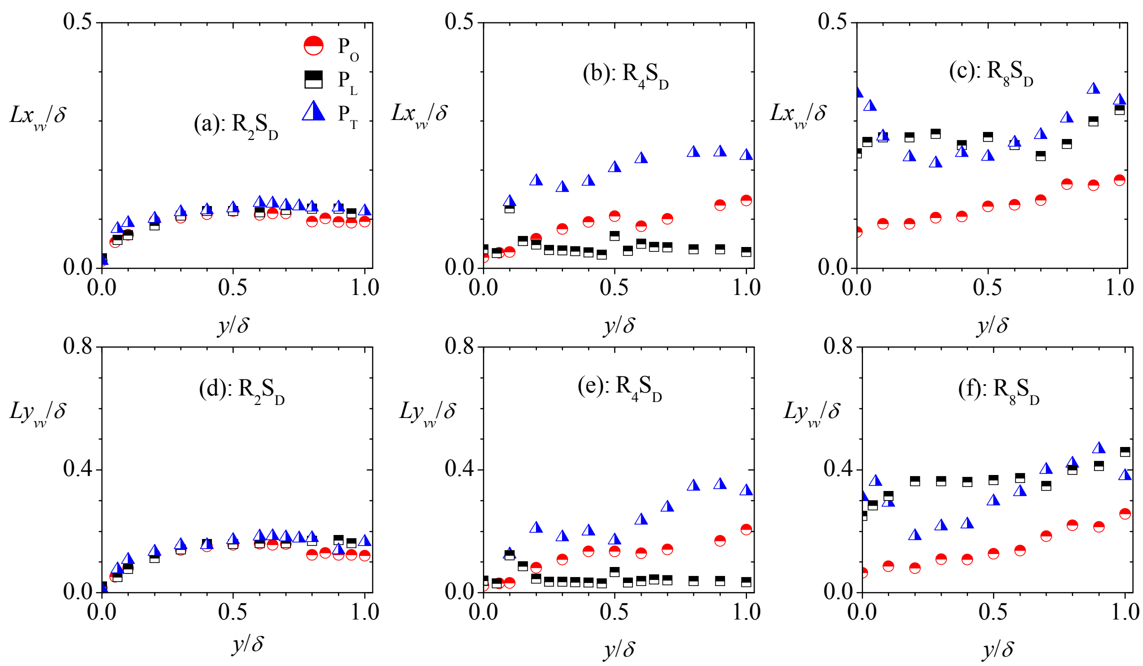

Figure 5.22: Average streamwise and wall-normal sizes of R_{vv} contours as a function of y/δ in the diverging section of ribs at 45° to approach flow.

5.2 EFFECTS OF RIB INCLINATION ANGLE ON THE FLOW

As observed earlier in the previous sections, inclined ribs induced secondary motion that caused the mean and turbulence statistics as well as the turbulence structure to vary across the span of the channel. In this section, data obtained at the mid-span (z = 0 mm) of the d-type, intermediate type and k-type ribs inclined at 45° and 30° to the approach flow are compared to the data over the corresponding 90° ribs to study the effects of rib inclination angle on the flow characteristics.

5.2.1 MEAN FLOW AND TURBULENCE STATISTICS

5.2.1.1 Boundary Layer Characteristics

Table 5.3 presents the boundary layer parameters for measurements at the mid-span of the d-type, intermediate type and k-type ribs at the various inclination angles, α. Although δ, δ^*, θ and H are reduced as the rib inclination angle decreases (except in the parallel section of d-type ribs where δ, δ^* and θ are larger over the 30° ribs), the reduction is not systematic with α over all the rib types. It should be noted that the most dramatic reduction in the boundary layer parameters is observed in the diverging section of the intermediate type and k-type ribs.

5.2.1.2 Mean Velocity Profiles in Outer Coordinates

The distributions of the mean velocity profiles in the outer coordinates at the mid-span of the ribs at various inclinations to the approach flow in both the parallel and diverging sections are shown in Figure 5.23. In both the parallel and diverging sections of the d-type ribs, only subtle variation in U/U_m can be discerned. However, in both the parallel and diverging sections of the intermediate type and k-types ribs, U/U_m is significantly reduced by the 90° ribs compared to the 45° and 30° ribs. This reduction extends to a considerable distance away from the wall, ensuring that the profiles are less uniform for a greater extent. The data reported by Tachie and Shah (2008) over k-type ribs also lends

Table 5.3: Boundary layer characteristics at the mid-span of 90°, 45° and 30° ribs.

Test	p/k	U_m m/s	δ mm	δ^* mm	θ mm	H	k/δ	K $\times 10^{-7}$	β	Re_θ	Re_τ
$R_2S_P\alpha_{90}P_O$	2	0.377	26.3	5.0	3.2	1.55	0.114	1.41	−0.05	1220	700
$R_2S_P\alpha_{45}P_O$	2	0.398	25.7	4.8	3.0	1.59	0.117	0.88	−0.04	1200	630
$R_2S_P\alpha_{30}P_O$	2	0.390	30.7	5.2	3.5	1.49	0.098	0.72	−0.04	1370	720
$R_4S_P\alpha_{90}P_O$	4	0.394	32.8	8.0	4.8	1.67	0.092	1.29	−0.07	1890	1010
$R_4S_P\alpha_{45}P_O$	4	0.402	28.2	5.9	3.8	1.56	0.106	1.79	−0.10	1530	750
$R_4S_P\alpha_{30}P_O$	4	0.376	27.8	4.5	3.1	1.45	0.108	5.17	−0.23	1170	640
$R_8S_P\alpha_{90}P_O$	8	0.380	36.8	10.0	5.5	1.81	0.081	1.93	−0.08	2100	1340
$R_8S_P\alpha_{45}P_O$	8	0.364	25.1	3.2	2.4	1.33	0.120	1.51	−0.05	880	530
$R_8S_P\alpha_{30}P_O$	8	0.358	25.5	3.1	2.3	1.33	0.118	2.65	−0.08	830	540
$R_2S_D\alpha_{90}P_O$	2	0.313	45.8	13.1	7.3	1.79	0.066	−23.95	2.08	2290	980
$R_2S_D\alpha_{45}P_O$	2	0.338	45.4	12.3	7.1	1.73	0.066	−17.49	1.85	2410	960
$R_2S_D\alpha_{30}P_O$	2	0.325	45.1	13.3	7.3	1.82	0.067	−14.57	1.42	2370	980
$R_4S_D\alpha_{90}P_O$	4	0.306	50.2	17.6	8.6	2.05	0.060	−20.67	2.07	2640	1130
$R_4S_D\alpha_{45}P_O$	4	0.261	35.5	8.6	5.5	1.55	0.085	−24.45	1.08	1440	660
$R_4S_D\alpha_{30}P_O$	4	0.312	30.5	7.0	4.5	1.55	0.099	−28.71	1.69	1400	580
$R_8S_D\alpha_{90}P_O$	8	0.300	54.3	19.2	9.4	2.04	0.055	−26.59	2.08	2820	1400
$R_8S_D\alpha_{45}P_O$	8	0.289	13.9	2.8	1.7	1.62	0.216	−30.88	0.66	490	250
$R_8S_D\alpha_{30}P_O$	8	0.301	14.7	2.2	1.5	1.44	0.195	−23.22	0.51	520	240

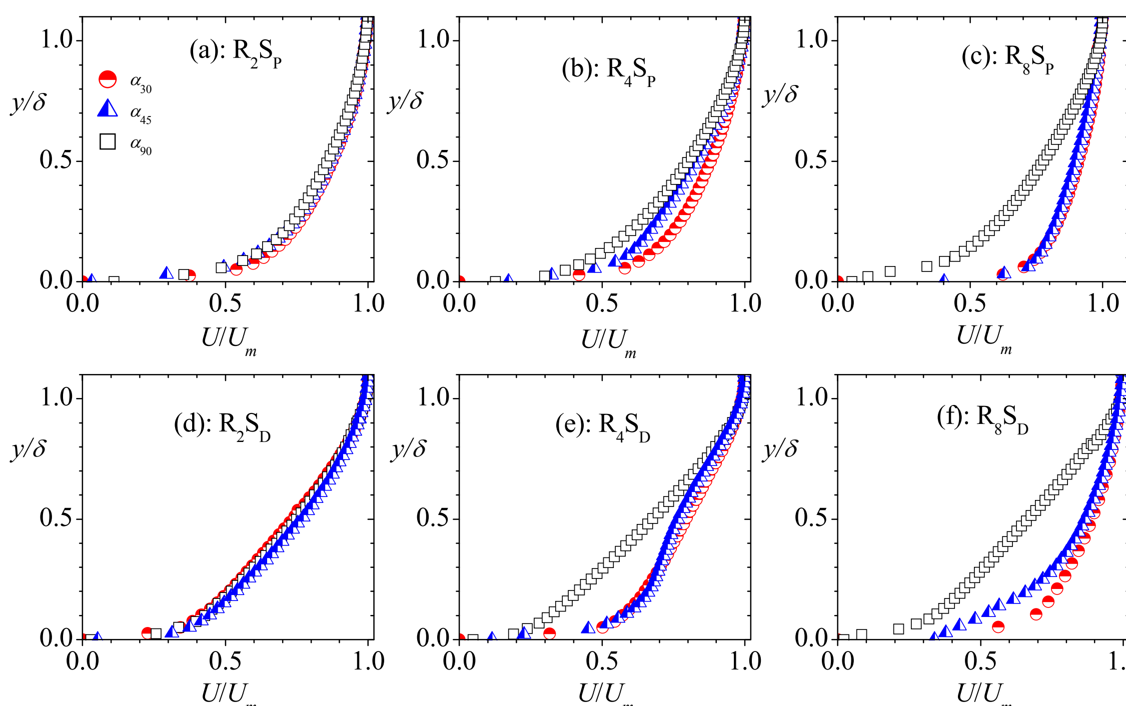

Figure 5.23: The distributions of the streamwise mean velocity profiles at the mid-span of 30°, 45° and 90° ribs in outer coordinates.

support to this observation: they observed that the U/U_m profile is more uniform for the ribs at 45° than the ribs at 90° to the approach flow. Moreover, in the present study the *U*-profiles over the ribs at 30° are more uniform. This is more obvious in Figure 5.23b and Figure 5.23f. Meanwhile, in the diverging section of the intermediate type ribs, the *U*-profile for the 45° ribs formed a characteristic kink within the region $0.28 < y/\delta < 0.96$.

5.2.1.3 Drag Characteristics

The friction velocity, U_τ and the friction coefficient, C_f decreased as the rib inclination angle is reduced (Table 5.4) in agreement with the results of Tachie and Shah (2008). This reduction is very dramatic over the *k*-type ribs and is least over the *d*-type ribs. In the parallel section of the *k*-type ribs for example, the friction coefficient is reduced by 63% and 62% of the C_f value obtained over ribs at 90°, respectively for ribs inclined at 45° and 30° to approach flow. Table 5.4 indicates that the downward shifting of the U^+ profiles over the ribs relatively to the classical logarithm law plot for a smooth wall, ΔB is reduced as the rib inclination angle is decreased, which is consistent with the results of Tachie and Shah (2008).

The roughness Reynolds number, k_s^+ increases as the rib inclination angle tends to be large. The k_s^+ values lower than 70 are considered to be in the transitionally rough regime whereas $k_s^+ > 70$ are in the fully rough regime (Schlichtling, 1979). Meanwhile, the values of the equivalent sand grain roughness indicate that for any given rib type (*d*-type, intermediate type and *k*-type ribs), a smaller size of uniform sand grains will be required to produce the same degree of roughness as α decreases.

Table 5.4 also indicates that the inclination of the ribs to the approach flow also strongly influenced the wake component of the mean flow. It is observed that in the parallel section of the 45° and 30° *k*-type ribs, both ΔU^+_{max} and Π values are negative, an indication that negative wake component is formed in their U^+-profiles. In the parallel section of the intermediate type ribs, and in the diverging section of the *d*-type and *k*-type ribs, the values of ΔU^+_{max} and Π drop as α decreases. Thus, the entrainment of low-momentum fluid in the outer region of the mean flow over these ribs is weakened as α decreased.

Table 5.4: Drag and wake parameters at the mid-span of 90°, 45° and 30° ribs

Test	U_τ cm/s	U_τ/U_m	C_f	E	ΔB	k_s^+	k_s/k	ΔU^+_{max}	Π
$R_2S_P\alpha_{90}P_O$	2.66	0.0706	0.0100	8.60	7.01	74	0.9	0.00	0.000
$R_2S_P\alpha_{45}P_O$	2.45	0.0615	0.0076	10.20	5.20	35	0.5	0.90	0.185
$R_2S_P\alpha_{30}P_O$	2.33	0.0597	0.0071	10.50	4.99	32	0.5	0.55	0.113
$R_4S_P\alpha_{90}P_O$	3.08	0.0781	0.0122	5.10	11.05	390	4.2	1.54	0.316
$R_4S_P\alpha_{45}P_O$	2.67	0.0664	0.0088	8.30	7.25	82	1.0	1.17	0.245
$R_4S_P\alpha_{30}P_O$	2.31	0.0615	0.0076	10.28	4.99	32	0.5	0.30	0.062
$R_8S_P\alpha_{90}P_O$	3.63	0.0954	0.0182	3.20	13.13	914	8.4	0.97	0.199
$R_8S_P\alpha_{45}P_O$	2.13	0.0585	0.0068	12.10	3.00	14	0.2	−0.75	−0.154
$R_8S_P\alpha_{30}P_O$	2.11	0.0589	0.0069	12.90	2.19	10	0.2	–1.15	–0.236
$R_2S_D\alpha_{90}P_O$	2.15	0.0686	0.0094	4.65	10.75	345	5.3	3.24	0.664
$R_2S_D\alpha_{45}P_O$	2.12	0.0627	0.0079	5.60	9.55	211	3.3	3.71	0.761
$R_2S_D\alpha_{30}P_O$	2.17	0.0667	0.0089	4.90	10.31	288	4.4	3.26	0.668
$R_4S_D\alpha_{90}P_O$	2.25	0.0734	0.0108	2.25	13.13	914	13.5	4.21	0.863
$R_4S_D\alpha_{45}P_O$	1.86	0.0712	0.0101	7.36	7.49	91	1.6	0.60	0.123
$R_4S_D\alpha_{30}P_O$	1.90	0.0608	0.0074	8.50	6.40	58	1.0	2.05	0.420
$R_8S_D\alpha_{90}P_O$	2.58	0.0859	0.0148	1.52	14.19	1412	18.2	2.86	0.586
$R_8S_D\alpha_{45}P_O$	1.77	0.0612	0.0075	12.15	2.56	12	0.2	0.56	0.115
$R_8S_D\alpha_{30}P_O$	1.65	0.0549	0.0060	13.80	0.75	6	0.1	0.49	0.100

5.2.1.4 Mean Velocity Defect Profiles

The defect velocity profiles are plotted to examine the effects of rib inclination on the outer layer of the mean flow. The defect velocity profiles scaled with U_τ and $U_m\delta^*/\delta$ are reported in Figure 5.24 and Figure 5.25. Irrespective of the velocity scale used, an excellent collapse of the defect velocity profile is observed over the *d*-type ribs in both

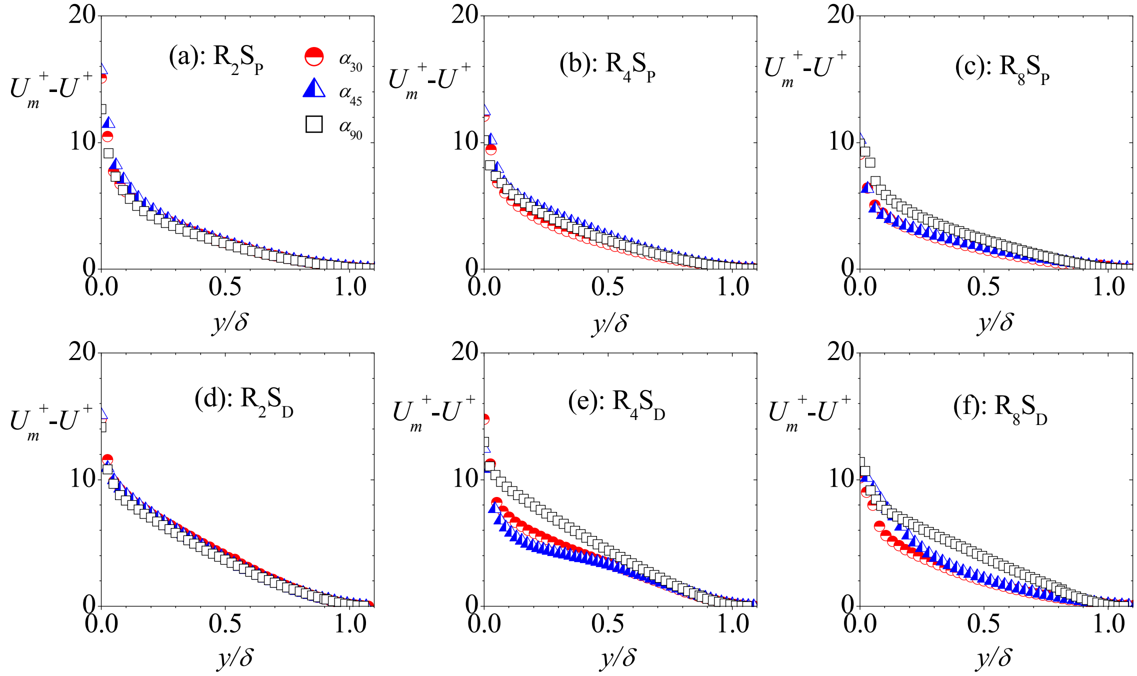

Figure 5.24: The distributions of the mean defect profiles over 30°, 45° and 90° ribs scaled with friction velocity and wall-normal axis scaled using boundary layer thickness.

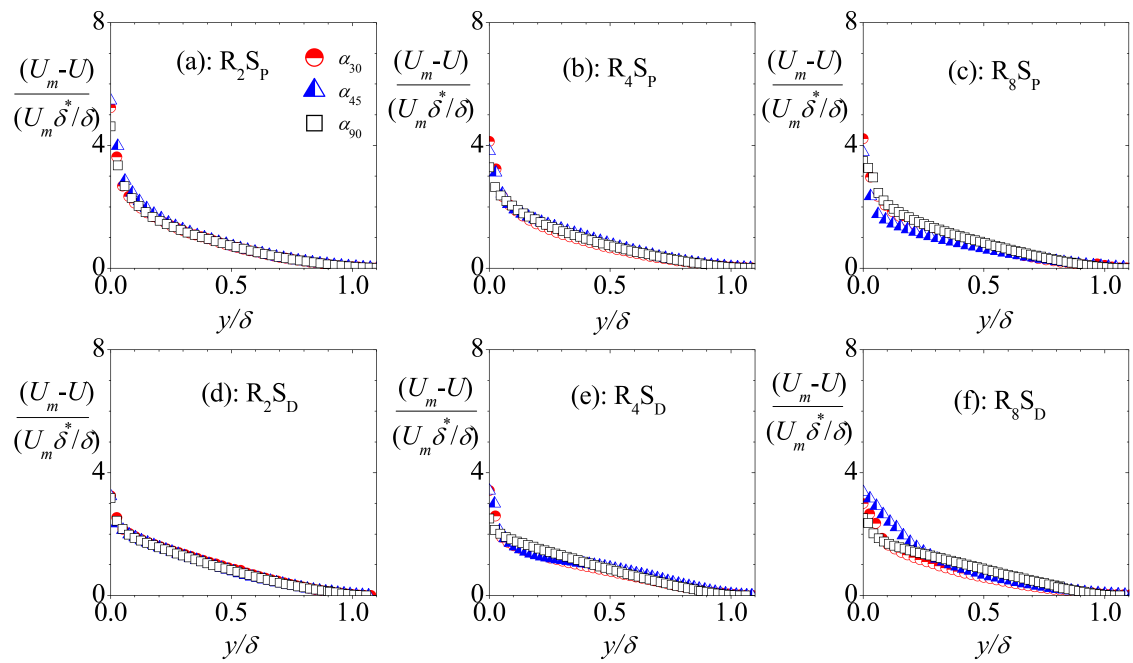

Figure 5.25: The distributions of the mean defect profiles over 30°, 45° and 90° ribs scaled with mixed outer velocity scale and wall-normal axis scaled using boundary layer thickness.

parallel and diverging sections. Over the intermediate type and k-type ribs, the friction velocity is unable to collapse the defect profiles. When the defect profiles are scaled with the mixed outer velocity scale, the profiles over intermediate type ribs collapsed very well in both the parallel and diverging section (Figures 5.25b and 5.25e). No collapse is observed for the defect profiles over the *k*-type ribs, however, the deviation among the profiles were minimized with the use of the mixed outer velocity scale.

5.2.1.5 Reynolds Stresses

Figure 5.26-Figure 5.28 shows the plots, respectively, for the streamwise Reynolds normal stress, wall-normal Reynolds normal stress and Reynolds shear stress in the outer coordinates. The distributions of the Reynolds stresses over *d*-type ribs in both the parallel section and diverging section are less sensitive to rib inclination angle. Note that in the diverging section, $\overline{u^2}$, $\overline{v^2}$ and $-\overline{uv}$ over the 90° ribs decay more rapidly from their peak. Over the intermediate type and *k*-type ribs, the distributions of $\overline{u^2}/U_m^2$, $\overline{v^2}/U_m^2$ and $-\overline{uv}/U_m^2$ are larger over the 90° ribs in both the parallel and diverging sections than over the 45° and 30° ribs. Furthermore, in the diverging section of the intermediate type and *k*-type ribs, the stresses over the 90° ribs exhibit a broader hump than observed over 45° and 30° ribs. Over the intermediate type ribs, $\overline{u^2}/U_m^2$ and $-\overline{uv}/U_m^2$ in the diverging section of ribs inclined at 45° formed a dent each in the regions $0.13 < y/\delta < 0.53$ (Figure 5.26e) and $0.13 < y/\delta < 0.61$ (Figure 5.28e), respectively. This dent in $\overline{u^2}$ and $-\overline{uv}$ is mainly attributed to low $\partial U/\partial y$ within this region (Figure 5.23e) since the dominant production term in $\overline{u^2}$ is $-\overline{uv}\partial U/\partial y$ and that for $-\overline{uv}$ is $\overline{v^2}\partial U/\partial y$. It will be recalled that the *U* profile in the diverging section of the intermediate type ribs inclined at 45° to

the approach flow formed a kink in the region $0.28 < y/\delta < 0.96$ (Figure 5.23e). The wall-normal transport velocities for the turbulence kinetic energy, V_q^+ and the Reynolds shear stress, V_{uv}^+ (not shown) were found to be negative in the region where the kink was observed in U, $\overline{u^2}$ and $-\overline{uv}$, indicating transport of q and $-\overline{uv}$ towards the wall. The implication is that, the productions of q and $-\overline{uv}$ (not shown) were diminished in this region in the diverging section. Note that this dent is not observed in the vertical turbulence motion since $\partial U/\partial y$ does not play any role in the production of $\overline{v^2}$ (Figure 5.27e). Meanwhile, in the diverging section of the intermediate type ribs, $\overline{v^2}$ over the 45° and 30° ribs does not decay with y, but grows gradually with y. It is also evident that in the diverging section of the intermediate type ribs, $\overline{v^2}/U_m^2$ is nearly similar for 45° and 30° ribs whereas in the parallel section of the *k*-type ribs, $\overline{u^2}/U_m^2$ for the 45° and 30° ribs collapsed.

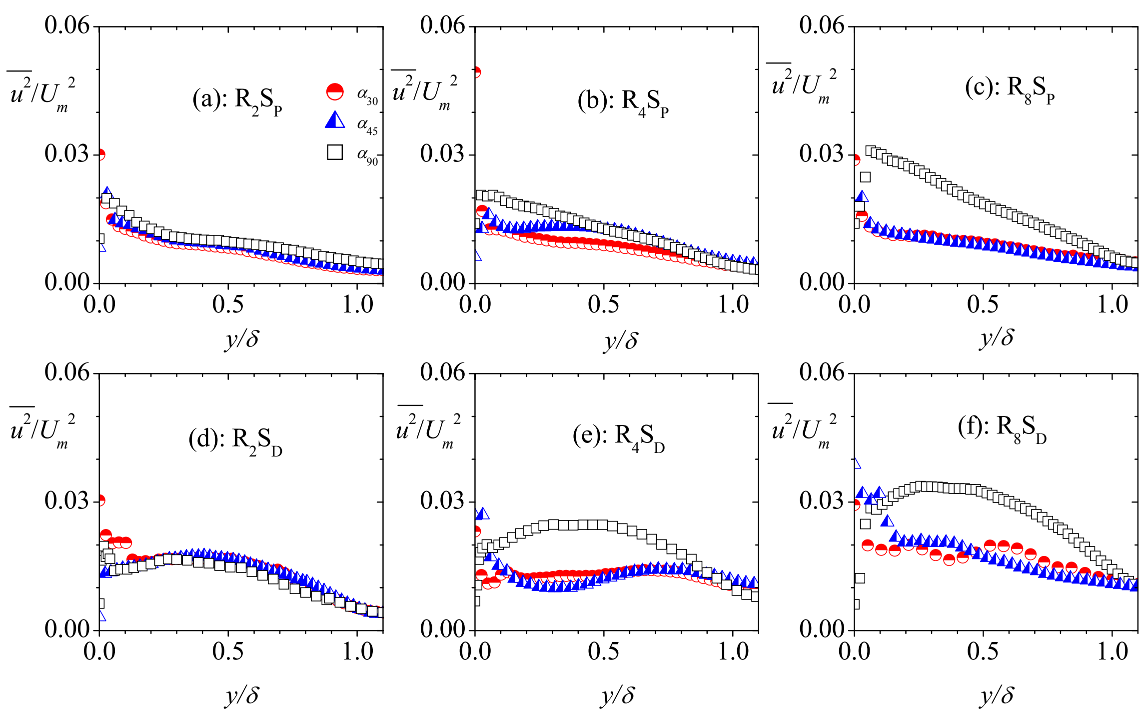

Figure 5.26: Distribution of streamwise Reynolds normal stress in the parallel and diverging sections of ribs at 30°, 45° and 90° normalized by U_m^2.

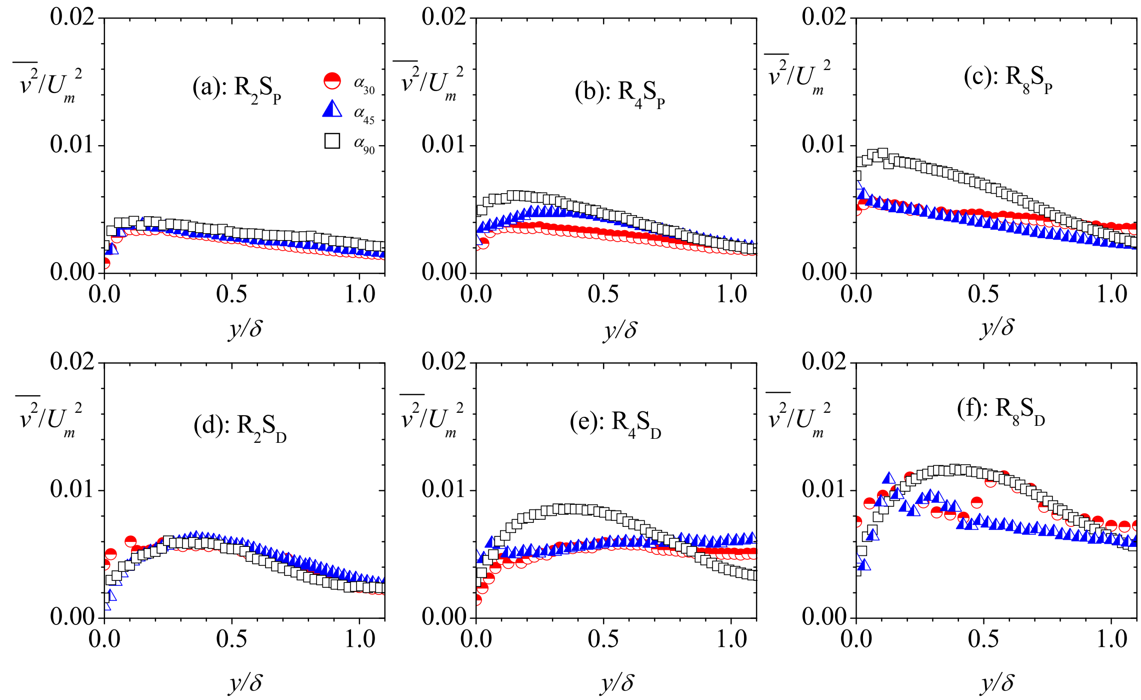

Figure 5.27: Distribution of wall-normal Reynolds normal stress in the parallel and diverging sections of ribs at 30°, 45° and 90° normalized by U_m^2.

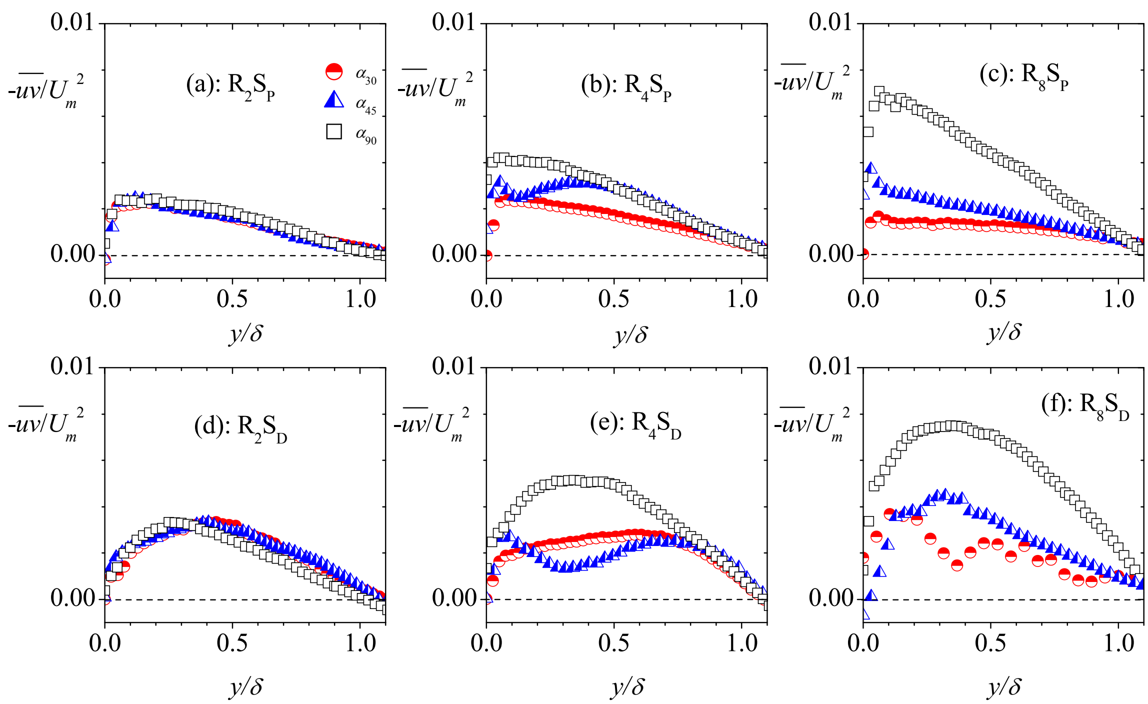

Figure 5.28: Distribution of Reynolds shear stress in the parallel and diverging sections of ribs at 30°, 45° and 90° normalized by U_m^2.

As demonstrated in the preceding paragraph and Section 5.2.1.3, ribs at 90° to approach flow increases the Reynolds stresses (except over the *d*-type ribs) and wall shear stress compared with the corresponding 30° and 45° ribs. Figure 5.29-Figure 5.31 presents the Reynolds stresses in the inner coordinates. Over the *d*-type ribs, the variations of $\overline{u^{+2}}$, $\overline{v^{+2}}$ and $-\overline{u^+v^+}$ with α in both the parallel section (Figure 5.29a, Figure 5.30a and Figure 5.31a) and diverging section (Figure 5.29d, Figure 5.30d and Figure 5.31d) are consistent with earlier remarks that the distribution of the stresses are less sensitive to rib inclination angle. In the parallel section, the stresses over 90° ribs are modestly reduced in the region $y < 0.5y_{uv}$ compared to those over ribs at 45° and 30°. As seen in Table 5.4, the wall shear stress diminished as the ribs inclination angle to the approach flow is decreased. Therefore, the weak effects of rib inclination angle on the stresses implies that the 45° and 30° ribs caused proportionate reduction in the wall shear

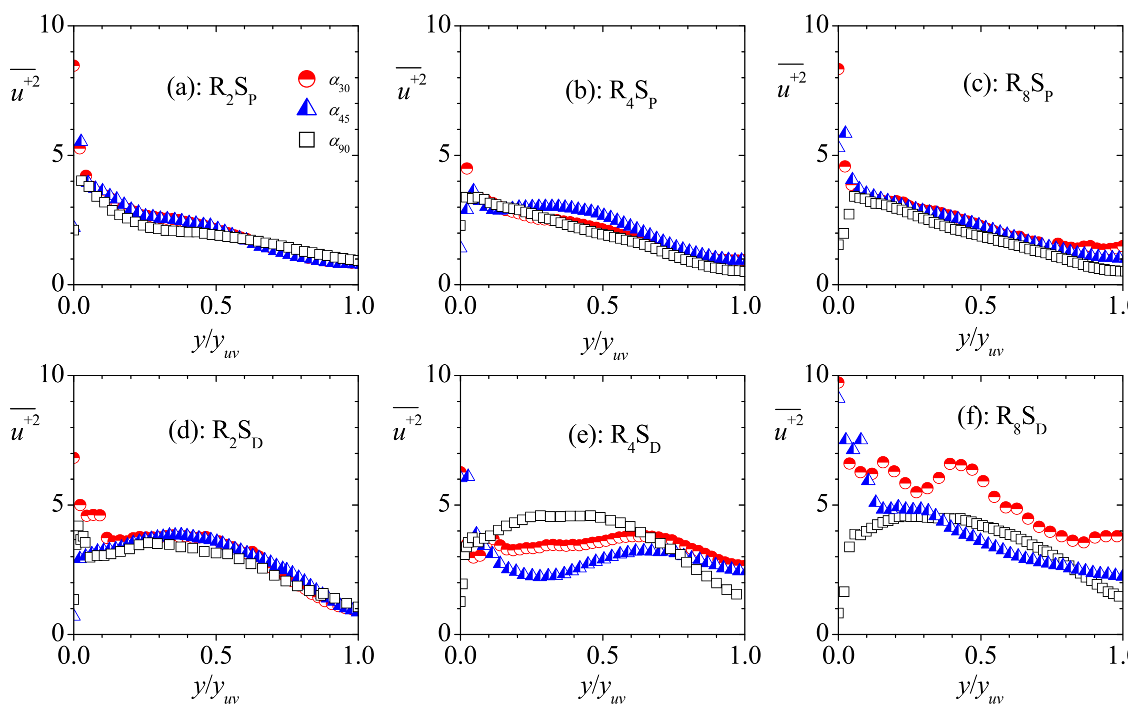

Figure 5.29: Distribution of streamwise Reynolds normal stress in the parallel and diverging sections of ribs at 30°, 45° and 90° normalized by U_τ^2.

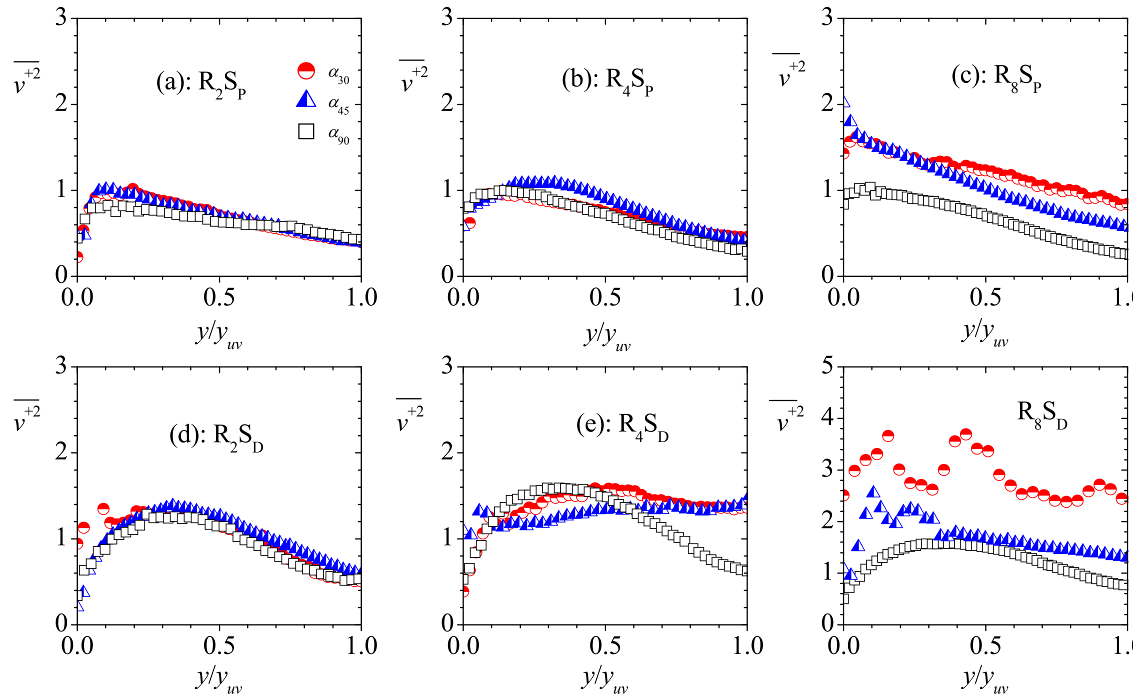

Figure 5.30: Distribution of wall-normal Reynolds normal stress in the parallel and diverging sections of ribs at 30°, 45° and 90° normalized by U_τ^2.

stress and the Reynolds stresses, so that their ratio is not significantly different from the data over the 90° ribs. Over the intermediate type ribs, $\overline{u^{+2}}$, $\overline{v^{+2}}$ and $-\overline{u^+v^+}$ are similar in the parallel section, except that the hump formed in the outer layer of these stresses over the 45° ribs tends to be dominant. In the diverging section of the intermediate type ribs, $\overline{u^{+2}}$, $\overline{v^{+2}}$ and $-\overline{u^+v^+}$ are larger over the ribs at 90° to the approach flow for $y/y_{uv} <$ 0.67. Beyond this location, the data sets over the ribs inclined at 45° and 30° to the approach flow are increased following a rapid decay of the stresses over the 90° ribs. In the parallel section of the *k*-type ribs, $\overline{u^{+2}}$ is independent of rib inclination angle whereas in the diverging section $\overline{u^{+2}}$ is more intense over the ribs inclined at 30° to the approach flow throughout the entire layer. Additionally, in both parallel and diverging sections, the wall-normal Reynolds stress, $\overline{v^{+2}}$ is least over the ribs inclined at 90° to the approach flow, and it attained maximum over ribs at 30° to approach flow. However, the larger distribution of $\overline{v^{+2}}$ over 30° ribs does not reflect in the corresponding $-\overline{u^+v^+}$, since its

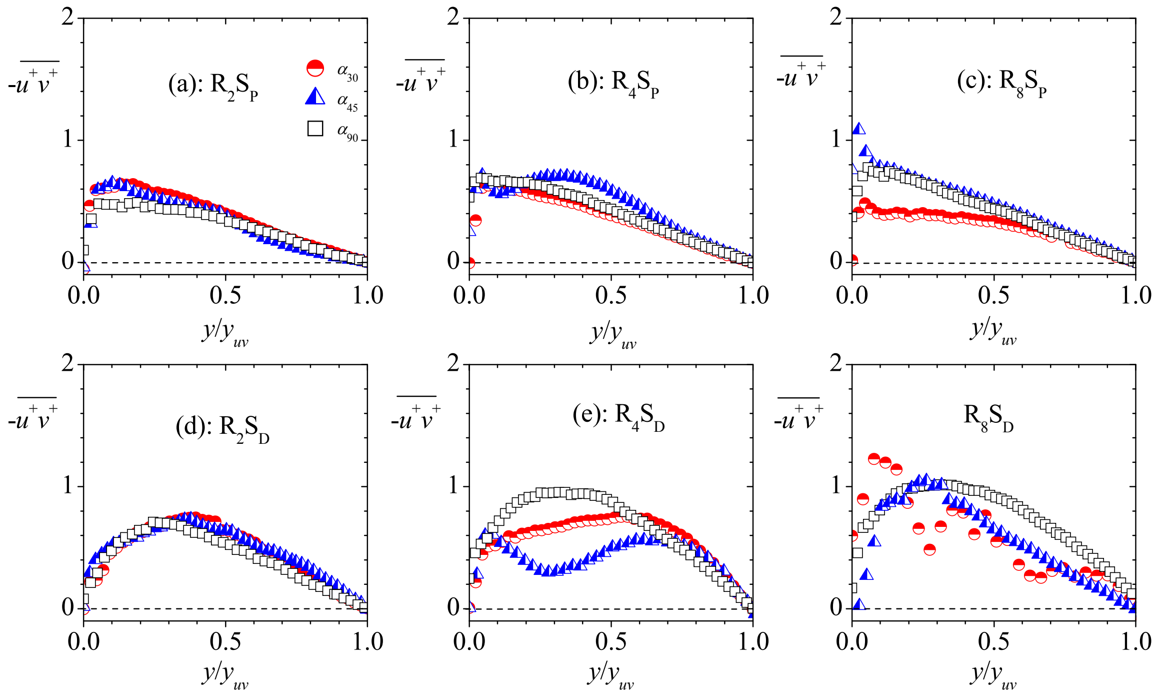

Figure 5.31: Distribution of Reynolds shear stress in the parallel and diverging sections of ribs at 30°, 45° and 90° normalized by U_τ^2.

Reynolds shear stress is least away from the wall compared to $-\overline{u^+v^+}$ over 45° and 90° ribs. On the other hand, $-\overline{u^+v^+}$ over the 45° and 90° ribs in the parallel section are nearly identical in magnitude. The present results for the streamwise Reynolds stress and Reynolds shear stress in the parallel section of the ribs inclined at 90° and 45° to the approach flow are at variance to the data reported by Tachie and Shah (2008). They observed a reduction in $\overline{u^{+2}}$ and $-\overline{u^+v^+}$ over the ribs inclined at 45° compared to the perpendicular ribs. This may be due to combined effects of symmetric roughness, higher background turbulence level and blockage ratio in their study. On the other hand, the increase observed for $\overline{v^{+2}}$ over ribs at 45° to the approach flow compared to the ribs at 90° to the approach flow is consistent with the data of Tachie and Shah (2008). However, the increase in the present $\overline{v^{+2}}$ is more dramatic and it extends across the entire layer of the flow whereas the previous study only observed the increase in the region beyond y = $0.3y_{uv}$.

5.2.1.6 Anisotropy of Reynolds Stresses

The distributions of the ratios $-\overline{uv}/\overline{u^2}$ and $\overline{v^2}/\overline{u^2}$ are shown in Figure 5.32 and Figure 5.33, respectively. Like the stresses, the ratios $-\overline{uv}/\overline{u^2}$ and $\overline{v^2}/\overline{u^2}$ over the d-type ribs are relatively less sensitive to rib inclination angle in both the parallel section (Figure 5.32a and Figure 5.33a) and diverging section (Figure 5.32d and Figure 5.33d). However, for $y > 0.5y_{uv}$ in the parallel section, the distribution of $-\overline{uv}/\overline{u^2}$ reveals subtle differences. In Figures 5.32b and 5.32e, except in the regions $0.17y_{uv} < y < 0.75y_{uv}$ and $0.12y_{uv} < y < 0.55y_{uv}$, $-\overline{uv}/\overline{u^2}$ is similar in both the parallel and diverging sections of the intermediate type ribs. The ratio of the normal stresses in the parallel section of the intermediate type ribs is unaffected by the rib inclination angle to the approach flow. Due to the larger distribution of the inactive motion compared to the active motion in the diverging section of the 90° ribs, $\overline{v^2}/\overline{u^2}$ is reduced over 90° ribs compared to the ratio over 45° and 30°

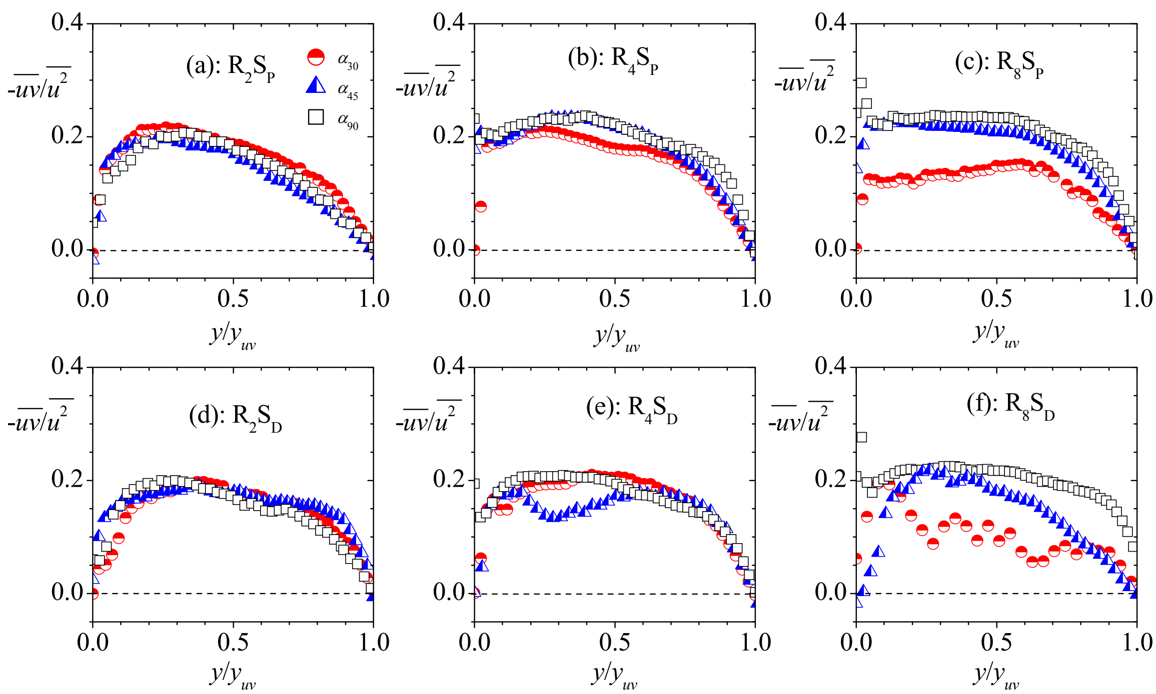

Figure 5.32: Distribution of $-\overline{uv}/\overline{u^2}$ in the parallel and diverging sections of ribs at 30°, 45° and 90°.

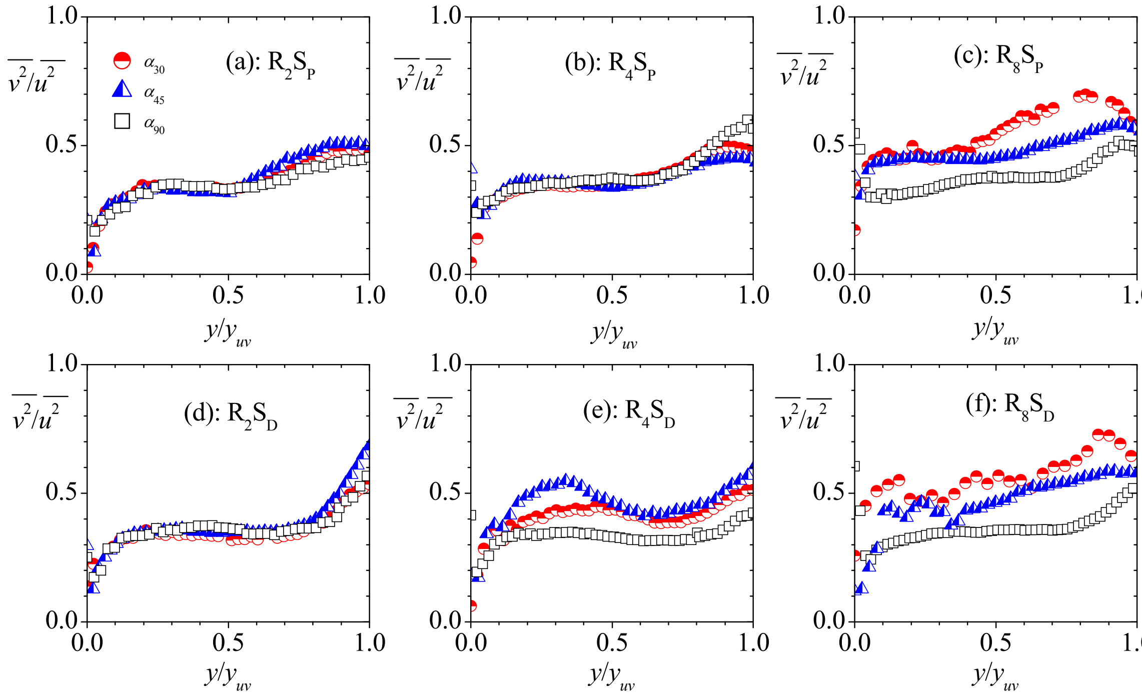

Figure 5.33: Distribution of $\overline{v^2}/\overline{u^2}$ in the parallel and diverging sections of ribs at 30°, 45° and 90°.

ribs. Thus, in the presence of adverse pressure gradient, the 90° ribs made the stresses more anisotropic. Over the k-type ribs, the ratio $-\overline{uv}/\overline{u^2}$ in both the parallel and diverging sections are always larger for the 90° ribs than 45° and 30° ribs, and it decreases with α. The behaviour of $-\overline{uv}/\overline{u^2}$ over the ribs inclined at 45° and 30° to the approach flow relative to the data for ribs at 90° is consistent with the data of Tachie and Shah (2008). Conversely, the corresponding ratio of the normal stresses is augmented over 30° ribs but it is lower over 90° ribs. This is due to enhanced production of v^2 compared to u^2over the 30° ribs. Therefore, the k-type ribs demonstrate that the anisotropy of the Reynolds stresses reduces as the inclination angle of the ribs is decreased. It also followed that, turbulence model using the isotropic assumption would perform better prediction of the flow over ribs at lower inclination angle to the approach flow than over ribs at 90° to the approach flow.

The distribution of the structure parameter is shown in Figure 5.34. The structure parameter over the d-type ribs is less sensitive to rib inclination angle in both the parallel and diverging sections. However, for $y > 0.5y_{uv}$ in the parallel section, the distribution of a_1 tends to demonstrate modest differences. Except in the region $0.17y_{uv} < y < 0.75y_{uv}$ where the structure parameter sags for the intermediate type ribs at 30° ribs, a_1 in the parallel section is also less sensitive to the orientation of the ribs to the approach flow (Figure 5.34b). In the diverging section, a_1 is larger over the ribs at 90° to the approach flow but, they are lower over ribs at 45° and 30° to the approach flow for $y < 0.6y_{uv}$. However, the k-type ribs demonstrate that, a_1 diminishes with decreasing rib inclination angle in both the parallel and diverging sections. The reduced level of a_1 over the 45° and 30° k-type ribs is due to considerable increase in $\overline{u^2}$ and $\overline{v^2}$ relative to $-\overline{uv}$.

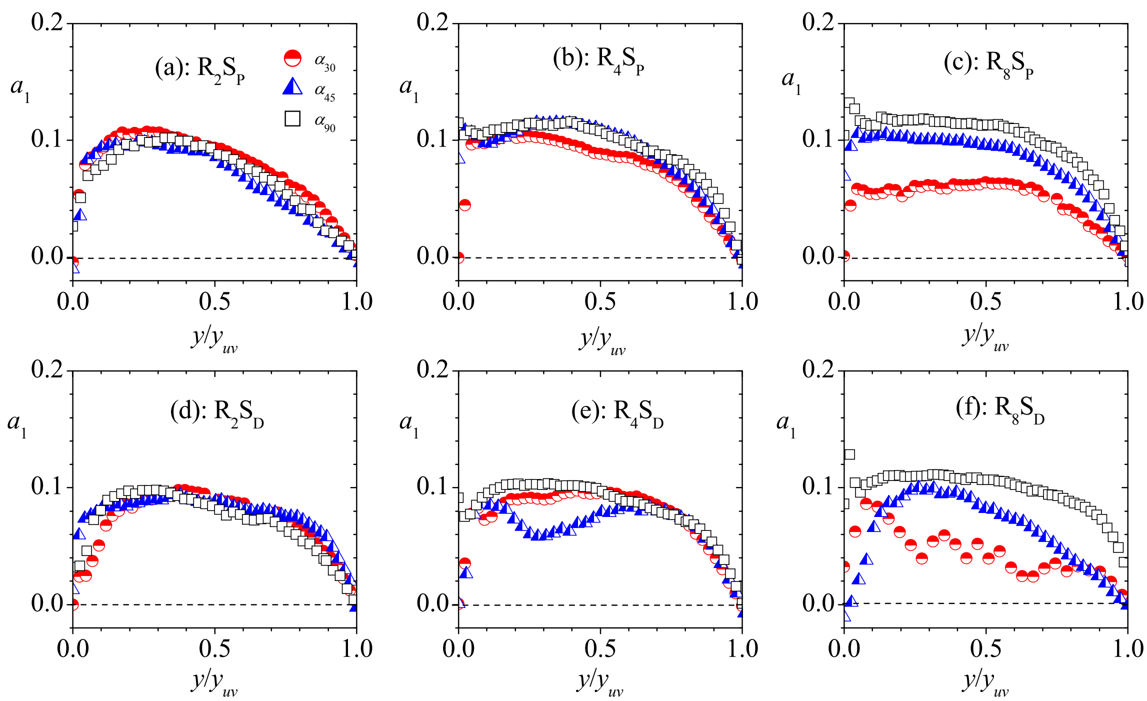

Figure 5.34: Distribution of Townsend structure parameter, a_1 in the parallel and diverging sections of ribs at 30°, 45° and 90°.

5.2.2 TURBULENCE STRUCTURE

5.2.2.1 Quadrant Decomposition

The quadrant decomposition is used to examine possible changes in the contribution by the turbulence structure to turbulence production at the mid-span due to variation in rib inclination angle to the approach flow. Figure 5.35 and Figure 5.36 show the fractional contributions to the Reynolds shear stress for H = 0 from the four quadrant events. The results in Figure 5.35 and Figure 5.36 demonstrate that the bursting process is altered by rib inclination, even over the d-type ribs where the Reynolds stresses were found to be less influenced by α in both the parallel and diverging sections. Over the d-type ribs both interaction motions ($Q1$ and $Q3$) are strengthened over the ribs at 45°, but they are weaker over ribs at 30°. The modification is most severe in the outer region ($y > 0.6\delta$). The intermediate type ribs revealed an increase in both $Q1$ and $Q3$ for ribs at 30° in the region $0.3\delta \leq y \leq 0.9\delta$, but those over ribs at 90° and 45° are in excellent agreement for

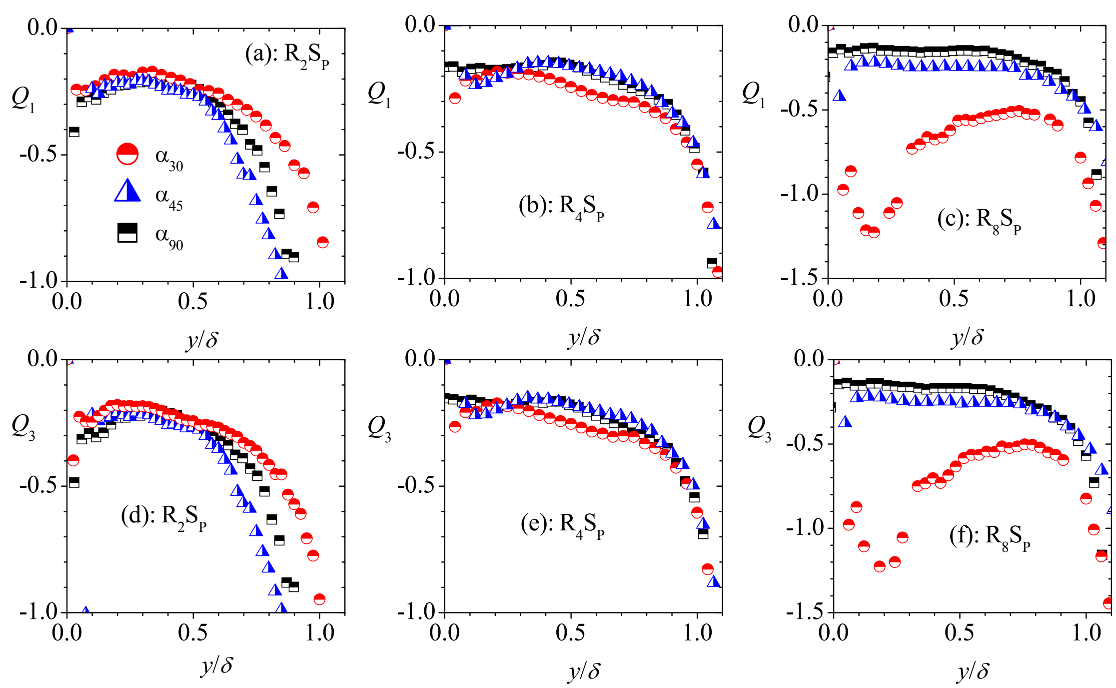

Figure 5.35: The distributions of the fractional contributions to $-\overline{uv}$ from first and third quadrants in the parallel section of ribs at 30°, 45° and 90° to the approach flow for $H = 0$.

the entire boundary layer. Meanwhile, the *k*-type ribs show that the interaction motions are significantly stronger for ribs at 30° in the entire boundary layer. These outward and inward interaction motions however diminished as α increased.

The corresponding ejection and sweep events are similar over the intermediate type ribs in the parallel section (Figures 5.36b and 5.36e). However, both the ejection and sweep events do not produce the same amount of $-\overline{uv}$ for all inclination angles, resulting in variation in $-\overline{uv}$ with α (Figure 5.28b and Figure 5.31b). For the *d*-type ribs, the fractional contributions from both ejections and sweeps to the Reynolds shear stress are unaffected by rib inclination angle near the wall, but for $y \geq 0.6\delta$ both $Q2$ and $Q4$ become stronger for the ribs inclined at 45° and weaker for the ribs at 30° to the approach flow. On the other hand, the *k*-types ribs at 30° produced intense ejection and sweep events. Although the difference in the distribution of $Q2$ and $Q4$ between ribs at 90° and 45° is small, the ejection and sweep events are weaker for ribs at 90° to the approach flow.

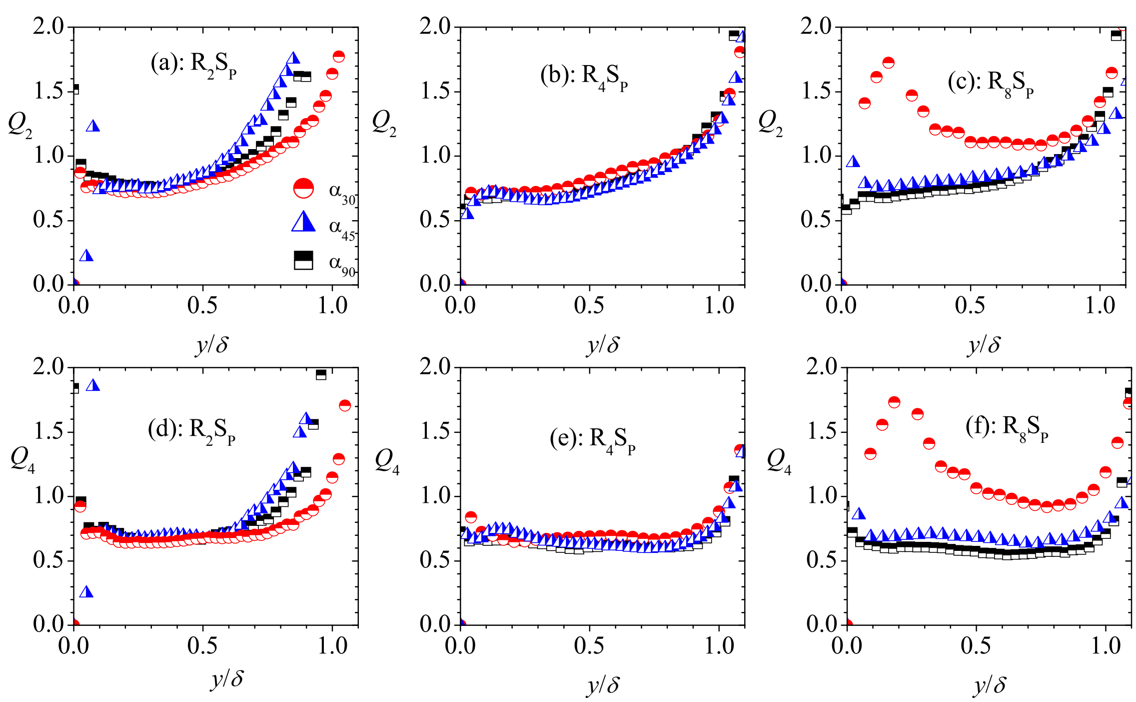

Figure 5.36: The distributions of the fractional contributions to $-\overline{uv}$ from second and fouth quadrants in the parallel section of ribs at 30°, 45° and 90° to the approach flow for $H = 0$.

Nevertheless, the strong $Q2$ and $Q4$ for ribs at 30° only produced very little Reynolds shear stress compared to ribs at 90° and 45° (Figure 5.28c and Figure 5.31c). Therefore, it is likely that inclusion of the smaller turbulence fluctuations (i.e., for H = 0) in the quadrant events, contributed significantly to $Q2$ and $Q4$ as well as $Q1$ and $Q3$ motions over the k-type ribs at 30° to the approach flow.

The fractional contributions of the four quadrant events to the Reynolds shear stress in the diverging section are reported in Figure 5.37 and Figure 5.38 for H = 0. In Figure 5.37a and 5.37d, the interaction motions over the d-type ribs tend to be stronger for ribs at 90° as the edge of boundary layer is approached. However, $Q1$ and $Q3$ are almost identical for ribs at 45° and 30°, except for the rapid rise observed as the wall is approached for ribs at 30°. Over the intermediate type and k-type ribs, the outward and inward interaction motions are stronger for ribs at 45° and they are weaker for ribs at 90°.

In Figures 5.38a and 5.38d, both $Q2$ and $Q4$ events are strengthened in the outer

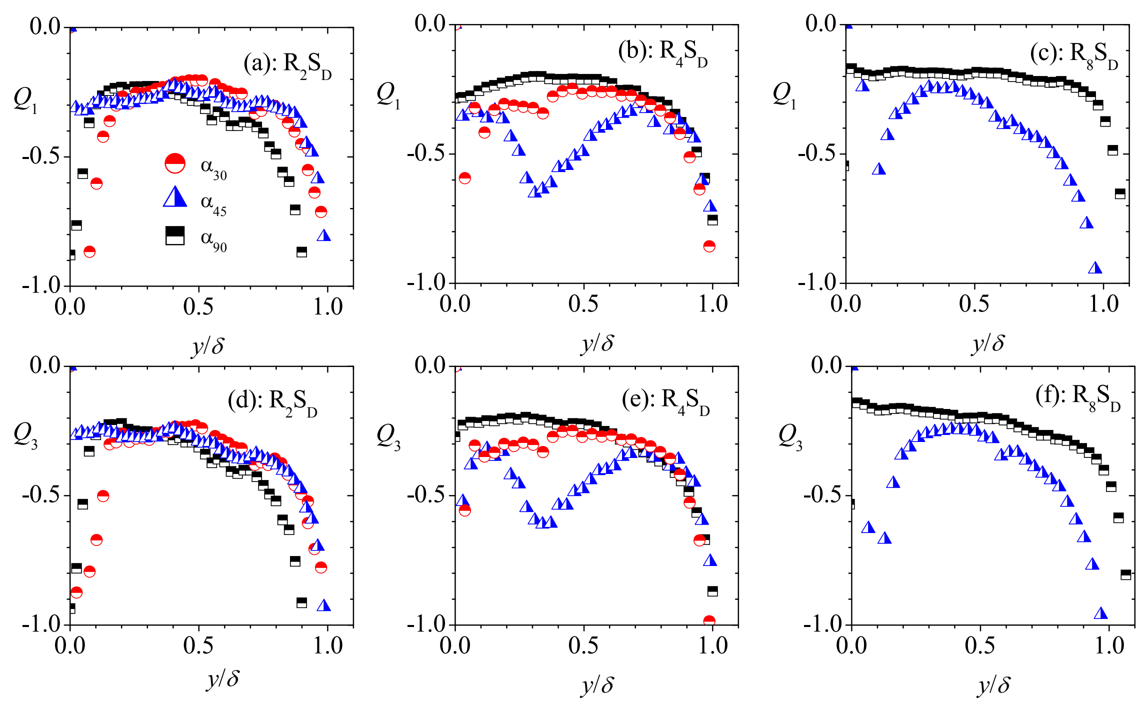

Figure 5.37: The distributions of the fractional contributions to $-\overline{uv}$ from first and third quadrants in the diverging section of ribs at 30°, 45° and 90° to the approach flow for H = 0.

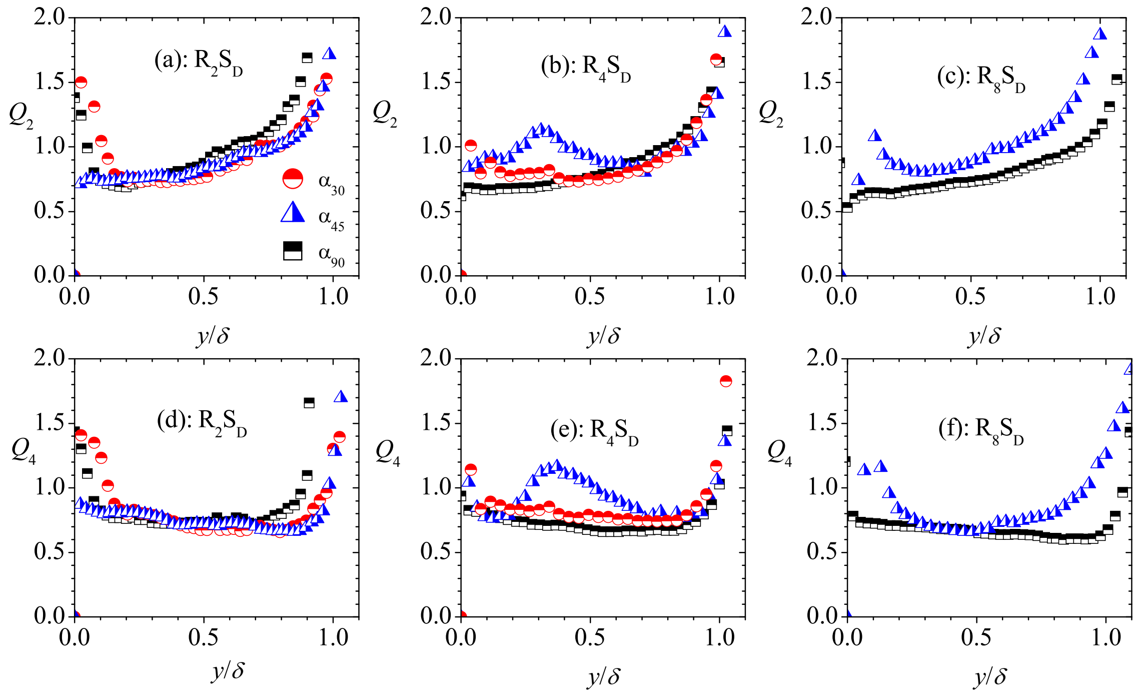

Figure 5.38: The distributions of the fractional contributions to $-\overline{uv}$ from second and fourth quadrants in the diverging section of ribs at 30°, 45° and 90° to the approach flow for $H = 0$.

region over the d-type ribs positioned perpendicular to the approach flow. Even though both $Q2$ and $Q4$ are similar for ribs at 45° and 30° to approach flow, a rapid rise is seen in both events for ribs at 30° as the wall is approached for $y < 0.2\delta$. This rise is caused by strong bursting by the coherent structures in the near-wall region. Over the intermediate type and k-type ribs, both the ejection and sweep events are stronger for ribs at 45° for most part of the boundary layer (5.38b-c and Figure 5.38e-f). These events are usually weaker for the ribs at 90°, however, over the intermediate type ribs, good agreement is noticed in the distribution of $Q2$ for ribs at 90° and 30° to the approach flow for $y > 0.35\delta$. The intense pumping of the low-velocity and high-velocity fluid by the vortices over intermediate type and k-type ribs inclined at 45° to the approach flow generated very small Reynolds shear stress compared to ribs at 90° and 30°.

5.2.2.2 Two-Point Correlation Coefficients

The two-point velocity correlations are presented to quantify average size and to further reveal any differences in the turbulence structure at the mid-span of the channel as the rib orientation is varied for each type of ribs.

The distributions of the streamwise and wall-normal one-dimensional profiles of R_{uu} correlation in the parallel section are reported in Figure 5.39. The distribution of the R_{uu} profiles in the streamwise direction over the *d*-type ribs is less sensitive to rib orientation, but the corresponding wall-normal profiles of R_{uu} collapsed. Consideration of the plots of R_{uu} correlation over intermediate type ribs revealed a subtle increase in the R_{uu} profiles for ribs at 45°. The most dramatic effect of rib inclination angle is revealed over the *k*-type ribs. Evidently, over the *k*-type ribs both the streamwise and wall-normal R_{uu} correlations diminished with decreasing α. Thus, the spatial structure embodied in R_{uu} correlation will increase as the rib inclination angle becomes larger.

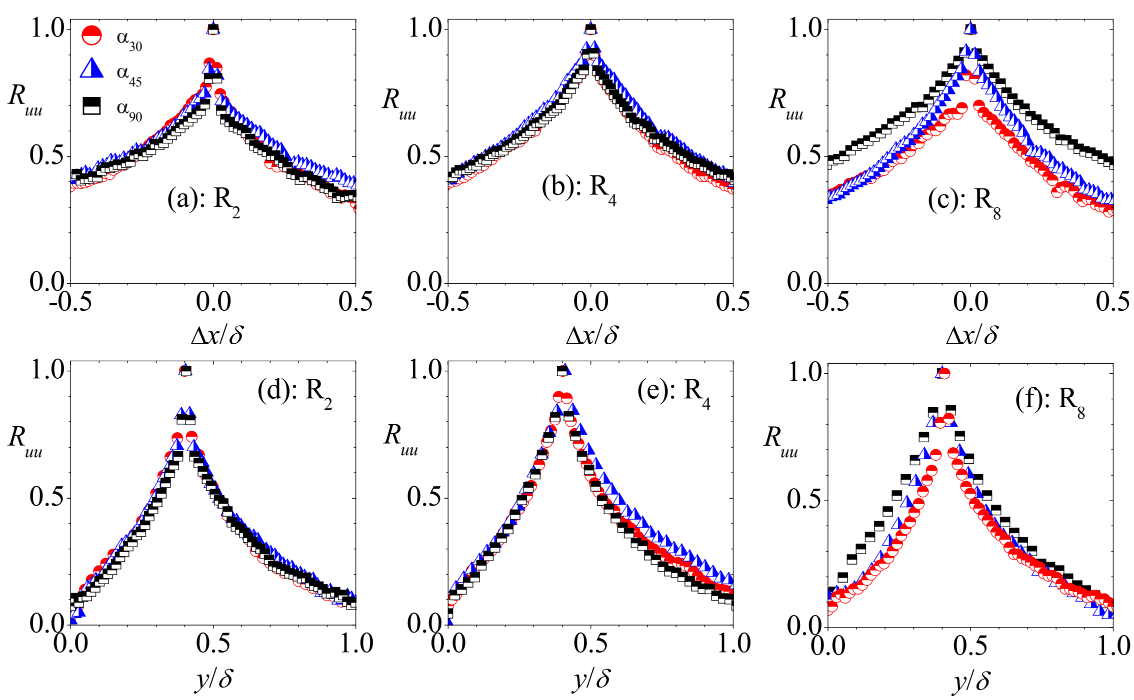

Figure 5.39: Streamwise and wall-normal one-dimensional profiles of R_{uu} at $y_{ref} = 0.4\delta$ in the parallel section of ribs at 30°, 45° and 90° to approach flow.

Figure 5.40 presents the estimated characteristics length-scales of R_{uu} correlation for the different inclination angles. For the *d*-type ribs, Lx_{uu}/δ is larger for ribs inclined at 45° to the approach flow than ribs at 90° and 30° (Figure 5.40a). However, only small variation in Ly_{uu}/δ is observed over the *d*-type ribs in the narrow region $0.5\delta \leq y \leq 0.8\delta$ (Figure 5.40d). Thus, the physical streamwise size of the hairpin packet is increased over the 45° ribs. In the case of the intermediate type ribs, near the wall at $y < 0.4\delta$, the streamwise size of the hairpin packet, Lx_{uu}/δ is magnified for ribs at 90° (Figure 5.40b), while the wall-normal size, Ly_{uu}/δ is unaffected by the rib inclination angle in this region (Figure 5.40e). In the outer layer ($y \geq 0.4\delta$), both Lx_{uu}/δ and Ly_{uu}/δ are larger over ribs at 45°. The reduction in Lx_{uu}/δ and Ly_{uu}/δ for ribs at 90° beyond $y = 0.4\delta$ may be due to ineffective stretching of the vortices as well as fewer vortices as the edge of the boundary layer is approached. For the *k*-type ribs, the distributions of Lx_{uu}/δ and Ly_{uu}/δ are significantly larger in most part of the boundary layer of the ribs inclined at 90° to the

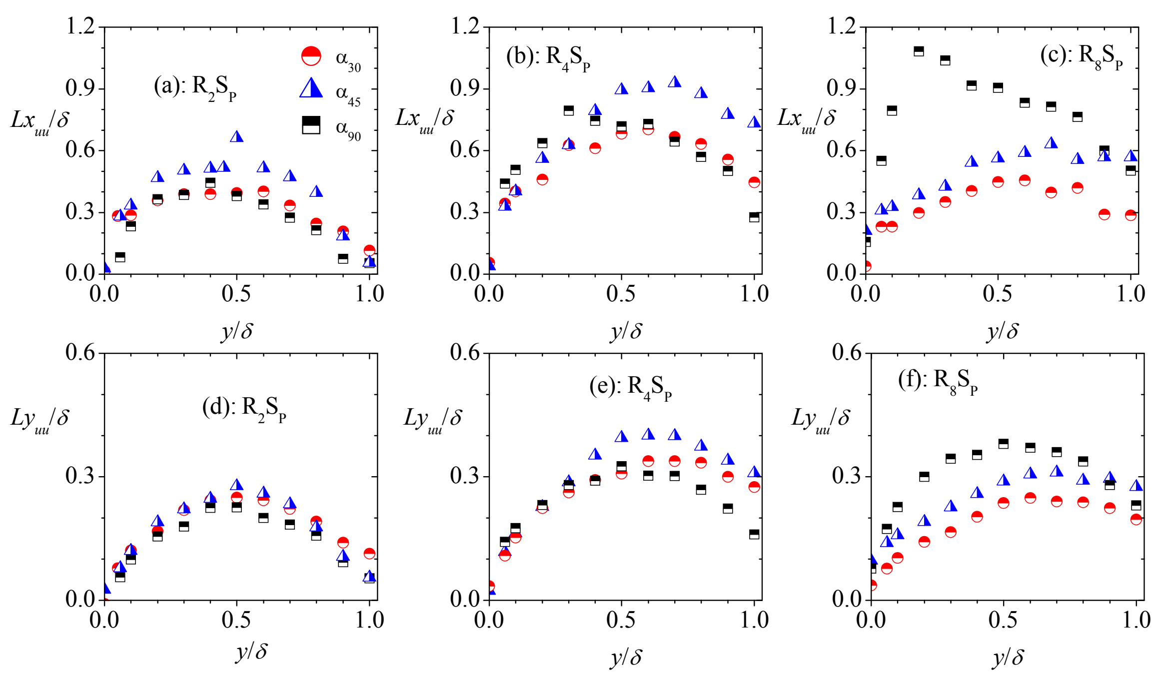

Figure 5.40: Average streamwise and wall-normal sizes of R_{uu} contours as a function of y/δ in the parallel section of ribs at 30°, 45° and 90° to approach flow.

approach flow, which is in good agreement with the profiles of the R_{uu} correlation. These length-scales over the *k*-type ribs decrease with decreasing α.

In the diverging section, distinct differences are observed in the distributions of one-dimensional profiles of R_{uu} over all the three types of ribs (Figure 5.41). For the case of the *d*-type ribs, pronounced variation due to rib inclination is observed in the streamwise profiles of R_{uu} than the wall-normal profiles of R_{uu}. Evidently, the R_{uu} correlation for ribs at 90° tends to be least whereas the R_{uu} correlation for the ribs at 45° is larger. However, a rapid decay in the wall-normal R_{uu} profile is observed for ribs at 45° as y/δ increases in the outer layer. Over the intermediate type and *k*-type ribs, both the streamwise and wall-normal profiles of R_{uu} correlation are diminished over ribs at 45°and 30°, with the former exhibiting the least values.

Both Lx_{uu}/δ and Ly_{uu}/δ over intermediate type and *k*-type ribs consisting of ribs at 90° to approach flow are considerable larger in most part of the boundary layer (Figure

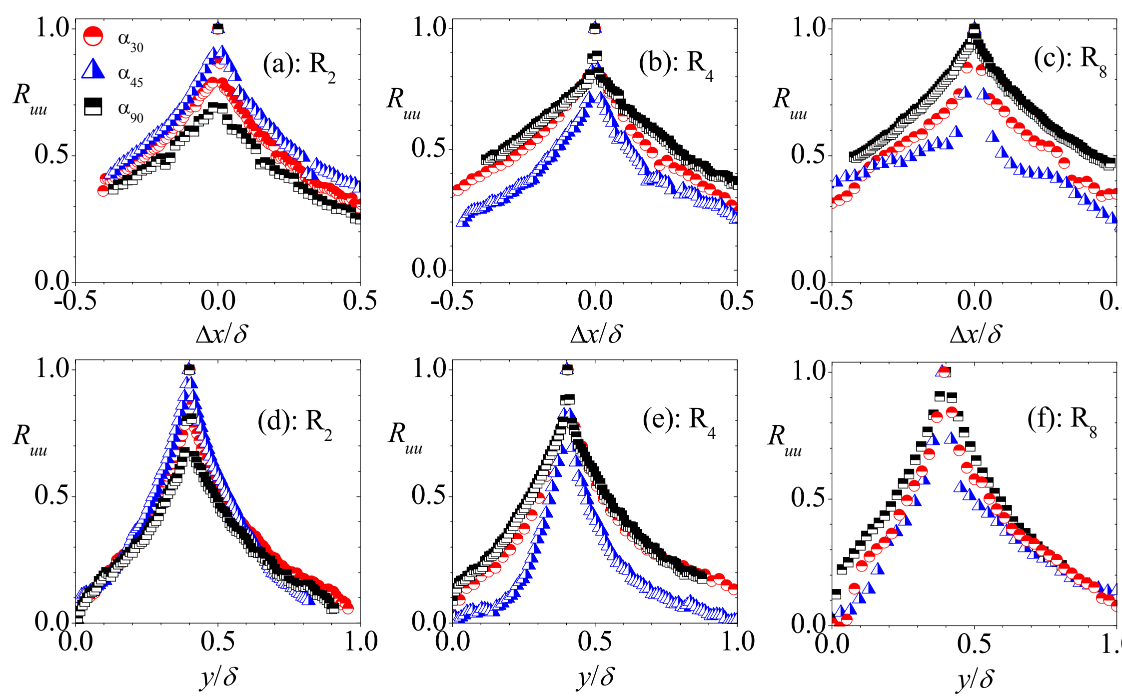

Figure 5.41: Streamwise and wall-normal one-dimensional profiles of R_{uu} at $y_{ref} = 0.4\delta$ in the diverging section of ribs at 30°, 45° and 90° to approach flow.

5.42). At locations where Lx_{uu}/δ and Ly_{uu}/δ drop for the ribs at 90°, a rise in the distributions of Lx_{uu}/δ and Ly_{uu}/δ is observed for ribs inclined at 30°. Meanwhile, the values of Lx_{uu}/δ and Ly_{uu}/δ are consistently lower for ribs positioned at 45°, suggesting that the size of the hairpin packet is diminished when the ribs are positioned at 45° to the approach flow due to strong effects of secondary motion on the formation of the building blocks of the packet and its growth. Interestingly, the distributions of Lx_{uu}/δ and Ly_{uu}/δ over *d*-type ribs are also in agreement with the distribution of R_{uu} profiles in the streamwise and wall-normal directions. In this case, Lx_{uu}/δ and Ly_{uu}/δ are magnified for ribs at 45° and they are reduced for ribs at 90°.

The profiles of R_{vv} correlation in the parallel section are reported in Figure 5.43. The streamwise and the wall-normal distributions of R_{vv} correlation over *d*-type ribs collapsed reasonably well for the three inclination angles (Figures 5.43a and 5.43d). Although similar collapse is evident over the intermediate type ribs, a subtle increase in

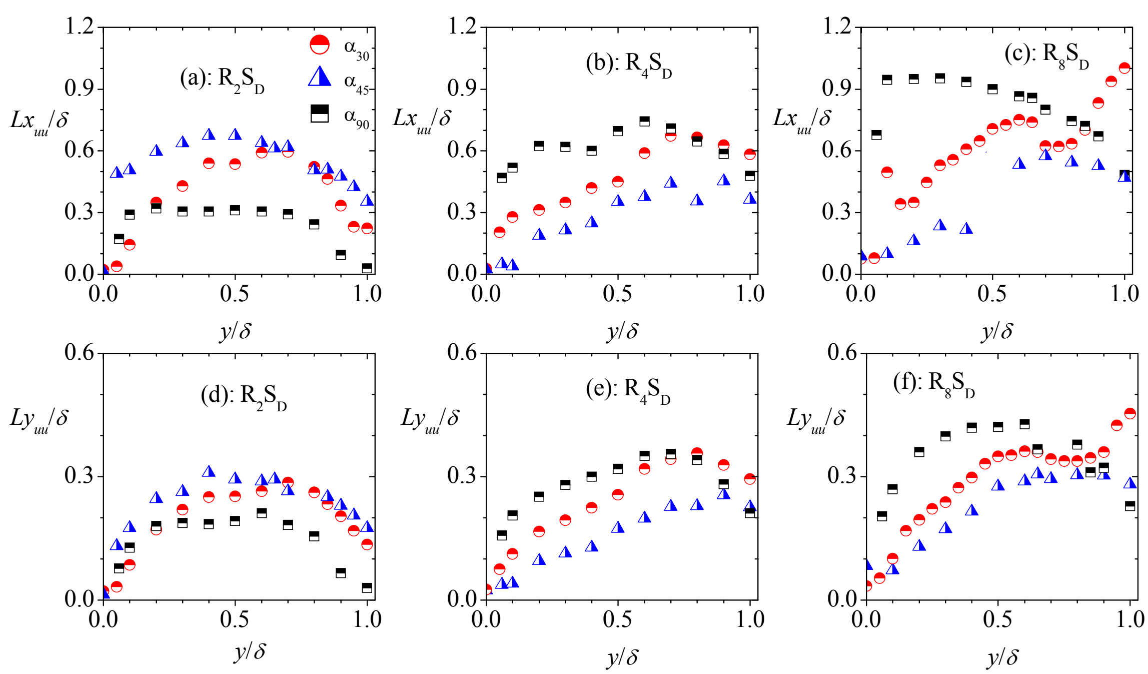

Figure 5.42: Average streamwise and wall-normal sizes of R_{uu} contours as a function of y/δ in the diverging section of ribs at 30°, 45° and 90° to approach flow.

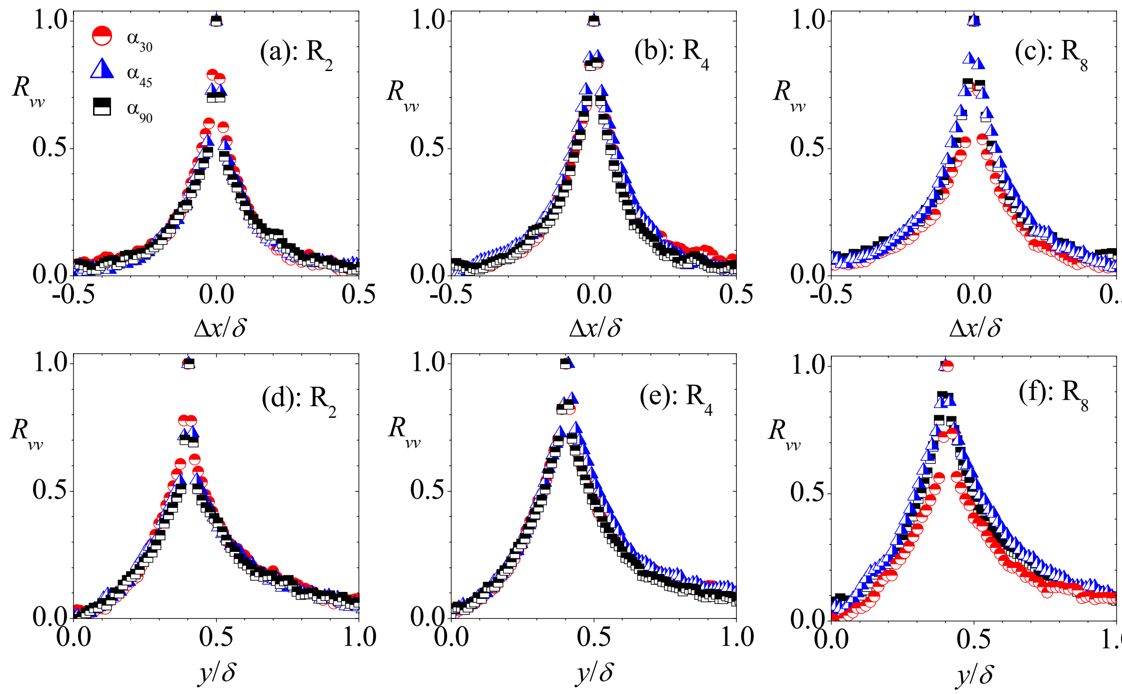

Figure 5.43: Streamwise and wall-normal one-dimensional profiles of R_{vv} at $y_{ref} = 0.4\delta$ in the parallel section of ribs at 30°, 45° and 90° to approach flow.

R_{vv} correlation is observed for ribs inclined at 45° to the approach flow, especially for the right tail (Figures 5.43b and 5.43e). The collapse in R_{vv} correlation over the *d*-type and intermediate type ribs implies that the rib orientation would have less influence on the spatial structure embodied in R_{vv} correlation over these types of ribs. Meanwhile, the *k*-type ribs revealed an increase in the profiles of R_{vv} correlation for ribs at 45° to the approach flow (Figures 5.43c and 5.43f). On the other hand, the lower R_{vv} correlation for ribs at 30° implied a reduction in the spatial extents of the R_{vv} contours.

Despite the collapse reported for the streamwise and wall-normal distribution of R_{vv} correlation over the *d*-type and intermediate type ribs, Lx_{vv}/δ and Ly_{vv}/δ were somewhat influenced by α (Figure 5.44). In this case, both Lx_{vv}/δ and Ly_{vv}/δ exhibit a modest increase over *d*-type ribs consisting of ribs inclined at 30° for $y > 0.2\delta$ whilst those for ribs perpendicular to approach flow are reduced. For the intermediate type ribs,

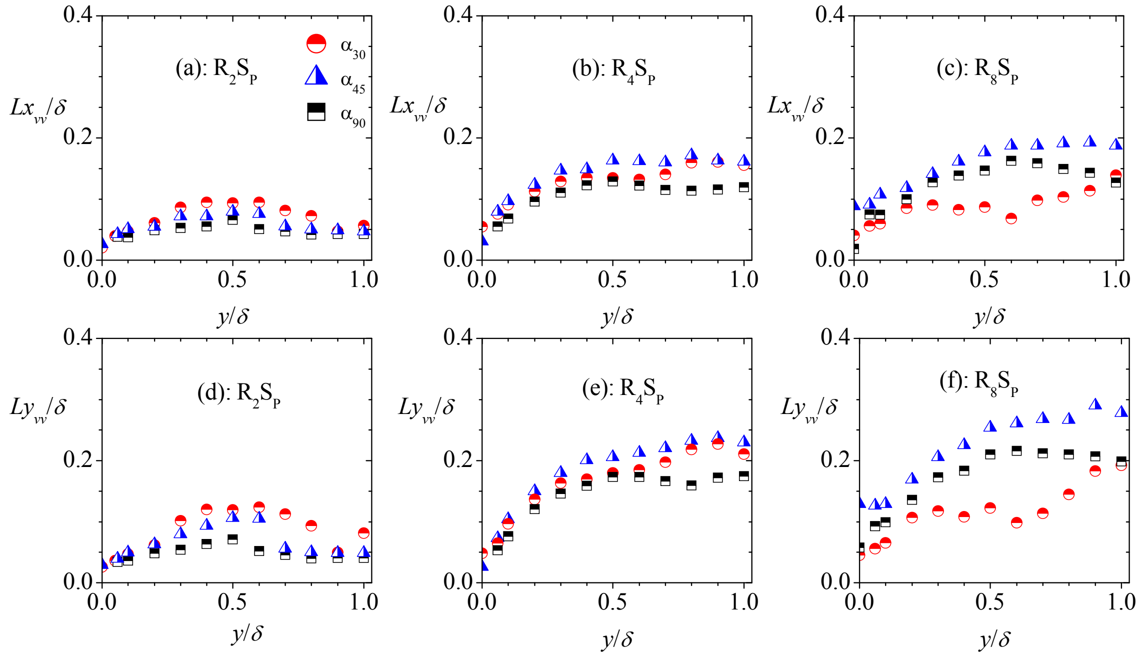

Figure 5.44: Average streamwise and wall-normal sizes of R_{vv} contours as a function of y/δ in the diverging section of ribs at 30°, 45° and 90° to approach flow.

however, slight magnification of Lx_{vv}/δ and Ly_{vv}/δ for ribs at 45° is revealed whereas a reduction is observed in the length-scales for ribs at 90°. The Lx_{vv}/δ and Ly_{vv}/δ over *k*-type ribs are apparently larger for ribs at 45° and least for ribs at 30°.

Figure 5.45 displays the streamwise and the wall-normal distributions of R_{vv} correlation in the diverging section of the ribs at 90°, 45° and 30° to the approach flow. In the diverging section of the *d*-type ribs, the R_{vv} correlation for ribs at 90° is least but, it is larger for ribs at 45°. Over the intermediate type ribs, the R_{vv} correlation collapsed for all inclination angles. Remarkable agreement is also evident in the streamwise distribution of R_{vv} profiles over *k*-type ribs (Figure 5.45c) but, the wall-normal profile is slightly reduced for ribs at 45° to the approached flow (Figure 5.45f).

Figure 5.46 reports the characteristics length-scales, Lx_{vv}/δ and Ly_{vv}/δ of the R_{vv} contours in the diverging section. Clearly, over the *d*-type ribs the average values of Lx_{vv}/δ and Ly_{vv}/δ are augmented by ribs at 45° while they are diminished by ribs at 90° to

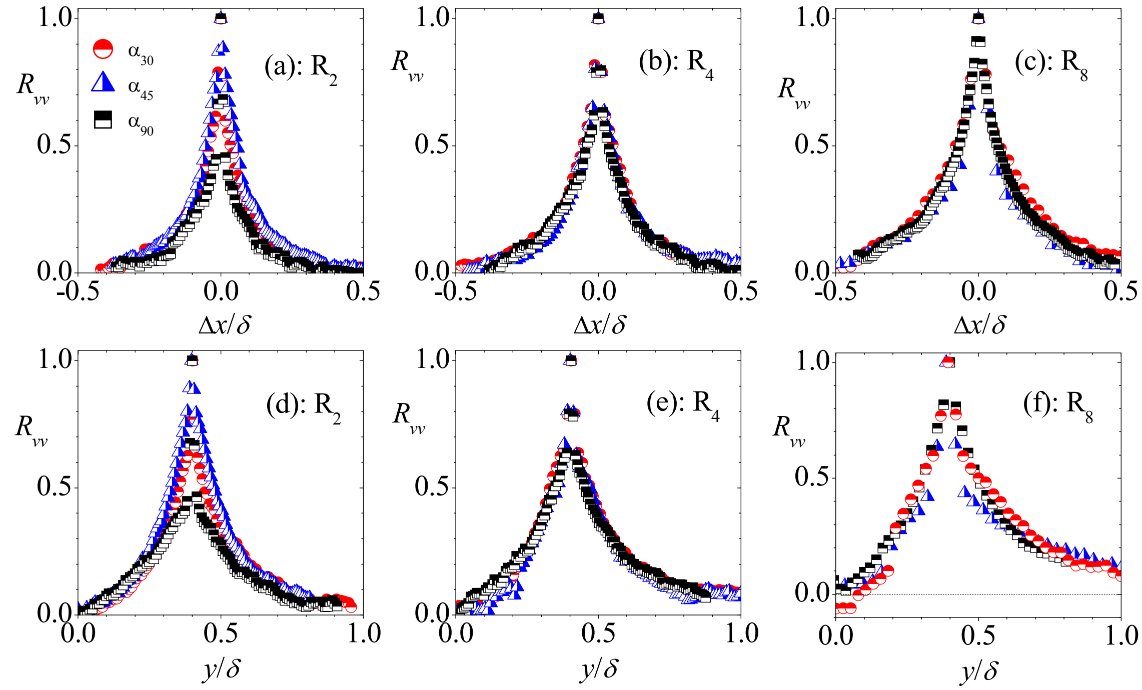

Figure 5.45: Streamwise and wall-normal one-dimensional profiles of R_{vv} at $y_{ref} = 0.4\delta$ in the diverging section of ribs at 30°, 45° and 90° to approach flow.

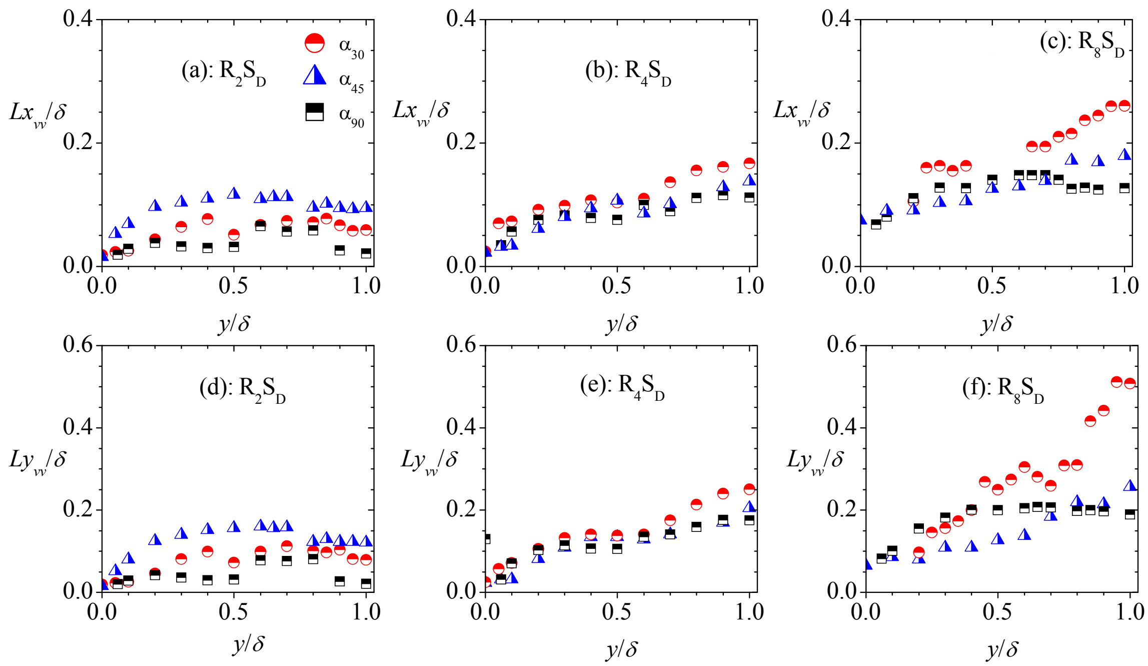

Figure 5.46: Average streamwise and wall-normal sizes of R_{vv} contours as a function of y/δ in the diverging section of ribs at 30°, 45° and 90° to approach flow.

the approach flow, which is in good agreement with the distribution of R_{vv} profiles. For the case of the intermediate type and k-type ribs, the distributions of Lx_{vv}/δ and Ly_{vv}/δ for ribs at 30° are enhanced. While no variation among both Lx_{vv}/δ and Ly_{vv}/δ for intermediate type ribs at 90° and 45° is observed, the distribution of Lx_{vv}/δ and Ly_{vv}/δ is least over k-type ribs at 45° for $y \leq 0.7\delta$.

The streamwise and the wall-normal profiles of R_{uv} in the parallel section are shown in Figure 5.47. Variations in the R_{uv} correlation with α are observed over all the three types of ribs, however the differences are more dramatic over the k-type ribs than the d-type and the intermediate type ribs. For example, over the k-type ribs, the magnitude of the streamwise and the wall-normal R_{uv} correlation is larger for ribs at 90° to the approach flow, but it is least for ribs at 30°. In fact, this distribution of R_{uv} correlation is similar to the distribution of the corresponding R_{uu} correlation in the

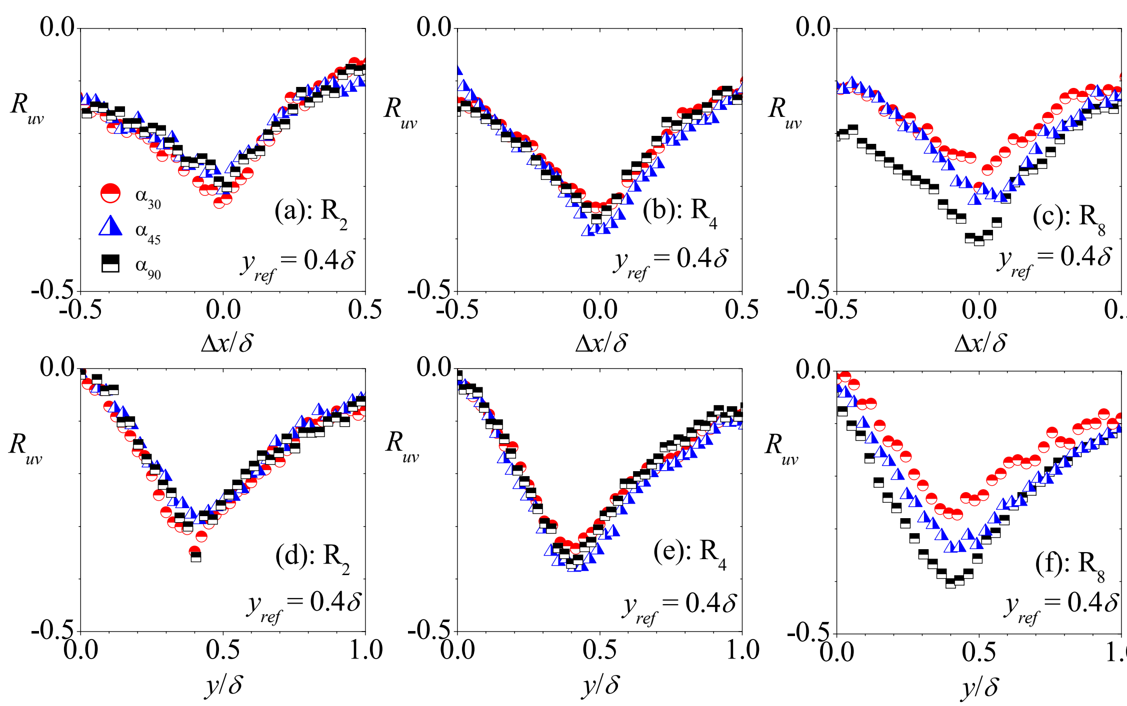

Figure 5.47: Streamwise and wall-normal one-dimensional profiles of R_{uv} at $y_{ref} = 0.4\delta$ in the parallel section of ribs at 30°, 45° and 90° to approach flow.

parallel section. Meanwhile, the small variation of R_{uv} correlation over the *d*-type and intermediate type ribs implies that at lower *p*/*k*, there is higher tendency for the spatial structures embodied in R_{uv} correlation to be less sensitive to rib inclination angle in the parallel section.

In the diverging section, however, the effects of rib inclination angle are very dramatic over each type of ribs, but as *p*/*k* increases the impact of rib orientation becomes stronger (Figure 5.48). The slight reduction of the R_{uv} correlation for ribs at 90° is an indication of a reduction in the spatial structure embodied in R_{uv} correlation over ribs at 90° (Figures 5.48a and 5.48d). Both the streamwise and the wall-normal profiles of R_{uv} correlation over the intermediate type and *k*-type ribs are reduced for ribs at 45°, but the R_{uv} correlation is mostly larger for the ribs at 90°.

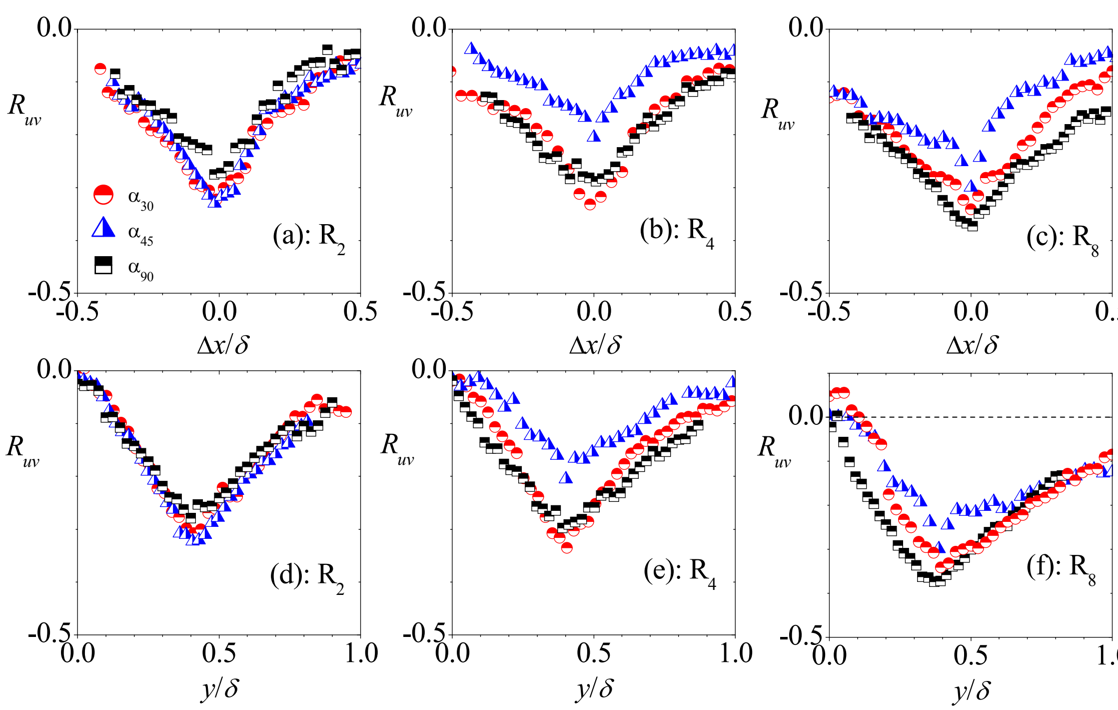

Figure 5.48: Streamwise and wall-normal one-dimensional profiles of R_{uv} at $y_{ref} = 0.4\delta$ in the diverging section of ribs at 30°, 45° and 90° to approach flow.

CHAPTER 6

EXAMINATION OF THE TURBULENCE STRUCTURES IN THE STREAMWISE-SPANWISE PLANE

In this chapter, the measurements in the *x*-*z* plane are used to examine the spanwise turbulence structures in the near-wall and outer regions of the flows over the smooth wall and *k*-type ribs at 90° and 45° to the approach flow. The structure analysis techniques implemented include Galilean decomposition of the instantaneous velocity fields, two-point correlations and linear stochastic estimate. This analysis of the structures in the *x*-*z* plane will provide more insight into the differences observed in the flow characteristics due to APG, roughness and rib inclination angle. The wall-normal locations of these measurements (presented in Table 3.2) have been regrouped in Table 6.1. In this table, y_{LL} denotes the nearest locations close to the wall followed by y_{UL} while y_{OL} represents typical locations in the outer region.

Table 6.1: Wall-normal locations for *x*-*z* plane measurements

Test	y_{LL}	y_{UL}	y_{OL}
SMS_P	$89\nu/U_\tau = 0.19\delta^+$	$156\nu/U_\tau = 0.33\delta^+$	0.75δ
SMS_D	$49\nu/U_\tau = 0.11\delta^+$	$81\nu/U_\tau = 0.18\delta^+$	0.75δ
$R_8S_P\alpha_{90}$	$206\nu/U_\tau = 0.18\delta^+$	$305\nu/U_\tau = 0.25\delta^+$	0.75δ
$R_8S_D\alpha_{90}$	$247\nu/U_\tau = 0.17\delta^+$	$527\nu/U_\tau = 0.36\delta^+$	0.75δ
$R_8S_P\alpha_{45}$	$182\nu/U_\tau = 0.28\delta^+$	$338\nu/U_\tau = 0.57\delta^+$	0.75δ
$R_8S_D\alpha_{45}$	$71\nu/U_\tau = 0.36\delta^+$	$125\nu/U_\tau = 0.58\delta^+$	0.75δ

6.1 INSTANTANEOUS VELOCITY FIELDS IN THE *X*-*Y* PLANE

Tomkins and Adrian (2003) examined the spanwise turbulence structures and their grow mechanisms in a ZPG turbulent boundary layer flow over smooth wall using PIV. These were achieved by conducting a series of measurements in the x-z plane at several y-locations from the buffer layer to the top of the logarithm region for Re_θ = 1015 and 7705. The flow fields revealed large-scale regions of momentum deficit elongated in the streamwise direction. These regions were bordered by vortices organized in the streamwise direction. Tomkins and Adrian (2003) defined an idealized vortex signature in the x-z plane. The idealized signature consists of two principal components: (a) two elliptical counter-rotating vortex patterns created by the intersection of the laser light sheet with the angled vortex legs, and (b) a low-momentum event created by backwards induction of the legs and the vortex head. They further recognized a stagnation point created at the interface between the induced low-momentum event and faster upstream fluid as a possible third element of the signatures in the x-z plane. As observed earlier (Chapter 4 and Chapter 5), the hairpin packets were inclined in the wall-normal direction, so that the elliptical shape of the legs is an end result of the intersection of the horizontally positioned laser light sheet with the angled vortex legs. It also follows that the sizes of the major and minor axes of the resulting ellipse (sectional view of the legs in x-z plane) vary with the size and angle of the hairpin vortex at a given y-location. Moreover, the inclination angle of hairpin vortices often varies with y. On the basis of these arguments, Tomkins and Adrian (2003) concluded that the hairpin vortex signature in the x-z plane varies with y. However, it should be noted that in turbulent flows vortex exists in different forms and may not possessed two legs as opined by Tomkins and Adrian (2003). It has been observed, for example, that one-legged hairpin vortices or cane-like vortical structures are more common than two-legged hairpin vortices (Robinson, 1991). Also, Tomkins and Adrian (2003) argued that it is possible for asymmetric hairpin vortices with one dominant leg to exist. This will lead to the appearance of only one elliptical vortex leg in the hairpin signature. The end result is that the associated low-speed region may also be asymmetric. Nonetheless, these features are also considered signatures of hairpin-like vortices (Tomkins and Adrian, 2003).

The instantaneous velocity fields for typical realizations over the smooth wall and *k*-type (90° and 45°) ribs in the *x*-*z* plane at various *y*-locations in the near-wall and outer regions are examined to reveal the spanwise structures (Figure 6.1-Figure 6.6). The Galilean decomposition is applied by removing a constant convection velocity U_c from each realization. This yielded low-speed and high-speed regions which are consistent with the low-speed and high-speed streaks reported in previous studies (Kline *et al*., 1967). Note that the flow is from left to right, so that vectors pointing to left depict low-speed fluid, and vice versa. Also shown at the background of these vector fields are the contours of the signed swirling strength ($\lambda_{ci}\omega_y/|\omega_y|$). The red patches are the retrograde (positive swirling strength) rotating in the anti-clockwise direction whereas the blue patches are the prograde (negative swirling strength) rotating in the clockwise direction. These vortices identified by the swirling strength represent the legs of the hairpin vortices. Over each surface, the flow field is populated with prograde and retrograde vortices that depict the legs of hairpin-like vortices. Some of these vortices are actually convecting at almost the same convection velocity used for the Galilean decomposition. In addition, most of these vortices are one-sided vortex signatures (Robinson, 1991; Tomkins and Adrian, 2003). However, Figures 6.3 and 6.4 revealed the presence of two-legged hairpin-like vortices among the one-legged hairpin-like vortices. These two-legged hairpin-like vortex signatures are encircled with ellipses. For example, Tomkins

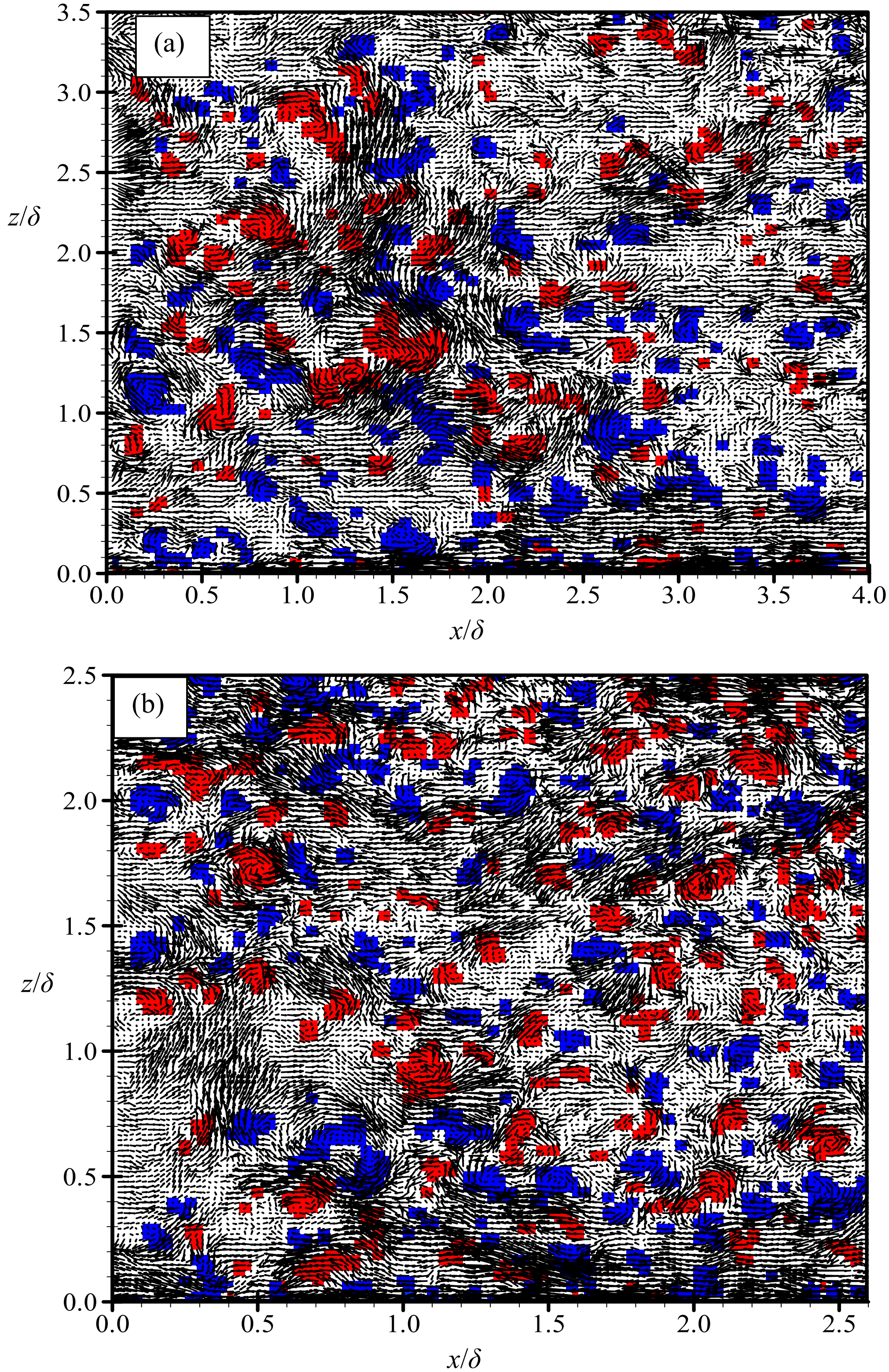

Figure 6.1: Instantaneous velocity field in the *x*-*z* plane over the smooth wall with positive swirl (red patches) and negative swirl (blue patches) superimposed: (a) parallel section at $y^+ = 156$, $U_c = 0.75U_m$ and (b) diverging section at $y^+ = 81$, $U_c = 0.70U_m$.

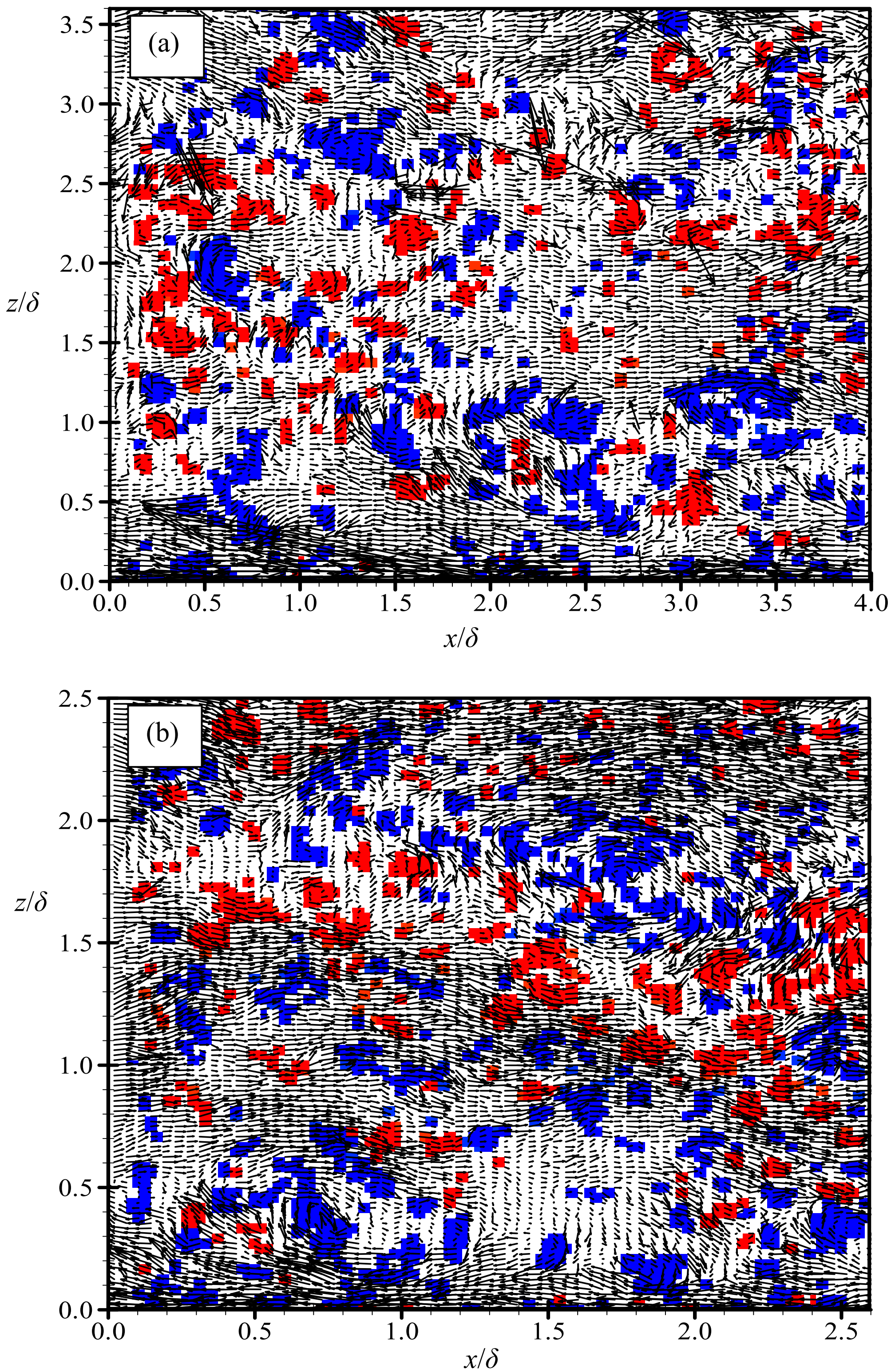

Figure 6.2: Instantaneous velocity field in the *x*-*z* plane over the smooth wall with positive swirl (red patches) and negative swirl (blue patches) superimposed: (a) parallel section at $y = 0.75\delta$, $U_c = 0.80U_m$ and (b) diverging section at $y = 0.75\delta$, $U_c = 0.77U_m$.

and Adrian (2003) also observed the presence of two-legged hairpin-like vortices among the one-legged hairpin-like vortices. Figure 6.4a revealed a pair of counter-rotating vortices that are placed side-by-side, but the downstream side of the vortex is tilted towards the side wall of the channel in the streamwise direction. The figure also displays a thin region of low-momentum fluid induced by the legs and the head of the vortex. This induced low-speed fluid is asymmetric consistent with the orientation of the legs of the vortex. At the upstream of this vortex, one can observed a high-speed fluid that is directed horizontally towards the asymmetric low-speed fluid, resulting in the formation of a stagnation point at the upstream of this hairpin vortex (Figure 6.4a). Since the dominant structures are one-legged hairpin-like vortices, the induced low momentum fluid regions are often asymmetric. Moreover, the vortices are not well aligned with each other.

The imperfect alignment of the vortices is common to all the rib-roughened surfaces with or without pressure gradient. It is apparent that for each set of the wall-normal locations, the population of the hairpin vortices in the diverging section exceeds that in the parallel section contrary to the observation in the *x*-*y* plane in Chapter 4. Moreover, the number of the hairpin vortices over the 90° ribs is more than those over the smooth wall (Figure 6.1-Figure 6.2) and 45° ribs (Figure 6.5-Figure 6.6). In fact, there is greater level of coherency in the vortex organization over the 90° ribs compared to the smooth wall and 45° ribs. Near the mid-span of the channel, the low-momentum region is bordered with train of vortices that formed hairpin packet (Figure 6.3a and Figure 6.4a). The structures in these figures extend beyond 3δ in the streamwise direction. The width of these structures varies from 0.5δ to 0.8δ in the spanwise direction. For ribs at 45°

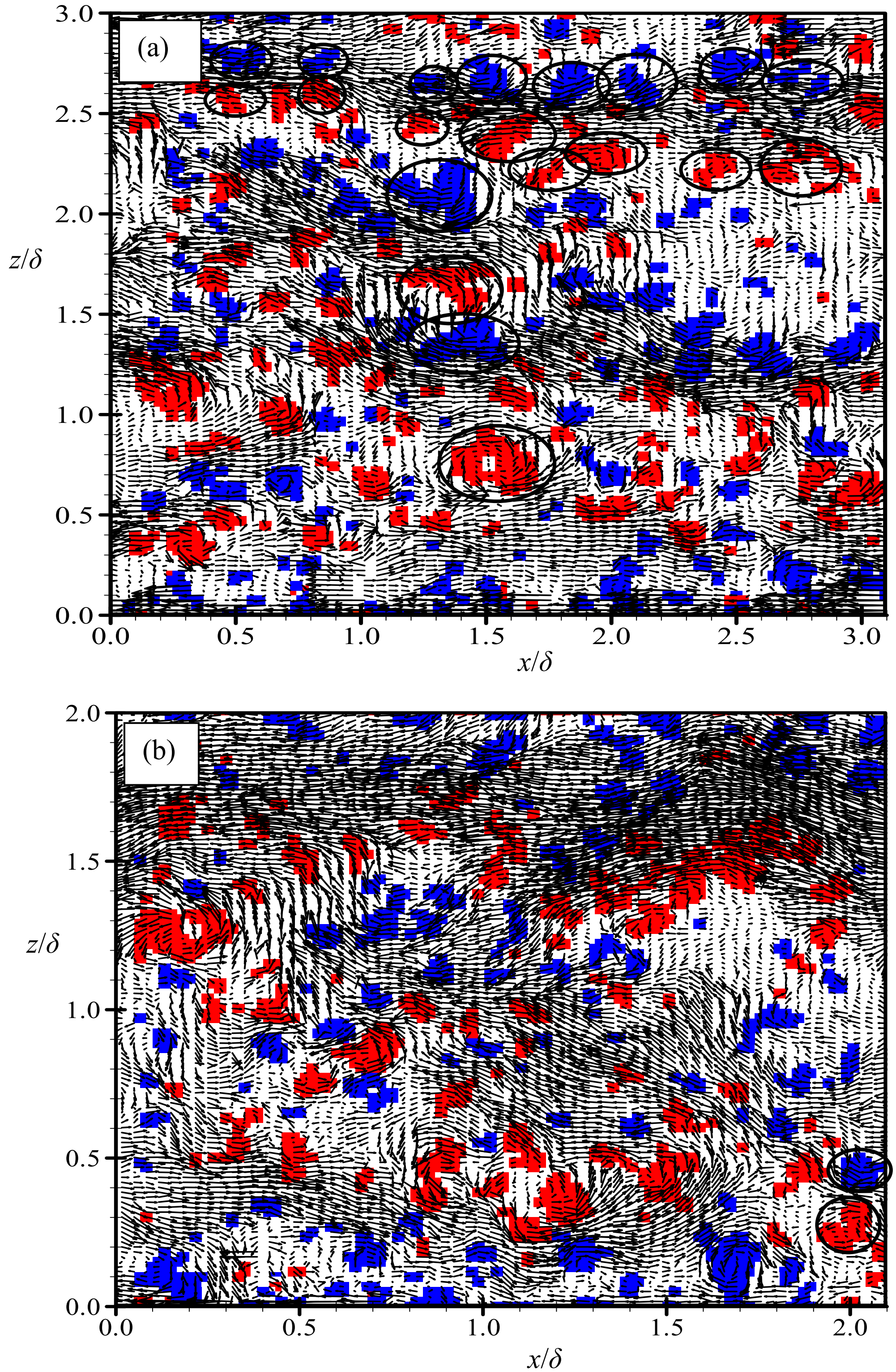

Figure 6.3: Instantaneous velocity field in the *x*-*z* plane over the $R_8\alpha_{90}$ ribs with positive swirl (red patches) and negative swirl (blue patches) superimposed: (a) parallel section at $y^+ = 305$, $U_c = 0.75U_m$ and (b) diverging section at $y^+ = 527$, $U_c = 0.70U_m$.

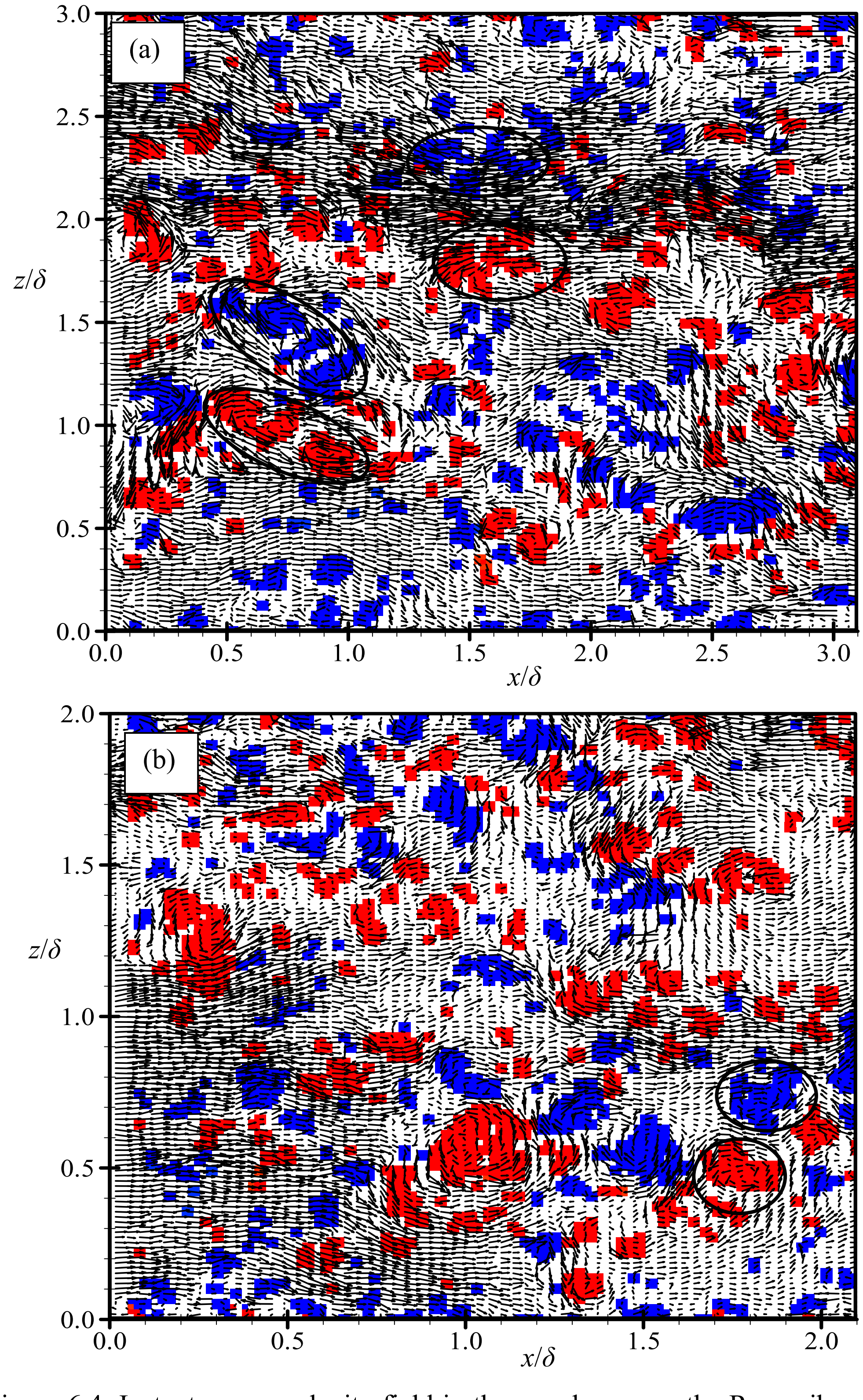

Figure 6.4: Instantaneous velocity field in the *x*-*z* plane over the $R_8\alpha_{90}$ ribs with positive swirl (red patches) and negative swirl (blue patches) superimposed: (a) parallel section at $y = 0.75\delta$, $U_c = 0.85U_m$ and (b) diverging section at $y = 0.75\delta$, $U_c = 0.70U_m$.

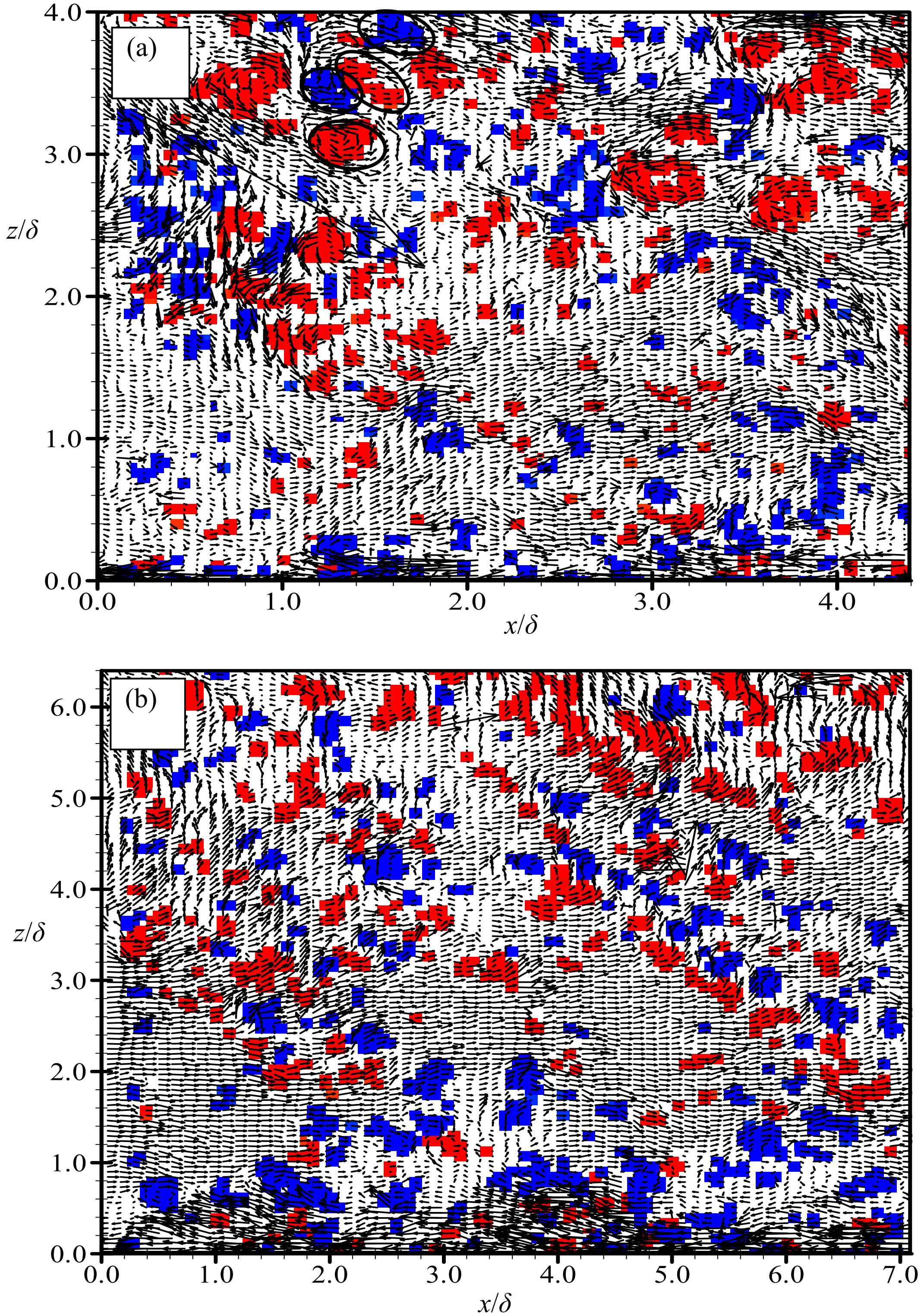

Figure 6.5: Instantaneous velocity fields in the *x*-*z* plane over 45° ribs with retrograde swirl (red patches) and prograde swirl (blue patches) superimposed: (a) parallel section at $y^+ = 338$, $U_c = 0.95U_m$ and (b) diverging section at $y^+ = 125$, $U_c = 0.95U_m$.

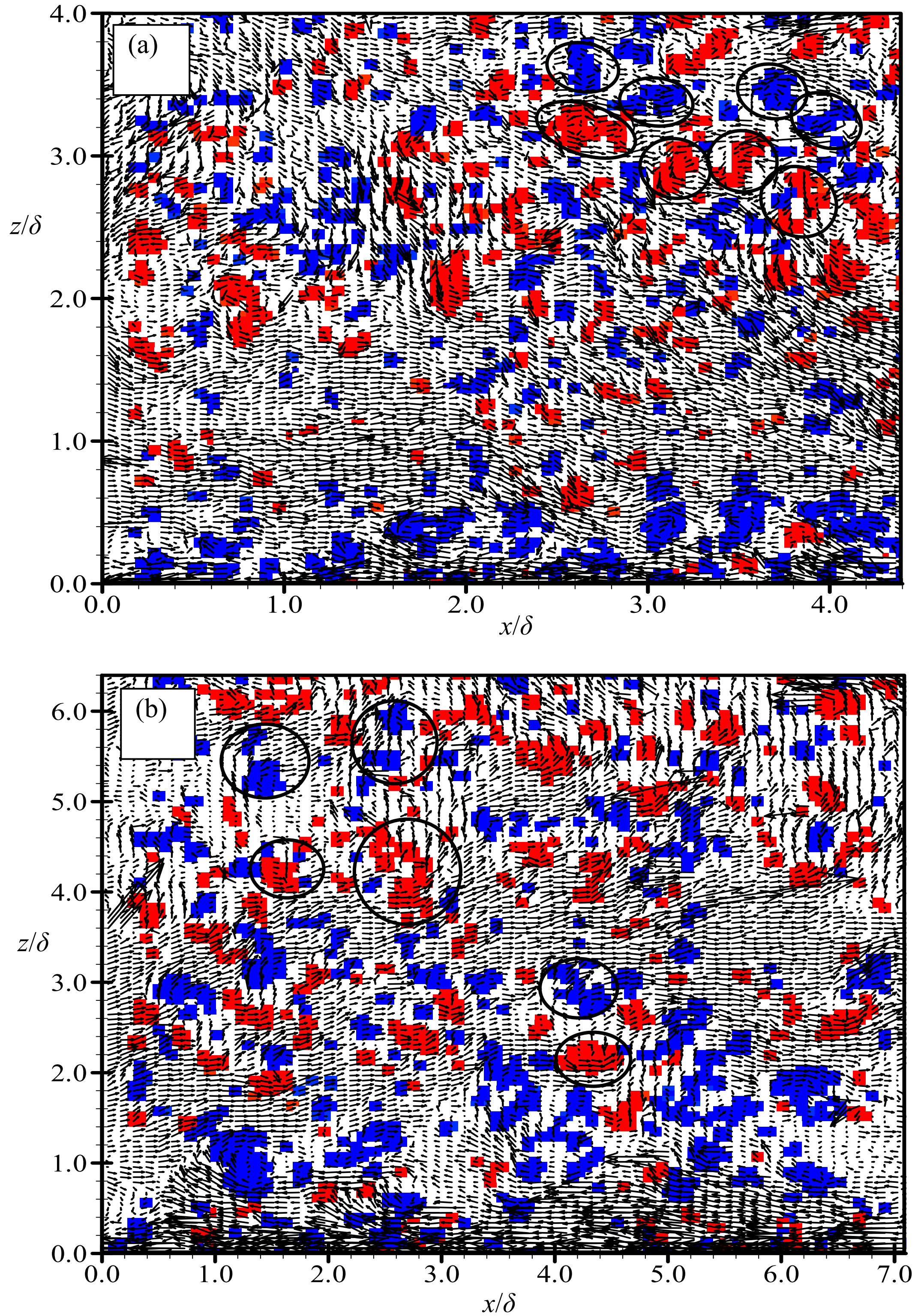

Figure 6.6: Instantaneous velocity fields in the *x*-*z* plane over 45° ribs with retrograde swirl (red patches) and prograde swirl (blue patches) superimposed: (a) parallel section at $y = 0.75\delta$, $U_c = 0.95U_m$ and (b) diverging section at $y = 0.75\delta$, $U_c = 0.95U_m$.

to the approach flow, the vectors are usually pointing towards the leading side of channel wall. Meanwhile, the hairpin vortices over ribs at 45° are smaller in size compared to those over ribs at 90°.

In addition, it is expected that further away from the wall, the population of the vortices should decrease. The results presented did not show such a distinct drop in the population of the vortices due to the presence of upper wall. In fact, the results presented by Volino *et al*. (2007) at $y = 0.1\delta$ and 0.4δ over both smooth wall and rough wall revealed that the vortex organization is independent of y-location and surface condition. Studies by Ganapathisubramani *et al*. (2003, 2005) and Tomkins and Adrian (2003), however, indicated that as one moves away from the wall beyond the logarithm region, the population of the hairpin vortices drops. It was also observed that the percentage of the vortices paired with a counter-rotating structure reduces farther away from the wall (Tomkins and Adrian, 2003). Tomkins and Adrian (2003) attributed this observation to disruption influence of turbulence on the older flow structures.

6.2 TWO-POINT VELOCITY CORRELATION

In order to provide statistical evidence for the observed hairpin packets in the previous section, the two-point correlation functions and the LSE are applied to the 6000 realizations and the average results are presented.

Figure 6.7 to Figure 6.9 shows the two-point auto-correlation in the longitudinal direction, R_{uu} for the smooth wall, and the k-type ribs inclined at 90° and 45° to the approach flow in the parallel and diverging sections. In these plots of R_{uu} contours, the outermost contour level is maintained at ±0.2. The R_{uu} contours are elliptical in shape, irrespective of roughness, rib orientation and APG as well as the wall-normal locations of

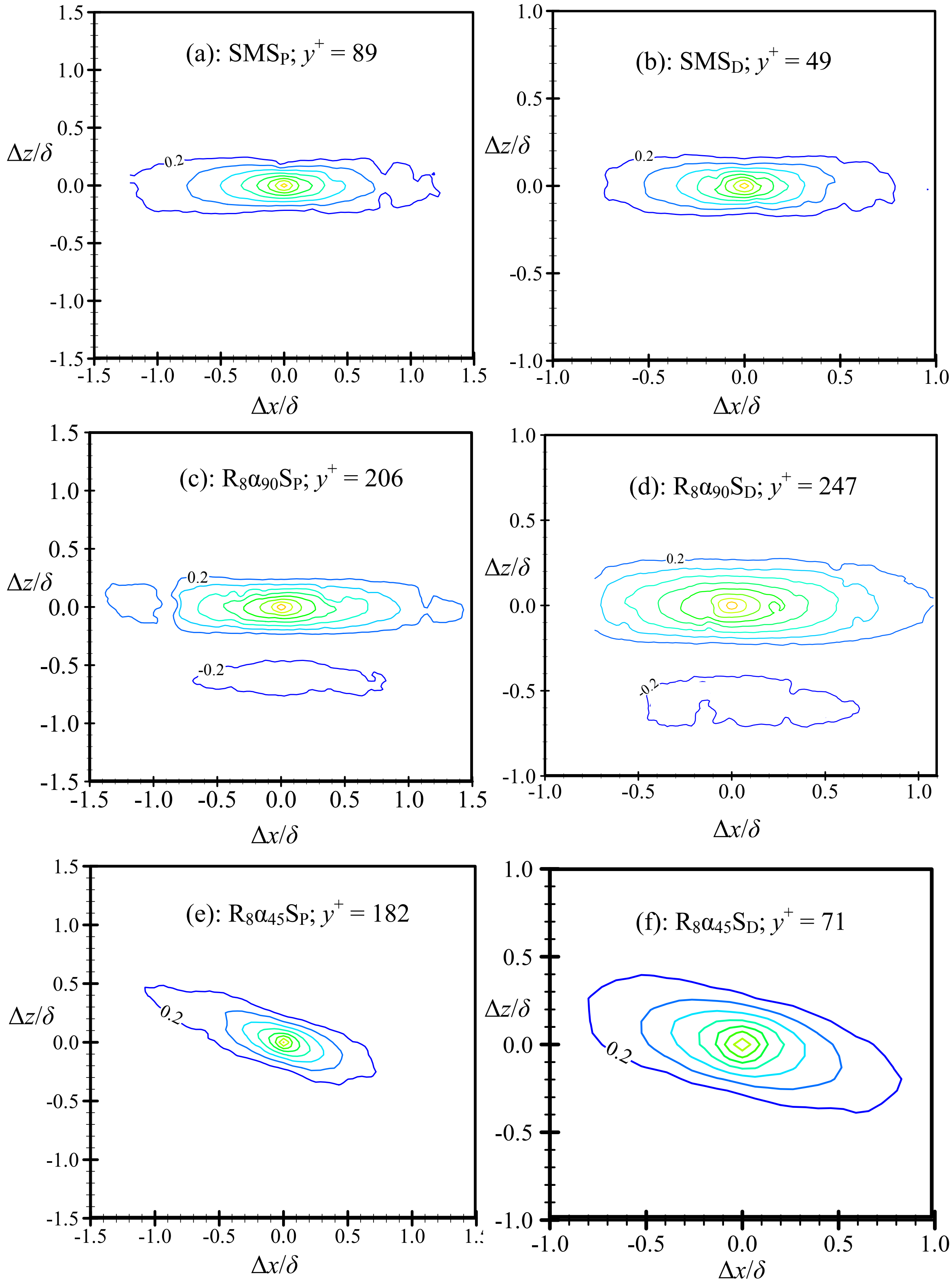

Figure 6.7: Contours of R_{uu} in the x-z plane at y locations denoted y_{LL}, outermost contour level of $R_{uu} = \pm 0.2$, contour increment is 0.1.

measurements. The R_{uu} contours have a considerable spatial coherence in the longitudinal direction over both the smooth wall and the ribs. The elongation of R_{uu} contours in the streamwise direction is in agreement with the hairpin vortex model. The R_{uu} contours for the 90° ribs indicate the presence of negative correlation with a shorter streamwise extent. In this case, the negative R_{uu} correlation is located adjacent to the positive R_{uu} correlation, demonstrating the presence of adjacent low-speed and high-speed zones that extend in the longitudinal direction. Near the wall of 90° ribs, the negative R_{uu} contour is situated close to the side wall (Figure 6.7c-d and Figure 6.8c-d), but at $y = 0.75\delta$ the negative R_{uu} contour is relocated to a region close to the mid-span of the channel (Figure 6.9c-d). It should also be noted that the negative correlation is narrower than the positive correlation. The R_{uu} contours over the smooth wall and 90° ribs are predominantly aligned in the streamwise direction. Over the 45° ribs, however, the R_{uu} contour is tilted in the flow direction so that the downstream tail of the contours is directed towards the side wall close to the leading edge of the ribs in both the parallel and the diverging sections. Such a significant tilt is due to the complex three-dimensional motion displayed by the 45° (as well as 30°) ribs. As noted earlier, inclined ribs induced three-dimensional secondary motions, in which case the fluid is driven towards the trailing edge and returned towards the leading edge of the ribs. Such motions of the fluid impact larger inclination angle to the hairpin packet as the vortices are vigorously subjected to spanwise fluid motions at an angle. This behaviour is also supported by the instantaneous velocity fields where the vectors corresponding to high-speed velocity are predominantly pointing to the leading side wall of the channel, and some of the vortices are aligned in this direction (Figure 6.5 to Figure 6.6).

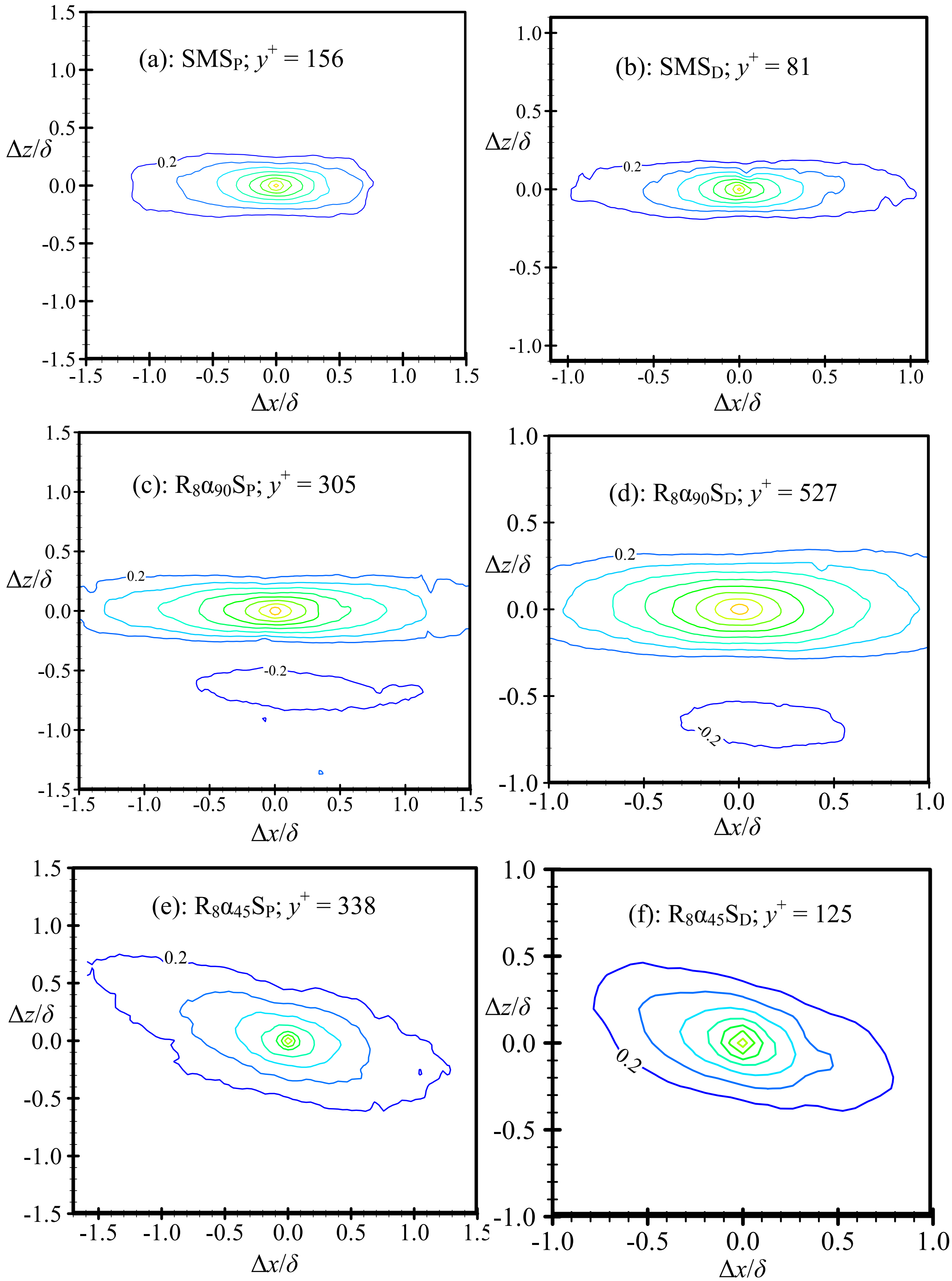

Figure 6.8: Contours of R_{uu} in x-z plane at y locations denoted y_{UL}, outermost contour level of $R_{uu} = \pm 0.2$, contour increment is 0.1.

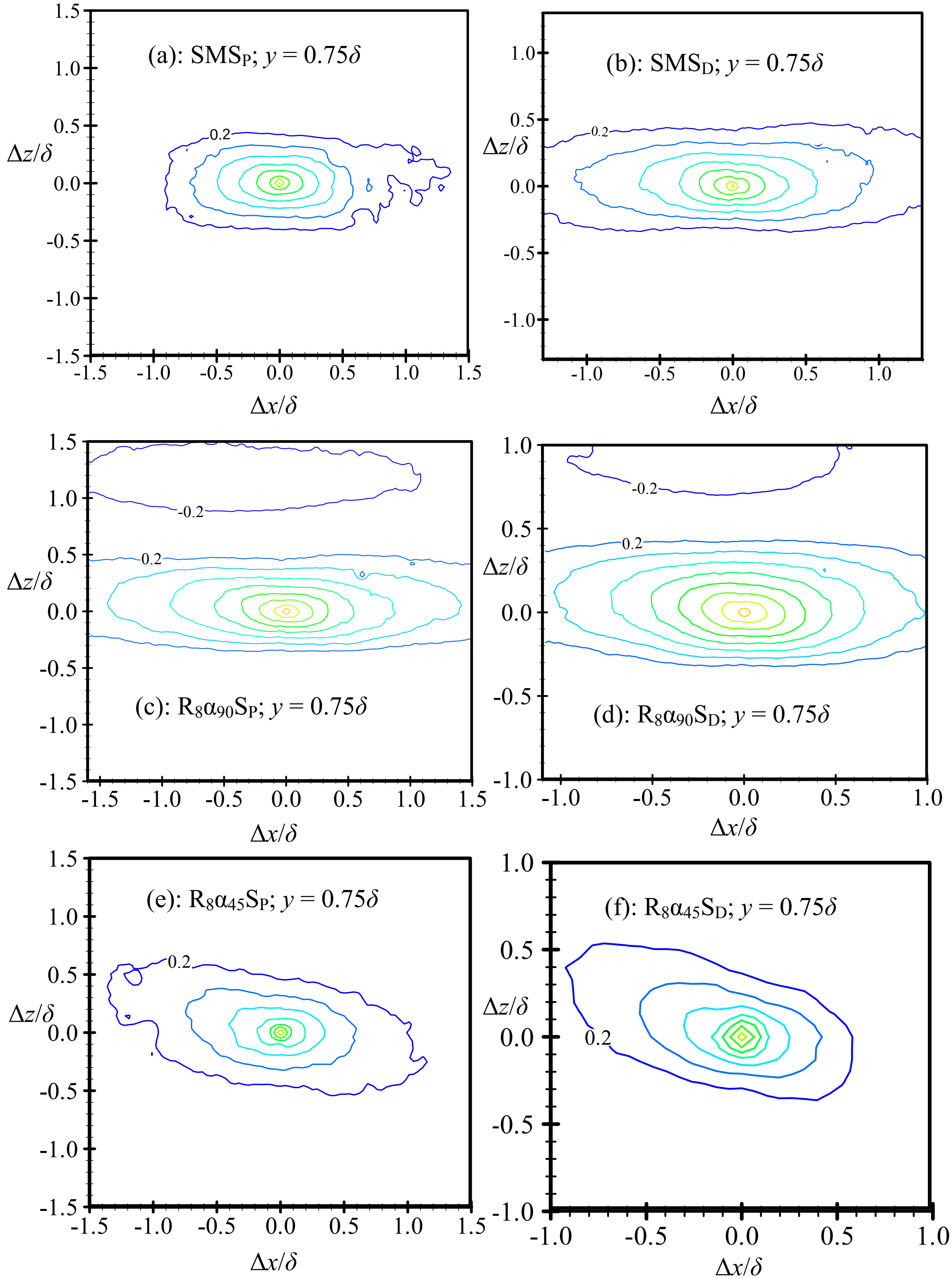

Figure 6.9: Contours of R_{uu} in x-z plane at $y = 0.75\delta$, outermost contour level of R_{uu} = ±0.2, contour increment is 0.1.

The inclination angles of R_{uu} (θx_{uu}) were estimated following the procedures used by Christensen and Wu (2005) and Volino *et al*. (2007) and the values for the inclined ribs are presented in Table 6.2. As noted earlier, the R_{uu} contours over the smooth wall and 90° ribs are predominantly aligned in the streamwise direction. For the ribs at 45°, Table 6.2 revealed that in the parallel section, the values of θx_{uu} decreases as the wall-normal distance increases. In the diverging section, however, θx_{uu} increases with increasing y. APG severely tilted the R_{uu} contours in the diverging section than in the parallel section. This further supports the earlier observation that the secondary motion is stronger in the presence of APG. The common effect of APG on the R_{uu} contours is to widen it over each surface. Thus, APG produces a wider region of low-momentum fluid in the diverging section.

The streamwise and spanwise slices of R_{uu} are shown in Figure 6.10. It should be noted that the R_{uu} correlation shown in Figure 6.10a-c extends further than the streamwise range considered. Thus, the flow is dominated by structures whose streamwise extent is longer than 3δ as noted earlier. The sharp drops in R_{uu} correlation over inclined ribs and smooth wall imply that there exists a relatively longer low-momentum region over the 90° ribs. In Figure 6.10a-c, the variations in profiles of R_{uu} with APG and roughness increase with distance away from the wall. In general, APG reduces the values of R_{uu} correlation, with the exceptions at y_{LL} and y_{OL}, respectively for the 45° ribs (Figure 6.10a)

Table 6.2: Angle of inclination of R_{uu} and R_{ww} contours over 45° ribs

Test	θx_{uu} (°)			θz_{ww} (°)		
	y_{LL}	y_{UL}	y_{OL}	y_{LL}	y_{UL}	y_{OL}
$R_8S_P\alpha_{45}$	19.3	17.1	12.5	61.0	70.2	81.2
$R_8S_D\alpha_{45}$	18.6	20.3	26.0	58.4	59.7	54.2

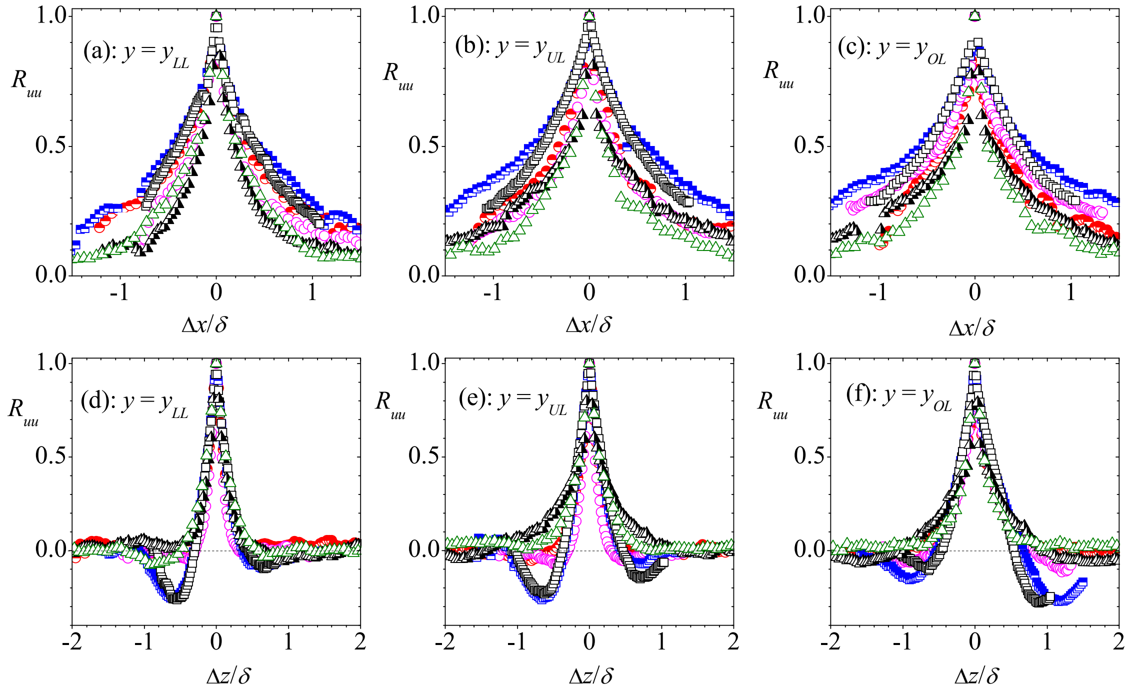

Figure 6.10: One-dimensional profiles of streamwise, (a)-(c) and spanwise, (d)-(f) slices through self-correlation point of R_{uu}. Symbols: SMS$_P$: ◓; SMS$_D$: ○; R$_8$S$_P$α$_{90}$: ⬒; R$_8$S$_D$α$_{90}$: □; R$_8$S$_P$α$_{45}$: ◭; R$_8$S$_D$α$_{45}$: △.

and the smooth wall (Figure 6.10c). At these locations over these surfaces, APG enhances the values of R_{uu} correlation, thereby increasing the size of the R_{uu} contours. This also implies formation of long low-momentum region in the diverging section at y_{OL} for smooth wall and at y_{LL} for ribs at 45°. Irrespective of the pressure gradient, ribs at 90° enhances the values of R_{uu} correlation compared to smooth wall and ribs at 45° to the approach flow. The implication is that the average size of the hairpin packet is increased by the 90° ribs, and that this surface condition induced intense and long low-speed region resulting in a long streamwise coherence in comparison to the smooth surface and ribs at 45°. This is consistent with the results in Chapter 4 and Chapter 5.

The corresponding one-dimensional spanwise profiles of R_{uu} are shown in Figure 6.10d-f. In most cases, the R_{uu} correlation in the spanwise direction falls spontaneously from its self-correlation value of 1 to negative value as $\Delta z/\delta$ increases in magnitude. It is apparent that the zero-crossing of the R_{uu} correlation in the spanwise direction varies with pressure gradient, roughness and rib inclination angle as well as the wall-normal locations. Table 6.3 shows a summary of the zero-crossing for R_{uu} correlations for positive and negative Δz. Over the smooth wall, for example, R_{uu} correlation crosses zero at $\Delta z/\delta = -0.50$ and 0.46 in the parallel section, at $\Delta z/\delta = \pm 0.30$ in diverging section for $y = y_{LL}$ (Figure 6.10d). Over the 90° ribs, the zero-crossing of R_{uu} correlation occurred at $\Delta x/\delta = -0.30$ and 0.38 in the parallel section, and $\Delta z/\delta = -0.30$ and 0.44 in the diverging section for $y = y_{LL}$. For the case of the 45° ribs, the zero-crossing of R_{uu} correlation occurred at $\Delta z/\delta = \pm 0.65$ in the parallel section, and $\Delta z/\delta = -0.51$ and 0.59 in the diverging section for $y = y_{LL}$. The dissimilarity in the values of positive $\Delta z/\delta$ and negative $\Delta z/\delta$ is an indication of the degree of asymmetry in R_{uu} correlation in the spanwise direction. Meanwhile, the occurrence of negative R_{uu} correlation on the either side of the positive self-correlation peak of R_{uu} correlation confirms the presence of alternating low-speed and high-speed fluid regions (as spanwise oriented streaks) in the spanwise direction. The streaks are spaced regularly but their strength (or peak) is not identical at both side of the primary correlation peak, especially over the ribs, due to lack of two-

Table 6.3: Zero-crossing of R_{uu} correlation in the spanwise direction

Test	y_{LL}		y_{UL}		y_{OL}	
	$-\Delta z/\delta$	$\Delta z/\delta$	$-\Delta z/\delta$	$\Delta z/\delta$	$-\Delta z/\delta$	$\Delta z/\delta$
SMS_P	0.50	0.46	0.53	0.53	0.85	1.00
SMS_D	0.30	0.30	0.30	0.30	0.55	0.80
$R_8S_P\alpha_{90}$	0.30	0.38	0.37	0.47	0.50	0.69
$R_8S_D\alpha_{90}$	0.30	0.44	0.37	0.47	0.48	0.55
$R_8S_P\alpha_{45}$	0.65	0.65	1.44	1.34	0.93	1.02
$R_8S_D\alpha_{45}$	0.51	0.59	0.85	0.92	2.36	2.10

Table 6.4: Locations of secondary self-correlation peaks relative to the primary positive self-correlation peak of R_{uu} correlation in the spanwise direction

Test	y_{LL}		y_{UL}		y_{OL}	
	$-\Delta z/\delta$	$\Delta z/\delta$	$-\Delta z/\delta$	$\Delta z/\delta$	$-\Delta z/\delta$	$\Delta z/\delta$
SMS_P	0.70	-	0.79	0.79	1.00	1.00
SMS_D	0.43	0.43	0.50	0.46	1.14	1.21
$R_8S_P\alpha_{90}$	0.63	0.60	0.66	0.74	0.89	1.79
$R_8S_D\alpha_{90}$	0.57	0.65	0.65	0.68	0.65	0.89
$R_8S_P\alpha_{45}$	0.91	-	1.88	1.65	1.59	1.59
$R_8S_D\alpha_{45}$	0.85	0.72	0.91	-	-	-

dimensionality of the mean flow and/or the presence of dominant asymmetric cane-like hairpin vortices. The streaks formed secondary correlation peaks of negative values on either side of the primary peak. Note that these secondary peaks are lower than the primary peak due to variation in the instantaneous spacing of the streaks. The distances between the secondary self-correlation peaks and the primary positive self-correlation peak of R_{uu} correlation in the spanwise direction are summarized in Table 6.4 for $\pm\Delta z$. These average streak spacings show considerable dependence on wall-normal location, pressure gradient, roughness and rib inclination angle.

The extents of R_{uu} in the longitudinal direction, Lx_{uu} and in the spanwise direction, Lz_{uu} based on R_{uu} = 0.5 contour level were estimated and presented in Table 6.5. The table provides further statistical evidence for the dependence of the turbulence structure on APG, roughness and rib inclination angle. Table 6.5 demonstrates that, except in the outer layer of the smooth wall (i.e., y_{OL}), the streamwise size of the R_{uu} contours in the diverging section of the smooth wall and the rib-roughened walls is shorter compared to the Lx_{uu}/δ in the parallel section. The reduction in Lx_{uu}/δ by APG is also consistent with the observation in the x-y plane (Chapter 4). As pointed out earlier, such a reduction implies that the stretching of the vortex becomes less efficient as the flow is under the

Table 6.5: Streamwise and spanwise sizes for R_{uu} and R_{ww} contours

Test	Lx_{uu}/δ			Lz_{uu}/δ			Lx_{ww}/δ			Lz_{ww}/δ		
	y_{LL}	y_{UL}	y_{OL}	y_{LL}	y_{UL}	y_{OL}	y_{LL}	y_{UL}	y_{OL}	y_{LL}	y_{UL}	y_{OL}
SMS_P	0.66	0.63	0.62	0.22	0.24	0.32	0.25	0.24	0.35	0.21	0.25	0.24
SMS_D	0.46	0.49	0.77	0.17	0.17	0.33	0.16	0.13	0.13	0.18	0.15	0.18
$R_8S_P\alpha_{90}$	0.88	1.67	1.09	0.22	0.30	0.42	0.17	0.19	0.23	0.19	0.23	0.31
$R_8S_D\alpha_{90}$	0.82	1.00	0.97	0.26	0.34	0.43	0.17	0.22	0.18	0.20	0.28	0.27
$R_8S_P\alpha_{45}$	0.43	0.42	0.39	0.24	0.28	0.25	0.21	0.32	0.27	0.27	0.47	0.39
$R_8S_D\alpha_{45}$	0.43	0.38	0.26	0.27	0.26	0.24	0.26	0.25	0.24	0.30	0.28	0.25

influence of APG. Moreover, APG reduced Lz_{uu}/δ over the smooth wall and 45° ribs, except at y_{LL}. In the case of 90° ribs, the Lz_{uu}/δ in the diverging section is increased by 2%-18% of the upstream values. It is also apparent that the increased tilting of R_{uu} contour in the diverging section compared to the parallel section contributes to the reduction in the length-scales of the R_{uu} contour in the diverging section of the 45° ribs. In the outer layer, Lz_{uu}/δ is independent of pressure gradient over each surface. Although, Krogstad and Skåre (1995) also observed that APG diminished the streamwise extent of R_{uu} contour relative to contour obtained in a ZPG boundary layer, they observed an enhancement of the spanwise size by APG.

The table also shows that an increase in the Lx_{uu}/δ is observed as y increases in the wall region of the smooth wall and 90° ribs. The Lx_{uu}/δ decreased in the outer layer over these surfaces. Meanwhile, Lz_{uu}/δ increases with y over the smooth wall and 90° ribs. The reduction of the streamwise extent of R_{uu} contour in the parallel section of the smooth wall as the outer layer is approached is consistent with the results of Ganapathisubramani *et al*. (2005) and Volino *et al*. (2007). Meanwhile, Volino *et al*. (2009) showed that in the outer region of *k*-type ribs, Lz_{uu}/δ is also 40% larger than the Lz_{uu}/δ obtained near the wall. Over the 45° ribs, as y increases the Lx_{uu}/δ decreased modestly in the parallel section but significantly in the diverging section due to the more significant tilting of R_{uu} contour as y increases. It is also evident that Lx_{uu}/δ and Lz_{uu}/δ for the 90° ribs are larger than those over the smooth wall and for 45° ribs at all heights, except very close to the 45° ribs. The reduction in streamwise and spanwise extents of R_{uu} contours for the 45° relative to those over the 90° ribs is partly due to the significant tilting of the R_{uu} contour for the 45° ribs. Meanwhile, the individual vortices observed over 45° ribs (Figures 6.5 and 6.6) are smaller in size and they are also less organized than those over 90° ribs (Figures 6.3 and 6.4).

The corresponding R_{ww} contours are shown in Figure 6.11-Figure 6.13. The shape, size and orientation of R_{ww} contour depend on the wall boundary condition and pressure gradient. The contours in the parallel section of the smooth wall are elongated owing to the stretching of the leg of the vortices in the streamwise direction. However, at $y^+ = 156$, the streamwise extent of the contour is shorter (Figure 6.12a). It should be noted that the observed streamwise extent of R_{ww} contours is considerably shorter compared to R_{uu} contour. The R_{ww} contours reported by Krogstad and Skåre (1995), Ganapathisubramani *et al*. (2005) and Volino *et al*. (2007) in ZPG were not elongated in the streamwise direction; instead the R_{ww} contour was compact in both the streamwise and spanwise directions. This was due to lack of streamwise and spanwise coherence in w' across the boundary layer. Meanwhile, in the outer region of the smooth wall flow in the parallel section, the R_{ww} contour formed 'secondary' contours which are not fully separated from the primary contour (Figure 6.13a). The presence of the secondary R_{ww} contour is likely caused by juxtaposing of the legs of another but weaker hairpin packets. This observation may provide support for the merging of the hairpin packets observed by Tomkins and

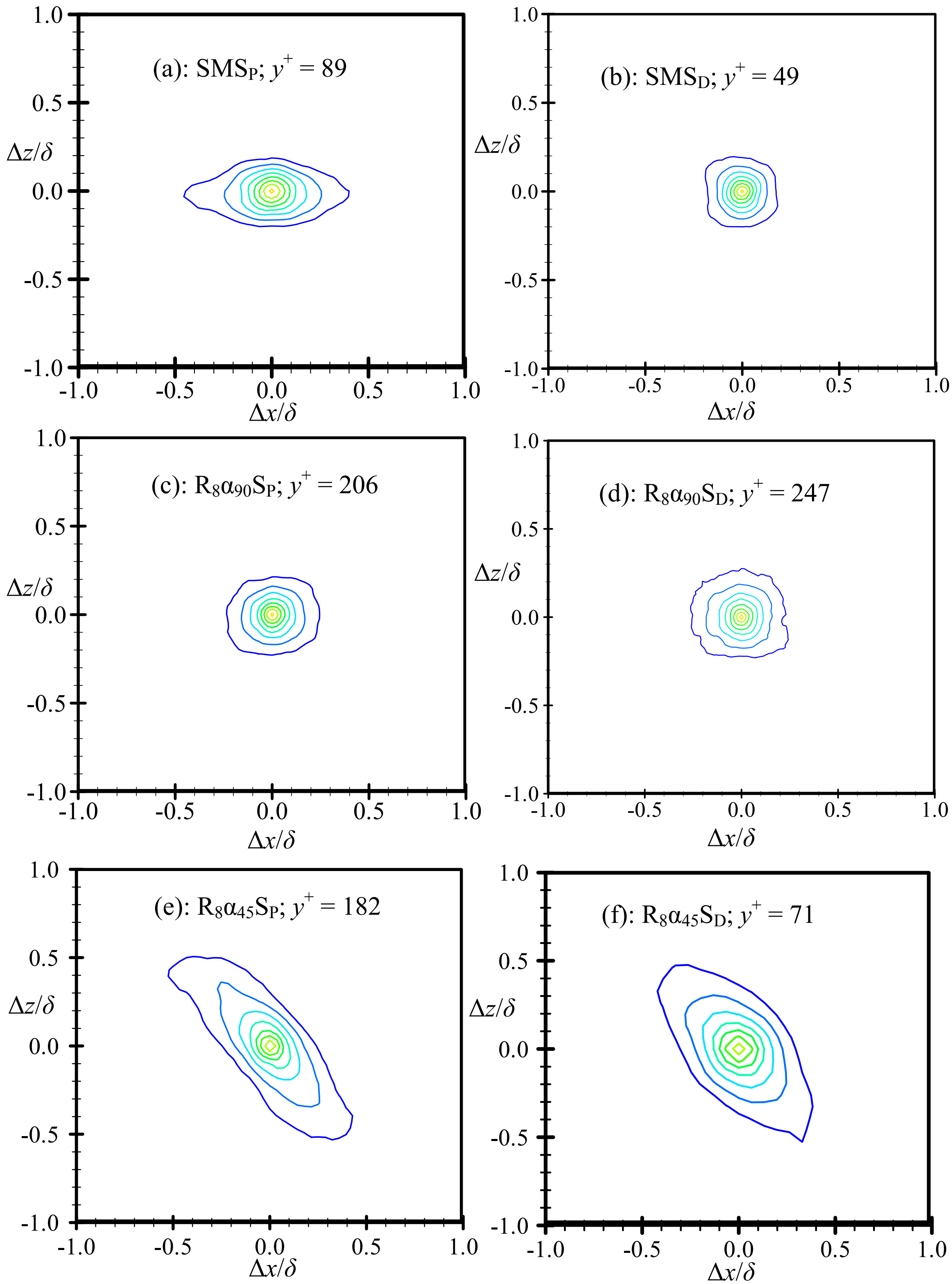

Figure 6.11: Contours of R_{ww} in the x-z plane at y locations denoted y_{LL}, outermost contour level of $R_{ww} = 0.2$, contour increment is 0.1.

Adrian (2003). Due to the compactness of R_{ww} contour in the diverging section of the smooth wall, both the streamwise and the spanwise sizes of R_{ww} contour in the parallel section of the smooth wall are larger than in the diverging section. However, Krogstad and Skåre (1995) observed that the contour of R_{ww} for the APG flow is stretched out considerably in the spanwise direction compared to the ZPG flow.

Figure 6.11-Figure 6.13 revealed that the R_{ww} contours over the 90° ribs are more compact in agreement with previous results. Unlike the smooth wall, APG enlarges the longitudinal and streamwise sizes of R_{ww} contour over the 90° ribs at all heights. A slight streamwise tilt coupled with spanwise elongation of the R_{ww} contour in outer layer is observed over the 90° ribs in both the parallel and diverging sections (Figure 6.13c-d). Note that in the parallel section, R_{ww} contour leans backward whereas in the diverging section R_{ww} contour leans forward.

When the ribs were inclined at 45° to the approach flow, significant changes are observed in the R_{ww} contour in comparison to the R_{ww} over the perpendicular ribs. In fact, the shape of R_{ww} over the 45° ribs is predominantly elliptical whereas the shape of R_{ww} over the 90° ribs is usually more compact. This is a further indication that the turbulence structure are not necessary the same over these two ribs. Moreover, for the 45° ribs, R_{ww} contours are tilted towards the side wall in the flow direction in both the parallel and diverging sections. This tilting is also a manifestation of the fluid being driven towards the trailing edge before it is returned towards the leading edge of the ribs. The angles of inclination of R_{ww} contour (θz_{ww}) are also presented in Table 6.2.

The R_{ww} contours are considerably tilted compared to the R_{uu} contours due to quasi-spanwise-streamwise motion. The table revealed that in the parallel section θz_{ww}

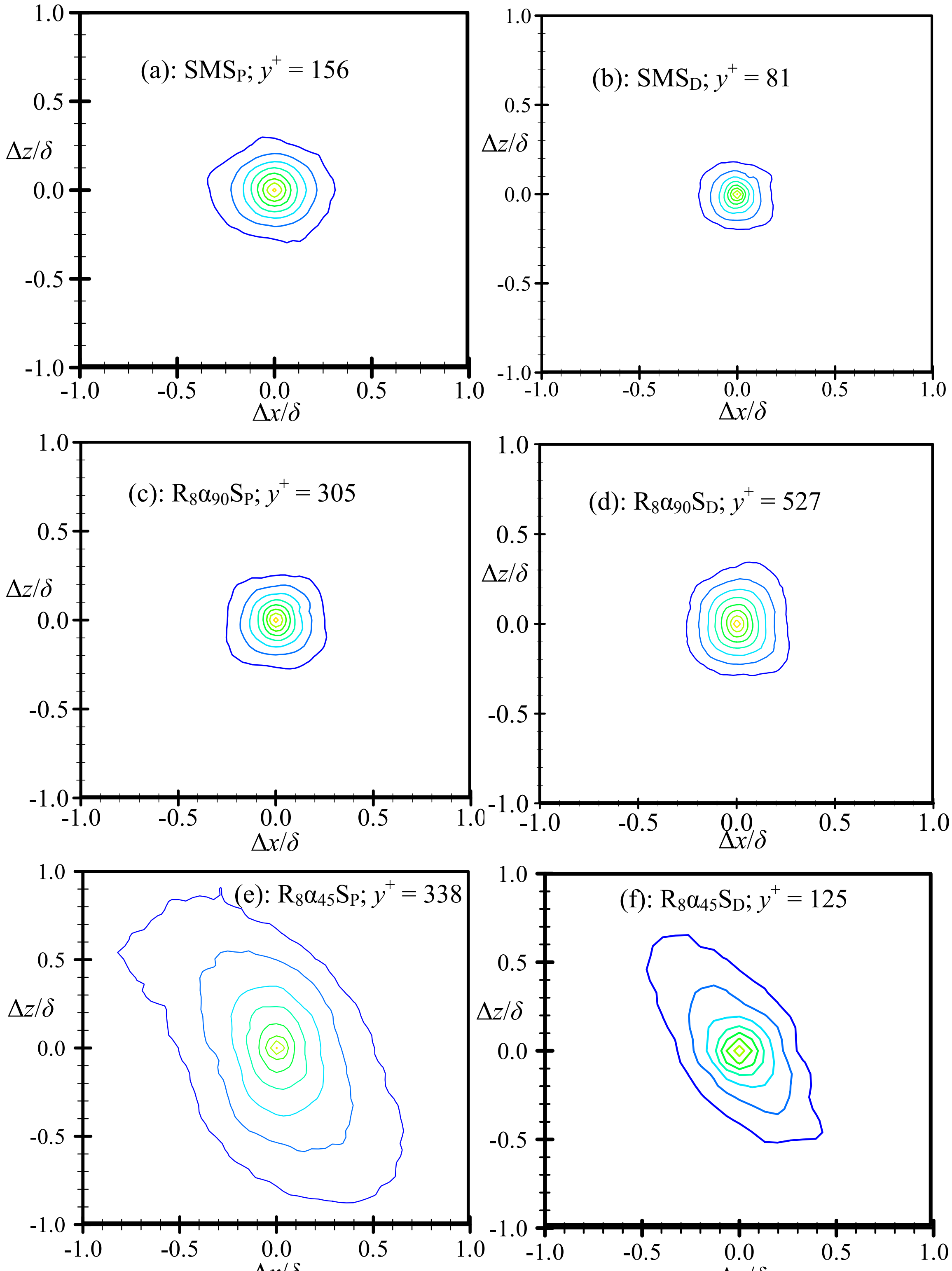

Figure 6.12: Contours of R_{ww} in the x-z plane at y locations denoted y_{UL}, outermost contour level of R_{ww} = 0.2, contour increment is 0.1.

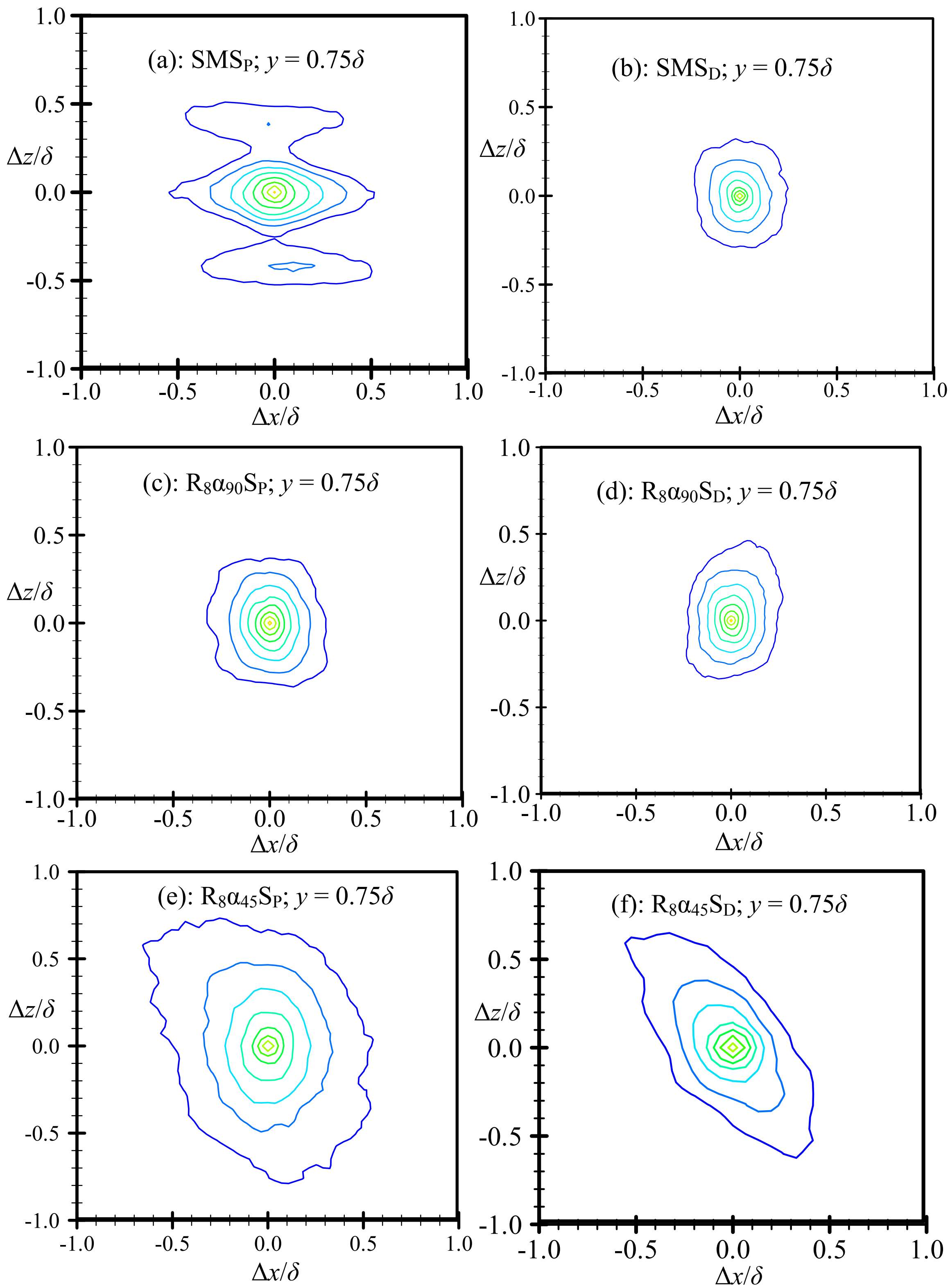

Figure 6.13: Contours of R_{ww} in the x-z plane at $y = 0.75\delta$, outermost contour level of R_{ww} = 0.2, contour increment is 0.1.

increased with y but it decreased at y_{OL} in the presence of APG. Unlike θx_{uu}, θz_{ww} is larger in the parallel section compared to the diverging section (Table 6.2). The significant tilting of R_{ww} over the 45° ribs in comparison to 90° ribs is also an indication of changes in the dynamics of the turbulence structures. The tilting of R_{ww} contour over the 45° ribs may explain the lower level of turbulence over these ribs. This is because such a tilt disorients the ejection and sweep mechanisms and lowers their effectiveness in producing turbulence.

The profiles of the streamwise and spanwise slices of R_{ww} contours are shown in Figure 6.14. Over the 90° ribs no distinct effect of APG on the one-dimensional profiles is observed, except at y = 0.75δ in Figure 6.14c where APG diminished the streamwise profiles. However, the results over the smooth wall and 45° ribs clearly showed that APG consistently reduced the values of R_{ww}. The results also showed that roughness

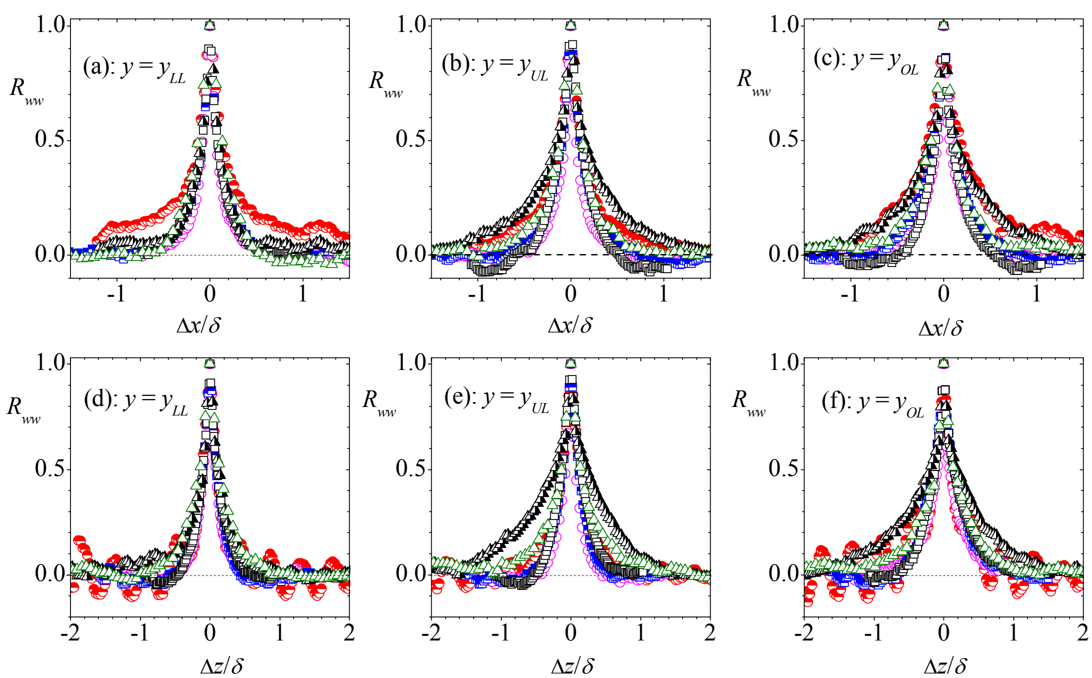

Figure 6.14: One-dimensional profiles of streamwise, (a)-(c) and spanwise, (d)-(f) slices through self-correlation point of R_{ww}. Symbols: SMS_P: ◓; SMS_D: ○; $R_8S_P\alpha_{90}$: ▬; $R_8S_D\alpha_{90}$: □; $R_8S_P\alpha_{45}$: ▲; $R_8S_D\alpha_{45}$: △.

diminished the values of R_{ww} over the 90° ribs in comparison to the results over the smooth wall. On the other hand, Volino *et al*. (2007) observed similarity in the distribution of R_{ww} over a mesh roughness and a smooth wall ZPG boundary layer. Meanwhile, the 45° ribs enhanced the values of R_{ww} correlation considerably relatively to R_{ww} correlation for the 90° ribs.

Table 6.5 demonstrates that APG diminished the sizes of R_{ww} contour over the smooth wall, 45° ribs and in the outer layer of the 90° ribs. It should be noted that over each surface, especially in the parallel section, there is an increase in Lx_{ww} and Lz_{ww} away from the lower wall due to the increase in the size of the representative average vortex structure. This is consistent with the observation by Krogstad and Skåre (1995), Ganapathisubramani *et al*. (2005) and Krogstad and Antonia (1994). It is evident that in the parallel section the ribs reduced the sizes of R_{ww} contours. The Lx_{ww} and Lz_{ww} of the R_{ww} contours for the 45° ribs are larger than those over the 90° ribs in both the parallel and diverging sections (Table 6.5).

Examination of the cross-correlation contours in the *x-z* plane also revealed differences in the turbulence structures over the smooth wall and the *k*-type ribs (Figure 6.15-Figure 6.17). In general, the R_{uw} contours reveal both negative and positive contour levels over each surface. Nevertheless, the shape, the size and the orientation of the R_{uw} contours depend on the type of the boundary condition and the pressure gradient. It should be noted that the variations of these attributes (sign, shape, size and orientation) of R_{uw} are in agreement with the flow induced by the legs of hairpin vortices to the sides of the low-speed regions. Volino *et al*. (2007) argued that fluid with $-u'$ was directed by vortices toward the self-correlation point of R_{uw} from both spanwise sides where w' is positive on either side. The fluid with the negative u' advances past self-correlation. It

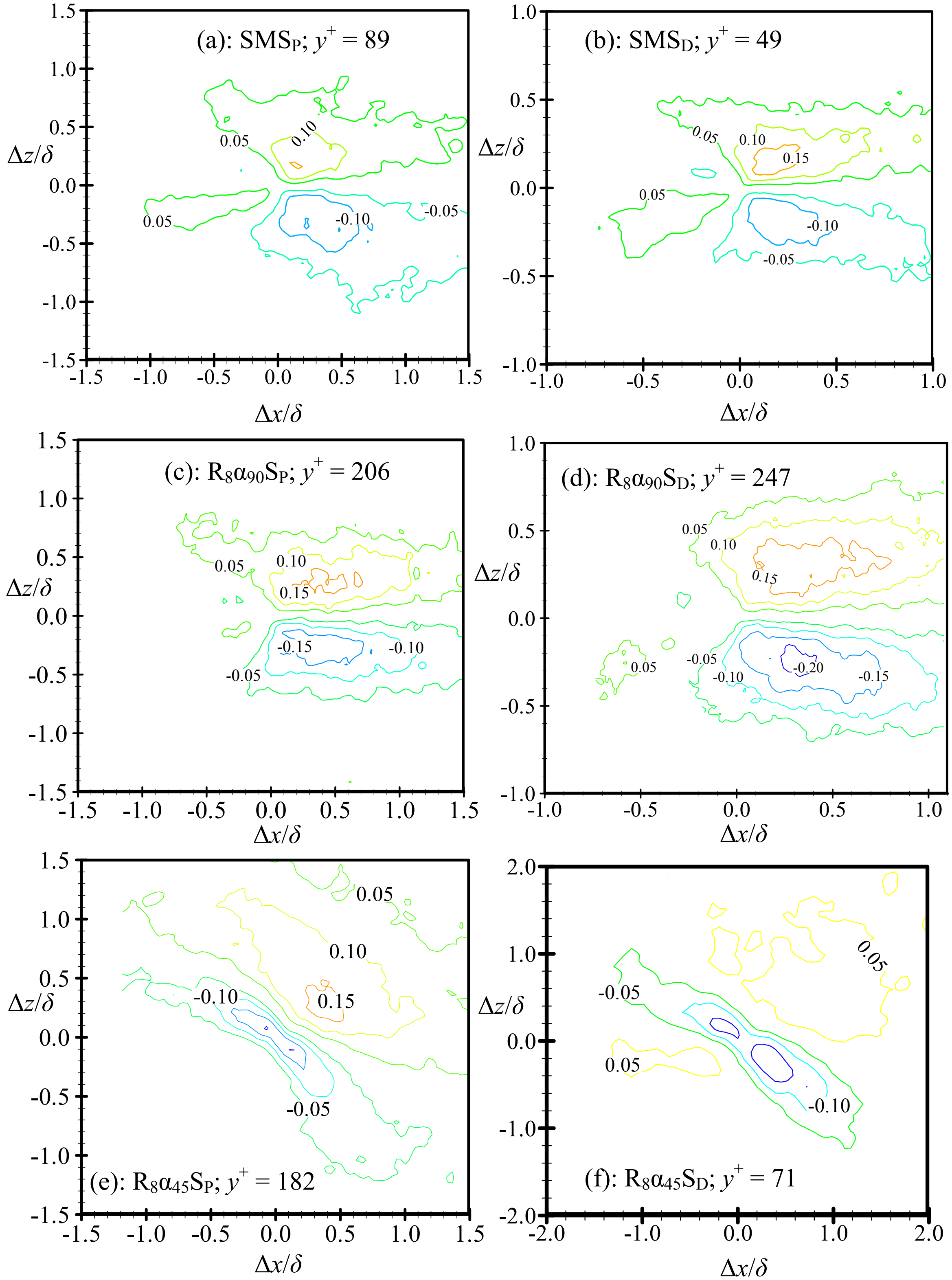

Figure 6.15: Contours of R_{uw} in the *x*-*z* plane at *y* locations denoted y_{LL}, outermost contour level of $R_{uw} = -0.05$, contour increment is -0.05.

then moves away from the self-correlation in the spanwise direction and w' changes sign on each side of the span. Indeed, Figure 6.7-Figure 6.9 revealed that the long streamwise coherence in R_{uu} contour is due to low-speed events. Therefore, the negative values of R_{uw} contours suggest that the slow-moving fluid is associated with positive w' (flow towards the mid-span of the channel from the side wall). Furthermore, the positive values of R_{uw} contours suggest that the slow-moving fluid is also associated negative w' (flow from the mid-span of the channel towards the side wall). Over each surface, R_{uw} contour varies in shape and size as y increases. In particular, the streamwise extent of R_{uw} contour is larger near the wall, and as y increases it drops. It should be noted that the maximum R_{uw} contour level varies for the various wall boundary conditions and pressure gradient. In most cases, the R_{uw} is larger downstream of the self-correlation point.

Over the smooth wall and 90° ribs, APG indeed increased the contour levels of R_{uw}, thereby increasing the magnitude of R_{uw} correlation in the diverging section of these surfaces in comparison to R_{uw} in the parallel section. Over the 45° ribs, however, APG reduced the contour levels.

It is evident that at each height the number of the contour levels of R_{uw} over the 90° ribs is higher than the levels of R_{uw} over the smooth wall. Moreover, the shape of the R_{uw} contours is not necessary the same over these surfaces at all the heights considered. Variations in the longitudinal and lateral sizes of the R_{uw} contours with roughness are also noticeable in Figure 6.15-Figure 6.17.

The effects of rib inclination on the R_{uw} contours are also evident in these plots. Although there are distinct variations in the shape, size and orientation of R_{uw} contour throughout the boundary layer, the contour level of R_{uw} correlation near the wall in the

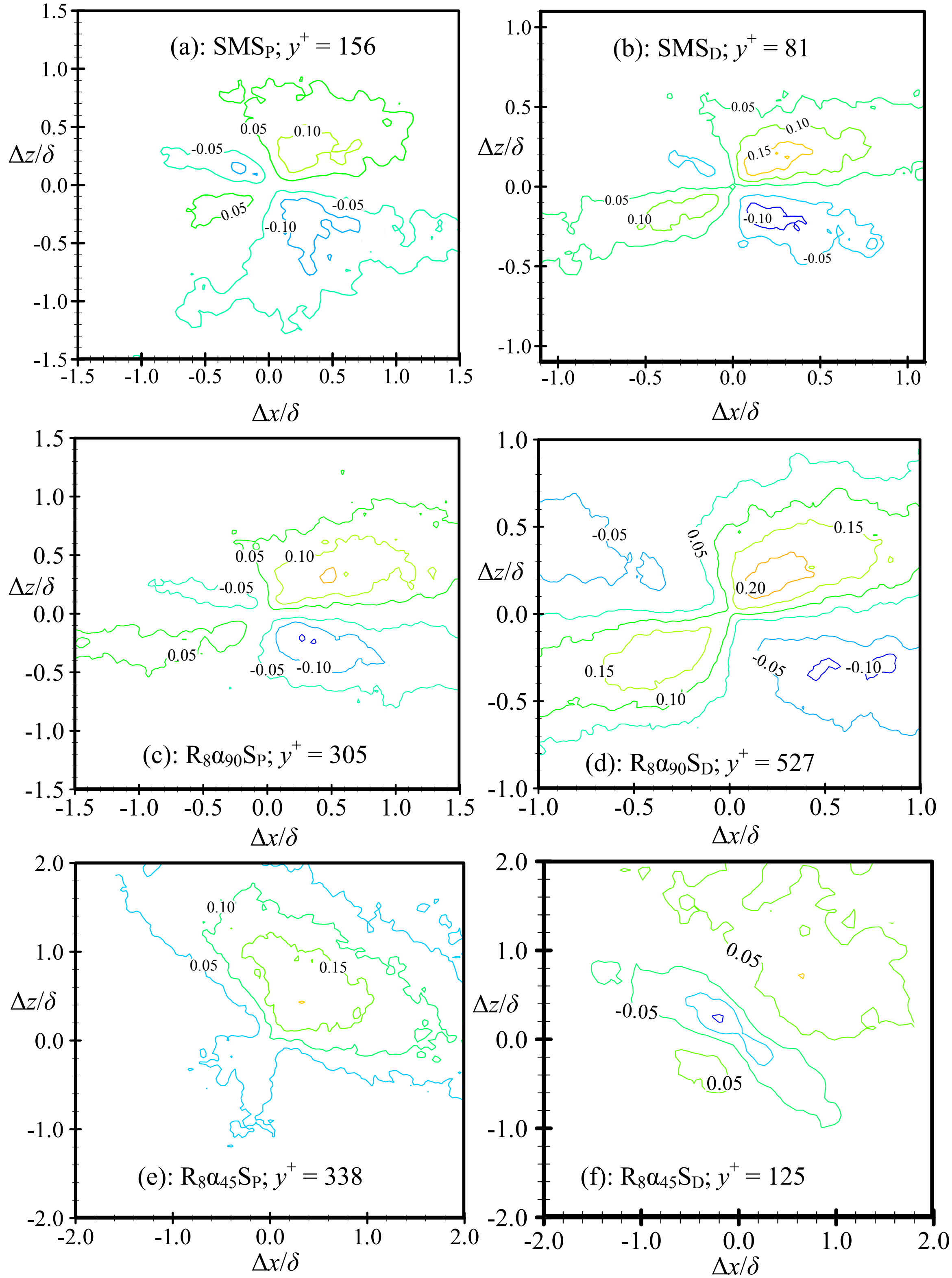

Figure 6.16: Contours of R_{uw} in the x-z plane at y locations denoted y_I, outermost contour level of $R_{uw} = -0.05$, contour increment is -0.05.

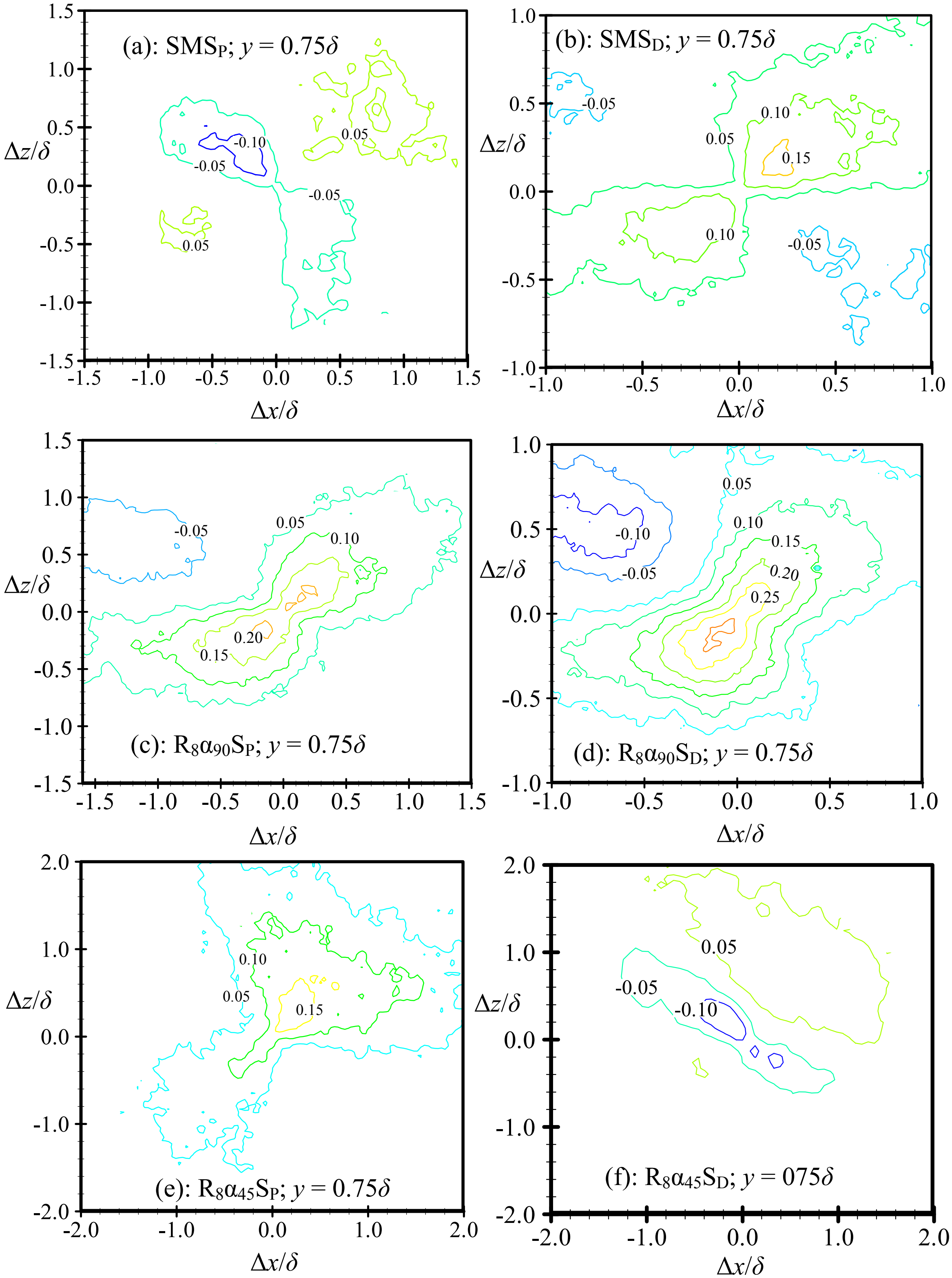

Figure 6.17: Contours of R_{uw} in the x-z plane at $y = 0.75\delta$, outermost contour level of R_{uw} = −0.05, contour increment is −0.05.

parallel section are similar in magnitude (Figures 6.15c and 6.15e, and Figure 6.16c and 6.16e). On the contrary, in the diverging section the contour levels of R_{uw} correlation are reduced over the 45° ribs as well as in the outer layer in the parallel section of the 45° ribs in comparison to the 90° ribs.

The distributions of the one-dimensional profiles of R_{uw} in the streamwise and spanwise directions are shown in Figure 6.18a-c and Figure 6.18d-f, respectively. Near the wall, no distinct effect of pressure gradient is observed over the smooth wall and the 90° ribs (Figures 6.18a and 6.18d). However, as y increases remarkable differences are seen in R_{uw} profiles over these surfaces. Over the smooth wall, the streamwise R_{uw} profiles in the diverging section at $y = y_{UL}$ and $y = 0.75\delta$ show positive peaks, whereas in the parallel section the profiles exhibit negative peaks. Similarly, in Figure 6.18f a weak negative peak is observed in the spanwise profiles of R_{uw} in the outer layer of the smooth

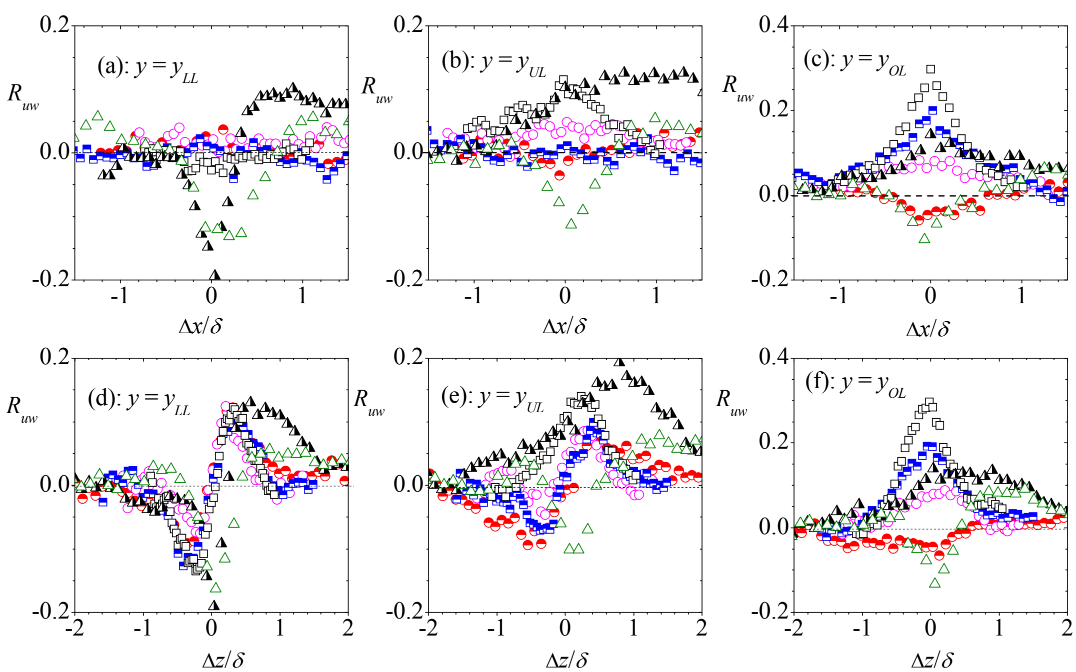

Figure 6.18: One-dimensional profiles of streamwise, (a)-(c) and spanwise, (d)-(f) slices through self-correlation point of R_{uw}. Symbols: SMS_P: ◓; SMS_D: ○; $R_8S_P\alpha_{90}$: ▀; $R_8S_D\alpha_{90}$: □; $R_8S_P\alpha_{45}$: ▲; $R_8S_D\alpha_{45}$: △.

wall. At $y = y_{LL}$ (Figure 6.18d) and $y = y_{UL}$ (Figure 6.18d), the R_{uw} profiles over smooth wall are clearly asymmetric and they both exhibit positive and negative peaks, however the peak value depends on the pressure gradient.

Although the streamwise R_{uw} profiles over the 90° ribs in the parallel and diverging sections exhibit positive peaks at $y = y_{UL}$ (Figure 6.18b) and $y = 0.75\delta$ (Figure 6.18c), the peak in the parallel section is much weaker compared to that in the diverging section. Similar to the smooth wall, the spanwise profiles over the 90° ribs are asymmetric at $y = y_{LL}$ (Figure 6.18d), however, there is no effect of APG at this location. At $y = y_{UL}$ (Figure 6.18d), the R_{uw} correlation in the diverging section remains largely positive with a strong peak whereas the R_{uw} correlation in the parallel section showed both positive and negative peaks, however weaker they are compared to that in the diverging section. As the outer layer is approached, the R_{uw} correlation in the parallel section displays only positive peak but it is still weaker than that in the diverging section.

On the other hand, the differences in R_{uw} correlation due to APG over the 45° ribs originated near the wall and propagated into the outer layer. In this case, both the streamwise and the spanwise profiles of R_{uw} were diminished by APG. Moreover, the distribution of R_{uw} correlation in the parallel section is positive at $y = y_{UL}$ (Figures 6.18b and 6.18e) and $y = 0.75\delta$ (Figures 6.18c and 6.18f), but in the diverging section R_{uw} correlation is both positive and negative.

The effect of roughness on the profiles of R_{uw} is weak near the wall, i.e., at y_{LL} in both the parallel and diverging sections (Figures 6.18a and 6.18d), and also at y_{UL} in the parallel section (Figures 6.18b and 6.18e). At y_{UL} in the diverging section, roughness acts jointly with APG to increase the values of R_{uw} correlation consistent with the higher number of contour levels. Similarly, R_{uw} correlation is enhanced by roughness in both the parallel and diverging sections at y_{OL} (Figures 6.18c and 6.18f), confirming that the effects of roughness extend into the outer layer. It should be noted that the sign of R_{uw} correlation at y_{OL} in the parallel section of the smooth wall is opposite to that of the corresponding 90° ribs due to the variation in the convection of the low-momentum fluid.

Consistent with the distributions of R_{uu} and R_{ww} profiles, the inclination of ribs revealed significant differences in R_{uw}. Close to the wall (at y_{LL} and y_{UL}), R_{uw} over the 45° ribs are usually larger than those over the 90° ribs. This could be due to intense secondary motions near the wall of the 45° ribs. On the contrary, in the outer layer R_{uw} is diminished over the 45° ribs.

6.3 LINEAR STOCHASTIC ESTIMATION

In the computation of the linear stochastic estimation in the *x-z* plane, both the positive and the negative swirling strengths as well as $u'w' < 0$ conditioning events were explored. However, only results corresponding to the prograde swirl are presented. The location for the conditioning event is similar to the location used for the computation of the two-point correlations presented earlier. The resulting vector fields were normalised by the magnitude of the vectors in order to retain unit magnitude of all vectors. Figure 6.19-Figure 6.27 shows the results in the *x-z* plane of the smooth wall (Figure 6.19-6.21), 90° ribs (Figure 6.22-6.24) and 45° ribs (Figure 6.25-6.27). Also included in these plots are the corresponding magnified views enveloping the location of the conditioning event with the contours of the stochastically estimated streamwise velocity component shown at the background. Over each surface, a strong clockwise swirling motion is revealed at the event location indicating the presence of large-scale coherence structure. This

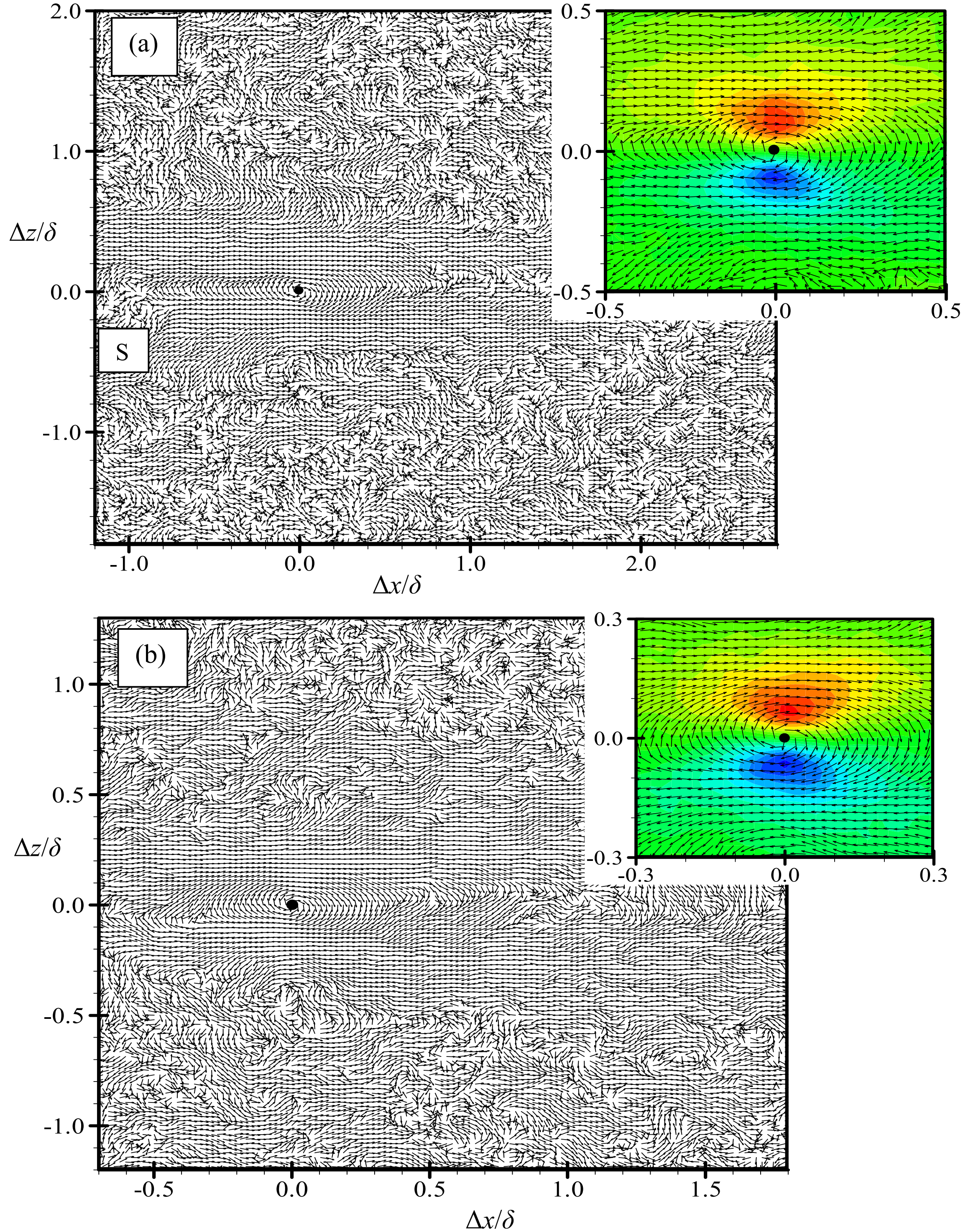

Figure 6.19: Linear stochastic estimation conditioned on prograde swirl event over smooth wall: (a), parallel section ($y^+ = 89$) and (b), diverging section ($y^+ = 49$). Shown at the side is the corresponding close-up view with the contour of conditionally averaged streamwise velocity at the background.

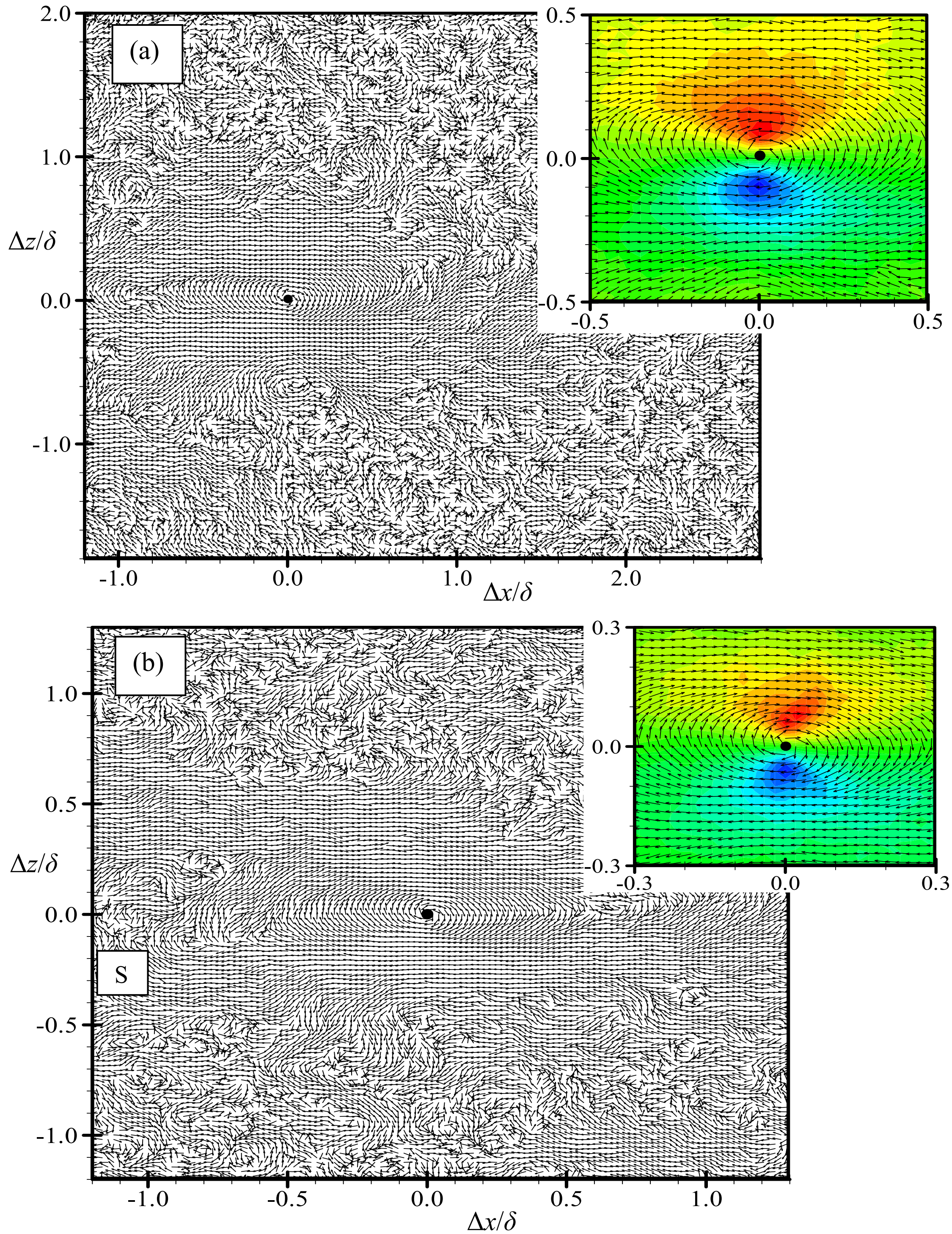

Figure 6.20: Linear stochastic estimation conditioned on prograde swirl event over smooth wall: (a), parallel section (y^+ = 156) and (b), diverging section (y^+ = 81). Shown at the side is the corresponding close-up view with the contour of conditionally averaged streamwise velocity at the background.

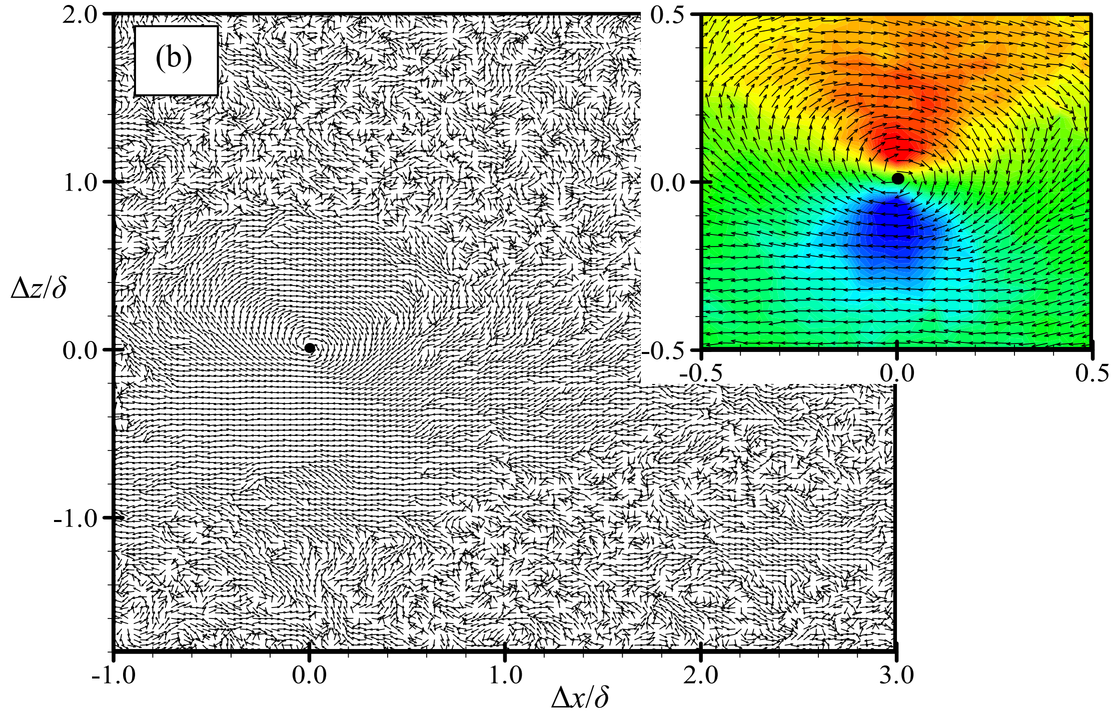

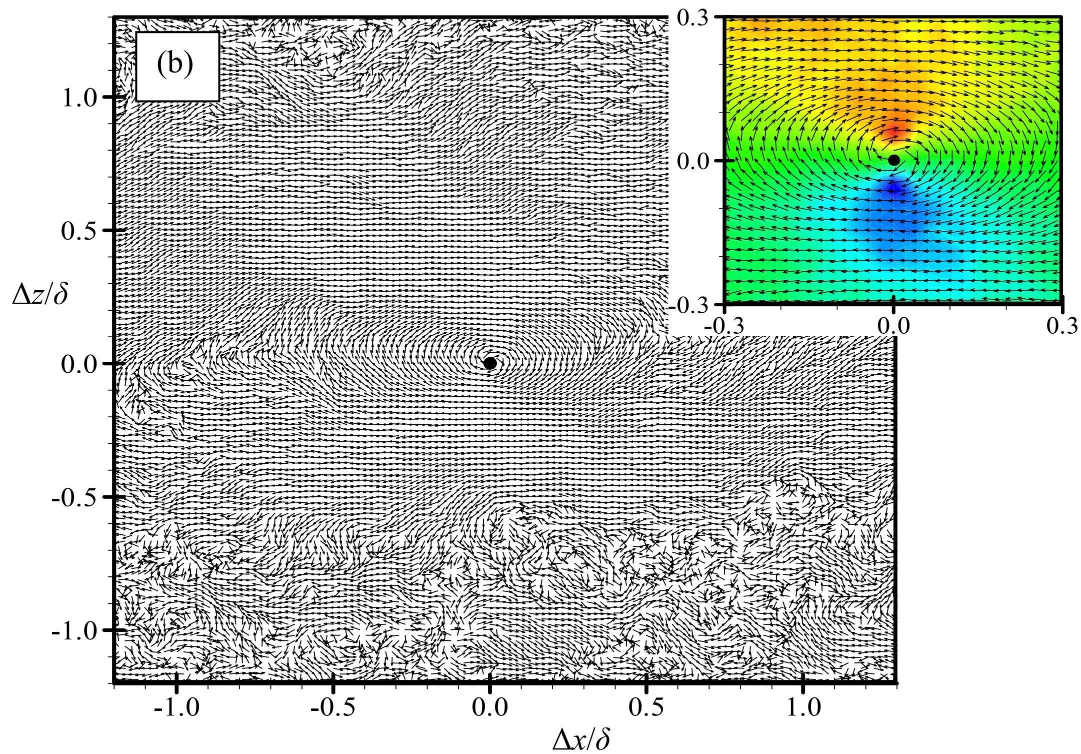

Figure 6.21: Linear stochastic estimation conditioned on prograde swirl event over smooth wall: (a), parallel section (y = 0.75δ) and (b), diverging section (y = 0.75δ). Shown at the side is the corresponding close-up view with the contour of conditionally averaged streamwise velocity at the background.

swirling motion is flanked in the $+\Delta z$ direction by positive stochastic velocity and in the $-\Delta z$ direction by negative stochastic velocity over each surface. Meanwhile, low-speed fluid is induced in the $-\Delta z$ direction of the conditioning event location as revealed by vectors directed towards reverse Δx direction. Similarly, high-speed fluid is induced in the positive Δz direction of the conditioning event location in agreement with the vectors directed towards the flow direction. Although a common swirling motion is observed at the event centre over each surface in either the parallel or diverging sections, noticeable differences due to pressure gradient, roughness and rib inclination angle as well as wall-normal location of the measurements are evident in these vector fields.

Over the smooth wall, a crease is formed along the Δx-axis passing through the conditioning event location. This crease usually extends further upstream and downstream of the conditioned point, sometime covering the entire length of the field of view depending on the measurement location. The crease can be viewed as a shear layer separating the low-speed fluid in $-\Delta z$ direction from the high-speed fluid in $+\Delta z$ direction. The low-speed fluid and high-speed fluid formed uniform momentum region each, which extends a considerable distance upstream and downstream of the conditioning point. The width of these regions varies with measurement location and pressure gradient. It is believed that these regions of elongated uniform momentum correspond to signatures of hairpin packets. For example, elongated low-speed fluid represents typical low-speed fluid that resides between the legs of vortices in the hairpin packet. Beyond the uniform momentum region in both $\pm\Delta z$ directions are regions of random motions, typified by random directions of the vectors. These regions of random motions that flanked the low-speed fluid region on one side and the high-speed fluid

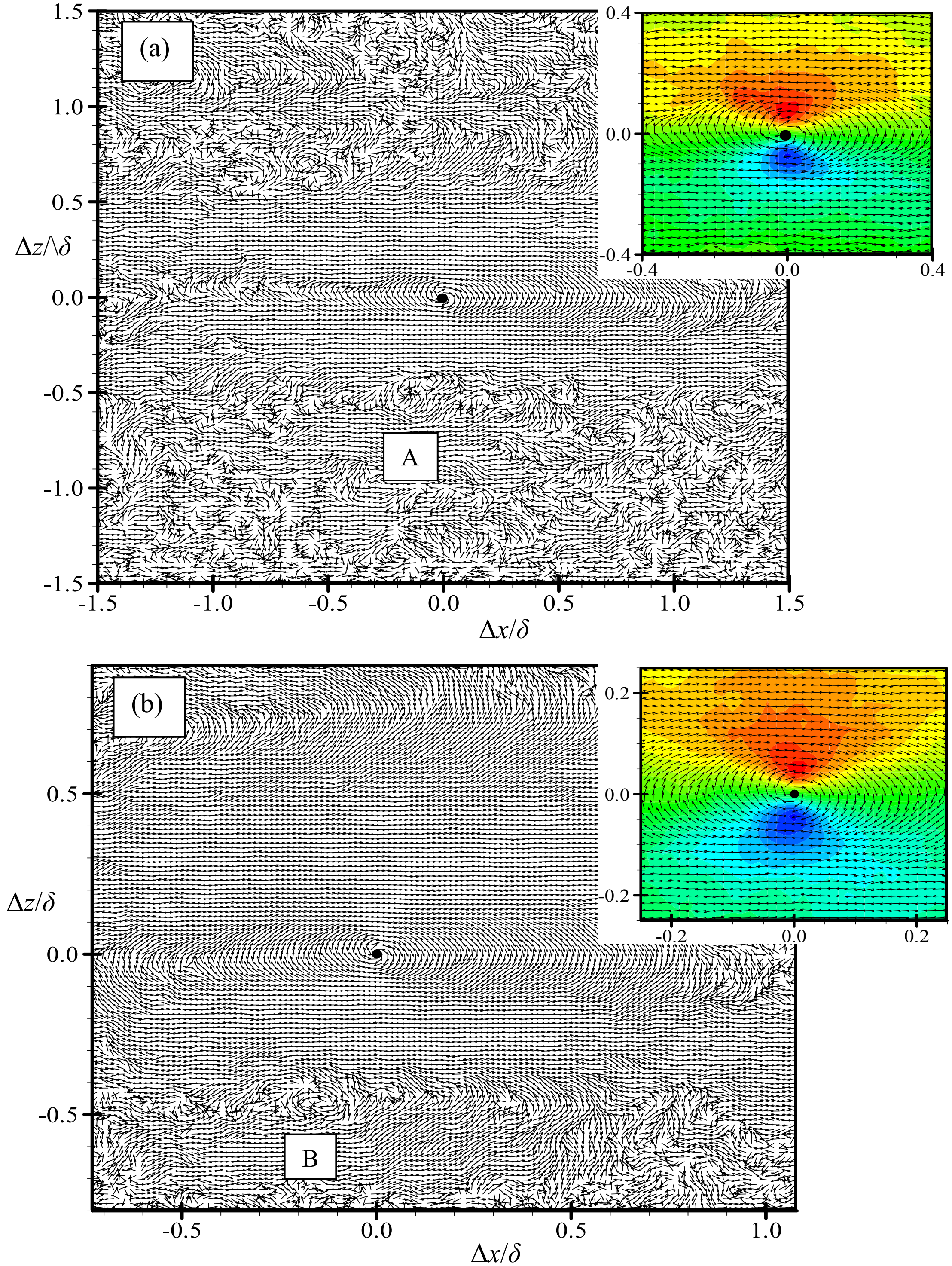

Figure 6.22: Linear stochastic estimation conditioned on prograde swirl event over 90° ribs wall: (a), parallel section ($y^+ = 206$) and (b), diverging section ($y^+ = 247$). Shown at the side is the corresponding close-up view with the contour of conditionally averaged streamwise velocity at the background.

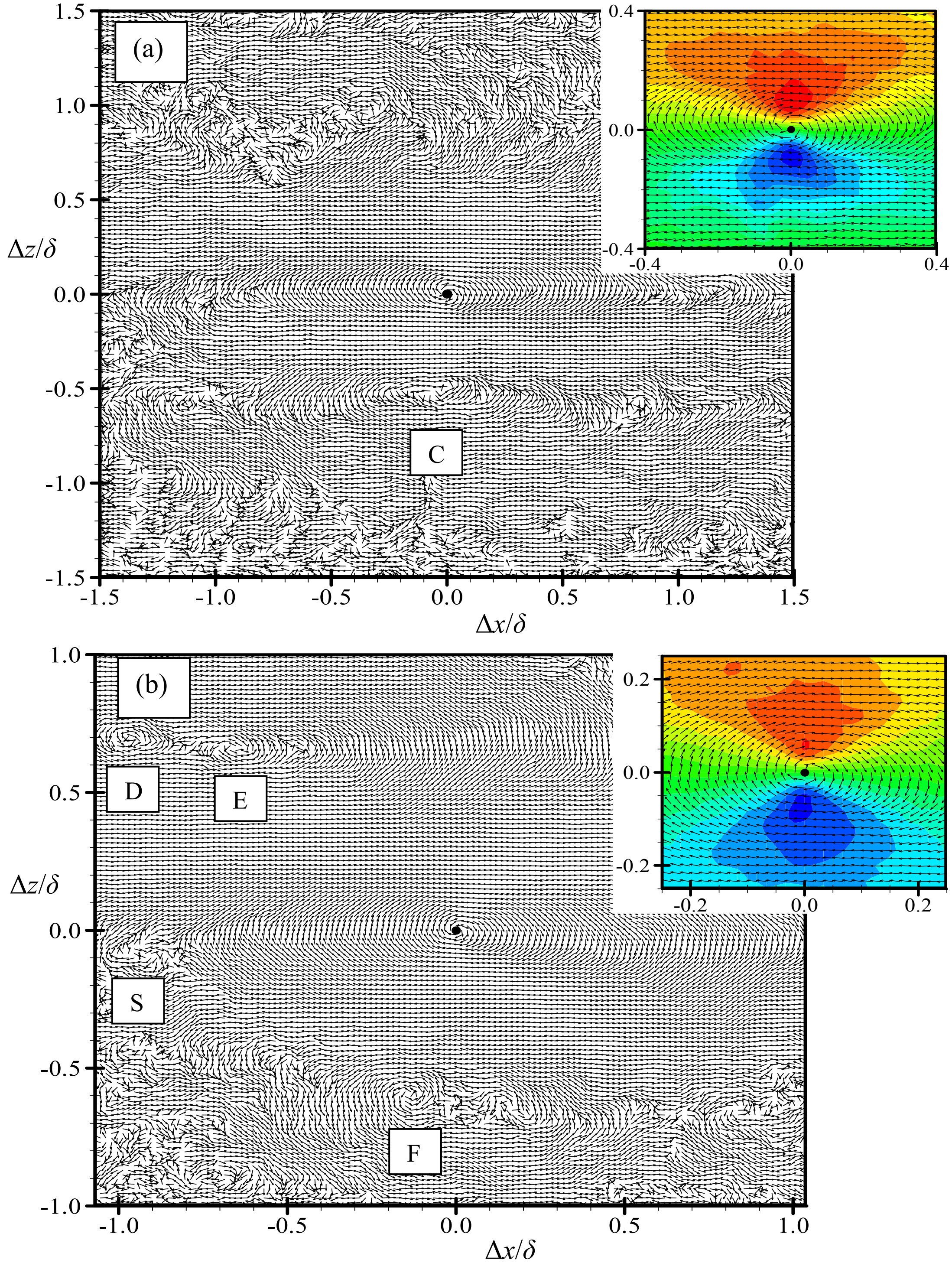

Figure 6.23: Linear stochastic estimation conditioned on prograde swirl event over 90° ribs: (a), parallel section ($y^+ = 305$) and (b), diverging section ($y^+ = 527$). Shown at the side is the corresponding close-up view with the contour of conditionally averaged streamwise velocity at the background.

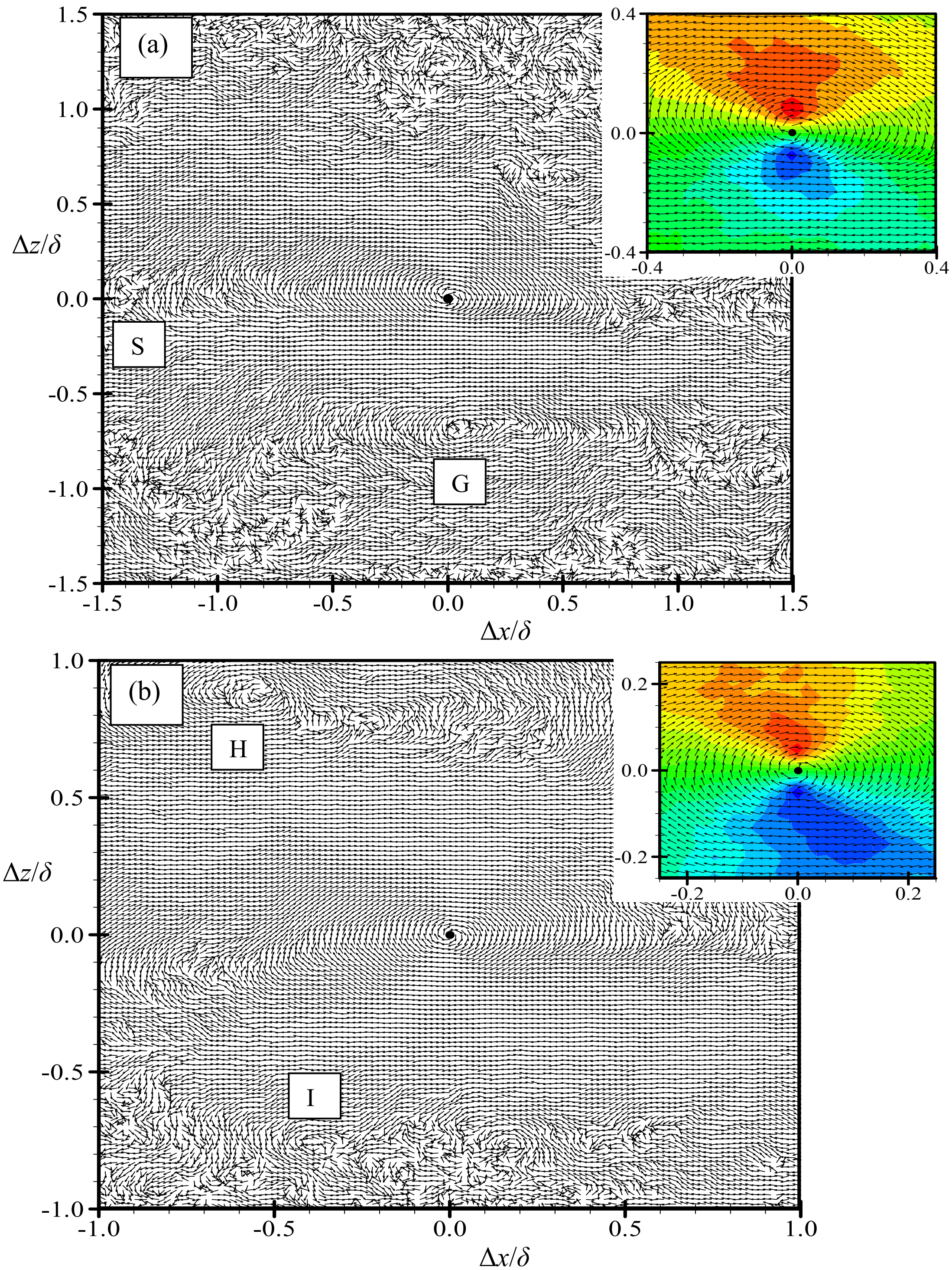

Figure 6.24: Linear stochastic estimation conditioned on prograde swirl event over 90° ribs: (a), parallel section (y = 0.75δ) and (b), diverging section (y = 0.75δ). Shown at the side is the corresponding close-up view with the contour of conditionally averaged streamwise velocity at the background.

region on the other side extend considerable distance in the Δx and Δz directions. However, these extents depend on the pressure gradient and measurement location. In general, larger regions of random motions are observed in the parallel section of the smooth wall than in the diverging section. Figure 6.19a and Figure 6.20b in the parallel and diverging sections of the smooth wall exhibit saddle point (S) near $\Delta x/\delta \approx -1.0$. According to Hambleton *et al*. (2006), this saddle point is associated the heads of smallest hairpin structures at the upstream end of inclined hairpin packet.

The 90° ribs revealed other interesting features in both the parallel and diverging sections besides those observed over the smooth wall. Figure 6.22 to Figure 6.24 revealed that the stochastically estimated velocity field over the 90° ribs demonstrated larger regions of low-speed fluid and high-speed fluid. As noted earlier, these regions correspond to regions of uniform momentum and they have considerable spanwise extent in the diverging section than in the parallel section. Over the 90° ribs additional creases or shear layers other than the crease passing through the conditioned point are formed in both $\pm\Delta z$ directions. The location of these creases varied with pressure gradient and wall-normal location. These additional creases are also bordered by uniform momentum regions whose width also depends on pressure gradient and the wall-normal location. Found in these shear layers are secondary swirling motions whose sense of rotation is opposite to that of the primary swirling motion observed at the conditioned point. Since these secondary swirling motions are located upstream of the primary swirl, they are motions likely induced by the legs of upstream hairpin structures. In Figure 6.23b, for example, two secondary swirling motions (D and E) are evident at $\Delta x/\delta = -0.66$ and -0.97 in the shear layer in the positive Δz direction. Another secondary swirl (F) is seen at $\Delta x/\delta = -0.14$ in the shear layer in negative Δz direction. A saddle point (S) is also evident at $\Delta x/\delta = -0.85$ along the crease passing through the conditioned point. Similar but less distinct secondary swirling motions are also evident in other measurement locations.

Over the 45° ribs, the swirling motion induced at the condition point is localized in the vicinity of the event. Surrounding the swirling motion is random motion caused by vectors that are randomly positioned. The region of random motion is larger than the region of organized motion. However, it is likely that the extent of the organized motion in the parallel section is larger in the parallel section than in the diverging section. The swirling motion over the 45° is often tilted consistent with the orientation of the two-point velocity correlations. In the diverging section, a weak secondary swirling motion is induced at the windward side of the primary swirling motion.

Some differences are obvious in the stochastically estimated vector fields over the smooth wall and rough wall in both the parallel section and diverging section. In general, the flow field over 90° ribs exhibits a large region of organised motion in comparison to the flow over the smooth wall and 45° ribs. This is consistent with the two-point velocity results, where large-scale coherent structures were observed over the 90° ribs. According to Hambleton *et al*. (2006), the regions where the vector fields are organised represent the scale of the average spatial coherence of a given event. In this case, the organized regions correspond to the zones where substantial number of events of similar size and shape are present compared to outside where the kinematics becomes random relative to the conditioning point. Moreover, the additional shear layers observed bordering the crease passing through the event location and the secondary swirling motions over 90° ribs are not common to the flow over the smooth wall and 45° ribs. Therefore, the present results indeed showed that rib roughness modified the outer layer of the flow.

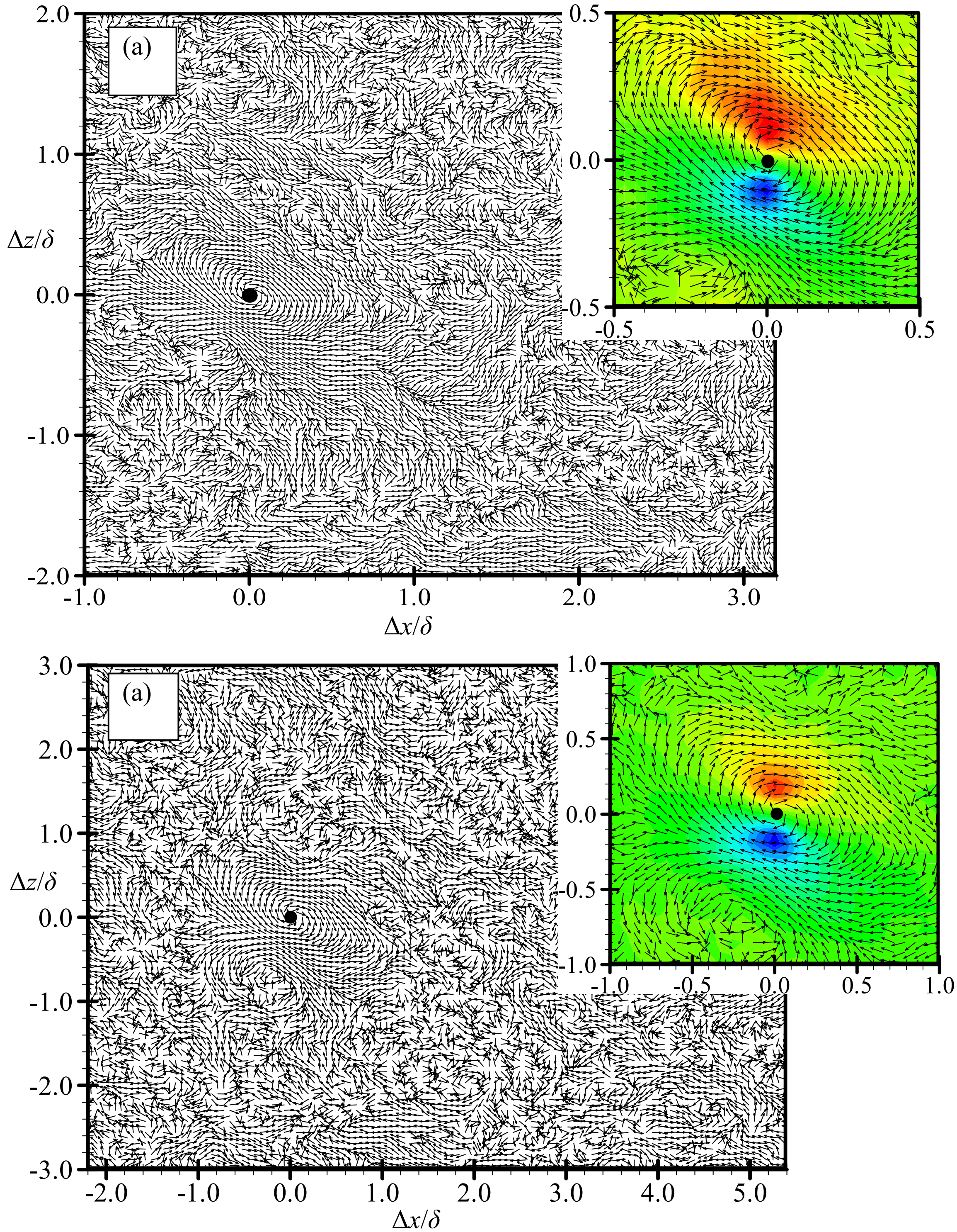

Figure 6.25: Linear stochastic estimated velocity fields in the *x*-*z* plane over 45° ribs conditioned on prograde swirl: (a) parallel section at y^+ = 182, and (b) diverging section at y^+ = 71. Shown at the side is the closed up view with the contour of conditionally average streamwise velocity superimposed at the background.

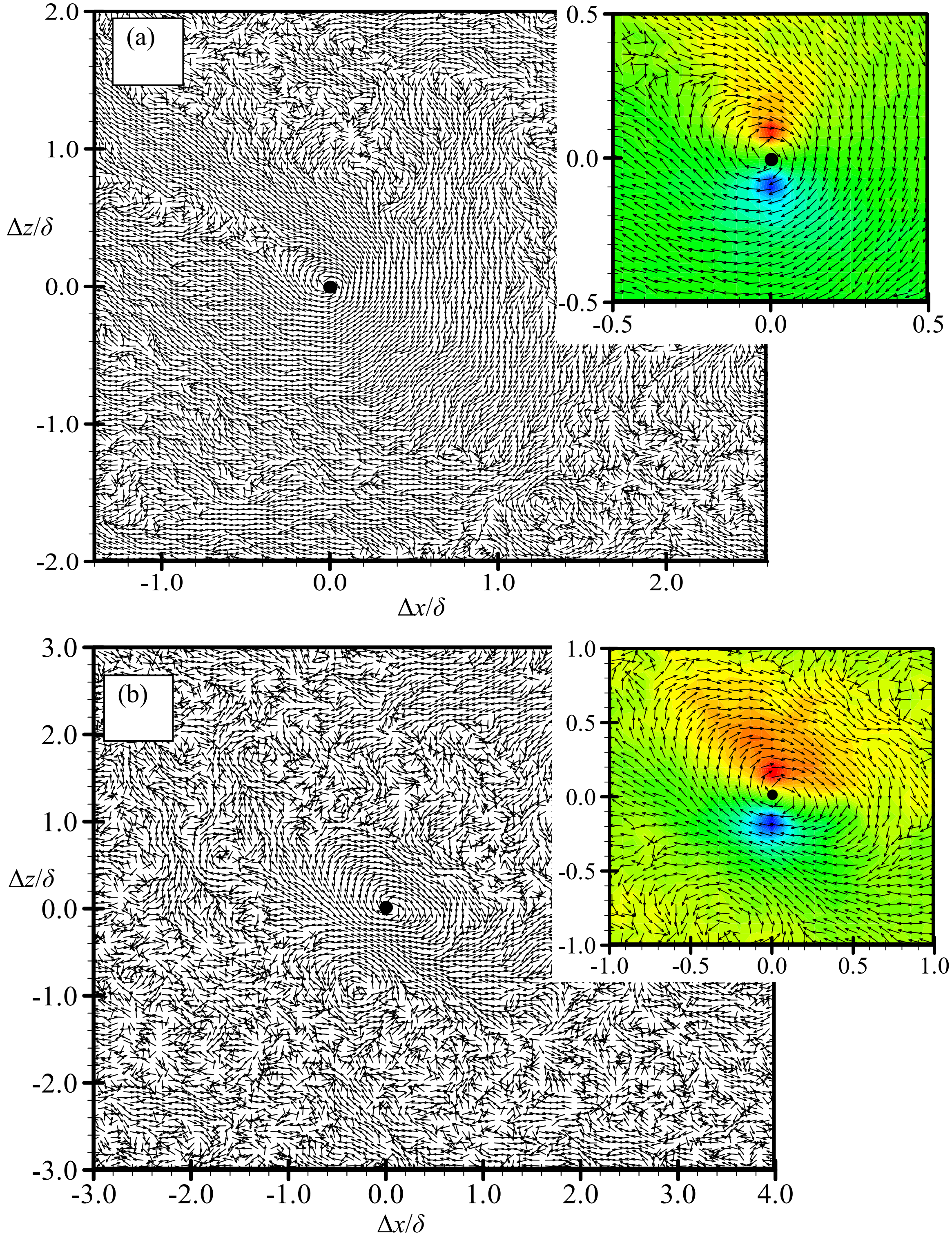

Figure 6.26: Linear stochastic estimated velocity fields in the *x*-*z* plane over 45° ribs conditioned on prograde swirl: (a) parallel section at $y^+ = 338$, and (b) diverging section at $y^+ = 125$. Shown at the side is the closed up view with the contour of conditionally average streamwise velocity superimposed at the background.

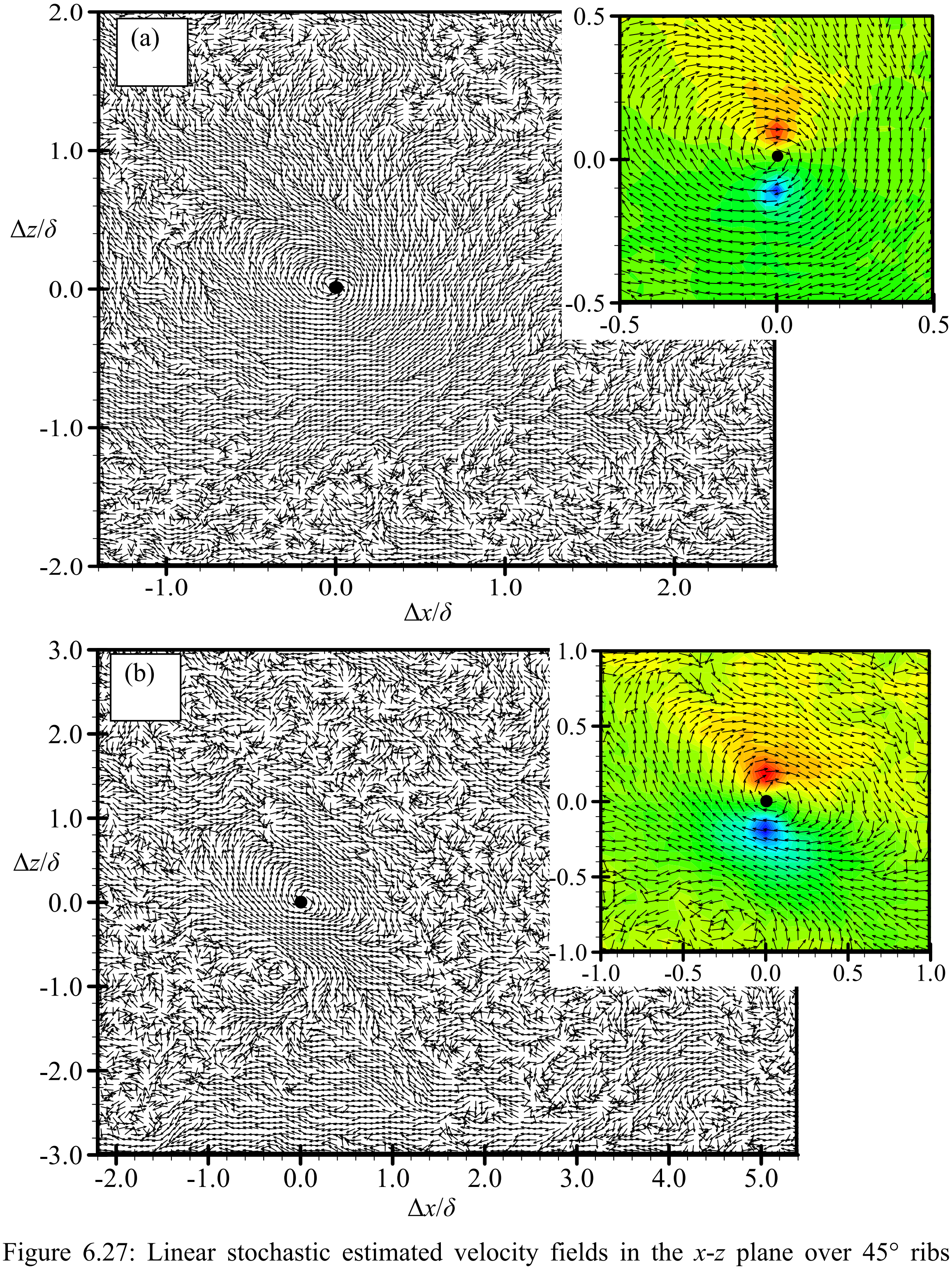

Figure 6.27: Linear stochastic estimated velocity fields in the *x*-*z* plane over 45° ribs conditioned on prograde swirl: (a) parallel section at $y = 0.75\delta$, and (b) diverging section at $y = 0.75\delta$. Shown at the side is the closed up view with the contour of conditionally average streamwise velocity superimposed at the background.

CHAPTER 7

CONCLUSIONS AND RECOMMENDATIONS

7.1 SUMMARY AND CONCLUSIONS

An experimental study of turbulent flows has been undertaken to investigate the effects of adverse pressure gradient, wall roughness and rib inclination angle on the mean flow characteristics, turbulence statistics and coherent structures. The mean flow was investigated using the mean velocities, boundary layer and drag parameters. The turbulence statistics used to study effects of APG, wall roughness and rib inclination angle include Reynolds stresses, Reynolds stress ratios, eddy viscosity, mixing length, and production terms for the turbulence kinetic energy and Reynolds shear stress. The effects of APG, roughness and rib orientation on the coherent structures were documented using the Galilean decomposition of the instantaneous velocity fields, contours of swirling strength, quadrant analysis, two-point velocity correlations and linear stochastic estimation. The main findings are as follows:

7.1.1 **Roughness Effects:** Due to the higher resistance generated by the ribs, the streamwise mean velocity profiles over the rough walls are less uniform compared to the profile over the smooth wall. Moreover, because of the large relative roughness used in the present study, no similarity in the outer layer was observed for the velocity defect profiles. Wall roughness enhanced the wall shear stress and the streamwise Reynolds normal stress ($\overline{u^2}$) proportionately and as a consequence, the streamwise Reynolds normal stress scaled with the friction velocity ($\overline{u^{+2}}$) in the parallel section was independent of wall roughness. In contrast, $\overline{v^{+2}}$ and $-\overline{u^+v^+}$ were significantly increased by roughness in both the roughness sublayer and outer region. The level of turbulence production was considerably enhanced by roughness, however, the eddy viscosity and mixing length were reduced by roughness, especially in the outer region.

Typical Galilean decomposed instantaneous flow fields over the smooth and rough walls revealed cores of hairpin vortices. It was observed that the flow fields over the 90° ribs were more populated with larger size vortex cores than over the smooth wall in both the parallel and diverging sections. Moreover, the vortices over the rough walls were accompanied with large-scale eruptions of fluid and larger low-speed region in comparison to structures observed over the smooth wall. It was observed that ejections, sweeps and interaction motions were stronger over the smooth wall than the events observed over the rough walls, yet the observed intense ejection and sweep events produced low Reynolds shear stress over smooth wall. The two-point velocity correlations showed that the average physical sizes of the turbulence structures over the smooth wall were larger than those over the *d*-type ribs but smaller than the sizes over the *k*-type ribs. The linear stochastic estimate revealed stronger prograde swirl and clearly defined crease over the rough walls compared to the smooth wall.

7.1.2 **Effects of APG:** For the smooth wall and 90° ribs, APG reduces the mean velocity drastically compared to the profiles obtained in the parallel section. The most dramatic effects of APG on the mean flow over these boundary conditions were observed over the ribs. The results also indicate that APG reduces the friction coefficient relative to the values obtained in the parallel section. Roughness parameters such as the roughness shift and equivalent sand grain roughness were increased by APG. For example, the values of k_s were 5-folds, 2-folds and 2-folds larger in the diverging section, respectively, for the *d*-type, intermediate type and *k*-type ribs than the corresponding values obtained in the parallel section. The turbulence levels were distinctly increased by APG compared to the results obtained in the parallel section. The occurrence of outer peak in the form of a broad and flat hump in the stresses and production terms for the APG flows indicates that the large-scale turbulence motions are more energetic in the outer layer than in the wall region.

It was observed that APG produced larger hairpin vortices than observed in the parallel section. Except for the intermediate type and *k*-type ribs where the ejections were relatively independent of APG, the ejection and sweep events as well as the interaction motions were intensified by APG. Over the smooth wall, APG remarkably reduced the physical sizes of the hairpin vortex packets. The streamwise and wall-normal extents of the structures were, however, less sensitive to APG over the 90° ribs.

7.1.3 Effects of Ribs Inclination: The formation of the secondary motion over the inclined ribs caused the boundary layer parameters to vary across the span of the ribs. It was also observed that the mean flow accelerates close to the leading edge of the ribs but it decelerates close to the trailing edge of the ribs relative to the flow at the mid-span of the channel. The effects of the secondary motion on the mean flow were more pronounced in the presence of APG than in the parallel section of the channel. The drag characteristics attained maximum close to the trailing edge. The Reynolds stresses were significantly enhanced close to the trailing edge and were usually lower close to the leading edge.

It was observed that the ejection and sweep events as well as interaction motions were strengthened by the secondary motion close to the leading edge than close to the trailing edge and at the mid-span of the ribs in the parallel section. However, in the diverging section, these quadrant events were often lower close to the leading edge of the ribs. Larger hairpin packets were formed close to the trailing edge of the ribs than at the mid-span and close to the leading edge of the ribs.

The results at the mid-span of 90°, 45° and 30° ribs revealed that ribs at lower inclination angles produced less resistance to the mean flow. The Reynolds stresses scaled with U_m were larger over ribs positioned perpendicular to the approach flow. On the other hand, the Reynolds stresses scaled with U_τ showed that, the turbulence level was higher over inclined ribs. The ratio of the Reynolds stresses indicate that the secondary flow associated with the inclined ribs caused the flow to be more isotropic than the flow over the perpendicular ribs.

The ejections, sweeps and the interaction motions were often weakened over the 90° ribs. These events increased with decreasing rib inclination angle in the parallel section but in the diverging section they are stronger over intermediate type and *k*-type ribs inclined at 45° to the approach flow. In the parallel section, the physical sizes of the structures embodied in R_{uu} correlation were larger over the *k*-type ribs at 90°, but for the *d*-type and intermediate type ribs the streamwise and the wall-normal extents of the structures were magnified over ribs inclined at 45° to approached flow. However, in the diverging section larger spatial structures were observed over intermediate type and *k*-type ribs at 90° to the approach flow whereas over *d*-type ribs, the length scales attained maximum for ribs inclined at 45°.

7.2 IMPLICATION TO TURBULENCE MODELS

The present studies provide a comprehensive experimental data for turbulent channel flows with or without adverse pressure gradient over ribs that were oriented at different inclination angles. These experimental data are useful benchmark data for validating and calibrating advanced turbulence models for fluid engineering applications. The observed low values of the structure parameter implies that in order to compute flows of these types in a low aspect ratio channel using turbulence models, lower values of structure parameter are required for the computation of C_μ (in which case, $C_\mu < 0.09$). Moreover, the variation of the structure parameter with boundary conditions suggests that for accurate prediction of the flows investigated in this study, different C_μ values should be employed in the turbulence models. The disparity in the relative roughness, k_s/k across the span of the inclined ribs suggests that a single value of k_s/k cannot be used in turbulence models to predict flows over inclined ribs.

The good agreement of both eddy viscosity and mixing length in the presence of adverse pressure gradient and roughness near the wall implied that mixing length based models would predict the flow better in the near wall region, irrespective of the boundary condition and pressure gradient.

In general, the ratio of the normal stresses increases as the edge of the boundary layer is approached, indicating that the flow is more isotropic in the core region than near the wall. Both APG and roughness tend to make the flow more anisotropic than the flow in the parallel section of the smooth wall. The low values of $\overline{v^2}/\overline{u^2}$, and the rapid variation of this ratio imply that turbulence models which employ isotropic assumptions will not be able to predict these flows accurately.

7.3 RECOMMENDATIONS FOR FUTURE WORK

The present study examined velocity fields over inclined ribs in a channel with or without APG using planar PIV techniques. Since some of the engineering applications of inclined ribs are in areas of heat transfer, it would be more informative to simultaneously measure the velocity and thermal fields. This would enable simultaneous examination of both velocity and thermal fields near the inclined ribs to further improve our understanding of drag reduction and convective heat transfer augmentation over these ribs.

The present measurements were made in streamwise-wall-normal and streamwise-spanwise planes due to the inherent limitations of the planar PIV used in the present study. It is recommended that volumetric velocity measurement techniques (e.g., holographic PIV) be applied to conduct complete three-component and three-dimensional velocity measurements. This would allow the evaluation of the complete Reynolds stress and velocity gradient tensors.

The present study employed standard PIV, making it unable to temporally resolve the evolution of the flow. It would be useful to employed time-resolved PIV to study the temporal evolution of the turbulence structure. The time-resolved PIV will also make it possible to obtain time-space correlations so that time scale of the turbulence structures can be obtained.

REFERENCES

Adrian, R. J. 1988, "Statistical Properties of Particle Image Velocimetry Measurements in Turbulent Flow", *In Laser Anemometry in Fluid Mechanics-III* (ed. R. J. Adrian, T Asanuma, D. F. G. Durao, F. Durst and J. H. Whitelaw), pp. 115-129, Springer

Adrian, R.J., 1991, "Particle-Imaging Techniques for Experimental Fluid", *Annual Review of Fluid Mech*anics, Vol. 23, pp. 261-304.

Adrian, R. J. and Moin, P. 1988, "Stochastic Estimation of Organized Turbulent Structure: Homogeneous Shear Flow", *Journal of Fluid Mechanics*, Vol. 190, pp. 531-539.

Adrian, R. J., Moin, P. and Moser, R. D., 1987, "Stochastic Estimation of Conditional Eddies in Turbulent Channel Flow", In *Proc. 1987 Summer Program, Report CTR-S87*, pp. 7-19, Center for Turbulence Research, Stanford University, Stanford, CA.

Adrian, R. J., Christensen, K. T. and Liu, Z.-C., 2000b, "Analysis and Interpretation of Instantaneous Turbulent Velocity Fields", *Experiments in Fluids*, Vol. 29, pp. 275-290.

Adrian, R. J., Meinhart, C. D., and Tomkins, C. D., 2000a, "Vortex Organization in the Outer Region of the Turbulent Boundary Layer", *Journal of Fluid Mechanics*, Vol. 422, pp. 1-54.

Alfredsson, P. H. and Johansson, A. V., 1984, "Time Scales in Turbulent Channel Flow", *Physics of Fluids*, Vol. 27, 1974-1981.

Alfonsi, G. and Primavera, L., 2007, "Dynamics of POD Modes in Wall Bounded Turbulent Flow", *Proceedings of the Royal Society A*., Vol. 463, pp. 593-612.

Andreopoulos, J., Durst, F., Zaric, Z. and Jovanovic, J., 1984, "Influence of Reynolds Number on Characteristics of Turbulent Wall Boundary Layers", *Experiments in Fluids*, Vol. 2 (1), 7-16.

Angele, K. P. and Muhammad-Klingmann, B., 2006, "PIV Measurements in a Weakly Separating and Reattaching Turbulent Boundary Layer", *European Journal of Mechanics B/Fluids*, Vol. 25, pp. 204-222.

Antonia, R. A. and Atkinson, D. J. 1973, "High-Order Moments of Reynolds Shear Stress Fluctuations in a Turbulent Boundary Layer", *Journal of Fluid Mechanics*, Vol. 58(3), pp. 581-593.

Antonia, R. A. and Krogstad, P. -Å., 2001, "Turbulence Structures in Boundary Layer over different Types of Surface Roughness ", *Fluid Dynamics Research*, Vol. 28(2), pp. 139-21.

Ashrafian, A., and Andersson, H. I., 2006a, "The Structure of Turbulence in a Rod-*Roughened* Channel", *International Journal of Heat and Fluid Flow*, Vol. 27, pp. 65-79.

Ashrafian, A., Andersson, H. I., 2006b, "Roughness Effects in Turbulent Channel Flow", *Progress in Computational Fluid Dynamics*, Vol. 6, pp. 1-20.

Ashrafian, A., Andersson, H. I., and Manhart, M., 2004, "DNS of Turbulent Flow in a Rod-Roughened Channel", *International Journal of Heat and Fluid Flow*, Vol. 25, pp. 373-383.

Aubertine, C. D. and Eaton, J. K., 2005, "Turbulence Development in a Non-Equilibrium Turbulent Boundary Layer with Mild Adverse Pressure Gradient", Journal of Fluid Mechanics, Vol. 532, pp. 345-364.

Aubertine, C. D. and Eaton, J. K., 2006, "Reynolds Number Scaling in a Non-Equilibrium Turbulent Boundary Layer with Mild Adverse Pressure Gradient", *International Journal of Heat and Fluid Flow*, Vol. 27, pp. 566-575.

Bakken, O. M., Krogstad, P.-Å., 2003, "Stress Measurement in a Rough Wall Channel Flow using Variable Angle Method of Calibration for X-probes", *Proceedings of Turbulence and Shear Flow Phenomena-3*, 1, pp. 105-110.

Bakken, O. M., Krogstad, P.-Å., Ashrafian, A., and Andersson, H. I., 2005, "Reynolds Number Effects in the Outer Layer of the Turbulent Flow in a Channel with Rough Walls", *Physics of Fluids*, Vol. 17, pp. 1-17.

Balachandar, R. and Bhuiyan, F., 2007, "Higher-Order Moments of Velocity Fluctuations in an Open-Channel Flow with Large Bottom Roughness", *Journal of Hydraulic Engineering* (ASCE), Vol. 131(1), pp. 77-87.

Balachander R., Hagel, K. and Blakely, D., 2002, "Velocity Distribution in Decelerating Flow over Rough Surfaces", *Canadian Journal of Civil Engineering*, Vol. 29, pp. 211-221.

Bandyopadhyay, P. R., 1980, "Large Structure with a Characteristic Upstream Interface in Turbulent Boundary Layers", *Physics of Fluids*, Vol. 23, pp. 2326-2327.

Bandyopadhyay, P. R., 1987, "Rough-Wall Turbulent Boundary Layers in the Transition Regime", *Journal of Fluid Mechanics*, Vol. 180, pp. 231-266.

Barenblatt, G. I., 1993, "Scaling Laws for Fully Developed Turbulent Shear Flows. Part 1: Basic Hypotheses and Analysis", *Journal of Fluid Mechanics*, Vol. 248, 521-529.

Bergstrom, D., Kotey, N., Tachie, M., 2002, "The Effects of Surface Roughness on the Mean Velocity Profile in a Turbulent Boundary Layer", *Journal of Fluids Engineering*, Vol. 124, pp. 664-670.

Bhaganagar, K., Kim, J. and Coleman, G., 2004, "Effect of Roughness on Wall-Bounded Turbulence", *Flow, Turbulence and Combustion*, Vol. 72, pp. 463-492.

Bogard, D. G. and Tierderman, W. G., 1987, "Characteristics of Ejections in Turbulent Channel Flow", *Journal of Fluid Mechanics*, Vol. 179, pp. 1-19.

Bonhoff, S. B., Parneix, S., Leusch, J., Johnson, B. V., Schabacker, J., and Bölcs, A., 1999, "Experimental and Numerical Study of Developed Flow and Heat Transfer in Coolant Channels with 45 Degree Ribs", *Int. Journal of Heat and Fluid Flow*, Vol. 20, pp. 311-319.

Bradshaw, P., 1967, "The Turbulent Structure of Equilibrium Turbulent Boundary Layers", *Journal of Fluid Mech.*, Vol. 29, pp. 625-645.

Bradshaw, P. and Pontikos, N. S., 1985, "Measurements in the Turbulent Boundary Layer on an 'Infinite' Swept Wing", *Journal of Fluid Mechanics*, Vol. 159, pp. 105-130.

Brodkey, R.S., Wallace, J.M., Eckelmann, H., 1974, "Some Properties of Truncated Turbulence Signals in Bounded Shear Flows", *Journal of Fluid Mechanics*, Vol. 63, pp. 209-224.

Brundrett, E. and Baines, W. D., 1964., "The Production and Diffusion of Vorticity in Duct Flow", *Journal of Fluid Mechanics*, Vol. 19(3), pp. 375-394.

Burattini, P., Leonardi, S., Orlandi, P., and Antonia, R. A., 2008, "Comparison between Experiments and Direct Numerical Simulations in a Channel Flow with Roughness on One Wall", *Journal of Fluid Mechanics*, Vol. 600, pp. 403-426.

Ching, C. Y., Djenidi, R. A. and Antonia, R. A., 1995, "Low-Reynolds Number Effects in a Turbulent Boundary Layer", *Experiments in Fluids*, Vol. 19, pp. 61-68.

Christensen, K. T. and Adrian, R. J., 2001, "Statistical Evidence of Hairpin Vortex Packets in Wall Turbulence", *Journal of Fluid Mechanics*, Vol. 431, pp. 433-443.

Christensen, K. T., and Wu, Y., 2005, "Characteristics of Vortex Organisation in the Outer Layer of Wall Turbulence", *Proceedings, 4th International Symposium on Turbulence and Shear Flow Phenomena*, Williamsburg, Virginia, Vol. 3, pp. 1025-1030.

Clauser, F. H., 1954, "Turbulent Boundary Layers in Adverse Pressure Gradients", *Journal of Aerospace Science*, Vol. 21, pp. 91-108.

Coceal, O., Dobre, A., Thomas T. G. and Belcher, S. E. 2007, "Structure of Turbulent Flow over Regular Arrays of Cubical Roughness," *Journal of Fluid Mechanics*, Vol. 589, pp. 375-409.

Coleman, H. W. and Steele, W. G., 1995, "Engineering Application of Experimental Uncertainty Analysis", *AIAA Journal*, Vol. 33, pp. 1888-1896.

Coleman, G. N., Ferziger, J. H. and Spalart, P. R., 1990, "A Numerical Study of the Turbulent Ekman Layer", *Journal of Fluid Mechanics*, Vol. 213, pp. 313-348.

Coles, D., 1956, "The Law of the Wake in the Turbulent Boundary Layer", *Journal of Fluid Mechanics*, Vol. 1, pp. 191-226.

Connelly, J. S., Schultz, M. P., and Flack, K. A., 2006, "Velocity-Defect Scaling for Turbulent Boundary Layers with a Range of Relative Roughness", *Experiments in Fluids*, Vol. 40, pp. 188-195.

Corino, E. R. and Brodkey, R. S., 1969, "A Visual Investigation of the Wall Region in Turbulent Flow", *Journal of Fluid Mechanics*, Vol. 37, pp. 1-30.

Cui, J., Patel, V. C. and Lin, C.-L., 2003, "Large-Eddy Simulation of Turbulent Flow in a Channel with Rib Roughness", *International Journal of Heat and Fluid Flow*, Vol. 24, pp. 372-388.

Cutler, A. D. and Johnston, J. P., 1989, "The Relaxation of a Turbulent Boundary Layer in an Adverse Pressure Gradient," *Journal of Fluid Mechanics*, Vol. 200, pp. 367-387.

Dean, R. B., 1978, "Reynolds Number Dependence of Skin Friction and Other Bulk Flow Variables in Two-Dimensional Rectangular Duct Flow", *Journal of Fluids Engineering,* Vol. 100, pp. 215-223.

DeGraaff, D. B and Eaton, J. K., 2000, "Reynolds-Number Scaling of the Flat-Plate Turbulent Boundary Layer", *Journal of Fluid Mechanics*, Vol. 422, pp. 319-346.

Djenidi, L., Antonia, R. A., Amielh, M. and Anselmet, F., 2008, "A Turbulent Boundary Layer Over A Two-Dimensional Rough Wall", *Experiments in Fluids*, Vol. 44, pp. 37-47.

Durst, F., Fischer, M., Jovanovic, J. and Kikura, H., 1998, "Methods to Set Up and Investigate Low Reynolds Number", Fully Developed Turbulent Plane Channel Flows", *Journal of Fluids Engineering*, Vol. 120(3), pp. 496-503.

Elsberry, K. Loeffler, J. Zhou, M. D. and Wygnanski, I., 2000, "An Experimental Study of a Boundary Layer that is Maintained on the Verge of Separation", *Journal of Fluid Mechanics*, Vol. 423, pp. 227-261.

Farge, M., Pellegrino, G. and Schneider, K., 2001, "Coherent Vortex Extraction in 3D Turbulent Flows Using Orthogonal Wavelets", *Physical Review Letters*, Vol. 87 (5), pp. 45011-45014.

Finnigan, J. J., 2000, "Turbulence in Plant Canopies", *Annual Review of Fluid Mechanics*, Vol. 32, pp. 519-571.

Flack, K. A., Schultz, M. P. and Shapiro, T. A., 2005, "Experimental Support for Townsend's Reynolds Number Similarity Hypothesis on Rough Walls", *Physics of Fluids*, Vol. 17, 035102.

Flack, K. A., Schultz, M. P. and Connelly, J. S., 2007, "Examination of a Critical Roughness Height for Boundary Layer Similarity", *Physics of Fluids*, Vol. 19, 095104.

Forliti, D. J., Strykowski, P. J. and Debatin, K., 2000, "Bias and Precision Errors of Digital Particle Image Velocimetry", *Experiments in Fluids*, Vol. 28, pp. 436-447.

Fujita, H., Yokosawa, H., and Hirota, M., 1989, "Secondary Flow to the Second Kind in Rectangular Ducts with One Rough Wall", *Experimental Thermal and Fluid Science*, Vol. 2, pp. 72-80.

Furuya, Y., and Miyata, M., 1972, "Visual Studies on the Wake of a Roughness Element Proximate to a Wall", *Mem. Fac, Engng.*, Nagoya University, Vol. 24, pp 278-293.

Furuya, Y., Miyata, M. and Fujita, H., 1976, "Turbulent Boundary Layer and Flow Resistance on Plates Roughened by Wires", *Journal of Fluid Engineering*, Vol. 98, pp. 635-644.

Ganapathisubramani, B., Longmire, E. K. and Marusic, I., 2003, "Characteristics of Vortex Packets in Turbulent Boundary Layers", *Journal of Fluid Mechanics*, Vol. 478, pp. 35-46.

Ganapathisubramani, B., Hutchins, N., Longmire, E. K. and Marusic, I., 2005, "Investigation of Large-Scale Coherence in a Turbulent Boundary Layer Using Two-Point Correlations", *Journal of Fluid Mechanics*, Vol. 524, pp. 57-80.

Gao, X., and Sundén, B., 2004, "Effects of Inclination Angle of Ribs on the Flow Behaviour in the Rectangular Ducts ", *Journal of Fluid Engineering*, Vol. 126, pp. 692-699.

George, W. K. and Castillo, L., 1997, "Zero-Pressure-Gradient Turbulent Boundary Layer", *Applied Mechanics Reviews*, Vol. 50, pp. 689-729.

Grass, A. J., 1971, "Structural Features of Turbulent Flow Over Smooth and Rough Boundaries", *Journal of Fluid Mech.*, Vol. 50, pp. 233-255.

Gui, L., Longo, J. and Stern, F., 2001, "Towing Tank PIV Measurement System, Data and Uncertainty Assessment for DTMB Model 5512", *Experiments in Fluids*, Vol. 31, pp. 336-346.

Hama, F. R., 1954, "Boundary-Layer Characteristics for Smooth and Rough Surfaces", *Trans. Soc. Naval Archit. Marine Eng.*, Vol. 62, pp. 333-358.

Hambleton, W. T, Hutchins, N. and Marusic, I., 2006, "Simultaneous Orthogonal-Plane Particle Image Velocimetry Measurements in a Turbulent Boundary Layer", *Journal of Fluid Mechanics*, Vol. 560, pp. 53-64.

Han, J. C., Glicksman, L. R, and Rohsenow, W. M., 1978, "An Investigation of Heat Transfer and Friction for Rib-Roughened Surfaces", *International Journal of Heat and Mass Transfer*, Vol. 21, pp. 1143-1156.

Hanjalic, K., and Launder, B. E., 1972, "Fully Developed Asymmetric Flow in a Plane Channel", *Journal of Fluid Mechanics*, Vol. 51, pp. 301-335.

Head, M. R. and Bandyopadhyay, P. 1981, "New Aspects of Turbulent Boundary Layer Structure", *Journal of Fluid Mechanics*, Vol. 107, pp. 297-338.

Hoagland, L. C., 1960, "Fully Developed Turbulent Flow in Straight Rectangular Ducts-Secondary Flow, its Cause and Effect on the Primary Flow", *Ph.D Thesis*, Mechanical Engineering Department, MIT, Cambridge, Massachusettes.

Hussain, A. K. M. F., 1983, "Coherent Structures – Reality and Myth", *Phys. Fluids* 26(10), pp. 2816-2850.

Hutchins, N. and Marusic, I., 2007, "Evidence of very long Meandering Features in the Logarithmic Region of Turbulent Boundary Layers", *Journal of Fluid Mechanics*, Vol. 579, pp. 1-28.

Hutchins, N., Nickels, T. B. and Marusic, I. and Chong, M. S., 2009, "Hot-Wire Spatial Resolution Issues in Wall-Bounded Turbulence", *Journal of Fluid Mechanics*, Vol. 635, pp. 103-136.

Ikeda, T., and Durbin, P., 2007, "Direct Simulations of a Rough-Wall Channel Flow", *Journal of Fluid Mechanics*, Vol. 571, pp. 235-263.

Jiménez, J., 2004, "Turbulent Flows over Rough Walls", *Annual Review of Fluid Mechanics*, Vol. 36, pp. 173-196.

Jimenez, J., Hoyas, S., Simens, M. P. and Mizuno, Y., 2009, "Comparison of Turbulent Boundary Layers and Channels from Direct Numerical Simulation", *Sixth International Symposium on Turbulence and Shear Flow Phenomena*, pp. 289-294.

Jimenez, J., Hoyas, S., Simens, M. P. and Mizuno, Y., 2010, "Turbulent Boundary Layers and Channels at Moderate Reynolds Numbers", *Journal of Fluid Mechanics*, Vol. 657, pp. 335-360.

Johansson, A. V., Alfredsson, P. H. and Eckerlmann, H., 1987, "On the Evolution of Shear-Layer Structures in Near-Wall Turbulence", In *Advances in Turbulence, Proc. First European Turbulence conference, Lyon, July 1986* (ed. G. Comte-Bellot and J. Mathieu), Springer.

Johansson, A. V., Alfredsson, P. H. and Kim, J., 1991, "Evolution and Dynamics of Shear Layer Structures in Near-Wall Turbulence," *Journal of Fluid Mechanics*, Vol. 224, pp. 579-599.

Kaftori, D., Hetsroni, G and Banerjee, S., "Particle Behaviour in the Turbulent Boundary Layer. I. Motion, Deposition, and Entrainment", *Phys. Fluids*, **7**(5), pp. 1095-1106.

Kameda, T., Mochizuki, S. and Osaka, H., 2004, "LDA Measurement in Roughness Sub-layer beneath Turbulent Boundary Layer Developed over Two-Dimensional Square Rough Surface", *12th International Symposium on the Application of Laser Techniques to Fluid Mechanics*, Lisbon, Portugal, 12-15 July 2004.

Kameda, T., Koreishi, K., Mochizuki, S. and Osaka, H., 2007, "Mechanism of Momentum Exchange near a Roughness Element for Rough Wall turbulent Boundary Layer (Flow Visualization of Eddy Formed in a Two-Dimensional Square Cavity)", *Journal of Fluid Science and Technology*, Vol. 2(1), pp. 196-204.

Keane, R. D. and Adrian, R. J., 1990, "Optimization of Particle Image Velocimetry, Part1: Doubled Pulsed System", *Measurement Science and Technology*, Vol. 1(11), pp. 1202-1215.

Keirsbulck, L., Labraga, L., Mazouz, A., Tournier, C., 2002, "Surface Roughness Effects on Turbulent Boundary Layer Structures", *Journal of Fluids Engineering*, Vol. 124, pp. 127-135.

Kim, J., Moin, J. and Moser, R., 1987, "Turbulence Statistics in Fully Developed Channel Flow at Low Reynolds Number", *Journal of Fluid Mechanics*, Vol. 177, pp. 133-166.

Kline S. J., and Robinson, S. K., 1989, "Quasi-Coherent Structures in the Turbulent Boundary Layer. Part 1: Status Report on a Community-Wide Summary of the Data", In: Kline S. H, Afgan N. H. (ed) Near Wall Turbulence. *Proceedings of Zaric Memorial Conference*, pp. 200-217, New York; Hemisphere.

Kline, S. J., Reynolds, W. C., Schraub, F. A. and Runstadler, P. W., 1967, "The Structure of Turbulent Boundary Layers", *Journal of Fluid Mechanics*, Vol. 30, pp. 741-773.

Kostas, J., Soria, J. and Chong, M., 2005, "A Comparison between Snapshot POD Analysis of PIV Velocity and Vorticity Data", *Experiments in Fluids*, Vol. 38, pp.146-160.

Krogstad, P.-Å., Andersson, H. I., Bakken, O. M., and Ashrafian, A., 2005, "An Experimental and Numerical Study of Channel Flow with Rough Walls", *Journal of Fluid Mechanics*, Vol. 530, pp. 327-352.

Krogstad, P., Antonia, R. A., Browne, L., 1992, "Comparison between Rough- and Smooth-Wall Turbulent Boundary Layers", *Journal of Fluid Mechanics*, Vol. 245, pp. 599-617.

Krogstad, P. -Å. and Antonia, R. A., 1994, "Structures of Turbulent Boundary Layers on Smooth and Rough Walls", *Journal of Fluid Mechanics*, Vol. 277, pp. 1-21.

Krogstad, P. -Å, Antonia, R. A., 1999, "Surface Roughness Effects in Turbulent Boundary Layers", *Experiments in Fluids*, Vol. 27, pp. 450-460.

Krogstad, P.-Å., Skåre, P. E., 1995, "Influence of a Strong Adverse Pressure Gradient on the Turbulent Structure in a Boundary Layer", *Physics of Fluids*, Vol.7, pp. 2014-2024.

Lee, S. H. and Sung, H. J., 2007, "Direct Numerical Simulation of Turbulent Boundary Layer Over a Rod-Roughened Wall", *Journal of Fluid Mechanics*, Vol. 584, pp. 125-146.

Lee, S.-H., Kim, J. H. and Sung, H. J., 2008, "PIV Measurements of Turbulent Boundary Layer over a Rod-Roughened Wall", *International Journal of Heat and Fluid Flow*, Vol. 29, pp. 1679-1687.

Lee, J.-H. and Sung, H. J., 2008, "Effects of an Adverse Pressure Gradient on a Turbulent Boundary Layer", *International Journal of Heat and Fluid Flow*, Vol. 29, pp.568-578.

Lee, J.-H. and Sung, H. J., 2009, "Structures in Turbulent Boundary Layers Subjected to Adverse Pressure Gradients", *Journal of Fluid Mechanics*, Vol. 639, pp. 101-131.

Lee, J., Lee, J. H, Lee, J.-H. and Sung, H.J., 2010, "Coherent Structures in Turbulent Boundary Layers with Adverse Pressure Gradients", *Journal of Turbulence*, Vol. 11(28), pp. 1-20.

Leonardi, S., Orlandi, P., Smalley, R. J., Djenidi, L., and Antonia, T. A., 2003, "Direct Numerical Simulation of Turbulent Channel Flow with Transverse Square Bars on One Wall", *Journal of Fluid Mechanics*, Vol. 491, pp. 229-238.

Leonardi, S., Orlandi, P., Antonia, R. A., 2005, "A Method for Determining the Frictional Velocity in a Turbulent Channel Flow with Roughness in the Bottom Wall", *Experiments in Fluids*, Vol. 38, pp. 796-800.

Leonardi, S., Orlandi, P., Djenidi, L. and Antonia, R. A., 2004, "Structure of Turbulent Channel Flow with Square Bars on One Wall", *International Journal of Heat and Fluid Flow*, Vol. 24, pp. 384-392.

Leutheusser, H. J., 1963, "Turbulent Flow in Rectangular Ducts", *Proceedings of the American Society of Civil Engineers* (*Hydraulics Div.*), pp. 1-19.

Ligrani, P. M., and Moffat, R. J., 1986, "Structure of Transitionally Rough and Fully Rough Turbulent Boundary Layers", *Journal of Fluid Mechanics*, Vol. 162, pp. 69-98.

Liu, O. K., Kline, S. J., Johnston, J. P., 1966, "An Experimental Study of Turbulent Boundary Layers on Rough Walls", *Report MD-15*, Department of Mechanical Engineering, Stanford University.

Lu, S. S., and Willmarth, W. W., 1973, "Measurements of the Structure of the Reynolds Stress in a Turbulent Boundary Layer", *Journal of Fluid Mechanics*, Vol. 60, pp. 481-512.

Mazouz, A., Labraga, L., Tournier, C., 1998, "Anisotropy Invariants of Reynolds Stress Tensor in a Duct Flow and Turbulent Boundary Layer", *Journal of Fluids Engineering*, Vol. 120, pp. 280-284.

Mei, R., Adrian, R. J. Hanratty, T. J., 1991, "Particle Dispersion in Isotropic Turbulence under Stokes Drag and Basset Force with Gravitational Settling", *Journal of Fluid Mechanics*, Vol. 225, pp. 481-495.

Meinhart, C. D. and Adrian, R. J., 1995, "On the Existence of Uniform Momentum Zones in a Turbulent Boundary Layer", *Physics of Fluids*, Vol. 7(4), pp. 694-696.

Mejia-Alvarez, R. and Christensen, K. T., 2010, "Low-Order Representations of Irregular Surface Roughness and their Impact on a Turbulent Boundary Layer", *Physics* of Fluids, Vol. 22, pp. 015106

Millikan C. B., 1938, "A Critical Discussion of Turbulent Flows in Channels and Circular Tubes", In: Den Hartog J. P, Peters H, editors. *Proceedings of the Fifth International Congress on Applied Mechanics*. New York: Wiley, pp. 386-392.

Miyake, Y., Tsujimoto, K. and Nagai, N., 2002, "Numerical Simulation of Channel Flow with a Rib-Roughened Wall", *Journal of Turbulence,* Vol. 3 (1), pp. 035.

Moin, P., Shih, T.-H., Driver, D. and Mansour N. N., 1990, "Direct Numerical Simulation of a Three-Dimensional Turbulent Boundary Layer", *Physics of Fluids A*, Vol. 2, pp. 1846-1853.

Monty, J. P., Harun, Z., Marusic, I., 2011, "A Parametric Study of Adverse Pressure Gradient Turbulent Boundary Layers", *International Journal of Heat and Fluid Flow*, Vol. 32. 575-585.

Monty, J. P., Hutchins, N., NG, H. C. H,. Marusic, I. and Chong, M. S., 2009, "A Comparison of Turbulent Pipe, Channel and Boundary Layer Flows", *Journal of Fluid Mechanics*, Vol. 632, pp. 431-442.

Moser, R. D., Kim, J. and Mansour N. N., 1999, "Direct Numerical Simulation of Turbulent Channel Flow up to $Re_\tau = 590$", *Physics of Fluids*, Vol. 11, pp. 943-945.

Nagano, Y. Tsuji, T. and Houra T., 1998, "Structure of Turbulent Boundary Layer Subjected to Adverse Pressure Gradient", *International Journal of Heat and Fluid Flow*, Vol. 19, pp. 563-572.

Nagano, Y., Hattori, H., and Houra, T., 2004, "DNS of Velocity and Thermal Fields in Turbulent Channel Flow with Transverse-Rib Roughness", *International Journal of Heat and Fluid Flow*, Vol. 25, pp. 393-403.

Nakagawa, H. and Nezu, I., 1977, "Prediction of the Contributions to the Reynolds Stress from Bursting Events in Open-Channel Flows", *Journal of Fluid Mechanics*, Vol. 80, pp. 99-128.

Nakayama, A., Yokota, D., 2002, "Rough-Surface Boundary Layer in Pressure Gradients", *Mem. Grad. School Sci. and Technol.*, Kobe Univ., Vol. 20-A: pp. 1-14.

Nickels, T. B., 2004, "Inner Scaling for Wall-Bounded Flows Subject to Large Pressure Gradients", *Journal of Fluid Mechanics*, Vol. 521, pp. 217-239.

Nickels, T. B., Marusic, I., Hafez, N., Hutchins, N. and Chong, M. S., 2007, "Some Predictions of the Attached Eddy Model for a High Reynolds Number Boundary Layer", *Philosophical Transactions of the Royal Society A*, Vol. 365, pp. 807-822.

Nikuradse, J., 1933, "Strömungsgesetze in Rauhen Rohren", *VDI-Forsch*. 361 (Engl. Transl. 1950. Laws of Flow in Rough Pipes. *NACA TM* 1292).

Okamoto, S., Seo, S., Nakaso, K., Kawai, I., 1993, "Turbulent Shear Flow and Heat Transfer over the Repeated Two-Dimensional Square Ribs on Ground Plane", *Journal of Fluids Engineering*, Vol. 115, pp. 631-637.

Osaka, H. and Mochizuki, S., 1988, "Coherent Structure of a d-type Rough Wall Boundary Layer", In *Transport Phenomena in Turbulent Flows: Theory, Experiment and Numerical Simulation* (ed. M. Hirata and N. Kasagi), pp. 199-211. Hemisphere.

Pailhas, G. Touvet, Y. and Aupoix, B., 2008, "Effects of Reynolds Number and Adverse Pressure Gradient on a Turbulent boundary Layer Developing on a Rough Surface", *Journal of Turbulence*, Vol. 9(43), pp.1-28.

Perry, A. E. and Jourbert, P. N., 1963, "Rough-Wall Boundary Layers in Adverse Pressure Gradients", *Journal of Fluid Mechanics*, Vol. 17, pp. 193-206.

Perry, A. E., Schofield, W. H., and Joubert, P. N., 1969, "Rough Wall Turbulent Boundary Layers", *Journal of Fluid Mechanics*, Vol. 37, pp. 383-413.

Piirto, M., Saarenrinne, P., Eloranta, H. and Karvinen, R., 2003, "Measuring Turbulence Energy with PIV in Backward-Facing Step Flow", *Experiments in Fluids*, Vol. 35, pp. 219-236.

Pope, S.B., 2000, "Turbulent Flows", Cambridge University Press.

Prandtl, L., 1925, "U¨ ber die ausgebildete Turbulenz", *ZAMM*, Vol. 5, pp. 136-139.

Prasad, A.K., 2000, "Particle Image Velocimetry", *Current Science*, Vol. 79, pp. 51-57.

Purtell, L. P., Klebanoff, P. S. and Buckley F. T., 1981, "Turbulent Boundary Layer at Low Reynolds Number", *Physics of Fluids*, Vol. 24 pp. 802-811.

Raffel, M., Willert, C.E. and Kompenhaus, J., 1998, "Particle Image Velocimetry: A Practical Guide", Springer Verlag.

Rapauch, M. R., 1981,"Conditional Statistics of Reynolds Stress in Rough-Wall and Smooth-Wall Turbulent Boundary Layers", *Journal of Fluid Mechanics*, Vol. 108, pp. 363-382.

Raupach, M. R., Antonia, R. A. and Rajagopalan, S., 1991, "Rough-Wall Turbulent Boundary Layers", *Applied Mechanics Reviews*, Vol. 108, pp. 1-25.

Robinson, S. K., Kline, S. J., Spalart, P. R., 1989, "A Review of Quasi-Coherent Structures in a Numerically Simulated Turbulent Boundary Layer", *NASA TM*-102191.

Robinson, S. K., 1991, "Coherent Motion in the Turbulent Boundary Layer", *Annual Reviews in Fluid Mechanics*, Vol. 23, pp. 601-639.

Robinson, S. K., 1993, "The Kinematics of Turbulent Boundary Layer Structure", *NASA Tech. Mem*. 103859.

Saikrishnan, N., Marusic, I. and Longmire, E. K., 2006, "Assessment of Dual Plane PIV Measurements in Wall Turbulence using DNS Data", *Experiments in Fluids*, Vol. 46, pp. 265-278.

Samuel, A.E. and Joubert, P.N., 1974, "A Boundary Layer Developing in an Increasingly Adverse Pressure Gradient", *Journal of Fluid Mechanics*, Vol. 66, pp. 481-505.

Scarano, F. and Riethmuller, M., 1999, "Iterative Multigrid Approach in PIV Image Processing with Discrete Window Offset", *Experiments in Fluids*, Vol. 26, pp. 513-523.

Schlichting, H., 1979, "Boundary-Layer Theory", Seventh ed. McGraw-Hill, New York.

Schofield, W. H., 1975, "Measurements in Adverse-Pressure Gradient Turbulent Boundary Layers with a Step Change in Surface Roughness", *Journal of Fluid Mechanics*, Vol. 70, pp. 573-593.

Schultz, M. P. and Flack, K. A., 2005, "Outer Layer Similarity in Fully Rough Turbulent Boundary Layers", *Experiments in Fluid*, Vol. 38(3), pp. 328-340.

Schultz, M. P. and Flack, K. A., 2007, "The Rough-Wall Turbulent Boundary Layer from the Hydraulically Smooth to the Fully Rough Regime", *Journal of Fluid Mechanics*, Vol. 580, pp. 381-405.

Schwarz, W. R., and Bradshaw, P., 1994, "Turbulence Structural Changes for a Three-Dimensional Turbulent Boundary Layer in a 30° Bend", *Journal of Fluid Mechanics*, Vol. 272, pp. 183-210.

Sendstad, O. and Moin, P., 1992, "The near Wall Mechanics of Three-Dimensional Turbulent Boundary Layers", Dept. of Mech. Engng, Stanford University, Thermosciences Div. Rep. TF-57.

Shah, M. K., Agelinchaab, M. and Tachie, M. F., 2008, "Influence of PIV Interrogation Area on Turbulent Statistics up to 4^{th} Order Moments in Smooth and Rough Wall Turbulent Flows", *Experimental Thermal and Fluid Science*., Vol. 32, pp. 725-747.

Shah, M. K., and Tachie, M. F., 2008, "PIV Study of Turbulent Flow in Asymmetric Converging and Diverging Channels", *ASME Journal of Fluid Engineering*, Vol. 130, pp.1-15.

Skåre, P. E. and Krogstad, P.-Å., 1994, "A Turbulent Equilibrium Boundary Layer near Separation", *Journal of Fluid Mechanics*, Vol. 272, pp. 319-348.

Spalart, P. R., 1988, "Direct Simulation of a Turbulent Boundary Layer up to Re_θ = 1410", *Journal of Fluid Mechanics*, Vol. 187, pp. 61-98.

Spalart, P. R., and Watmuff, J. H., 1993, "Experimental and Numerical Study of a Turbulent Boundary Layer with Pressure Gradients", *Journal of Fluid Mechanics*, Vol. 249, pp. 337-371.

Stern, F., Muste, M., Berninati, L. M. and Eichinnger, W. E., 1999, "Summary of Experimental Uncertainty Assessment Methodology with Example", *IIHR Technical Report* no. 406, The University of Iowa, Iowa City, I.A.

Tachie, M. F., 2007, "Particle Image Velocimetry Study of Turbulent Flow over Transverse Square Ribs in an Asymmetric Diffuser", *Physics of Fluids*, Vol. 19, pp. 1-15.

Tachie, M. F., and Shah, M. K., 2008, "Favourable Pressure Gradient Flow over Straight and Inclined Ribs on Both Channel Walls ", *Physics of Fluids*, Vol. 20, pp. 1-22.

Tachie, M. F., Agelinchaab, M. and Shah, M. K., 2007, "Turbulent Flow over Transverse Ribs in Open Channel with Converging Side Walls", *International Journal Heat Fluid Flow*, Vol. 28, pp. 683-707.

Tachie, M. F., Paul, S. S., Agelinchaab, M., and Shah, M. K., 2009, "Structure of Turbulent Flow Over 90° and 45° Transverse Ribs", *Journal of Turbulence*, Vol. 10, pp. 1-20.

Tani, J*., 1987, "Turbulent* Boundary Layer Development *over Rough* Surfaces", In: Perspectives in Turbulence Studies. Springer.

Tay, G. F. K., Kuhn, D. C. S., and Tachie, M. F., 2009, "Influence of Adverse Pressure Gradient on Rough-Wall Turbulent Flows", *International Journal of Heat and Fluid Flow*, Vol. 30 (2), pp. 249-265.

Teitel, M. and Antonia, R. A., 1991, "Comparison between Outer Region of Turbulent Boundary Layer and Channel Flows", *Experiments in Fluids*, Vol. 11, pp, 203-204

Tennekes, H. and Lumley, J.L., 1972, "A First Course in Turbulence", MIT Press.

Theodorsen, T., 1952, "Mechanism of Turbulence", In *Proc. Second Midwestern Conference on Fluid Mechanics*. Mar. 17-19, Ohio State University, Columbus, Ohio.

Tomkins, D. D. and Adrian R. J., 2003, "Spanwise Structure and Scale Growth in Turbulent Boundary Layers", *Journal of Fluid Mechanics*, Vol. 490, pp. 37-74.

Townsend, A. A., 1961,"Equilibrium Layers and Wall Turbulence", *Journal of Fluid Mechanics*, Vol. 11, pp. 97-120.

Townsend, A. A., 1976, "The Structure of Turbulent Shear Flow", 2nd ed. Cambridge University Press.

Tsikata, J. M. and Tachie, M. F., 2012, "Adverse Pressure Gradient Turbulent Flows over Rough Walls", *Int. Journal of Heat and Fluid Flow* (*In Press,* DOI: http://dx.doi.org/10.1016/j.ijheatfluidflow.2012.11.001).

Volino, R. J. Schultz, M. P. Flack, K. A., 2007, "Turbulence Structure in Rough- and Smooth-Wall Boundary Layers," *Journal of Fluid Mechanics*, Vol. 592, pp. 263-293.

Volino, R. J., Schultz, M. P., and Flack, K. A., 2009, "Turbulence Structure in a Boundary Layer with Two-Dimensional Roughness", *Journal of Fluid Mechanics*, Vol. 635, pp. 75-101.

von Karman, T., 1930, "Mechanishe aehnlickeit and Turbulenz". Nachr Ges Wiss Göttingen, pp. 58-76.

Wallace, J. M., Eckelmann, H., and Brodkey, R. S., 1972, "The Wall Region in Turbulent Shear Flow", *Journal of Fluid Mechanics*, Vol. 54, pp. 39-48.

Wei, T. and Willmarth, W. W., 1989, "Reynolds-Number Effects on the Structure of a Turbulent Channel Flow", *Journal of Fluid Mechanics*, Vol. 204, pp. 57-95.

Westerweel, J., Draad, A. A., Th. Van der Hoeven, J. G., and Oord van, J., 1996, "Measurement of Fully Developed Turbulent Pipe Flow with Digital Particle Image Velocimetry", *Experiments in Fluids*, Vol. 20, pp. 165-177.

Willert, C. E. and Gharib, M., 1991, "Digital Particle Image Velocimetry", *Experiments in Fluids*, Vol. 10, pp. 181-193.

Willmarth, W. W. and Lu, S., 1972, "Structure of the Reynolds Stress near The Wall", *Journal of Fluid Mechanics*, Vol. 55 (1) pp. 65-92.

Wu, Y. and Christensen, K. T., 2006, "Population Trends of Spanwise Vortices in Wall Turbulence", *Journal of Fluid Mechanics*, Vol. 568, pp. 55-76.

Wu, Y. and Christensen, K. T., 2007, "Outer Layer Similarity in the Presence of a Practical Rough-Wall Topography", *Physics of Fluids*, Vol. 19, pp. 085108.

Zagarola, M. V. and Smits, A. J., 1998, "Mean-Flow Scaling of Turbulent Pipe Flow", *Journal of Fluid Mechanics*, Vol. 373, pp. 33-79.

Zhou, J., Adrian, R. J., Balachandar, S. and Kendall, T. M., 1999, "Mechanisms for Generating Coherent Packets of Hairpin Vortices in Channel Flow", *Journal of Fluid Mechanics*, Vol. 387, pp. 353-396.

Zhou, J., Meinhart, C. D., Balachandar, S. and Adrian, R. J., 1997, "Formation of Coherent Hairpin Packets in Wall Turbulence", In *Self-Sustaining Mechanisms of Wall Turbulence* (ed. R. L. Panton), pp. 109-134, Computational Mechanics, Southampton, UK.

APPENDIX A

FLOW QUALIFICATION

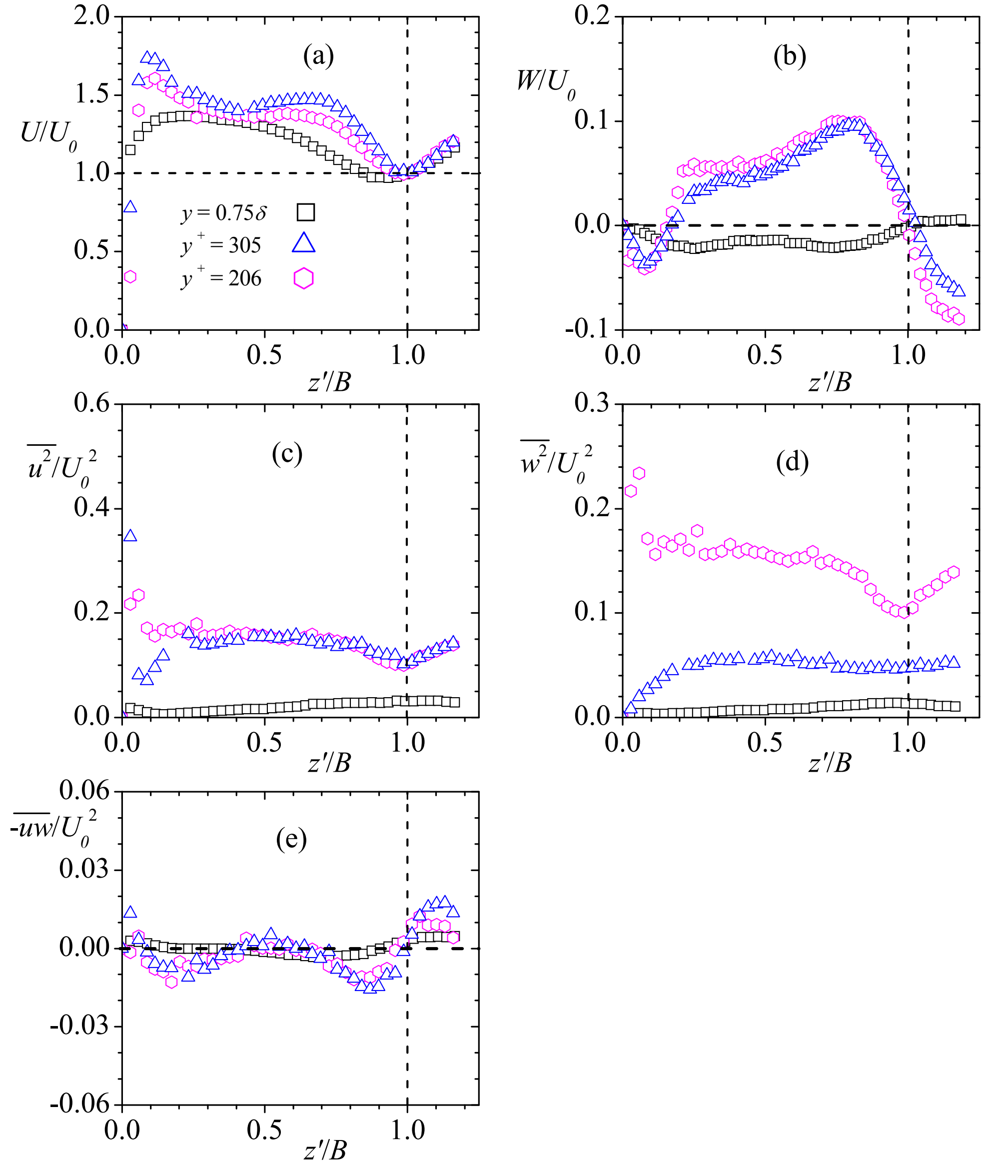

Figure A.1: Distribution of mean velocities (U/U_0 and W/U_0) Reynolds stresses ($\overline{u^2}/U_0^2$, $\overline{w^2}/U_0^2$ and $-\overline{uw}/U_0^2$) for $R_8S_P\alpha_{90}$ ribs in the parallel section at various y-locations.

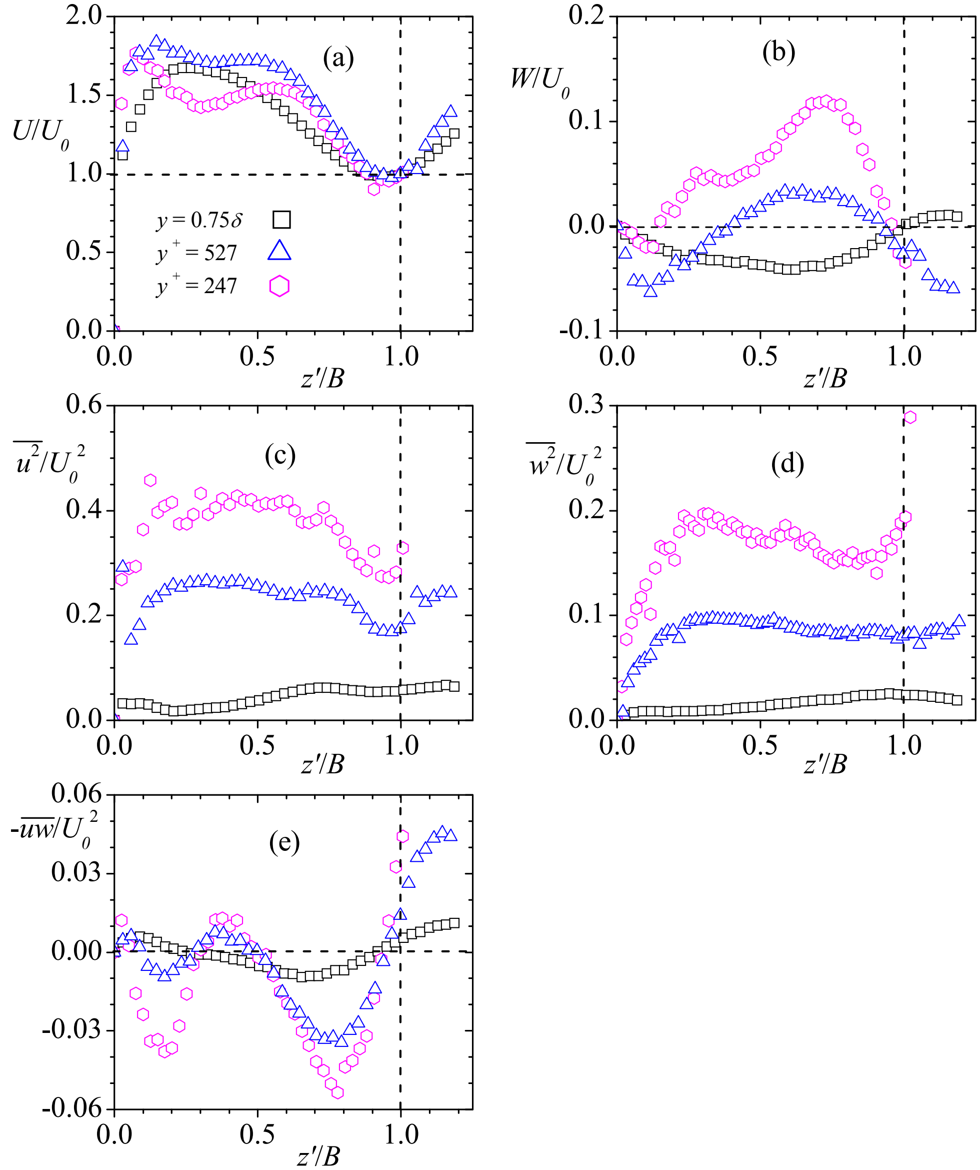

Figure A.2: Distribution of mean velocities (U/U_0 and W/U_0) Reynolds stresses ($\overline{u^2}/U_0^2$, $\overline{w^2}/U_0^2$ and $-\overline{uw}/U_0^2$) for $R_8S_D\alpha_{90}$ ribs in the diverging section at various y-locations.

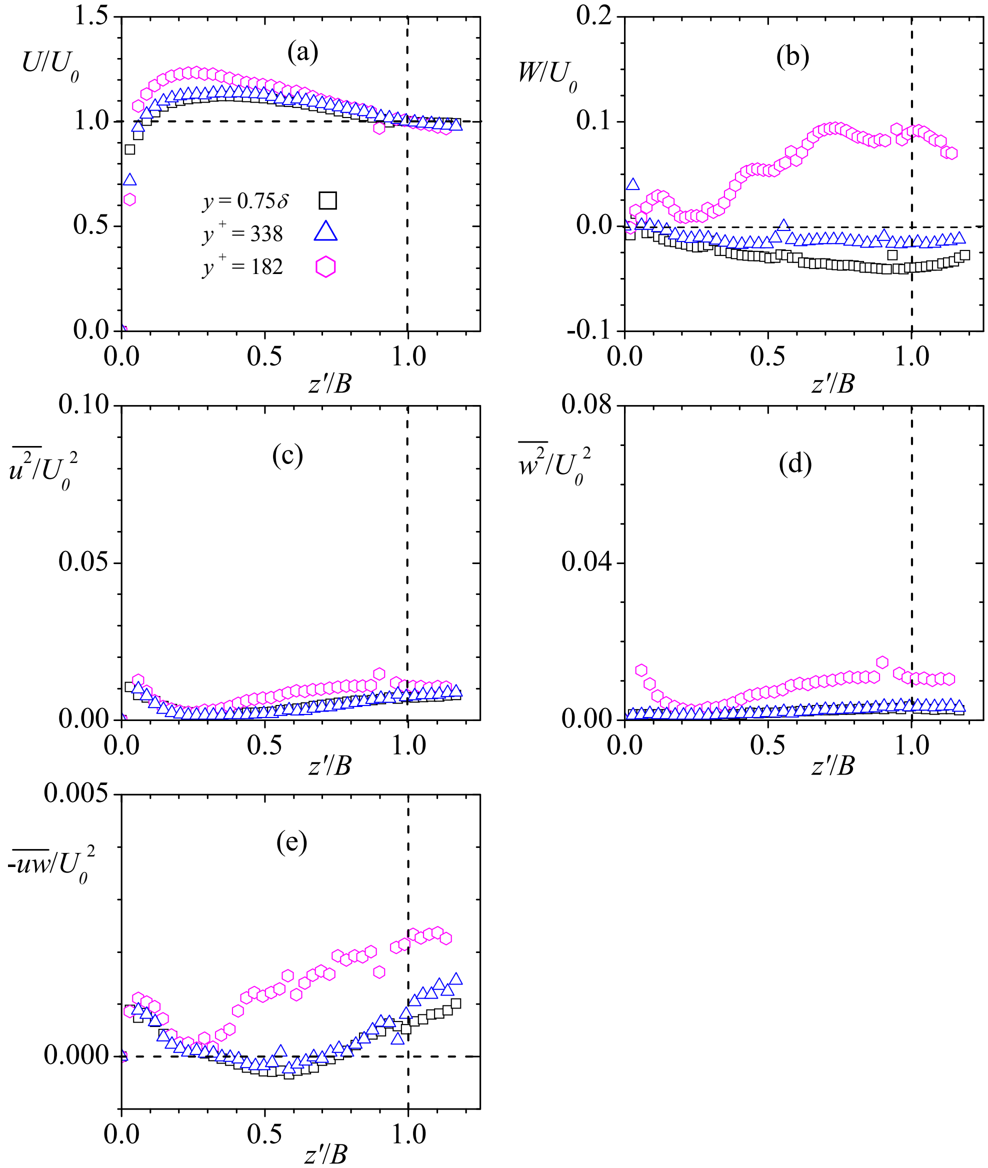

Figure A.3: Distribution of mean velocities (U/U_0 and W/U_0) Reynolds stresses ($\overline{u^2}/U_0^2$, $\overline{w^2}/U_0^2$ and $-\overline{uw}/U_0^2$) for $R_8S_P\alpha_{45}$ ribs in the parallel section at various y-locations.

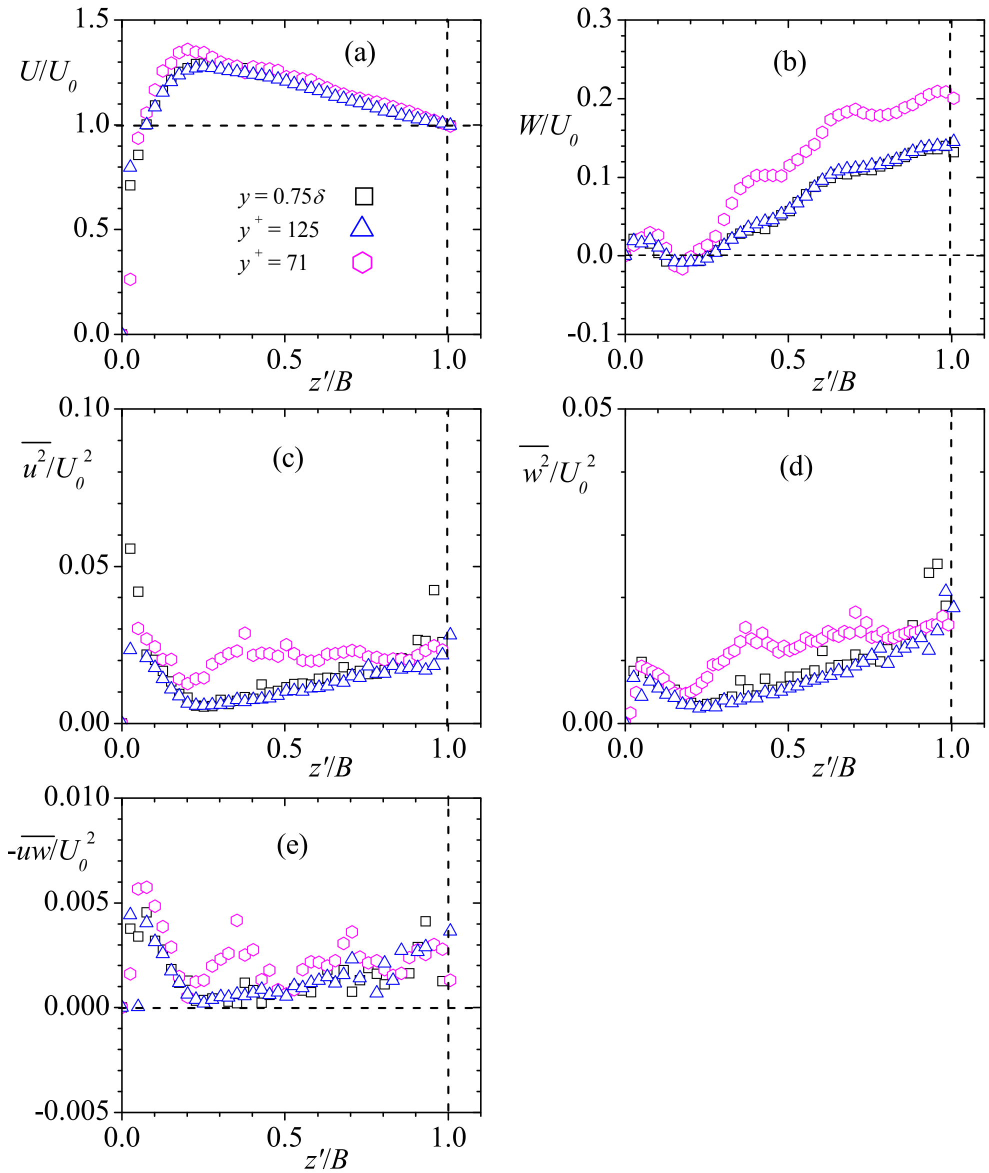

Figure A.4: Distribution of mean velocities (U/U_0 and W/U_0) Reynolds stresses ($\overline{u^2}/U_0^2$, $\overline{w^2}/U_0^2$ and $-\overline{uw}/U_0^2$) for $R_8S_D\alpha_{45}$ ribs in the diverging section at various y-locations.

APPENDIX B

ERRORS AND ERROR ANALYSIS IN PIV

The errors inherent in PIV measurements are discussed in this appendix. The sources of errors and the techniques used to analyze the error in the present study are reported. The complete uncertainty analysis for this study is also presented.

B.1 MEASUREMENT ERROR

Measurement is an act of assigning a value to some physical variables. The relative closeness of agreement between an experimentally determined value of a quantity to its true value indicates the accuracy of the measurement. The difference between the experimentally determined value and the true value is the measurement error. However, the true values of measured quantities are unknown. Therefore, estimation of the error must be made and that estimate is called an uncertainty.

Coleman and Steele (1995) have presented detailed uncertainty assessment methodology. Stern *et al.* (1999) provided comprehensive guidelines for incorporation of uncertainty assessment methodology into the test process and documentation of results. In general, the total error is composed of two components: precision, P, and bias, B. According to Coleman and Steele (1995), precision error contributes to the scatter of the data, and bias error is due to systematic error. The evaluation of bias uncertainty in PIV measurements and its contribution to the total measurement uncertainty was reported by Gui *et al.* (2001). Forliti *et al.* (2000) reported that the evaluation of bias and its gradient can be minimized effectively by using Gaussian digital masks on the interrogation window. This will eventually reduce the measurement uncertainty. In PIV measurements, the sources of error include: inappropriate selection of time between image pairs, sub-pixel displacement bias, insufficient sample size, effect of velocity gradients, spatial resolution. The uncertainties include particle response to fluid motion, light sheet positioning, light pulse timing, and the error arising from the peak-finding algorithm to determine the average particle displacement.

B.1.1 MINIMIZING MEASUREMENT ERROR

Errors in PIV measurements can be minimized through careful selection of experimental conditions such as time between image pairs. The major contributor to the bias error is peak locking. Peak locking is due to sub-pixel particle displacement being biased toward integer values. During image acquisition and image processing, a number of steps were taken to reduce peak locking. The particle image diameters were estimated to be approximately 2.0 pixels and 2.3 pixels. These values are in good agreement with the value of 2.0 pixels recommended by Raffel *et al.* (1998) to minimize peak locking. Figure B.1 shows histograms of typical instantaneous images over the smooth wall and a rough wall in both parallel and diverging sections. No discernible peak locking can be detected, suggesting that the contribution of peak locking to the bias error is minimal. The large sample size of 6000 instantaneous images also reduces the precision error.

In flows with large mean velocity gradients (for example, boundary layer flows), the effect of velocity gradient bias errors is an important concern. The velocity gradients tend to broaden the displacement peak and reduce the amplitude. It was recommended by Keane and Adrian (1992) that for the cross-correlation technique, to achieve an acceptable valid detection probability of 95%, the acceptable velocity gradients should follow the expression:

$$\frac{M_f \Delta U_y \Delta t}{d} < 0.03 \qquad \text{(B.1)}$$

where, $\Delta U_y = (\partial U/\partial y)(d/2)$, Δt is the time between the two laser pulses and d is the length of the interrogation area. The estimated values using the expression on the left-hand side of Eq. B.1 in the inner region of the smooth wall and a typical rough wall are summarized in Table B.1. The table reveals that Eq. B.1 is satisfied over the smooth and rough walls.

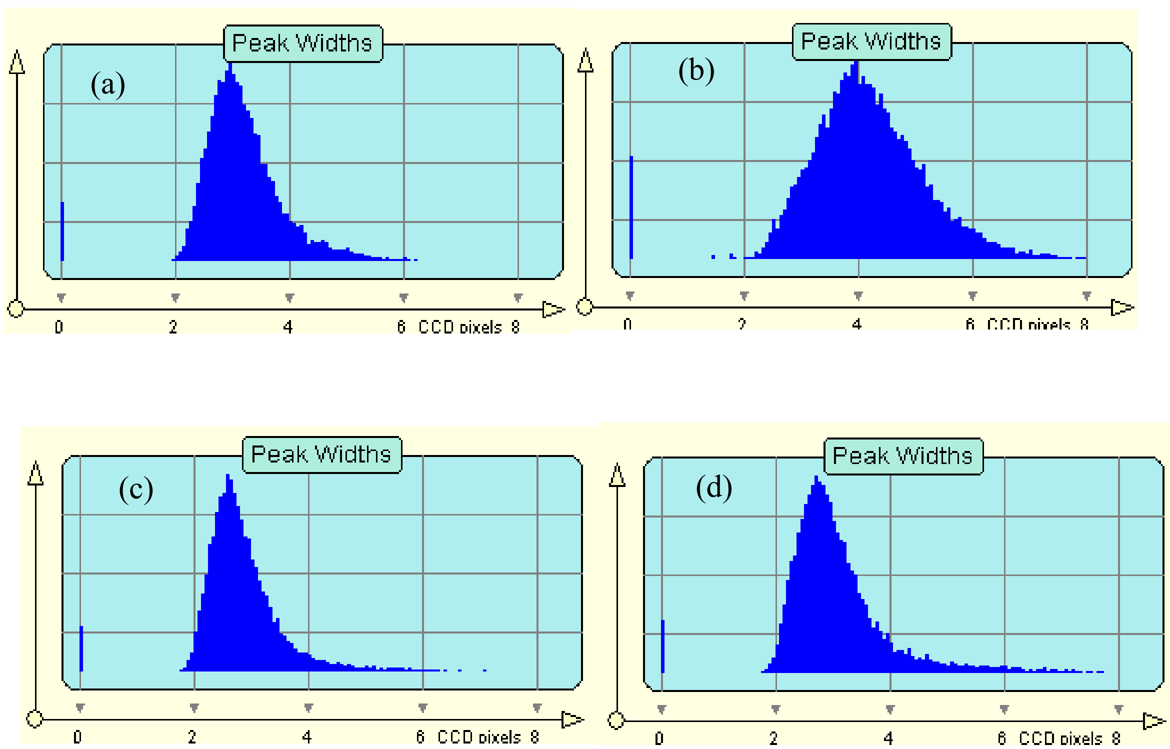

Figure B.1: Histograms of typical instantaneous images over smooth wall and a typical rough wall: (a) SMS_P, (b) SMS_D, (c) $R_8S_P\alpha_{90}P_0$ and (d) $R_8S_D\alpha_{90}P_0$.

Table B.1: Summary of Results from Eq. B.1 over selected wall boundary conditions

Test	y/δ (–)	M_f (–)	Δt (s)	$\partial U/\partial y$ (s^{-1})	ΔU_y (ms^{-1})	$M_f \Delta U_y \Delta t/d$ (–)
SMS_P	0.094	3.10E–01	2.40E–04	29.32E+00	5.58E–03	1.09E–03
SMS_D	0.091	3.10E–01	3.20E–04	7.87E+00	1.50E–03	3.91E–04
$R_8S_P\alpha_{90}$	0.108	3.05E–01	2.40E–04	32.77E+00	6.36E–03	1.20E–03
$R_8S_D\alpha_{90}$	0.106	3.05E–01	3.45E–04	13.66E+00	2.65E–03	7.19E–04

For PIV measurements, the interrogation area size should be as small as possible in order to improve spatial resolution. With improved spatial resolution, the smallest spatial scales in the flow are resolved. In contrast, the dynamic range of the measured velocity increases with larger interrogation area sizes, suggesting that larger interrogation area sizes are desirable for achieving large velocity dynamic range. Therefore, a compromise between spatial resolution and velocity dynamic range is required in selecting interrogation area size. The dynamic range in PIV measurements based on pixel displacement level is the displacement divided by the sub-pixel accuracy. The sub-pixel accuracy is a function of many parameters, for which most are beyond the PIV system itself and it is therefore often unknown. Usually, 0.1 pixel accuracy is used as a realistic value (Scarano and Riethmuller, 1999). In the present measurements, it was ensured that particle displacement was less than ¼ of the size of the interrogation area as recommended by Willert and Gharib (1991). For a typical PIV interrogation area of 32 pixels $\times$ 32 pixels, the maximum displacement is about 8 pixels so that the velocity dynamic range is of the order of 8/0.1 = 80.

B.1.2 ERROR ESTIMATION

Adrian (1991) argued that random influences can be summed into a single error, and this can be found by repeating the measurement. According to Prasad (2000), the random influences in PIV generally scale with the particle image diameter as:

$$\sigma_{random} = cd_i \tag{B.2}$$

where, d_i is the effective particle diameter and c is a constant whose value is between 0.05 and 0.10, depending upon experimental conditions. From the foregoing, a complete uncertainty analysis of the PIV measurement involves identifying and quantifying both the bias and the precision errors in each part of the measurement procedure. The uncertainty analysis of the present measurements follows the AIAA standard derived and explained by Coleman and Steele (1995).

B.1.2.1 Biased Error

In PIV measurements, the instantaneous velocity at any point is the average fluid velocity for an interrogation region and is described by the following equation (Gui *et al.* 2001):

$$u_i = \frac{\Delta s L_0}{\Delta t L_I}, \tag{B.3}$$

where i equals 1 and 2 for the x and y coordinates, respectively, Δt is the time interval between laser pulses, Δs is the particle displacement from the correlation algorithm, L_0 is the width of the camera view in the object plane, and L_1 is the width of the digital image. The bias limit of the measured velocity is determined with a root-sum-square (RSS) of the elementary bias limits based on the sensitivity coefficients given as:

$$B_{u_i}{}^2 = \theta_{L_0}^2 B_{L_0}^2 + \theta_{L_I}^2 B_{L_I}^2 + \theta_{\Delta s}^2 B_{\Delta s}^2 + \theta_{\Delta t}^2 B_{\Delta t}^2, \tag{B.4}$$

where the sensitivity coefficients, θ_x, are defined as

$$\theta_X = \frac{\partial u_i}{\partial X}, \quad X = (L_0,\ L_I, \Delta t, \Delta s) \tag{B.5}$$

The classification of bias error sources and contribution to the bias limits for U and V were performed for the various test conditions. An illustration of this classification has been provided in Table B.2 and Table B.3 for the inner region of the fully developed channel flow over smooth wall. The manufacturer's specifications of the elementary bias limits for Δt and Δs are also shown in Tables B.1 and B.2. The bias limit for L_0 is obtained from a calibration procedure. Note that percentage bias errors in U and V are both expressed as a percentage of U.

Table B.2: Bias limits of the local streamwise mean velocity (U) in the inner region of SMS_P (at $y/\delta = 0.094$).

Variable	Magnitude	B_x	θ_x	$B_x\theta_x$	$(B_x\theta_x)^2$
L_0 (m)	4.88E−02	5.00E−04	5.86E+00	2.93E−03	8.59E−06
L_I (pix)	2.05E+03	5.00E−01	−1.40E−04	−6.98E−05	4.87E−09
Δt (s)	2.40E−04	1.00E−07	−1.19E+03	−1.19E−04	1.42E−08
Δs (pix)	2.88E+00	1.27E−02	9.92E−02	1.26E−03	1.59E−06
U (m/s)	2.86E−01				
				$\Sigma(B_x\theta_x)^2$ =	1.02E−05
				Bias error =	3.19E−03
				%Bias error =	1.12%

Table B.3: Bias limits of the local wall-normal mean velocity (V) in the inner region of SMS_P (at $y/\delta = 0.094$).

Variable	Magnitude	B_x	θ_x	$B_x\theta_x$	$(B_x\theta_x)^2$
L_0 (m)	4.88E-02	5.00E-04	−4.88E-02	−2.44E-05	5.95E-10
L_I (pix)	2.05E+03	5.00E-01	1.16E-06	5.80E-07	3.37E-13
Δt (s)	2.50E-04	1.00E-07	9.92E+00	9.92E-07	9.83E-13
Δs (pix)	2.40E-02	1.27E-02	9.92E-02	1.26E-03	1.59E-06
V (m/s)	-2.38E-03				
				$\Sigma(B_x\theta_x)^2$ =	1.59E-06
				Bias error =	1.26E-03
				%Bias error =	0.44%

B.1.2.2 Precision Error

The precision error, P, of a measured variable, X is given by

$$P_x = \frac{K \cdot \sigma}{\sqrt{N}}, \tag{B.6}$$

where K is the confidence coefficient and has a value of 2 for a 95% confidence level for sample size of N images. The symbol σ is the standard deviation of the sample of N readings of the variable X, and is defined as:

$$\sigma = \sqrt{\frac{1}{N-1}\sum_{k=1}^{N}\left(X_k - \overline{X}\right)^2}\ , \qquad \text{(B.7)}$$

where $\bar{X}$ is the mean given by the equation;

$$\overline{X} = \frac{1}{N}\sum_{k=1}^{N} X_k \quad . \qquad \text{(B.8)}$$

In order to compute the standard deviation using Eq. B.7, 6000 images were acquired and the standard deviations of U and V were obtained at the same locations in the inner and outer regions. In the inner region, for example, the standard deviation for U and V were approximately 14.1% and 5.7% of the local streamwise velocity, respectively. From Eq. B.6, the estimated precision errors of U and V for SMS_P are approximately 0.36% and 0.15% respectively.

B.1.2.3 Total Error

The total uncertainty, E, in the result u_i is the RSS of the bias and precision limits, given by

$$E_X = \sqrt{B_X^2 + P_X^2} \qquad \text{(B.9)}$$

The total uncertainty was obtained from the values of the bias and precision errors obtained earlier and Eq. B.9 to be ±1.62% and ±0.72% for U and V, respectively, in the inner region. The measurement uncertainty in turbulence intensities and Reynolds stresses was estimated to be ±4% and ±8%, respectively. The uncertainty in the triple velocity products and energy budget terms is on the order of ±12%. Close to the ribs, the uncertainties in the mean velocities are estimated to be ±2.25% and ±1.72% of the local mean velocity, respectively, for U and V. For the Reynolds stresses uncertainty close to the ribs is estimated to be ±10%.

APPENDIX C

WALL-NORMAL MEAN VELOCITY AND MOMENTUM FLUX

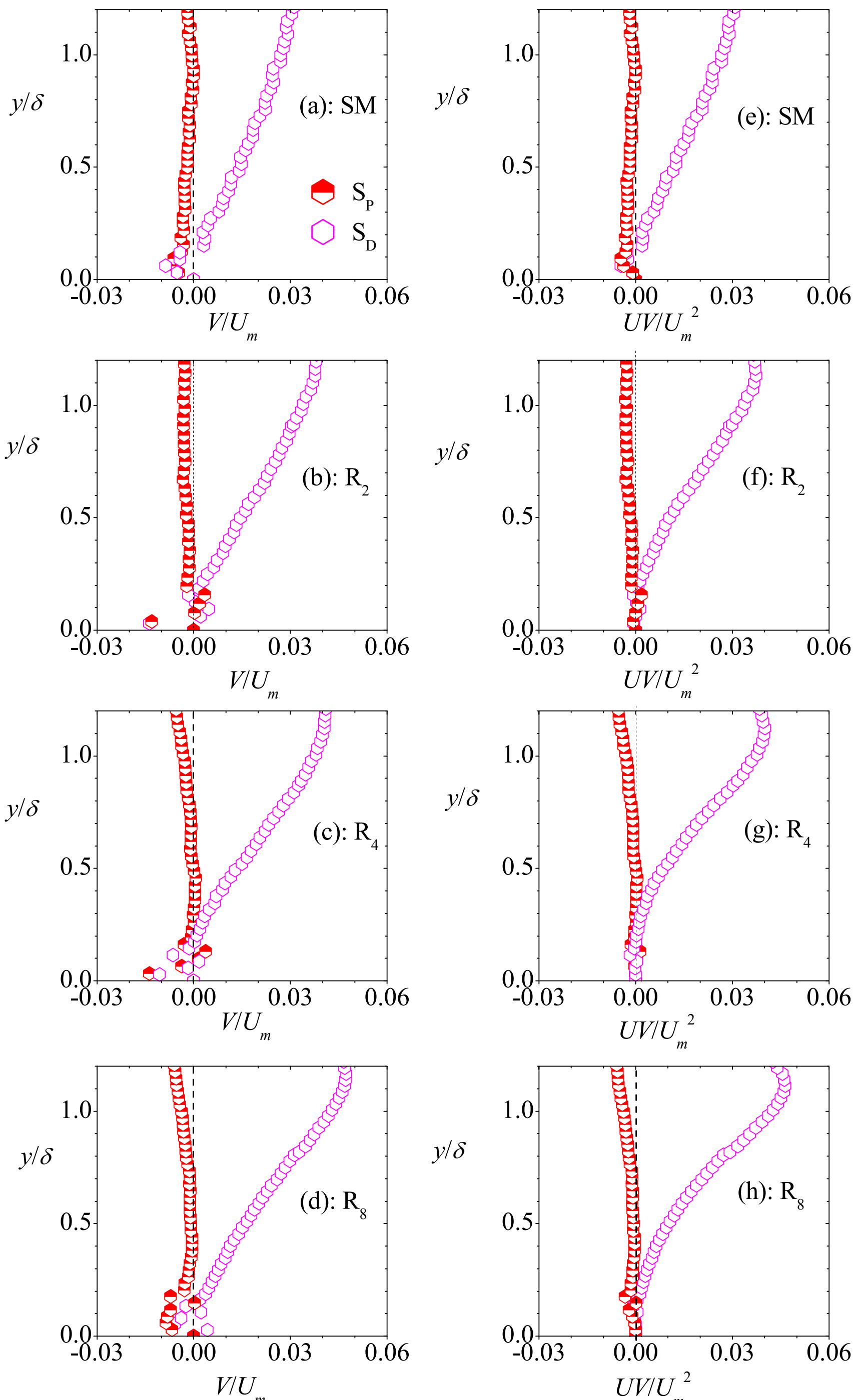

Figure C.1: Comparison of wall-normal velocity (V/U_m) and mean momentum flux (UV/U_m^2) in the parallel and diverging sections over the smooth and rough walls.

APPENDIX D

GALILEAN DECOMPOSITION OVER *D*-TYPE 90° RIBS

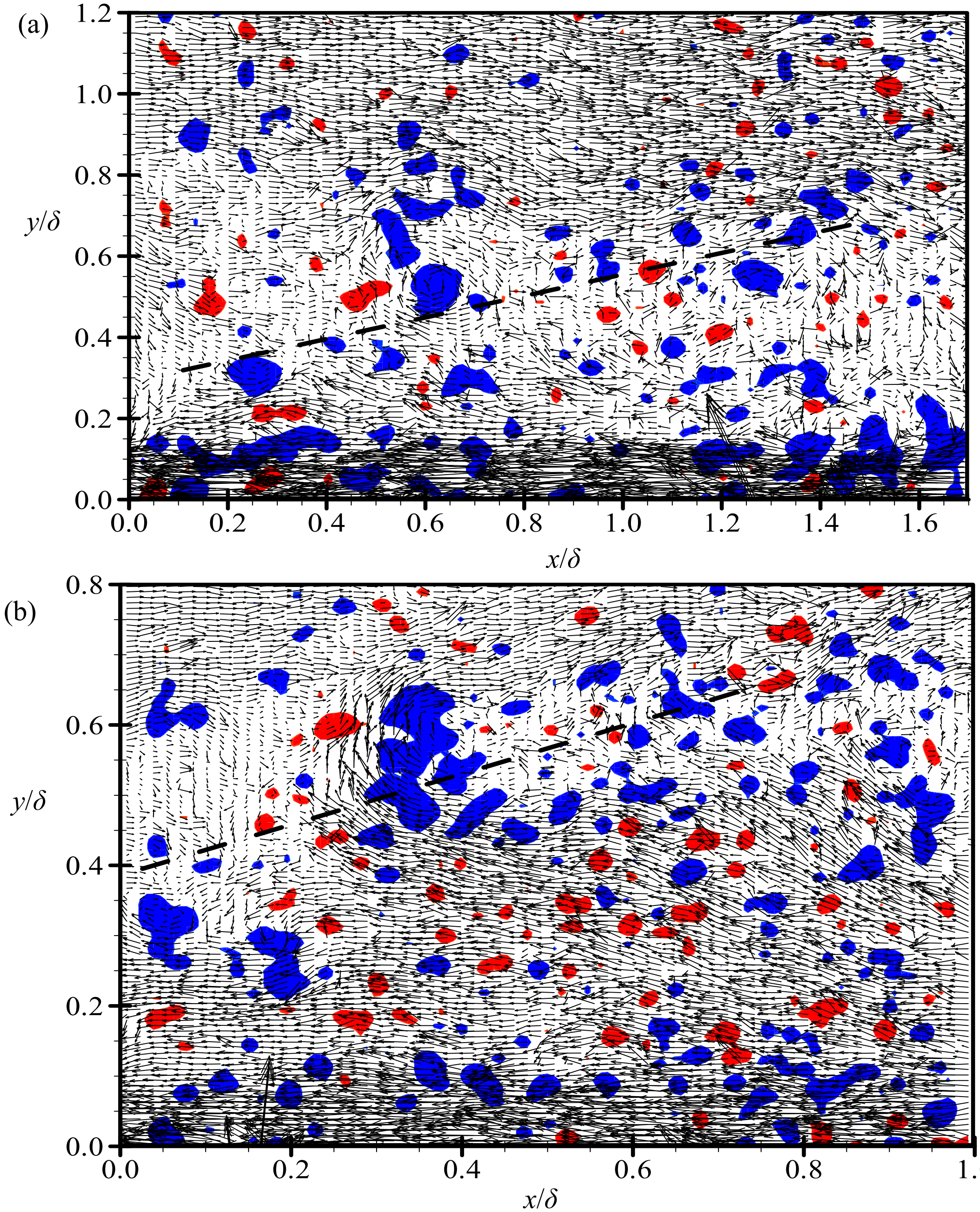

Figure D.1: Galilean decomposed instantaneous velocity fields over *d*-type rough wall in the *x*-*y* plane with contours of swirling strength at the background: (a) $R_2S_P\alpha_{90}$; $U_c = 0.80U_m$ and (b) $R_2S_D\alpha_{90}$; $U_c = 0.71U_m$.